University of Alberta

Design of Amorphous Diffusion Barriers for Cu Metallization

by

Neda Dalili

A thesis submitted to the Faculty of Graduate Studies and Research
in partial fulfillment of the requirements for the degree of

Doctor of Philosophy

in

Materials Engineering

Chemical and Materials Engineering Department

Spring 2014
Edmonton, Alberta

Dedications

To millions of children who get no chance at education.

To the memory of my father and his devotion to freedom.

To my family, who supported me each step of the way.

Abstract

The incorporation of Cu interconnects into the manufacturing of integrated circuits has accompanied several modifications to the fabrication process and the associated material systems. The new fabrication process involves the development of dual damascene process, while the new materials systems include development of diffusion barrier materials. The latter imposes a critical challenge as Cu is a fast diffuser in Si and the adjacent dielectric layers, and results in device deterioration and failure. Technology development has been driven mainly by continuous feature size scaling, thus the developed barrier will be required to perform satisfactorily at the continuously reduced thicknesses. The conventional barriers used for Cu interconnects are TaN_x based films which require the deposition of an additional Cu seed layer prior to filling of the interconnects by electrochemical deposition. In the face of reducing feature size and barrier thickness, there has been great interest in developing diffusion barriers that are amenable to direct electrodeposition of Cu without the need for a seed layer. However, there is a need for a suitable guide for selecting material systems suitable for diffusion barrier applications.

In this thesis, a systematic approach is adopted to select an amorphous, low resistivity diffusion barrier material with the possibility of direct electrodeposition of Cu. After comprehensive consideration of possible alloys, the Ta-Rh system is selected as the candidate barrier. Thermodynamic calculations are performed to select the most stable amorphous composition in the system. The predictions made based on the thermodynamic calculation are verified by detailed structural

characterizations. The performance of the selected $TaRh_x$ alloy as a diffusion barrier is evaluated by metallurgical and electrical characterizations. The metallurgical characterizations are performed by *in-situ* and *ex-situ* heating experiments on Si/diffusion barrier/Cu stacks. The common issues associated with *in-situ* transmission electron microscopy heating of Cu metallization stacks are identified and addressed. The electrical characterizations are performed by monitoring the capacitance-voltage characteristics of metal oxide semiconductor capacitors after bias temperature stress testing. For comparison, TaN_x barriers are deposited and tested as diffusion barriers using a similar methodology. The reliability of the developed barrier system is compared with the current industry solution, *i.e.* TaN_x.

Acknowledgments

I would like to gratefully acknowledge my supervisor, Dr. Douglas Ivey, for everything he thought me, for his guidance and for his encouragements. I am also very grateful to my co-supervisor, Dr. Qi Liu, who always provided me with a different perspective on my research. I want to thank my supervisors for their patience during the planning and development of this research work while I was finding my way as a graduate student. I specifically want to thank them for encouraging me to take on different projects and responsibilities in addition to my research project.

I would also like to thank the third member of my supervisory committee, Dr. Anastasia Elias, for her valuable suggestions during my work. In addition, I would like to thank my fellow students who were always available to discuss new ideas, specifically Dr. Lucy Nolan, Dr. Peter Kalisvaart and Mr. Brian Olsen. I am thankful to the office staff, graduate coordinators, and the IT personnel of the Department of Chemical and Materials Engineering who provided administrative and technical assistance to me. I am very grateful to Dr. Ken Cadien and Dr. Fraser Forbes who were always patiently available to discuss my queries.

This work was performed in several public laboratories in addition to our own laboratories. I would like to offer my special thanks to Dr. Douglas Barlage, who allowed me access to the Kiethley probe station for a lot of hours, and for his valuable discussions along the way. The last part of this research would not have been possible without access to this probe station. In addition, I want to extend my gratitude to Dr. David Mitlin for providing access to the sputtering equipment.

I would also like to thank the staff of the Alberta Centre for Surface Engineering and Science (ACSES) and National Research Council - National Institute for Nanotechnology (NRC-NINT), particularly Dr. Anqiang He, Mr. Martin Kupsta and Mr. Peng Li who constantly provided their expertise to assist with preparing samples and performing experiments. This work would have never made it off the drawing board, without the support of Micralyne MEM Foundary. Many special thanks are extended to Mr. Glen Fitzpatrick and Dr. Siamak

Akhlaghi for providing me with metalized wafers and for being available for scientific discussions on the project. I am also thankful to the Nanofab staff for training me on various equipments and for being available to answer my technical questions.

I like to acknowledge the financial assistance I received from Natural Sciences and Engineering Research Council of Canada, Alberta Innovates – Technology Futures and the University of Alberta.

Most importantly, none of this would have been possible without the love and support of my family, to whom I dedicate this thesis: Haydeh Sarrafzadeh, Roozbeh Dalili and Ryan Saunders. Mom, you were my first and best teacher, thank you for putting up with me being worlds away and for being my source of strength all these years. Roozbeh, your example showed me how to truly love math and physics and was the reason I took this path. Thank you for that and for continuing to show interest in my work. Ryan, your love, encouragement and endless optimism helped me overcome setbacks and stay focused on the “light at the end of the tunnel”. Thank you for all the proof-readings, for patiently discussing my research and for making Canada home for me.

Table of contents

1 Introduction 1

1.1 Motivation 1

1.2 Proposed approach and research objectives 3

1.3 Thesis outline 5

1.4 References 8

2 Literature Review……...……..… 9

2.1 Introduction 9

2.2 Dual damascene process 11

2.3 Cu-Si system and impact of Cu on devices 13

2.4 General aspects of diffusion in thin films 19

2.4.1 Effect of large potential gradients 19

2.4.2 Effect of high density of high diffusivity paths 20

2.5 Materials specifications for diffusion barriers 23

2.5.1 Amorphous metallic systems 25

2.5.1.1 Donald and Davis model for predicting glass-forming ability of various systems 28

2.5.1.2 Miedema and Niessen model for predicting the composition range of the glassy phase 29

2.5.2 Materials suitable for direct electrodeposition of Cu 30

2.6 Candidate diffusion barriers for Cu metallization 32

2.6.1 Inert barriers 32

2.6.1.1 Refractory metal nitrides 33

2.6.1.2 Refractory metal alloys 42

2.6.2 Functional barriers 46

2.7 Material design process employed for selection of a diffusion barrier..... 47
2.8 Characterization and evaluation of barriers 48
2.8.1 Metallurgical mode 48
2.8.1.1 Auger electron spectroscopy (AES) 49
2.8.1.2 Secondary ion mass spectroscopy (SIMS) 51
2.8.1.3 X-ray diffraction (XRD) 51
2.8.1.4 Scanning electron microscopy (SEM) 52
2.8.1.5 Transmission electron microscopy (TEM) 54
2.8.1.6 Four point probe resistivity measurement (FPP) 57
2.8.2 Electrical mode 58
2.8.2.1 Evaluation of electrical properties of MOS capacitors 59
2.9 References 65
3 Thermal and electrical stability of TaN_x diffusion barriers 71
3.1 Introduction 71
3.2 Materials and methods 74
3.3 Results and discussion 77
3.3.1 Metallurgical failure characterization 77
3.3.1.1 Resistivity measurement 77
3.3.1.2 $Si/SiO_2/TaN_x/Cu$ metallization stack 78
3.3.1.3 $Si/TaN_x/Cu$ metallization stack 82
3.3.2 Electrical failure characterization 91
3.4 Conclusions 95
3.5 References 97
4 Stability and failure mechanism of the Ta-Rh amorphous structures 99

4.1 Introduction 99
4.2 Materials and methods 100
4.3 Thermodynamic calculations 101
4.4 Results and discussion 105
4.4.1 Gibbs free energy calculation and $TaRh_x$ alloy properties 105
4.4.2 Diffusion barrier performance of amorphous $TaRh_x$ 110
4.5 Conclusions 118
4.6 References 120
5 *In-situ* TEM study of stability of $TaRh_x$ diffusion barriers 122
5.1 Introduction 122
5.2 Materials and methods 123
5.3 Results and discussions 125
5.3.1 Evolution of TEM sample design 125
5.3.2 Diffusion mechanism and compound growth 130
5.4 Conclusions 134
5.5 References 136
6 Evaluation of $TaRh_x$ diffusion barriers using bias temperature stress 137
6.1 Introduction 137
6.2 Materials and methods 139
6.3 Results and discussions 144
6.3.1 Capacitance measurements 144
6.3.2 SIMS depth profiling 151
6.3.3 TEM observations 153
6.4 Conclusions 155
6.5 References 157

7 General discussion and conclusions 158

7.1 Overview and summary 158

7.2 Future work 163

7.3 References 165

Appendix A-1 166

A-1 Matlab code for thermodynamic calculations 166

Appendix A-2 173

A-2 A cryo-XPS study of electroplating solutions for Au-Sn solder packaging 173

List of Tables

Table 2-1 Enthalpy of formation (kJ/mole) of metal oxides per atoms of oxygen for metals that facilitate direct electrodeposition of Cu [8]. 31

Table 2-2 Summary of the properties and deposition processes for various studied TaN_x diffusion barriers. a: amorphous; RF: radio frequency; RBS: Rutherford backscattering; RTA: rapid thermal annealing; SEM: scanning electron microscopy; TEM: transmission electron microscopy; EDX: energy dispersive X-ray spectroscopy; STEM: scanning TEM, XRD: X-ray diffraction; FPP: four point probe resistivity measurements; AFM: atomic force microscopy; DC: direct current; GDOES: glow discharge optical emission spectroscopy; AAS, atomic absorption spectroscopy; AES: Auger electron spectroscopy; PECVD: plasma enhanced chemical vapor deposition; MOCVD: metal-organic chemical vapor deposition; XPS: X-ray photoelectron spectroscopy; SIMS: secondary ion mass spectroscopy; ALD: atomic layer deposition; TBTDET: *tetr*-butylimido (trisdiethylamido) tantalum; PEALD: plasma enhanced ALD; XRF: X-ray fluorescence. 38

Table 2-3 Summary of the properties and deposition processes of the various studied refractory metal alloy diffusion barriers. For description of acronyms refer to the caption in Table 2-2. 44

Table 3-1 Flatband voltage (V_{FB}) of $Si/SiO_2/TaN_x/Cu$ capacitors before and after BTS at 140°C and under various gate bias and time conditions. 92

Table 4-1 Parameters needed for the chemical term contribution to the formation enthalpy of solid solutions. The units for $n_{ws}^{1/3}$ are in density units (d.u.: 4×10^{22} electron/cm^3) [11]. 104

Table 6-1 Flatband voltage shift (ΔV_{FB}) and Cu^+ concentration values for MOS capacitors with no barrier/Cu, $TaRh_x$/Cu and TaN_x/Cu gate metallizations after being subjected to BTS at 2MV/cm at 200°C for 90 min. Note that the flatband voltage shift values are calculated by subtracting the reference flatband voltage shifts from the measured values. 149

List of Figures

Figure 1–1 The relationship between various chapters of this thesis. 6

Figure 2–1 Schematic showing multilayer stack of Cu interconnect and dielectric layers. Reproduced from [4]. 11

Figure 2–2 Schematic of steps for a typical dual damascene process. Reproduced from [2]. 13

Figure 2–3 The Cu-Si phase diagram [10]. 14

Figure 2–4 Diffusivities of various impurities in Si [2]. 17

Figure 2–5 Schematic showing the various regimes of grain size, L, and dislocation density, ρ_d, where lattice diffusion (l), grain boundary diffusion (b) or dislocation enhanced diffusion (d) are dominant for a thin film with an fcc structure. Each map corresponds to diffusion at a specific T/T_m fraction. Reproduced from [39]. 23

Figure 2–6 Schematic showing a typical TTT diagram for the liquid-crystalline phase transformation. Path "a" shows the fast cooling of the liquid to form an amorphous structure. Paths "c" and "b" show the various heat treatments resulting in crystallization of the amorphous structure. Reproduced from [55]. .. 26

Figure 2–7 The Ta-N phase diagram [92]. 37

Figure 2–8 Schematic showing the configuration for four point probe measurement and the geometry of a thin rectangular slice. 58

Figure 2–9 Schematic showing the cross-section of a MOS capacitor. Reproduced from [153]. 61

Figure 2–10 (a) Energy band diagram of an unbiased MOS capacitor with a p-type substrate, (b) energy band diagram of the MOS capacitor in (a) after a voltage equal to V_{FB} is applied to the gate (flatband condition). Reproduced from [38]. 61

Figure 2–11 Typical high frequency C-V characteristic of a MOS capacitor with p-type substrate. Reproduced from [153]. 62

Figure 3–1 Variation in resistivity for Cu/TaN_x/Si and Cu/TaN_x/SiO_2/Si samples as a function of annealing temperature. Note that 0°C indicates the as-

deposited samples and the lines are for emphasizing the trend and have no physical meaning. 78

Figure 3–2 XRD patterns obtained from $Si/SiO_2/TaN_x/Cu$ samples upon annealing at various temperatures. 80

Figure 3–3 TEM BF micrographs of as-deposited $Si/SiO_2/TaN_x/Cu$ sample prepared by conventional dimpling and sputtering methods. (a) Plan-view sample prepared from TaN_x layer after removing the Cu film. (b) Cross-sectional view of TaN_x layer showing the low density networks running through the thickness. Note that the Cu layer is detached from the surface as a result of sample preparation. 81

Figure 3–4 TEM BF micrographs of $Si/SiO_2/TaN_x/Cu$ sample after annealing at 900°C for 30 min. (a) Cross-sectional view of the sample prepared by FIB technique. (b) Plan-view sample prepared from top Cu layer together with the corresponding SAD pattern. The precipitates are marked by arrows in both micrographs. 81

Figure 3–5 XRD patterns obtained from (a) Si/TaN_x (14 nm)/Cu and (b) Si/TaN_x (62 nm)/Cu samples upon annealing at various temperatures. 84

Figure 3–6 Plan-view TEM BF micrograph of TaN_x layer annealed at 600°C and the corresponding SAD pattern obtained from the region marked showing an hcp-Ta_2N grain close to a [0001] zone axis. The Ta_2N crystals are embedded in an amorphous matrix marking the onset of crystallization. 85

Figure 3–7 (a) Cross-sectional TEM BF micrograph of Si/TaN_x (62 nm)/Cu annealed at 800°C for 30 min. (b) Higher magnification BF micrograph of area marked with the rectangle in (a) together with EDX line scan profiles obtained from the line marked in micrograph (b). The direction of the scan is shown by an arrow on the line. The reacted regions are identified as 1,4: Cu_3Si; 2: SiO_2; 3: $TaSi_2$. 87

Figure 3–8 (a) Plan-view TEM BF micrograph of top reacted layers of Si/TaN_x (14nm)/Cu sample annealed at 700°C for 30 min. (b) SAD pattern taken from the Cu-silicide particle in (a). The details of the pattern are plotted in the drawing where the closed circles represent reflections from the [111] zone axis of

η´´-Cu_3Si, open circles show the[101] zone axis for η´´-Cu_3Si and the "x" symbols mark the spots formed by double diffraction. 88

Figure 3–9 SIMS depth profiles of as deposited and annealed Si/TaN_x (62 nm)/Cu samples. Note that the Cu layer has been removed after annealing and prior to depth profiling. 90

Figure 3–10 Schematic showing the series of reactions happening as Si/TaN_x/Cu stacks are annealed. 1) As-deposited sample at room temperature (RT) with sharp interfaces; 2) partial crystallization to Ta_2N; 3) reaction at T_f accompanied by localized formation of Cu_3Si particles and a continuous layer of $TaSi_2$ on surface; 4) growth of SiO_2 and formation of voids as a result of cooling and exposure to air. 91

Figure 3–11 Cumulative non-failures (fraction of non-leaky capacitors) as a function of BTS time for two different BTS conditions: 140°C, 2 MV/cm and 140°C, 4 MV/cm. 93

Figure 3–12 Cross-sectional TEM BF micrograph of MOS capacitors stressed at (a) 140°C and 2 MV/cm for 15 min (leakage current density of $2x10^{-8}$ A/cm^2) and (b) 140°C and 4 MV/cm for 15 min (leakage current density of $3x10^{-3}$ A/cm^2). 94

Figure 3–13 SIMS depth profiles of Cu and Ta in a capacitor stressed at 140°C and 4 MV/cm for 15 min (leakage current density of $3x10^{-3}$ A/cm^2) compared with an as-deposited capacitor. Note that the Cu layer has been removed after annealing and prior to depth profiling. 95

Figure 4–1 Calculated Gibbs free energies of the amorphous, intermetallic and the relevant bcc and fcc solid solutions phases for the Ta-Rh system at 298 K calculated using the Miedema and Niessen model. The region of stability for the amorphous phase and crystalline phases as determined by experimental observations are also marked. Films with 27 and 70 at% Ta have a two phase crystalline + amorphous structure. 107

Figure 4–2 High resolution TEM micrographs of as-deposited $TaRh_x$ films with (a) 27 at% Ta and (b) 52 at% Ta. 107

Figure 4–3 SAD patterns collected from plan-view TEM samples of (a) pure Rh, $Ta_{10}Rh_{90}$ and $Ta_{20}Rh_{80}$ and (b) pure Ta and $Ta_{80}Rh_{20}$. 109

Figure 4–4 Variation in resistivity for as-deposited Si/$TaRh_x$ (50 nm) samples as a function of composition. The dotted line shows the best fit for solid solution resistivity for Ta dissolved in Rh according to the Matthiessen and Nordheim rules. 110

Figure 4–5 XRD patterns obtained from Si/$Ta_{45}Rh_{55}$ (13 nm)/Cu samples after annealing at various temperatures in 5% H_2/95% N_2 gas for 30 min. 112

Figure 4–6 (a) Secondary electron (SE) micrograph of the top surface of Si/$Ta_{45}Rh_{55}$ (13nm)/Cu annealed at 550°C for 30 min showing the precipitates formed on the surface. (b) Cross-sectional TEM BF micrograph from a region with the particles shown in (a). (c) Higher magnification BF micrograph of the area marked with a rectangle in (b) showing the RhSi particles formed at the Si/$Ta_{45}Rh_{55}$ interface which are marked by arrows. 114

Figure 4–7 Plan-view TEM BF micrograph of a sample prepared from the reacted area at Si/$Ta_{45}Rh_{55}$ interface of Si/$Ta_{45}Rh_{55}$ (13 nm)/Cu sample annealed at 550°C. A large area SAD pattern showing the presence of RhSi particles at the interface is also included. 115

Figure 4–8 Plan-view TEM BF micrograph of a sample prepared from Si/$Ta_{45}Rh_{55}$ (50 nm) sample annealed at 700°C. A large area SAD pattern showing alloy partitioning and formation of $TaSi_2$ and RhSi particles is also included. 116

Figure 5–1 (a) TEM BF micrograph of as-deposited Si/(43 nm)$TaRh_x$/Cu prepared by FIB. (b) Sequence of BF TEM micrographs of Si/(13 nm)$TaRh_x$/Cu sample showing void growth during *in-situ* heating at 550°C. 126

Figure 5–2 Series of BF TEM micrographs of Si/(43 nm)$TaRh_x$/Cu sample showing rapid surface diffusion of Cu on the surface of Si during *in-situ* heating at 750°C. Image 1 was recorded after isothermal heating for 16 min and 42 s. Images 2-6 were recorded at time intervals of 4 sec. Some of the Cu clusters on the Si surface are marked by the black arrows. 129

Figure 5–3 (a) Room temperature BF TEM micrograph of Si/(43 nm)$TaRh_x$/Cu sample after *in-situ* annealing at 750°C for 35 min showing the extent of diffusion of Cu on Si surface and the single crystalline nature of the Cu film. Some of the Cu clusters on the Si surface are marked by the black arrows. (b) Room temperature SE micrograph of Si/(43 nm)$TaRh_x$/Cu sample after *in-situ* annealing at 750°C for 35 min revealing surface diffusion of Cu on $TaRh_x$ and Si layers, as evidenced by the particles protruding from the surface. The particles are marked by the white arrows on the micrograph. The image was taken at 40° tilt relative to the electron beam. 129

Figure 5–4 Series of BF TEM micrographs of Si/(43 nm)$TaRh_x$/Cu lamella coated with 10 nm of C2 film on both surfaces and then heated *in-situ* at 750°C for (1) 52 min, (2) 55 min and 20 s, (3) 58 min and 40 s and (4) 102 min. The series shows the nucleation and growth of a protrusion at the $TaRh_x$/Si interface. 131

Figure 5–5 (a) BF TEM micrograph of the first particle to nucleate and grow on Si/(43 nm)$TaRh_x$/Cu lamella coated with 10 nm of C2 on both surfaces after *in-situ* heating at 750°C for 102 min. EDX line scan profiles for $TaL_{\beta 3}$, SiK_{α}, $RhL_{\alpha 1}$ and $CuL_{\alpha 1\text{-}2}$ signals are superimposed on the micrograph. (b) Nanodiffraction pattern taken from the Rh-rich grain component of the particle shown in (a); the grain is indexed to orthorhombic RhSi near the [$\underline{5}$33] zone axis. 131

Figure 5–6 BF TEM micrograph of a smaller particle at an earlier stage of growth on Si/(43 nm)$TaRh_x$/Cu lamella coated with 10 nm of C2 on both surfaces, after *in-situ* heating at 750°C for 102 min. Also shown are EDX line scan profiles for $TaL_{\beta 3}$, SiK_{α}, $RhL_{\alpha 1}$ and $CuL_{\alpha 1\text{-}2}$ signals superimposed on the micrograph. 132

Figure 5–7 (a) Cross-sectional BF TEM micrograph of Si/(13 nm)$TaRh_x$/Cu sample showing the complex reaction morphology after *ex-situ* annealing at 550°C for 30 min. The SAD pattern is collected from an orthorhombic RhSi particle near the [2$\underline{5}$1] zone axis. (b) Room temperature BF TEM micrograph of Si/(43 nm)$TaRh_x$/Cu lamella coated with 10 nm of C2 on both surfaces after *in-*

situ annealing at 750°C for 102 min showing the distribution of Rh silicide particles at the Si/$TaRh_x$ interface..... 133

Figure 6–1. (a) Top view of the probe station used for BTS testing and (b) a schematic showing the various parts of the setup. 1) Stainless steel vacuum chamber, 2) heating stage, 3) heating element, 4) thermocouple feed through, 5) connector pins, 6) connector plate, 7) alignment holes and 8) screws to ensure proper contact..... 143

Figure 6–2 Typical *C-V* characteristics of (a) capacitors with $TaRh_x$/Cu gate metallization before and after being subjected to TS at 200°C for 180 min and after BTS at 2 MV/cm at 200°C for various times and (b) capacitors with $TaRh_x$/Al gate metallizations after being subjected to BTS at 2 MV/cm at 200°C for 90 min..... 146

Figure 6–3 Typical *C-V* characteristics of capacitors with $TaRh_x$, no barrier and TaN_x before and after being subjected to BTS at 2MV/cm at 200°C for 90 min. 148

Figure 6–4 Examples of deformed *C-V* characteristics of capacitors with $TaRh_x$, no barrier and TaN_x before and after being subjected to BTS at 2MV/cm at 200°C for 90 min. 150

Figure 6–5 Percentage of deformed *C-V* curves of capacitors with $TaRh_x$, TaN_x and no barrier after being subjected to BTS at 2MV/cm at 200°C for 90 min. 151

Figure 6–6 Topside SIMS depth profiles of Cu and Rh for an as-deposited capacitor and a capacitor with $TaRh_x$/Cu gate metallization stressed at 2 MV/cm at 200°C for 180 min..... 152

Figure 6–7 Backside SIMS depth profiles of Na, Rh and Cu for an as-deposited capacitor, a capacitor thermally stressed at 200°C for 180 min and a capacitor stressed at 2MV/cm at 200°C for 180 min..... 153

Figure 6–8 Cross-sectional TEM BF micrograph of (a) an as-deposited MOS capacitors and (b) a capacitor stressed at 200°C for 90 min. In (b) the Cu layer has been removed prior to FIB sectioning. 155

Nomenclature

a	lattice parameter volume contractions in compounds
a_{res}	slice dimension for resistivity measurement
b	lattice parameter grain boundary diffusion nucleus shape factor
b_{res}	slice dimension for resistivity measurement
c	lattice parameter concentration
C	capacitance
$C_{Nordheim}$	Nordheim constant
C_{ox}	oxide capacitance
d	dislocation diffusion
D	diffusion coefficient
D_l	diffusion coefficient for the lattice
D_o	frequency factor
ΔG_a^f	Gibbs free energy of formation for amorphous
$\Delta \overline{G}_{a\text{-}s}^{\,i}$	corrected Gibbs free energy of fusion of pure metal
ΔG^f	Gibbs free energy of formation
ΔG_{ss}^f	Gibbs free energy of formation for solid solution
$\Delta G^o{}_T$	Gibbs free energy of reaction at temperature T
ΔH_{ampl}	amplitude term for chemical enthalpy
ΔH_a^f	enthalpy of formation for amorphous
ΔH_c	chemical enthalpy term
$\Delta H_c^{A \text{ in } B}$	enthalpy of formation of dilute solution of A in B
$\Delta H_c^{B \text{ in } A}$	enthalpy of formation of dilute solution of B in A
ΔH_e	elastic enthalpy term
$\Delta H_e^{A \text{ in } B}$	elastic energy term for dilute solution of A in B
$\Delta H_c^{B \text{ in } A}$	elastic energy term for dilute solution of B in A
ΔH_l^M	enthalpy of mixing for liquid alloy
ΔH_m	molar heat of fusion

ΔH_{ss}^{f}	enthalpy of formation for solid solution
ΔH_{str}	structural enthalpy term
$\Delta H_{a\text{-}s}^{i}$	corrected enthalpy of fusion of pure metal i
ΔS^{M}	entropy of mixing
ΔT^{*}	Donald and Davis' parameter
E	electric field
E_C	conduction band edge
E_F	Fermi level energy
E_K	K shell energy
$E_{K\alpha 1}$	$K_{\alpha 1}$ X-ray energy
$E_{KL3M2,3}$	KL3M2,3 Auger energy
E_{L3}	L_3 shell energy
$E_{M2,3}$	$M_{2,3}$ shell energy
E_o	vacuum level energy
E_V	valence band edge
f_B^{A}	surface concentration for A when surrounded by B
F	driving force
G	Gibbs free energy shear modulus of pure elements
G_{corr}	correction factor for resistivity measurement
H	height of the dielectric
I_{nucl}	frequency of homogenous nucleus formation
I	current
J	atomic flux joules
k	Boltzmann constant
k_n	constant for nucleation
K	bulk modulus
l	lattice diffusion
L	length of the metal line dimensions of rectangular grains
n	scaling factor

n_{ws}	electron density of the Wigner-Seitz cell
N_a	substrate doping concentration
N_A	Avogadro's number
P	potential field MN model constant
P_{O2}	partial pressure of oxygen
P_{N2}	partial pressure of nitrogen
q	charge of an electron
Q	activation energy for diffusion MN model constant
Q_{sub}	substrate charge
Q_{ox}	oxide charge
R	resistance gass constant
s_{res}	probe spacing for resistivity measurement
t	diffusion time
t_{ox}	oxide thickness
t_{res}	thickness of the film for resistivity measurement
t_x	crystallization time
T	height of the metal line temperature
T_f	failure temperature
T_g	glass transition temperature
T_m	melting temperature
T_r	reduced melting temperature
T_x	crystallization temperature
T_l	liquidus temperature
T_l^{mix}	rule of mixture liquidus temperature
T_l^o	ideal solution liquidus temperature
v	atomic volume
W	width of the metal line
x	mole fraction of an element

x_A^s	surface concentration function for A in alloy form
x_B^s	surface concentration function for B in alloy form
x_{ox}	distance from metal/oxide interface
X	spacing between the metal lines
	diffusion distance
Z	half of the spacing of dislocations
V	atomic volume voltage
V_A^{alloy}	molar volume of A corrected for alloying effects
V^{pure}	molar volume of pure element
V_{FB}	flatband voltage
V_g	gate voltage
V_T	threshold voltage

Greek symbols

α	dimensionless parameter for nucleation an empirical constant for MN model
β	bcc phase in Cu-Si system dimensionless parameter for nucleation
γ	cubic phase in Cu-Si system
δ	tetragonal phase in Cu-Si system
ε	permittivity of the dielectric cubic phase in Cu-Si system mechanical strain
ε_s	substrate permittivity
η	rhombohedral phase in Cu-Si system viscosity
θ	collection angle for XRD
κ	hcp phase in Cu-Si system
μ	Micro internal chemical free energy
π	pi number
ρ	resistivity

ρ_d	density of dislocations
$\rho(x_{ox})$	volume density of charge distribution
ρ_{matrix}	resistivity of the matrix in an alloy
σ	mechanical stress
σ_{int}	liquid-crystal interfacial tension
φ	electric potential
φ_m	metal work function
φ_s	substrate work function
$\emptyset^*$	electronegativity of pure elements
Ω	ohm

Abbreviation

at%	atomic percent
A	amperes
AAS	atomic absorption spectroscopy
AC	alternating current
ACSES	Alberta Centre for Surface Engineering and Science
ADF	annular dark field
AES	Auger electron spectroscopy
AFM	atomic force microscopy
ALD	atomic layer deposition
bcc	body centered cubic
BEOL	back end of the line
BF	bright field
BTS	bias temperature stress
C	centigrade
C1	sputtered carbon
C2	electron beam evaporated carbon
cm	centimeter
CBED	convergent beam electron diffraction
CMP	chemical mechanical polishing

CMOS	complementary metal oxide semiconductor
CTE	coefficient of thermal expansion
CUMFF	Carleton University MicroFabrication Facility
CVD	chemical vapor deposition
d.u.	density units
DC	direct current
eV	electron volts
EDX	energy dispersive X-ray spectroscopy
EELS	electron energy loss spectroscopy
ETEM	environmental TEM
fcc	face centered cubic
FEG	field emission gun
FEOL	front end of the line
FIB	focused ion beam
FPP	four point probe
FWHM	full width at half maximum
g	grams
GDOES	glow discharge optical emission spectroscopy
hcp	hexagonal closed packed
hr	hour
HAADF	high angle annular dark field
HDMS	hexamethyl disilazane
HRTEM	high resolution TEM
Hz	hertz
ICs	integrated circuits
IDL	inter-metal dielectric layer
kV	kilovolts
K	Kelvin
mrad	milliradians
min	minutes
mm	millimeters

MHz	mega hertz
MN	Miedema and Niessen
MOCVD	metal-organic chemical vapor deposition
MOS	metal oxide semiconductor
MV	mega volts
nA	nano ampere
nm	nanometer
NRC-NINT Nanotechnology	National Research Council - National Institute for
ppb	part per billion
pA	pico ampere
PDF	powder diffraction files
PEALD	plasma enhanced ALD
PECVD	plasma enhanced CVD
PVD	physical vapor deposition
RBS	Rutherford backscattering;
RCA	radio corporation of America
RF	radio frequency
RIE	reactive ion etching
RT	room temperature
RTA	rapid thermal annealing
s	sec
sccm	standard cubic centimeters per minute
SAD	selected area diffraction
SE	secondary electron
SEM	scanning electron microscopy
SIMS	secondary ion mass spectroscopy
STEM	scanning TEM
TBTDET	*tetr*-butylimido (trisdiethylamido) tantalum
TEM	transmission electron microscopy
ToF	time-of-flight

TS	thermal stress
TTT	time temperature transformation
XPS	X-ray photoelectron spectroscopy
XRD	X-ray diffraction
XRF	X-ray fluorescence

1 Introduction

1.1 Motivation

Interconnects in integrated circuits (IC's) are metal lines of low resistivity that distribute signals and provide power to the various systems on the chip. One of the figures of merit for design of an IC is its characteristic *RC* time delay (product of line resistance (*R*) and capacitance (*C*)). To achieve high-speed transmission and improved performance, the geometries of transistors are continuously scaled down. This scaling of devices, however, is detrimental to the performance of interconnects to the level that *RC* time delays become the bottleneck in achieving high-speed transmission [1,2]. Since the creation of IC's, the Al/SiO_2 material system was used as the interconnect/dielectric system. In order to battle *RC* time delays, Cu has replaced Al interconnects in ultralarge-scale integration (ULSI) structures because of its lower bulk resistivity and the SiO_2 dielectric is being replaced by the low-κ dielectrics [3]. However, Cu has its own set of problems and challenges such as: *i*) the fast diffusivity of Cu in Si and SiO_2 under thermal and/or electrical stresses, *ii*) the lack of a suitable dry or wet chemical etching recipe for Cu and *iii*) poor adhesion to the dielectric layer [4]. These challenges have led to the development of dual damascene process which relies on etching of the dielectric layer instead of etching of the Cu layer. The deposition of Cu and the associated layers in high aspect ratio vias and lines ensues. The latter imposes yet another challenge where an appropriate deposition method, capable of filling the high aspect ratio vias without voids or seams, has to be utilized. The semiconductor industry has adopted electrochemical deposition of Cu [2].

To alleviate the problem of Cu diffusion and intermixing with Si and SiO_2, the addition of an effective diffusion barrier layer between the active region of the device and the Cu layer is necessary. Diffusion in thin films is controlled by the relative contributions from bulk and high diffusivity paths, *i.e.*, grain boundaries and dislocations. According to the model suggested by Ballufi and Blakely [5], at

an operating temperature of $T < 0.5T_m$ (where T_m is the absolute melting temperature of the substrate), the activation energy for high diffusivity paths, especially grain boundaries, is lower than the activation energy for bulk diffusion. Bulk diffusion rates, on the other hand, scale with the inverse of T_m [5]. Satisfactory barrier properties can be achieved by a combination of an amorphous structure (minimum high diffusivity paths) and a high T_m material (to minimize bulk diffusion). In the metallization stacks currently in use, amorphous TaN_x barriers with $x \leq 1$ are the material of choice [6]. However, TaN_x forms a surface oxide which limits the adhesion of electrodeposited Cu. In order to avoid adhesion problems, a Cu seed layer is deposited on TaN_x barriers to facilitate electrodeposition of Cu [7]. With the scaling of device sizes and the associated scaling of available space for metal lines and vias, the combined thicknesses of the barrier and seed layers occupy a valuable volume of the interconnect, which would otherwise be available to the low resistivity Cu interconnect. One approach to address this issue is to design a diffusion barrier material that possesses other functionality such as the ability to allow direct electrodeposition of Cu [6].

The development of a suitable diffusion barrier material for Cu metallization has been ongoing for over three decades [8]. For the reasons explained in the paragraph above, there has been great interest in the last decade to develop functional barriers that are conducive to direct electrodeposition of Cu (seedless barriers). Development of seedless barriers has been largely catalyzed by Lane *et al*'s [7] work in 2003 that identified a family of elements that are suitable for direct electrodeposition of Cu in standard acidic baths. Unfortunately, none of these materials serve as robust barriers when deposited in pure or solid solution forms, mainly due to the high density of high diffusivity paths in their microstructure [6]. There have been several attempts to find an appropriate alloying system that improves the barrier performance of these seedless elements. However, the approach taken so far is an arbitrary material selection process. Development of a materials selection guide that helps identify an appropriate alloying element and a range of compositions within that alloying system remain a critical challenge.

1.2 Proposed approach and research objectives

The main objective of this thesis is to develop an amorphous alloy suitable as a diffusion barrier for Cu metallization. A thermodynamic approach to material selection process is adopted. The candidate diffusion barrier material must satisfy a stringent list of properties including high conductivity, thermal stability, glass forming ability and the direct electrodeposition of Cu. A systematic study is performed on the alloys of seedless elements identified by Lane *et al* [7] with Ta. The latter is selected as it is stable in contact with Cu, has a high T_m at 3017°C and is compatible with the dual damascene fabrication methods [9]. The thermodynamic study considers three criteria: *i*) the phase diagrams of Cu-X systems (where X is one of the seedless elements), *ii*) the glass forming ability of the intertransition system of Ta-X based on the model suggested by Donald and Davis [10], *iii*) the most stable amorphous composition in the Ta-X system based on the model suggested by Miedema and Niessen [11]. Based on the first two criteria, Ta-Rh is selected as the candidate diffusion barrier. The model by Miedema and Niessen [11] is employed to estimate the Gibbs free energies of formation for supersaturated solid solutions, amorphous phases and structurally simple intermetallic phases. The thermodynamic model is validated by deposition of various compositions of Ta-Rh alloys and detailed structural analysis by X-ray diffraction (XRD) and transmission electron microscopy (TEM). Based on the thermodynamic calculations and structural characterization results, two compositions are selected as candidate diffusion barriers.

The reliability of a diffusion barrier system can be evaluated by monitoring either the metallurgical or the electrical characteristics of the metallization stack. The metallurgical mode of characterization is usually performed on blanket films of the diffusion barrier directly deposited onto Si, Si/SiO_2, or Si/low-κ dielectrics. In the current study, stacks of Si/diffusion barrier/Cu are annealed followed by characterization by depth profiling and microstructural analysis techniques. Diffusion of Cu through the barrier at the failure temperature usually occurs rapidly and results in formation of several compounds. The characterization techniques used include depth profiling by secondary ion mass spectroscopy

(SIMS), four point probe resistivity (FPP) measurement, XRD, scanning electron microscopy (SEM), TEM equipped with an energy dispersive X-ray spectrometer (EDX) and with an electron energy loss spectrometer (EELS).

In conventional metallurgical characterization, the sequence of diffusion and reaction is speculated by inspecting the post-failure reaction morphology. In this respect, *in-situ* heating in TEM provides a great tool for direct observation of the diffusion and reaction phenomena. However, there are several challenges associated with *in-situ* TEM heating of the Cu metallization stacks. For example, Cu atoms exhibit high mobility on the surface at temperatures exceeding 600°C or under intense electron beam radiation [12-14]. Unexpected melting of Cu lamellae at lower than equilibrium temperatures [12] and/or formation of voids at the Cu/diffusion barrier interface [15,16] are other encountered issues. A novel sample preparation technique is developed to circumvent these issues and directly observe the series of reactions responsible for the failure of $TaRh_x$ barriers.

After initial metallurgical characterization, it is important to test the reliability of the diffusion barriers by electrical characterization which offers better sensitivity and is better suited for detection of the onset of Cu diffusion and device degradation. Additionally, during device operation diffusion of Cu is driven by a combination of temperature and electric fields and it is essential to include both in any reliability tests. Therefore, the reliability of $TaRh_x$ diffusion barriers is evaluated by bias temperature stress (BTS) testing of metal oxide semiconductor (MOS) capacitors. The capacitance-voltage (*C-V*) characteristics of the MOS devices are studied in detail and compared with the SIMS depth profiling information and cross-sectional TEM observations. One of the objectives of this part of this research is to assess the sensitivity of metallurgical and electrical characterization methods.

As discussed before, TaN_x barriers are the material of choice in the current ULSI devices. It is necessary to compare the reliability of $TaRh_x$ diffusion barriers with that of TaN_x barriers with similar thickness and morphology. Therefore, amorphous TaN_x films are deposited by reactive sputtering and studied by both

metallurgical and electrical characterization methods. A methodology similar to that used for $TaRh_x$ barriers is used to facilitate a direct comparison between the developed barrier system and the current industry solution.

1.3 Thesis outline

This thesis provides a detailed description of development of a low-resistivity, amorphous diffusion barrier alloy suitable for direct electrodeposition of Cu. This thesis is composed of seven chapters and two appendices. Chapter 1 provides an introduction to this study, and outlines the objectives and the research approaches used throughout this study. Chapter 2 provides a review of the literature related to design of a diffusion barrier material. General aspects of diffusion in thin films, materials specifications for diffusion barriers and available thermodynamic models and criteria for predicting a glass-forming alloy are reviewed. A comprehensive review of the candidate diffusion barriers for Cu metallization and the characterization and evaluation methods employed are provided. The compiled information is utilized to explain the material design process used to select a diffusion barrier.

Chapter 3 examines the stability of TaN_x diffusion barriers by thermal annealing and metallurgical characterization. This chapter also describes the initial attempts at electrical characterization of MOS devices. This part of the study provided a great learning experience that influenced the successful testing of devices in the later chapters. Chapter 4 describes the development of a guide for selecting a stable amorphous alloy that can be applied as a diffusion barrier. The thermodynamic model is explained in detail and compared with experimental observations. The reliability of the selected $TaRh_x$ alloy is evaluated by metallurgical characterization methods. The Matlab code, developed for the thermodynamic calculations, is included in Appendix A-1.

Chapter 5 outlines the development of a novel sample preparation method and its successful implementation in *in-situ* TEM heating experiments for direct observation of diffusion and reaction mechanisms involved in failure of diffusion barriers. The results from this chapter are compared with the *ex-situ* observations

presented in Chapter 4. In Chapter 6 the reliability of $TaRh_x$ and TaN_x barriers is evaluated by electrical characterization methods, namely by monitoring the *C-V* characteristics of MOS devices before and after BTS and thermal stressing. Chapter 7 comprises the general discussions, conclusions and recommendations of this work.

The correlation between the various chapters of this thesis is demonstrated in Figure 1–1. The outcomes from electrical measurements in Chapter 3 show the need for improving the experimental design and building a probe station setup with controlled ambient. This is demonstrated in Chapter 6. The metallurgical characterization performed in Chapter 3 provides a baseline for comparison of the developed diffusion barrier system presented in Chapter 4. Chapter 5 provides clarification for the reaction morphology observed in Chapter 4. The knowledge gained from earlier chapters is employed in Chapter 6 to evaluate the reliability of the designed diffusion barrier system.

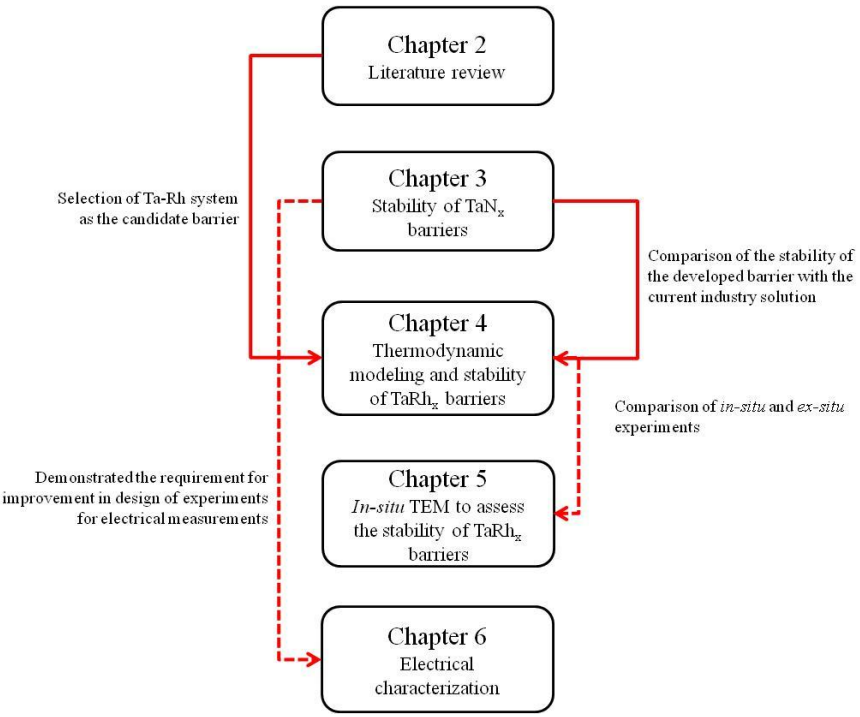

Figure 1–1 The relationship between various chapters of this thesis.

Appendix A-2 presents the results of work done, early in the PhD program, on the stability and chemistry of electroplating solutions for Au-Sn solders used in

device packaging. This work is not included in the main body of the thesis as it is not directly related to the diffusion barrier work. However, the work was successful and led to a peer reviewed journal publication.

1.4 References

[1] H.S. Rathore, K. Chanda, Semiconductor Manufacturing Handbook (McGraw-Hill, USA, 2005) pp. 4.1-4.13.
[2] T. Gupta, Copper Interconnect Technology (Springer, USA, 2009).
[3] H.Y. Wong, N.F. Mohd Shukor, N. Amin, Microelectron. J. **38**, 777-82 (2007).
[4] P.V. Zant, Microchip Fabrication (McGraw-Hill, USA, 2004) pp. 401-15.
[5] R.W. Balluffi, J.M. Bkakely, Thin Solid Films. **25**, 363-92 (1975).
[6] A.E. Kaloyeros, E.T. Eisenbraun, K. Dunn, O. van der Straten, Chem. Eng. Commun. **198**, 1453-81 (2011).
[7] M.W. Lane, C.E. Murray, F.R. McFeely, P.M. Vereecken, R. Rosenberg, Appl. Phys. Lett. **83**, 2330-2 (2003).
[8] S.-. Wang, MRS Bull. **19**, 30-40 (1994).
[9] P.R. Subramanian, D.E. Laughlin, Bull. Alloy Phase Diagr. **10**, 652-5 (1989).
[10] I.W. Donald, H.A. Davies, J. Non-Cryst. Solids. **30**, 77-85 (1978).
[11] G.J. Van der Kolk, A.R. Miedema, A.K. Niessen, J. Less-Common Met. **145**, 1-17 (1988).
[12] D. Kiener, Z. Zhang, S. Šturm, S. Cazottes, P.J. Imrich, C. Kirchlechner, G. Dehm, Philos. Mag. **92**, 3269-89 (2012).
[13] Z. Liu, Y. Bando, Adv. Mater. **15**, 303-5 (2003).
[14] P.-. Wang, Y.-. Zhao, G.-. Wang, T.-. Lu, Nanotechnology. **15**, 218-22 (2004).
[15] J.H. An, P.J. Ferreira, Appl. Phys. Lett. **89,** 151919.1-3 (2006).
[16] M. Martinez, M. Legros, T. Signamarcheix, L. Bally, S. Verrun, L. Di Cioccio, C. Deguet, Thin Solid Films. **530**, 96-9 (2013).

2 Literature Review

2.1 Introduction

Fabrication of integrated circuits (ICs) consists of two main steps: the front end of the line (FEOL) and the back end of the line (BEOL). In the FEOL the active and passive parts of the circuit are fabricated on the Si wafer, while in the BEOL metal layers (metallization) are added to connect the devices on the chip [1]. These metal layers comprise the interconnect system of the ICs and provide power/ground and distribute clock and other signals to various systems on the chip [2]. Since their creation in the 1960s, the design of ICs has followed a trend of shrinking device sizes and increasing density of devices per chip to improve performance, reduce power and reduce cost per transistor. The area available to interconnects has continuously become smaller thus requiring that the third spatial dimension is exploited. Multilevel metallization was therefore introduced in the 1980s to minimize the overall wire-length distribution for submicron complementary metal-oxide-semiconductor (CMOS) technologies [3]. In the multilevel metallization scheme, the metal layers are electrically isolated from each other by a layer of dielectric material called an inter-metal dielectric layer (IDL). Various layers of interconnects are connected to each other by contact holes or vias [1].

To improve transistor performance and speed, in the CMOS FEOL the junction depth and the oxide thickness are continuously scaled to smaller values. The FEOL scaling accompanies scaling in the BEOL which results in thinner and closely spaced metal lines [3]. A simple model for BEOL interconnect scaling is shown in Figure 2–1. The signal propagation speed in an interconnect is dictated by its parasitic capacitance or *RC* time delays which is described by the product of resistance (*R*) and capacitance (*C*) as follows:

$$RC = 2\varepsilon\rho\left(\frac{L^2}{TH} + \frac{L^2}{WX}\right) \qquad \text{Equation 2-1}$$

where ρ is the resistivity of the interconnect metal, ε is the permittivity of the dielectric and *L*, *H*, *W*, *X* and *T* are dimensions of the metal line and the dielectric and can be found in Figure 2–1 [4]. Assuming that the interconnect and the dielectric dimensions are scaled by a factor of *n* (*n* > 1), the scaled *RC* delay time is given by:

$$R'C' = 2\varepsilon\rho\left(\frac{L^2}{\left(\frac{T}{n}\right)\left(\frac{H}{n}\right)} + \frac{L^2}{\left(\frac{W}{n}\right)\left(\frac{X}{n}\right)}\right) = n^2RC \qquad \text{Equation 2-2}$$

In this model, it is assumed that the interconnect length remains constant since long-distance connections do not scale. Chips are getting smaller, but because more devices are being fabricated on a chip, longer interconnects are required [3]. Equation 2-2 clearly shows that *RC* time delays increase with BEOL interconnect scaling. With the scaling of devices to a sub-quarter-micron node, the *RC* time delay dominates the gate delay and therefore hinders the speed improvement expected from FEOL scaling [5]. Since the invention of ICs, Al and its alloys in combination with SiO_2 were used as the primary materials for interconnecting lines and dielectric layers. According to Equation 2-1, to reduce *RC* time delay, both the resistivity of the interconnect line and the permittivity of the dielectric have to be reduced. As a result Al with a bulk resistivity of 3 $\mu\Omega$cm has been replaced by Cu with a bulk resistivity of 1.8 $\mu\Omega$cm and SiO_2 dielectric is being replaced by low-κ dielectrics [3]. Production of Cu-based devices was made available by IBM for the first time in 1998, followed quickly by Motorola [1]. Besides lower resistivity, Cu also offers more efficient heat dissipation, better resistance to electromigration failure, superior thermo-mechanical properties and improved resistance to stress migration [4].

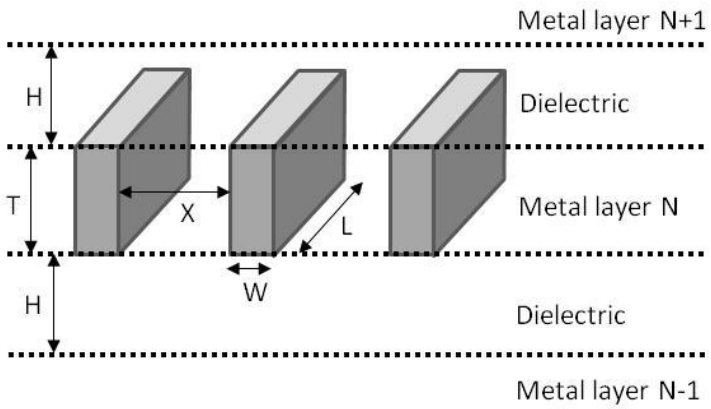

Figure 2–1 Schematic showing multilayer stack of Cu interconnect and dielectric layers. Reproduced from [4].

Despite these advantages, the shift to Cu/ low-κ dielectric system has generated significant processing technology and materials selection challenges. Copper is a fast diffuser in Si and SiO_2 [6,7], Cu does not adhere well to SiO_2 or low-κ dielectrics and efforts to develop an effective Cu etch process has failed [4]. To avoid the complications of Cu metal etching, the dual damascene process was developed to fabricate Cu interconnects. The dual damascene process and the mechanisms of diffusivity of Cu in Si and SiO_2 are briefly reviewed in this chapter. To prevent diffusion of Cu, a diffusion barrier layer is needed between Cu and the Si substrate or the dielectric layer. The mechanisms of diffusion in thin films pertinent to diffusion barrier design and the materials specifications crucial to the stability of diffusion barriers are explained in this chapter. Following this, an overview of the criteria used in this work to select a potential barrier is given. The closing section of this chapter examines the characterization methods available to evaluate the stability of a potential diffusion barrier.

2.2 Dual damascene process

The challenges associated with transitioning from Al to Cu metallization have led to the development of a unique process specifically designed to fabricate Cu interconnects. In Al/SiO_2 interconnect technology, the metal layer is patterned first followed by deposition of an IDL. However, Cu is difficult to etch by reactive ion etching (RIE) and, therefore, damascene processes based on etching a

trench in the dielectric and filling up the trench with the metal layer are employed [2]. In the dual damascene process both the high aspect ratio via and the wider lines are filled with Cu in a single step. A schematic of the sequence of dual damascene process is shown in Figure 2–2. First a thick dielectric layer is deposited on the first metal layer. Two lithography and etching steps define vias and lines. The vias and lines are then coated by a diffusion barrier layer and a seed layer to prevent Cu diffusion and to facilitate its deposition, respectively. Copper is then deposited to fill the vias and lines. With the continuous shrinking of minimum feature size, the semiconductor industry has faced the challenge of developing a deposition technique capable of filling the high aspect ratio vias without voids or seams [2]. Physical vapor deposition, chemical vapor deposition and electrochemical deposition methods have been considered for production of Cu interconnects. The semiconductor industry has adopted electrochemical deposition due to its conformality in high aspect ratio vias, low cost and low deposition temperature [4]. However, the standard diffusion barriers form a passive surface oxide and Cu cannot be deposited from standard acidic baths directly on the diffusion barrier layer. To facilitate the reduction of Cu ions, a Cu seed layer is deposited on the diffusion barrier to perform as the cathode [8].

To ensure complete filling, the lines and vias are overfilled by electrochemical deposition of Cu. Before proceeding to the next metallization layer, the Cu overburden is removed by a chemical mechanical polishing (CMP) step. In this process the surface is mechanically abraded using a slurry that contains abrasives and chemical etching agents. The metallization stack is then encapsulated by a capping layer which prevents interlayer diffusion and acts as an etch stop layer for the next damascene step [2]. With more layers, materials and processing steps, interface stability and control have become essential. Additionally, with the downscaling of feature size, the aspect ratio of the vias are continuously increasing and the space available to the combined barrier/seed/Cu layers is becoming smaller. Consequently, the barrier and seed layers occupy a large volume of the interconnect layer, which would otherwise be available to Cu electrodeposition. Considering that only Ag has a lower resistivity than Cu, any

barrier material would increase the effective resistance of the metallization stack [5]. Therefore, to meet the stringent requirements of shrinking device size, the thickness of the barrier and seed layer are continuously decreasing, with a barrier thickness of 2.4 nm at the 32 nm node technology [9]. At these thicknesses barrier conformality, thickness uniformity and stability become crucial to the overall functionality of the structure. A review of the diffusion barriers under study and some approaches that are being taken to alleviate these problems are given in the following sections.

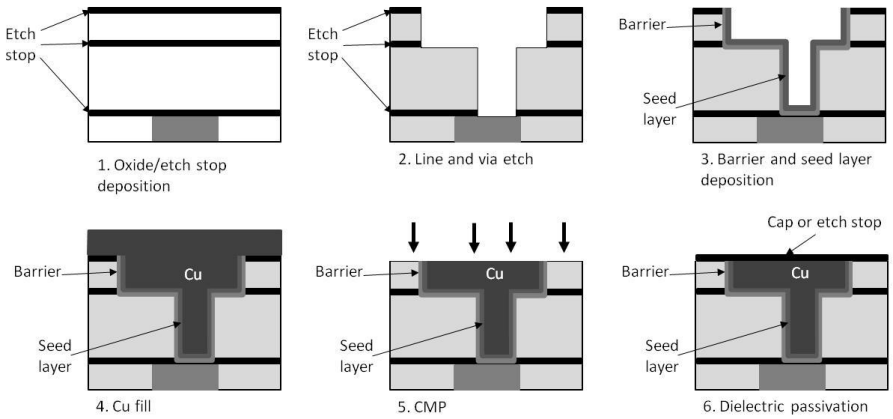

Figure 2–2 Schematic of steps for a typical dual damascene process. Reproduced from [2].

2.3 Cu-Si system and impact of Cu on devices

The equilibrium Cu-Si phase diagram is shown in Figure 2–3. There is a strong chemical affinity between Cu and Si as evidenced by the occurrence of eight intermetallic compounds in the system. Oleisinski and Abbaschian [10] reviewed and compiled and experimental data on the crystal structure of phases in the Cu-Si system as follows:

i. The hcp phase, κ, which is stable in the temperature range 552 to 842°C.

ii. The bcc phase, β, which is stable in the temperature range 785 to 852°C.

iii. The cubic phase, γ, which decomposes peritectoidally at 729°C.

iv. The tetragonal phase, δ, which is stable in the temperature range 710 to 824°C.

v. The cubic phase, ε, which decomposes peritectoidally at about 800°C.

vi. The orthorhombic phase, η´´, which is stable below 570°C.

vii. The rhombohedral phase, η´, which is stable in the temperature range 467 to 620°C.

viii. The rhombohedral phase, η, which melts at 859°C.

Copper dissolves interstitially in Si [11] and the interstitial solid solution has a maximum solubility of 0.00009 at% Cu at about 800°C [12]. Extrapolation of the solubility curve for Cu in Si to room temperature results in a negligible value of less than 1 Cu atom per 1 cm^3 volume of Si [6]. In contrast, Cu can dissolve up to 11.25 at% Si at the peritectoid temperature of 824°C [10]. As a result, upon cooling of a contaminated Si wafer, all the Cu will precipitate, form stable complexes, agglomerate or diffuse out to the surface of the wafer [6]. On the other hand, the maximum solubility of Cu in SiO_2 is suggested to be around 0.04 to 0.4 at% [13].

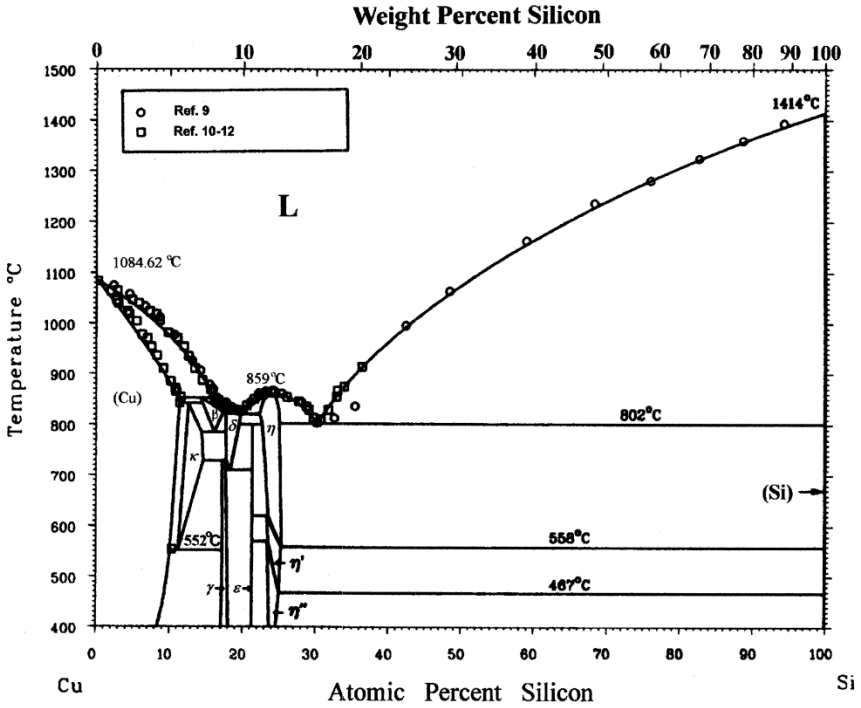

Figure 2–3 The Cu-Si phase diagram [10].

The irregular electronic structure of Cu, that distinguishes it from other 3d metals, is that instead of the $3p^6 3d^9 4s^2$ configuration, one of the electrons from the 4s subshell moves to 3d subshell, giving a configuration of $3p^6 3d^{10} 4s^1$. Upon ionization in vacuum, Cu^+ takes a stable, closed-shell configuration of $3p^6 3d^{10}$ [6]. It is well-known that Cu is always singly ionized in Si [11]. It is possible that Cu^+ keeps its vacuum electronic configuration (*i.e.*, a closed shell $3d^{10}$ configuration) after entering the Si structure. Based on this theory, Cu^+ is very small and relatively inactive in Si [6]. However, Estreicher [14] suggested that the electronic configuration of interstitial Cu is not as simple as $3d^{10}$. Based on this theory, some electrons are transferred from the 3d subshell to the 4 sp subshell. This allows Cu to form weak but covalent bonds to a wide range of impurities and defects such as shallow acceptors, dislocations, grain boundaries, stacking faults, etc. [14].

The diffusivity of Cu in Si is compared with other impurities in Si in Figure 2–4 [2]. It is obvious that diffusivity of Cu is by far higher than that of any other impurity in Si. This behavior can be explained based on the above mentioned closed-shell electronic configuration of Cu. The exceptionally small radius of Cu and the weakness of covalent interactions with Si result in high diffusivity of Cu [6,15]. It should be noted that since interstitial Cu is positively charged, its diffusivity is dependent not only on the temperature, but also on the type and the level of doping of the Si wafer. Istratov *et al* [16] calculated the intrinsic diffusivity (D_{int}), which is the diffusivity value independent of trapping sites, for Cu in low B-doped Si as follows:

$$D_{int} = 3 \times 10^{-4} \times \exp\left(-\frac{0.18\ eV\ or\ 17.4\frac{kJ}{mole}}{kT}\right)\ (\mathrm{cm^2/s}) \qquad \text{Equation 2-3}$$

where k is the Boltzmann constant and T is the temperature in Kelvin [16]. Based on this equation, Cu can diffuse through a standard p-type 10 Ωcm Si wafer in about 15 hours at room temperature [16]. As mentioned before, the solubility of Cu in Si at room temperature is negligible and all the Cu diffused in Si leaves the interstitial sites to form one of the following five defect configurations: *i*) interaction with point defects and formation of defect complexes, *ii*) precipitation

of Cu-silicide particles in the bulk or at the lattice defects, *iii*) decoration of line or planar defects such as dislocations, grain boundaries, etc., *iv*) outdiffusion to the surface and *v*) segregation in heavily p-doped regions.

It has been shown that the dissociation energy of Cu from defects is quite small due to the high diffusivity of Cu. Therefore, the majority of Cu complexes with other impurities and defects are not stable and only slow down Cu's diffusion towards more stable sinks [6]. Generally, the concentration of point defect complexes with Cu is lower than 0.1% of the total Cu concentration in Si. Regardless of these low concentrations, Hall effect measurements showed that Cu produces both acceptor and donor levels in the bandgap of Si (*e.g.*, E_C – (0.15 to 0.2) eV, E_V + (0.41 to 0.46) eV, E_V + (0.20 to 0.23) eV and E_V + (0.09 to 0.1) eV). In these expressions E_V and E_C denote the top edge of the valence band and the bottom edge of the conduction band in the energy diagram of Si, respectively. A comprehensive review of these electrically active levels and their origins is given by Istratov and Weber [17].

Precipitation of Cu-silicide particles in Si has been observed frequently and various compounds are reported; examples include β-CuSi [18], a metastable diamond structure of CuSi [19], and η´´-Cu_3Si [20-24]. Among these, the most frequently observed phase is η´´-Cu_3Si which is suggested to have an orthorhombic structure with the following lattice parameters: a = 7.68 nm, b = 7.00 nm and c = 2.19 nm [23]. This phase, however, is a nonstoichiometric compound and the superlattice structure is predicted to vary with composition. A distinctive feature of Cu_3Si precipitates is the lattice expansion associated with its formation. The volume of a unit cell of Cu_3Si per Si atom is 0.046 nm^3 while the volume of a unit cell of Si per Si atom is 0.020 nm^3. To accommodate the volume difference associated with silicide formation, Si atoms are forced out of the Si lattice forming Si self-interstitials. This phenomena is accompanied by the formation of extrinsic dislocation loops which indicate generation of Si self-interstitials or absorption of lattice vacancies during the precipitation process [20,21,25].

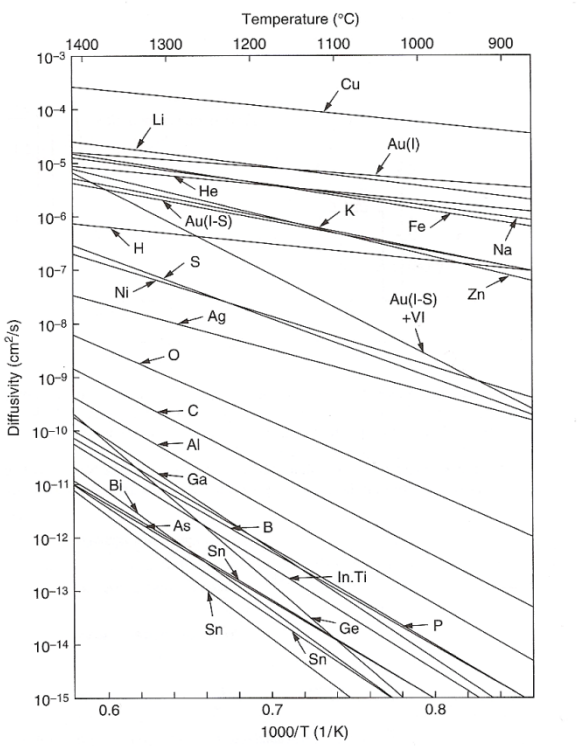

Figure 2–4 Diffusivities of various impurities in Si [2].

Copper-silicide precipitates form a set of closely spaced states or a defect band close to the middle of the Si bandgap. The width of this band depends on the size of the silicide precipitates [17]. Istratov *et al* [26] observed that Cu-silicides are positively charged in p-type Si and negatively charged in n-type Si. As a result, the electrostatic interaction between the positively charged interstitial Cu and charged precipitates play an important role in nucleation and growth of silicide particles. The repulsion between the positively charged silicides in p-type Si and interstitial Cu creates a nucleation barrier while the columbic interaction enhances the nucleation and growth of silicides in n-type Si [26]. This explains the observation that diffusion of Cu to p-n junction results in formation of Cu-silicides starting from the n-side of the junction [27,28].

Another distinctive feature of Cu-silicide particles is the catalytic oxidation of the Si substrate in the presence of Cu_3Si precipitates at room temperature. In this process, the room temperature oxidation process leaves a thick amorphous

silicon oxide layer beneath the Cu_3Si precipitates. The suggested mechanism for this phenomenon is as follows: O_2 is dissociated into atomic oxygen on the surface of the silicide. Atomic oxygen then reacts with Cu_3Si to form SiO_2 and Cu according to:

$$Cu_3Si + 2O \rightarrow SiO_2 + 3Cu \qquad \text{Equation 2-4}$$

The Cu atoms released in this reaction, can move to the Si substrate and form more Cu_3Si. This process continues catalytically as long as there is enough supply of oxygen diffusing inward [22,29-32].

The electrically active defects that are formed as a result of Cu diffusion in Si are observed to cause a drop in minority carrier lifetime. This effect is more pronounced for n-type Si than for p-type Si since out-diffusion of Cu is more pronounced in p-type Si [33]. Therefore, the concentration of electrically active defects is lower in p-type Si. Strong recombination activity is also observed for Cu-silicide precipitates [34,35]. This is consistent with the formation of a defect band in the middle of the bandgap, as discussed above. Copper contamination is observed to increase the leakage current of a reverse-biased shallow p-n junction by destruction of the entire diode structure through formation of Cu_3Si precipitates [27,28,36]. Diffusion of Cu into the gate oxide has been observed to increase the leakage current [37], induce threshold voltage instabilities and reduce the oxide breakdown voltage of metal-oxide-semiconductor (MOS) capacitors [38]. MOS capacitors are used in the current study to evaluate the performance of diffusion barriers and therefore are of great importance to this study. The effect of Cu diffusion on performance of MOS capacitors is discussed in detail in Section 2.8.2.1.

It is clear from the above discussion that Cu can detrimentally affect the device performance at very low concentrations. Due to the high diffusivity of Cu in Si and in the dielectric layer, these detrimental concentrations can be reached as a result of the high fabrication temperatures or during device operation. Therefore, the design of an effective diffusion barrier that prevents contamination of Si and

SiO_2 layers is crucial to high yield and reliability of the devices throughout the whole lifetime of the chip. The following sections explain the design process of a suitable barrier starting with diffusion in thin films.

2.4 General aspects of diffusion in thin films

Diffusion in thin film packages in IC's differs from the ordinary diffusion that occurs in bulk specimens in many aspects, namely: *i*) a large driving force, originating from thermal, chemical, electrical, mechanical and other potentials, exists over a small dimension, *ii*) a high density of high diffusivity paths, such as grain boundaries and dislocations and the interaction between these defects and surfaces and interfaces, further complicates diffusion mechanisms and *iii*) other factors such as film stress and impurities also affect diffusion, etc. [39]. The various combinations of defects and potential gradients lead to the complex nature of diffusion-related problems in thin films, which are discussed in the following two sections.

2.4.1 Effect of large potential gradients

A driving force (F) in a multicomponent system gives rise to an atomic flux (J) expressed by the following equation:

$$J = c\frac{D}{kT}F \qquad \text{Equation 2-5}$$

where c is the concentration of the diffusing species with diffusivity of D, k is the Boltzmann constant and T is the temperature. The gradient of the potential field (P) describes the driving force as:

$$F = -\nabla P \qquad \text{Equation 2-6}$$

This potential field can originate from various sources, such as concentration ($kT\ln c$), internal chemical free energy ($\mu(c)$), and electric potential (φ) as follows:

$$P = kT\ln c + \mu(c) + q\varphi + \cdots \qquad \text{Equation 2-7}$$

where q is the charge. Accordingly, the atomic flux (J) can be written as:

$$J = -D\nabla c - \frac{Dc}{kT}\left[\nabla\left(\mu(c)\right) - qE\right] + \cdots \qquad \text{Equation 2-8}$$

where E is the electric field [40,41]. It is evident from this expression that atomic flux depends on several factors; namely *i*) concentration gradient which is usually referred to as the diffusion term, *ii*) the internal chemical free energy gradient, e.g., the presence of a stable compound and *iii*) external constraints such as electric field and stress. For multilayered devices, the steep concentration gradient — as a result of proximity of the interfaces — together with the external forces, such as applied electric field and deformation stresses, give rise to fast diffusion of species through thin films. The transition to Cu interconnects generates large driving forces for diffusion; namely *i*) Cu in proximity to Si forms a stable η´´-Cu_3Si phase leading to a high internal chemical energy gradient and *ii*) the diffusivity of interstitial Cu in Si (D) is higher than any other impurity due to the irregularly small size of Cu^+ and the weak covalent interaction with the Si lattice as explained in Section 2.3 [6,41]. According to Equation 2-8, interlayer diffusion can be minimized by reducing the atomic mobility and by minimizing the driving force. Therefore, an effective diffusion barrier decreases the diffusivity of Cu (D_{Cu}) and reduces the internal chemical energy gradient ($\nabla(\mu(c))$). A thermodynamically stable diffusion barrier, which is in equilibrium with the materials in contact under the external driving forces, is required. The diffusivity of Cu through the barrier layer (D_{Cu}), on the other hand, depends on the relative contributions of bulk and high diffusivity paths. For barriers, these factors not only are intrinsic properties of the barrier material but also depend on the film microstructure and, hence, the deposition method [42].

2.4.2 Effect of high density of high diffusivity paths

Thin film deposition methods often result in a high density of defects, including grain boundaries and dislocations. It has been established that the mean jump frequency of atoms at grain boundaries, dislocations and on the surface is higher than that of the same atom in the bulk lattice [40]. These defects, therefore, provide very efficient paths for mass transport and for this reason are called high diffusivity paths [39]. The diffusion process is, therefore, determined by the relative contribution of these high diffusivity paths and the bulk lattice to the

overall mass transport. The diffusion coefficient (D) along the individual paths or in the lattice is given by the Arrhenius equation.

$$D = D_o \exp(-\frac{Q}{RT}) \qquad \text{Equation 2-9}$$

where D_o is frequency factor, Q is the activation energy for diffusion and R is the gas constant [40]. The activation energy for diffusion along individual paths is a function of the value T/T_m (where T_m is the absolute melting point of the substrate). Diffusion through high diffusivity paths becomes dominant at relatively low temperatures since the activation energy for high diffusivity paths is lower than that for lattice diffusion. The relative contribution of the mass fluxes through the lattice, dislocations and grain boundaries for a single phase fcc metal has been estimated by Balluffi and Blakely [39]. This model assumes a thin film containing rectangular grains of dimension L running through the entire thickness and a density ρ_d of uniformly distributed dislocations positioned in a direction perpendicular to the surface. The regions of grain size and dislocation density, where different fluxes (grain boundary, dislocation and lattice) dominate, were plotted at different T/T_m fractions. This plot is shown in Figure 2–5. The values of L and ρ_d, which usually occur in thin films, are marked by the broken rectangle. As can be seen, at lower temperatures grain boundary and dislocation enhanced diffusion become dominant and replace lattice diffusion. Additionally, grain boundary diffusion becomes more dominant over dislocation enhanced diffusion. For example a film with a grain size in the 1 μm range corresponds to log ($1/L$) = 4 and according to Figure 2–5 grain boundary diffusion would always dominate for this microstructure. According to this model, diffusion in thin metallic films with normal grain structures and defect densities is completely dominated by high diffusivity paths and especially grain boundaries at T/T_m<0.5 [39].

The distribution of the diffusing species in thin films with high diffusivity paths depends on several factors including the geometry of high diffusivity paths, the duration of diffusion and the relative magnitude of the diffusion coefficient of individual paths. Harrison [43] suggested a three regime kinetic model to explain the geometry of diffusion. This model was originally developed for dislocations

but is shown to also be suitable for grain boundaries [40]. The model assumes a thin film with an array of dislocations that are running perpendicular to the surface with a radius a and separation $2Z$. The mean diffusion distance in the lattice is given by $\sqrt{D_l t}$, where D_l is the diffusion coefficient for the lattice and t is the diffusion time. Based on this model there are three kinetic regimes defining the geometry of diffusion as follows:

i. Type A kinetics for $\sqrt{D_l t} \gg Z$. The diffusing atoms interact with several high diffusivity paths while diffusing a sufficient distance into the lattice. The isoconcentration contours are relatively flat and parallel to the surface.

ii. Type B kinetics for $Z \gg \sqrt{D_l t} \gg a$. Each high diffusivity path is isolated and provides an initial fast diffusion path. Diffusion slows down as some of the diffusing atoms leak into the grain by lateral lattice diffusion.

iii. Type C kinetics for $\sqrt{D_l t} < a$. The diffusing atoms only move along the high diffusivity paths with no loss to the surrounding grains [43].

Type A diffusion can occur for films with an unusually high density of high diffusivity paths, such as films with a nanocrystalline structure where the distance between adjacent grains is very small. Type B and C are more frequently observed for thin films [39,40,42]. The above discussion points to the detrimental effect of the number and geometry of high diffusivity paths on the reliability of diffusion barriers. An amorphous structure with a high crystallization temperature or a single crystal structure is an ideal barrier while a polycrystalline barrier with a columnar structure — all grain boundaries perpendicular to the surface — is the poorest barrier [39,41,44]. Accordingly, conditions for the formation of amorphous metallic systems and their properties are discussed in Section 2.5.1.

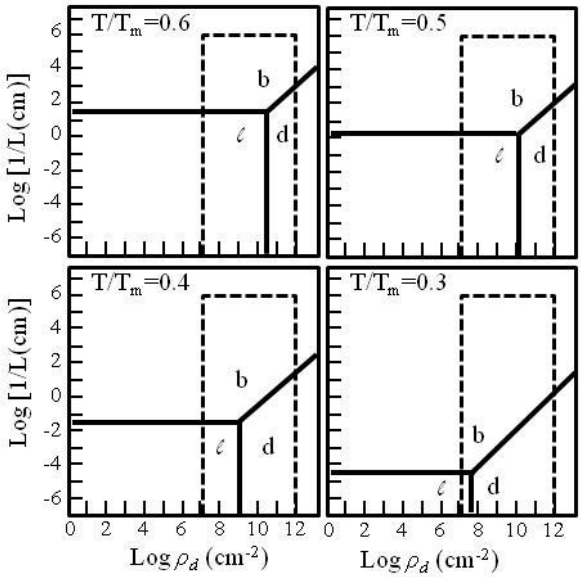

Figure 2–5 Schematic showing the various regimes of grain size, L, and dislocation density, ρ_d, where lattice diffusion (l), grain boundary diffusion (b) or dislocation enhanced diffusion (d) are dominant for a thin film with an fcc structure. Each map corresponds to diffusion at a specific T/T_m fraction. Reproduced from [39].

2.5 Materials specifications for diffusion barriers

It is evident from the above discussion that the shift to Cu/low-κ dielectrics generates a critical need for the development of a diffusion barrier system that prevents diffusion of Cu under thermal and electrical driving forces. There are several requirements for an ideal diffusion barrier, which are usually in conflict with each other. Additionally, with the downscaling of device sizes, the barrier thickness is continuously decreasing with a barrier thickness of 2.4 nm at the 32 nm node technology [9]. The driving force gradients become very steep over such small thicknesses and the requirement of conformality, continuity and stability become more stringent [5]. The suitable candidate must exist in equilibrium with Si, Cu and SiO_2 to minimize the contribution of the internal chemical energy gradient ($\nabla(\mu(c))$) (Equation 2-8) and to prevent any reaction and intermixing of the barrier with the materials in contact. It is observed that the lattice diffusion coefficient is proportional to the melting temperature of the substrate [45].

Consequently, to reduce the lattice diffusivity, a material with a high melting temperature is required.

As explained in Section 2.4.2, diffusion in thin metallic films is dominated by high diffusivity paths, especially grain boundaries. The diffusion barrier should, therefore, have an amorphous structure with high thermal stability (high crystallization temperature). The thermodynamic condition that results in a thermally stable amorphous structure is defined in Section 2.5.1. In addition, in conventional metallization stacks, the barrier is deposited directly on the dielectric material followed by deposition of a seed layer that facilitates electrodeposition of Cu (Section 2.2). The combined thickness of these layers occupy valuable space in the via which would otherwise be available to the low-resistivity Cu interconnect. With the continuous shrinking of feature size, the formation of Cu vias and lines is facing significant challenges due to the limited space available to the Cu interconnect. One suggested solution is the development of a barrier that also acts as the seed layer for electrodeposition of Cu [8]. These types of materials are called seedless barriers and are further explained in Section 2.5.2. In addition to these factors, the barrier material must satisfy the following specifications:

- Relatively large electrical conductivity (resistivity <1000 $\mu\Omega$cm).
- Low overall contact resistance (<25000 $\mu\Omega$cm) for the resulting metallization stack.
- Strong adhesion to Cu to eliminate self diffusion of Cu along the interface and thereby reduce electromigration.
- Strong adhesion to the adjacent dielectric material, particularly to the low-κ dielectric materials which release cure reaction byproducts.
- Suitable texture to promote the growth of the Cu layer in the (111) direction, since the highest resistance to electromigration in fcc metals like Cu is achieved when all (111) planes are aligned parallel to the interface.
- Acceptable thermal conductivity to provide enough cooling in the face of increasing heat and power densities.

- Compatibility with Cu metallization processes; for example, the barrier material must be compatible with the CMP step of the dual damascene process.
- Availability of a deposition process, which is capable of depositing a dense, highly conformal film (dual damascene process in the aggressive aspect ratios of dense devices), with minimum internal stress (stress is a driving force for diffusion) and within the thermal budget of the device, *i.e.*, lower than 450°C.
- Ability to maintain all the above mentioned requirements at continuously reduced thickness for smaller feature sizes [46-52].

Finding a barrier material and the corresponding deposition process that satisfies all these requirements is not an easy task. In the following sections the thermodynamic condition for forming an amorphous structure and the design of seed-less barriers is discussed.

2.5.1 Amorphous metallic systems

The search for an amorphous metallic system suitable for diffusion barrier applications involves two steps. First a binary or ternary alloy with high glass-forming ability needs to be selected. Then a detailed thermodynamic analysis needs to be performed to select the composition with the highest glass-forming ability in the system. A review of the available literature related to these two questions is discussed in this section. A "glass" or "amorphous" solid lacks long-range order but rather exhibits short-range order (on the order of five atomic distances). A typical temperature-time-transformation (TTT) diagram for the liquid-crystal transformation is shown in Figure 2–6. For metallic systems, if the liquid is cooled fast enough (following path "a" in Figure 2–6) to avoid the nose of TTT diagram, crystallization can be circumvented and a glassy structure can be formed. On this diagram T_g is the glass transition temperature, which is the temperature at which the viscosity of the liquid changes discontinuously with temperature. This temperature corresponds to the transition from equilibrium liquid to a frozen-in, non-equilibrium structure [53,54]. Such drastic cooling rates

can be achieved by either rapid liquid quenching or atomic condensation methods. Examples of the latter include physical vapor deposition (PVD), chemical vapor deposition (CVD), ion implantation, etc. The solid structures produced by both these methods are referred to as “amorphous”. However, it has been reported that the various alloys prepared by these two methods possess different physical properties [53-58].

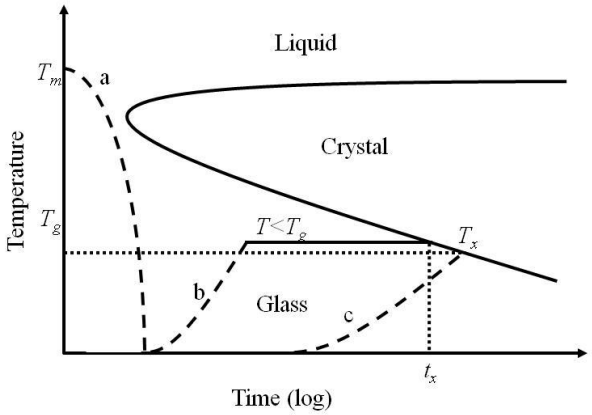

Figure 2–6 Schematic showing a typical TTT diagram for the liquid-crystalline phase transformation. Path “a” shows the fast cooling of the liquid to form an amorphous structure. Paths “c” and “b” show the various heat treatments resulting in crystallization of the amorphous structure. Reproduced from [55].

According to Figure 2–6, the stability of the amorphous structure can be defined by the time, t_x, or temperature of crystallization, T_x. The glass can be crystallized following one of the two paths: *i*) path “c” where the structure is heated slowly until crystallization at T_x or *ii*) path “b” where the structure is heated to a temperature lower than T_g and kept isothermally until crystallization after a certain time, t_x. Therefore, a universal crystallization temperature or time cannot be defined for a system and the thermal stability of an amorphous structure depends on both the annealing condition and its previous thermal history. The properties of the glassy phase, such as density, diffusivity, resistivity, and internal energy, depend on the cooling rate. The structures produced at a higher cooling rate possess a higher diffusivity and relax structurally at lower temperatures [53,55,59].

There have been several attempts to model the glass-forming ability of metallic systems based on various factors such as enthalpy of formation [60,61], atomic size difference of the constituent elements [57], valence electron concentration and electronegativity [62], and reduced glass transition temperature (T_g/T_m) [56], among others. These criteria have been developed for glasses prepared by liquid quenching methods. Atomic condensation techniques, on the other hand, provide a highly effective cooling rate and yield amorphous structures of metallic systems that cannot be obtained by liquid quenching [53,55,63]. The alloy systems and the range of composition over which amorphous phases can be obtained by atomic deposition methods are somewhat different than those obtained by liquid quenching methods. Some of the criteria suggested for obtaining amorphous structure by atomic deposition methods are: *i*) an atomic size difference larger than 10% between the constituent elements [64], *ii*) an equilibrium phase diagram with limited terminal solubility which basically originates from the former [61] and *iii*) inclusion of impurities which are proposed to reduce the mobility of adatoms on the surface and thereby inhibit the large displacement of condensed atoms required to form a crystalline structure [53].

Based on these correlations, the studied glass-forming binary alloys can be classified into three groups as follows:

i. Transition or noble metal alloys containing semimetals (Fe-B, Pd-Si).

ii. Alkaline metal glasses (Mg-Zn, Ca-Zn, Ca-Al, Mg-Cu), alkaline metal-transition metals (Ti-Be, Zr-Be), alkaline metal-rare earth metals (La-Al, La-Ga) and transition metal-rare earths (Gd-Co, Tb-Fe).

iii. Intertransition metal alloys which include early transition-late transition metals ($Cu\text{-}Ti_{35\text{-}70}$, $Cu\text{-}Zr_{27.5\text{-}75}$, $Ni\text{-}Zr_{33\text{-}42,\ 60\text{-}80}$, $Nb\text{-}Ni_{40\text{-}66}$ and $Ta\text{-}Ni_{40\text{-}70}$) and early transition-Ir or Rh ($Nb_{35}Ir_{45}$, $Ta_{55}Rh_{45}$) [53,55,57,58,63,65,66].

Despite the relative success of all these models in predicting stability of some metallic glasses, they are not universally applicable. In addition, most of these models offer qualitative measures of glass-forming ability based on geometrical

or thermodynamic data that are not readily available for all systems. In this respect, we chose the model suggested by Donald and Davies [67] that predicts and compares the glass-forming ability of various systems based on the simple parameter of melting temperature. Afterwards, the thermodynamic model by Van de Kolk *et al* [68], known as the Miedema and Niessen model, is used to predict the effect of composition on the stability of amorphous phase. These two models are explained in the next two sections.

2.5.1.1 Donald and Davis model for predicting glass-forming ability of various systems

The kinetic analysis, based on the simple nucleation theory by Turnbull [56] assuming that the molar difference in heat capacity for the liquid and crystal is zero, gives the following expression for the steady state frequency of homogenous nucleus formation:

$$I_{nucl} = \frac{k_n}{\eta} \exp\left(-\frac{b\alpha^3\beta}{T_r(\Delta T_r)^2}\right) \qquad \text{Equation 2-10}$$

where k_n is a constant, η is the viscosity, b is the nucleus shape factor ($16\pi/3$ for a sphere), $T_r=T/T_m$ and $\Delta T_r=1-T_r$. α and β are dimensionless parameters defined as

$$\alpha = \frac{(N_A V^2)^{1/3}\sigma_{int}}{\Delta H_{\mathrm{m}}} \qquad \text{Equation 2-11}$$

$$\beta = \frac{\Delta H_{\mathrm{m}}}{RT_m} \qquad \text{Equation 2-12}$$

where N_A is Avogadro's number, V is the molar volume of the crystal, σ_{int} is the liquid-crystal interfacial tension, R is the gas constant and ΔH_m is the molar heat of fusion. In order for nucleation to be suppressed and an amorphous structure to be formed, a smaller nucleation frequency is needed. This is mainly determined by the cooling rate, the viscosity and the expression $\alpha\beta^{1/3}$. This analysis showed that liquids with $\alpha\beta^{1/3}>0.9$ always form an amorphous structure, unless seeded. Additionally, it was shown based on Equation 2-12 that nucleation frequency (I_{nucl}) varies inversely with the reduced glass transition temperature (T_g/T_m). The glass-forming tendency, therefore, increases with the value of T_g/T_m [56].

Knowledge of the T_g value for the system is required if T_g/T_m is to be used as the glass-forming parameter. This value is not available for material systems which have not been studied yet and cannot be used for prediction of the glass-forming ability of an unknown system.

Marcus and Turnbull [69] modified the glass-forming criterion suggested by Turnbull [56] and suggested that the glass-forming ability of a system can be predicted by calculation of the departure of the liquidus temperature (T_l) from the ideal solution liquidus temperature (T_l^o), using the normalized parameter:

$$\frac{\Delta T}{T_l^o} = \frac{T_l^o - T_l}{T_l^o} \qquad \text{Equation 2-13}$$

$$T_l^o = \frac{\Delta H_m^A T_m^A}{\Delta H_m^A - R\ln(1-x)T_m^A} \qquad \text{Equation 2-14}$$

where ΔH_m^A and T_m^A are the heat of fusion and melting point of the solvent, x is the mole fraction of the solute and R is the gas constant. It was shown that a larger value of the normalized parameter indicated a better glass-forming ability [69]. However, Donald and Davies [67] observed deviations from this model for systems that showed solid solubility or compound formation. Instead, they proposed a simpler normalized parameter as follows:

$$\Delta T^* = \frac{\Delta T}{T_l^{mix}} = \frac{T_l^{mix} - T_l}{T_l^{mix}} \qquad \text{Equation 2-15}$$

$$T_l^{mix} = T_m^A x_A + T_m^B x_B \qquad \text{Equation 2-16}$$

where T_m^A and T_m^B are the melting temperatures of the pure elements in a binary alloy with x_A and x_B mole fractions. This parameter was shown to be a promising guide for assessing the glass-forming ability of the alloys and 60 out of 68 glass-former systems had a normalized parameter higher than 0.2 [67].

2.5.1.2 Miedema and Niessen model for predicting the composition range of the glassy phase

The composition range of the amorphous phase in binary metallic systems can be predicted by comparing the Gibbs free energy of the amorphous phase with

the Gibbs free energy of supersaturated crystalline solid solutions. Miedema and coworkers [60,61,68,70-73] developed a semi-empirical model for intertransition metals that can predict the enthalpy of formation of a statistical solid solution and an amorphous phase. The enthalpy of formation for a supersaturated statistical solid solution (ΔH_{ss}^{f}) is given by:

$$\Delta H_{ss}^{f} = \Delta H_c + \Delta H_e + \Delta H_{str} \qquad \text{Equation 2-17}$$

According to this relationship, the enthalpy has three contributions: *i*) ΔH_c or the chemical term related to the differences in electronegativity and the differences in electron density at the boundary of the Wigner-Seitz cell of the two constituent elements, *ii*) ΔH_e or the elastic term related to the elastic energy due to the difference in the sizes of the constituent elements and *iii*) ΔH_{str} or the structural term related to the preference of transition metals to crystallize in one of the three simple structures, *i.e.*, fcc, bcc or hcp [72-74]. The enthalpy of formation of the amorphous phase (ΔH_a^f) is given by:

$$\Delta H_a^f = \Delta H_l^M + x_A \Delta \mathrm{H}_{a-s}^{A} + x_B \Delta H_{a-s}^{B} \qquad \text{Equation 2-18}$$

where $\Delta \mathrm{H}_{a-s}^{i}$ is the enthalpy of fusion of the pure metals, corrected for structural relaxation that occurs in the amorphous phase, and ΔH_l^M is the enthalpy of mixing for the liquid alloy. For a liquid alloy, both the elastic and structural terms can be neglected and, therefore, $\Delta H_l^M = \Delta H_c$ [60,68]. The details of this model are further discussed in Chapter 4, where the Gibbs free energies of the solid solution and the amorphous phases for the selected binary alloy of this study are calculated and presented.

2.5.2 Materials suitable for direct electrodeposition of Cu

Industry standard acid-based baths for electrodeposition of Cu consist of a copper sulfate solution and sulfuric acid with additives that facilitate conformal filling in the Cu-damascene structure. The Cu^{2+} ions are reduced and deposited at the cathode and the sulfate ions (SiO_4^{2-}) are oxidized at the anode. The reduction process requires an electrically conductive cathode that facilitates nucleation and

growth of the Cu film [75]. Therefore, the cathode surface needs to have a native oxide that is either conductive or is not stable in the Cu plating solution [5]. In this respect, a simple criterion was identified and tested by Lane *et al* [8] for selecting materials suitable for direct electrochemical deposition of Cu. This criterion is based on comparison of the Gibb free energies of formation for the metal oxide (ΔG^f_{M-O}) and Cu oxide (ΔG^f_{Cu-O})

$$\left|\Delta G^f_{M-O}\right| < \left|(\Delta G^f_{Cu-O})\right| \qquad \text{Equation 2-19}$$

Based on this criterion, Lane *et al* [8] identified a list of metals that allow for direct Cu electrodeposition in standard acidic baths. These metals together with the enthalpy of formation of their corresponding oxides per oxygen atom are compiled in Table 2-1.

Table 2-1 Enthalpy of formation (kJ/mole) of metal oxides per atoms of oxygen for metals that facilitate direct electrodeposition of Cu [8].

Metal	Cu	Pt	Pd	Ru	Rh	Ir	Ag
$\left\|\Delta \boldsymbol{H}^{\boldsymbol{f}}_{\boldsymbol{M-O}}\right\|$	163	42	84	75	113	138	21

The validity of this selection criterion was demonstrated by the possibility of direct electrodeposition of Cu on Pd, Rh and Ru films without any seed layer [8]. It should be noted that this criterion does not consider the pH of the electrochemical baths and a better indicator of the electrochemical nature of a surface can be found in Pourbaix diagrams. Based on these diagrams, the stability of a phase in an aqueous system can be assessed as a function of the potential and the pH of the system [5]. An alternative method of deposition of Cu interconnects is electroless plating where deposition of Cu occurs by reduction of a metal salt bath in the presence of a catalyst. The catalytic substrate oxidizes the reducing agent, facilitating Cu deposition [76]. Marumo *et al* [77] have studied electroless deposition of Cu and showed that, depending on the solution, the catalytic substrate can be one of the following seven metals: Pt, Pd, Ag, Ru, Au, Rh and Ir

[77]. Comparison of Marumo [77] and Lane [8] results, further demonstrates the validity of the selection criteria presented by Equation 2-19.

2.6 Candidate diffusion barriers for Cu metallization

As pointed out in the previous sections, due to the dependence of the diffusivity of Cu on the melting temperature of the barrier (Section 2.4.2), a barrier material with high melting temperature is highly desirable. Furthermore, the barrier has to be in equilibrium with the materials in contact (Section 2.4.1), be an easy glass-former (Sections 2.4.2 and 2.5.1) and have relatively low resistivity (Section 2.5). Additionally, there is great interest in barriers that facilitate direct electrodeposition of Cu without the need for a seed layer (Section 2.5.2). In this respect, a large number of materials systems have been studied for diffusion barrier applications. In this section, a summary of the studied barriers with a focus on the current industry solutions is given. The corresponding materials systems are organized into two categories, based upon their performance type. These are inert barriers and functional barriers.

2.6.1 Inert barriers

Refractory metallic systems with their high melting temperature and chemical inertness are deemed as viable candidates for diffusion barriers for Cu metallization [51]. Various diffusion barrier systems based on refractory metals and their binary and ternary alloys have been suggested and studied. Some examples include *i*) pure refractory metals, such as Ta, Ti, and W [78,79], *ii*) refractory metal silicides, such as $TaSi_2$, and W_xSi_{1-x} [80,81], *iii*) ternary barriers, such as $Ta_xSi_yN_{1-x-y}$, and $W_xSi_yN_{1-x-y}$ [81,82], *iv*) carbon-based alloys and compounds, such as amorphous carbon [83], *v*) refractory metal nitrides, such as TaN_x, TiN_x, and W_2N [84-86], and *vi*) refractory metallic alloys, such as $TaIr_x$, and $NiNb_x$ [87,88]. Several comprehensive reviews of these materials are available in the literature [5,44,48-50].

The single metal systems of group *i* have poor thermal stability and mainly fail by grain boundary diffusion [78,79]. Refractory metal silicides (group *ii*) have some directional bonding, resulting in a more complex crystal structure, and thus

great tendency to vitrify. Established thermodynamic data has confirmed that silicides of the form MSi_2 can easily react with Cu to form Cu_3Si. M-Si compounds with Si content lower than MSi_2 (e.g., M_5Si_3) are in equilibrium with Cu, but they react with Si [51]. The ternary systems of group *iii* with two nonmetal elements can form highly stable, amorphous barriers. However, due to the presence of nonmetal bonding, these systems usually possess low electrical conductivity which can adversely affect the barrier properties [53,55,59]. Among these systems, refractory metal nitrides (group *v*) are promising diffusion barriers and TaN_x compounds are currently the predominant industry solution. Refractory metal alloys (group *vi*) offer an excellent combination of low resistivity, glass-forming ability and thermal stability. A summary of diffusion barrier materials that fall under these two categories are given here.

2.6.1.1 Refractory metal nitrides

Polycrystalline Ti and TiN are the most commonly used barriers for Al-based interconnect systems. A Ti barrier is shown to fail by reaction with Cu at temperatures as low as 350°C [49] while TiN fails through grain boundary diffusion [89]. Ramberg *et al* [51] discussed that the group III and IV transition metals (Sc, Y, La, Ti, Zr, Hf) are extremely reactive with Cu and form stable compounds. On the other hand, group V and VI (V, Ta, Nb, Cr, Mo, W) transition metals are reliable as they are immiscible with Cu.

Of all the refractory metal nitrides, Ta-N compounds are the predominant industry solution owing to their desirable thermodynamic stability with Cu and high melting points. TaN_x phases are closed-packed structures of Ta with N atoms at the interstitial sites. Thus, bulk diffusion of Cu through the barrier is unlikely (minimum vacant sites) [90]. Ta-N diffusion barriers enhance the electromigration stability of the metallization stack by inducing a (111) texture in Cu [91]. This system includes a variety of different compounds such as Ta_2N, TaN, Ta_5N_6, Ta_4N_5, and Ta_3N_5. The phase diagram of Ta-N system is shown in Figure 2–7 [92]. Stoichiometry of the TaN_x films (controlled by the deposition process and suitable post treatment) plays an important role in the performance of the barrier.

Tetragonal Ta_3N_5 has a resistivity of 6×10^6 $\mu\Omega$cm while hexagonal TaN has a resistivity of 130 $\mu\Omega$cm. Therefore, any reaction or deposition method that leads to formation of Ta_3N_5 must be avoided. TaN, on the other hand, has a larger absolute value of enthalpy of formation (-120 kJ/mol) as compared with Ta_2N (-98 kJ/mol) and exhibits a higher melting temperature (3090°C) compared with Ta_2N (2050°C). The composition range of stability for Ta_2N at room temperature is 22-33 at% N, while TaN only forms at 50 at% N (Figure 2–7). Consequently, to deposit a barrier consisting mainly of TaN phase, the stoichiometry of the barrier and the deposition conditions must be strictly controlled [92].

The barrier performance of TaN_x compounds has been studied by several researchers. A detailed summary of the experimental results obtained in the evaluation of TaN_x barriers by thermal annealing experiments is given in Table 2-2. The type, condition and source of deposition, the crystal structure and resistivity of the film, the stack configuration, the maximum time/temperature combination at which the barrier is stable, the phases formed and the characterization techniques are tabulated. The stability temperature is defined as the highest temperature at which compound formation or diffusion of Cu is not detected.

The properties of TaN_x films, such as structure, composition, conformality and barrier performance, are primarily determined by the deposition method and processing conditions. The partial pressure of nitrogen during sputtering has been shown to determine the stoichiometry of deposited TaN_x films from a Ta target. The phases deposited by increasing N_2 partial pressure are bcc or tetragonal pure Ta, bcc-Ta solid solution, hcp or amorphous Ta_2N, fcc-TaN and high resistivity Ta_5N_6; these appear in succession as the N content increases [93-96]. The binary phase diagram of the Ta-N system, given in Figure 2–7, shows considerable terminal solid solubility in bcc-Ta and the eutectic lying between the stable intermetallic phases is a relatively high temperature reaction. This system, thus, does not meet the thermodynamic criteria, discussed in Section 2.5.1, to be an easy glass former. However, several attempts have been made to fabricate

amorphous TaN_x films. As can be seen in rows 3-5 and 12-14 of Table 2-2, amorphous or a mixture of amorphous and crystalline TaN_x phases can be deposited by reactive sputtering in N_2/Ar from a Ta target. Tsukimoto *et al* [97] utilized a $N_2/(N_2+Ar)$ partial pressure greater than 0.15 to attain amorphous TaN_x films, but speculated that the columnar structure of the films with several micro-voids can deteriorate the diffusion barrier properties. The reliability of these films in a Cu interconnect scheme, however, was not examined [97]. Alternatively, an amorphous TaN_x phase can be deposited by reactive sputtering at a composition near Ta_2N (row 12 of Table 2-2) or by N_2 plasma treatment resulting in significantly lower values of resistivity (rows 8-9 and 11 of Table 2-2).

As the feature size and the barrier is scaled down, the conformality of the barrier over aggressive topographies and thickness control over the entire feature are becoming critical factors. Consequently, CVD (rows 15-18 of Table 2-2) and more recently atomic layer deposition (ALD - rows 19-22 of Table 2-2) have been identified as more promising thin film deposition techniques when compared with the traditional sputtering methods. In general, CVD processes rely on the "catalytic role of the substrate in the deposition reaction" and, therefore, can yield highly conformal films in high aspect ratio features. Some key factors that need to be considered when studying the applicability of CVD processes for diffusion barrier applications are: *i*) the controlled reaction must be feasible within the thermal budget of device fabrication (<450°C) and *ii*) the deposited film has to be conductive with low resistivity (minimize the concentration of impurity contamination) [50]. Generally, CVD-deposited barriers offer more conformal coverage than barriers deposited by sputtering methods. The films deposited by thermal CVD based on metal-organic precursors (rows 15-17 of Table 2-2) are shown to be highly conformal but electronically insulating and are not suitable for barrier applications. This is due to the strong metal bond to the organic ligand in the precursor, which is difficult to break. Additionally, the deposition temperature of these films is above the thermal budget of the system. Among various available CVD techniques, a plasma enhanced CVD (PECVD) process using a $TaBr_5/N_2+H_2$ source has been successful to form low resistivity TaN films.

However, the high deposition temperature, little control over the thickness of the film and poor stability when compared to sputter-deposited films (row 17 of Table 2-2), has created more interest in modified sputtering (*e.g.*, ionized sputtering) and ALD technologies [5].

ALD offers excellent conformality and the ability to control the thickness of the barrier at the atomic scale [98]. The ALD process is based on self-limiting adsorption of monolayers of the precursor followed by introduction of appropriate reactants that break down the precursor. Separate introduction of the precursor and the reactant, and purging of the chamber in between, result in controlled deposition of a single molecular layer of the thin film. This growth cycle is repeated until the desired thickness of the film is achieved [44]. Thermal approaches towards ALD of TaN_x have been mostly based on NH_3 as the reactant gas (rows 19-20 of Table 2-2). Despite their great conformality, these films usually possess high resistivity due to inclusion of several impurities in the film. Alternatively, plasma enhanced ALD (PEALD), where plasma activated reactants are introduced, has been utilized to deposit TaN_x diffusion barriers with acceptable resistivity and improved adhesion to the underlying dielectric (rows 21-22 of Table 2-2). Although a large number of these materials have been reported as satisfactory diffusion barriers, their relative high deposition temperature and high resistivity values still remain a challenge to the industry.

Since TaN_x barriers are the current industry solutions, any new barrier material needs to be compared against TaN_x stacks. However, comparison of the stability temperature, thickness of the studied barriers and the resulting reaction morphologies of various TaN_x-based barriers in Table 2-2 indicates the wide range of stabilities reported for these barriers. Therefore, prior to examining any new material it was essential to initially examine the reliability of amorphous TaN_x barriers to create a baseline for comparison.

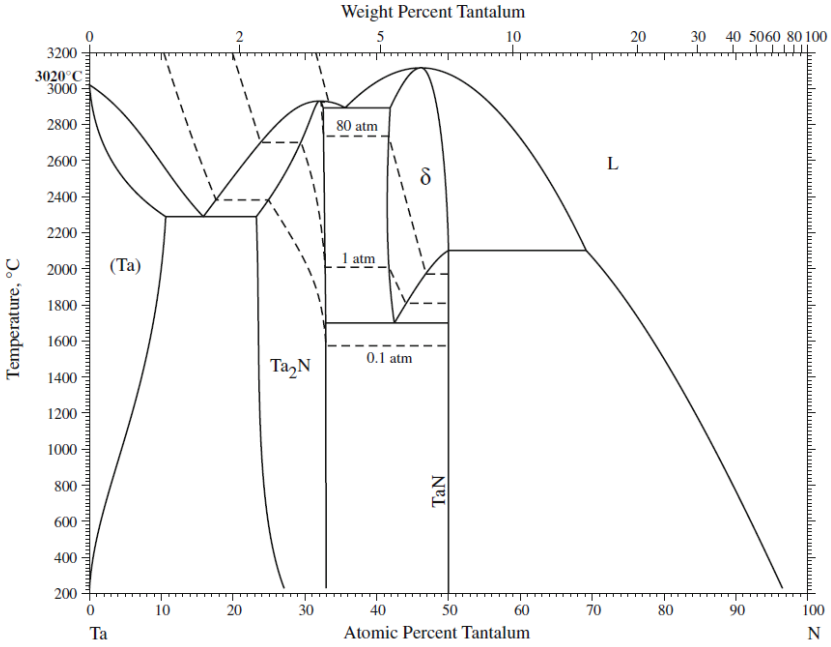

Figure 2–7 The Ta-N phase diagram [92].

Table 2-2 Summary of the properties and deposition processes for various studied TaN_x diffusion barriers. a: amorphous; RF: radio frequency; RBS: Rutherford backscattering; RTA: rapid thermal annealing; SEM: scanning electron microscopy; TEM: transmission electron microscopy; EDX: energy dispersive X-ray spectroscopy; STEM: scanning TEM, XRD: X-ray diffraction; FPP: four point probe resistivity measurements; AFM: atomic force microscopy; DC: direct current; GDOES: glow discharge optical emission spectroscopy; AAS, atomic absorption spectroscopy; AES: Auger electron spectroscopy; PECVD: plasma enhanced chemical vapor deposition; MOCVD: metal-organic chemical vapor deposition; XPS: X-ray photoelectron spectroscopy; SIMS: secondary ion mass spectroscopy; ALD: atomic layer deposition; TBTDET: *tetr*-butylimido (trisdiethylamido) tantalum; PEALD: plasma enhanced ALD; XRF: X-ray fluorescence.

No	Process	Source	Deposition temperature (°C)	Structure	Film resistivity ($\mu\Omega$cm)	Stack properties (nm)	Stability temperature/ annealing ambient	Reaction morphology	Characterization techniques	Ref
1	RF reactive magnetron sputtering	Ta target 5%N_2/Ar	----	Ta_2N	200	Cu /(50)TaN_x/ Si <100>	650°C/30 min (He)	Ta_3Si_5 + $TaSi_2$ (@800°C)+ Cu_3Si + a-SiO_2	*In-situ* resistivity measurement, RBS, SEM, TEM/EDX	[85]
2	RF reactive magnetron sputtering	Ta target 5%N_2/Ar	----	TaN	560	Cu /(8) TaN_x/ Si <100>	600°C/30 min (5%H_2/N_2)	----	XRD, RBS, TEM	[99]
						Cu /(25)TaN_x/ Si <100>	700°C/30 min (5%H_2/N_2)	----		
3	DC reactive magnetron sputtering	Ta target 15 cm^3/s N_2 flow rate	----	Nanocrystalline or amorphous $TaN_{1.09}$	632	Cu/(50)TaN_x/ Si <100>	650°C/60 s (RTA in N_2)	----	FPP, SEM/EDX, XRD, AFM	[91]
4	RF reactive sputtering	Ta target 2% N_2/Ar	----	Amorphous + fcc-TaN	----	Cu/(150)TaN_x/ Si <111>	600°C/30 min (vacuum)	Cu_3Si	*In-situ* heating in XRD, XRD, TEM	[100, 101]
						Cu/(50)TaN_x/(50)Ta/(50)TaN_x/Si <111>	700°C/30 min (vacuum)	----		

No	Process	Source	Deposition temperature (°C)	Structure	Film resistivity ($\mu\Omega$cm)	Stack properties (nm)	Stability temperature/ annealing ambient	Reaction morphology	Characterization techniques	Ref
5	RF reactive sputtering	Ta target 2.5 sccm N_2/Ar	----	Amorphous Ta-20 at%N	----	Cu/(10)TaN_x/ Si <100>	500°C/60 min (vacuum)	$TaSi_2$ + Cu_3Si	XRD, GDOES, AAS, SEM, TEM	[102]
		Ta target 3.5 sccm N_2/Ar		Amorphous + fcc-TaN			600°C/60 min (vacuum)	Cu_3Si		
6	RF reactive magnetron sputtering	Ta target N_2/Ar	----	Ta_2N	----	Cu/(100)TaN_x/ TaO_x/ Si <100>	600°C/60 min (vacuum)	----	RBS, FPP, XRD, SEM, TEM	[103]
7	Pulse-laser deposition	TaN target	600°C	Single crystal, fcc-TaN	----	Cu/(50)TaN/ TaN/ Si <100>	15 nm diffusion of Cu @ 700°C/30 min	----	XRD, TEM, STEM	[104, 105]
8	RF magnetron sputtering + N ion implantation	Ta target + 10^{15} N^+/cm^2	----	Amorphous + Ta	----	Cu/(100)TaN_x/ Si <100>	500°C/30 min (N_2)	$TaSi_2$ + Cu_3Si + Cu_4Si	SEM, XRD, FPP	[106]
		Ta target + 10^{17} N^+/cm^2		Amorphous + Ta_2N			700°C/30 min (N_2)	----		
9	RF magnetron sputtering + N ion implantation	Ta target + $5x10^{16}$ N^+/cm^2	<100°C	Amorphous + tetragonal Ta	----	Cu/(50)TaN_x/ SiO_2/Si <100>	500°C/60 min (vacuum)	----	AES, XRD	[107]
		Ta target + 10^{17} N^+/cm^2		Amorphous + Ta_2N + Ta_4N	----			----		
10	RF reactive sputtering	Ta target + N_2/Ar	----	bcc-TaN	----	Cu/(10)TaN_x/ Si <100>	600°C/60 min (N_2)	$TaSi_2$ + Cu_3Si	TEM, SEM/EDX, XRD	[108]
11	RF sputtering + plasma treatment in PECVD system	Ta target + 30 min plasma treatment	----	Amorphous + Ta_2N	----		700°C/60 min (N_2)	$TaSi_2$ + Ta_5Si_3 + Cu_3Si		

No	Process	Source	Deposition temperature (°C)	Structure	Film resistivity ($\mu\Omega$cm)	Stack properties (nm)	Stability temperature/ annealing ambient	Reaction morphology	Characterization techniques	Ref
12	RF reactive magnetron sputtering	Ta target + N_2/Ar	----	Amorphous + Ta_2N (20-50 at% N)	<300	TaN_x/Si <100>	Crystallize at 600 °C/65 min (vacuum)	----	XRD, FPP, TEM	[96]
				$TaN+Ta_5N_6$ (>50 at% N)	Insulating		800°C/65 min (vacuum)	-----		
13	RF reactive magnetron sputtering	Ta target + N_2/Ar	25°C	Amorphous	----	Cu/(100)TaN_x/ Si <100>	Crystallize at 500°C, stable up to 700°C/30 min (vacuum)	$TaSi_2$ + Cu_3Si	FPP, XRD, SEM	[109]
			100°C	Amorphous + Ta_2N	----		700°C/30 min (vacuum)	$TaSi_2$		
			200°C	Ta_2N (002) preferred orientation	----		700°C/30 min (vacuum)	$TaSi_2$		
14	RF reactive magnetron sputtering	Ta target $N_2/(N_2+Ar)<$ 0.10	----	fcc-TaN	----	Cu/(30)TaN_x/	----	----	XRD, TEM	[97]
		Ta target $N_2/(N_2+Ar)>$ 0.15		Amorphous with columnar void structure						
15	MOCVD	Metal amino compounds/ NH_3	200°C	Ta_3N_5	Insulating	TaN_x/Si <100>	----	----	RBS, XPS, TEM	[110]
16	MOCVD	$((Et_2N)_3Ta=Net)+(Ta(\eta^2-EtN=CMeH)/NH_3$	500-650°C	Cubic-TaN + tetragonal Ta_3N_5 + C and O contamination	----	----	----	----	SEM, XRD,	[111]

No	Process	Source	Deposition temperature (°C)	Structure	Film resistivity ($\mu\Omega$cm)	Stack properties (nm)	Stability temperature/ annealing ambient	Reaction morphology	Characterization techniques	Ref
17	MOCVD	$(NEt_2)_3Ta{=}NBu^t/NH_3$	650°C	fcc-TaN + C and O contamination	920	Cu/(60)TaN_x/ Si<100>	500°C/30 min (vacuum)	Cu_3Si + a-SiO_2	SEM, FPP, AES, SIMS, RBS	[90]
	Reactive sputtering	Ta target + N_2/Ar	25-80°C	fcc-TaN	380		550°C/30 min (vacuum)	Cu_3Si + a-SiO_2		
18	PECVD	$TaBr_5/N_2/H_2$	350-450°C	Cubic-TaN + Br contamination	150	TaN_x/Si <100>	----	----	XRD, FPP, AFM, AES, RBS, SEM	[47]
19	ALD	$Ta[N(CH_3)_2]_5/NH_3$	275°C	Nanocrystalline fcc-TaN + C, O and H contamination	----	Cu/(10)TaN_x/ Si<100>	----	----	AES, XPS, XRD, TEM, SIMS	[112]
20	ALD	TBTDET/ NH_3	250°C	Amorphous TaN_x (x=1) C and O contamination	500-1000	(30)TaN_x/ SiO_2/Si<100>	----	----	SEM, TEM, AFM, AES	[113]
21	PEALD	$TaCl_2$ + H_2/N_2 plasma	300°C	Cubic- Ta	<400	TaN_x/ SiO_2/Si<100>	----	----	RBS, XRD, SEM, TEM	[114]
22	PEALD	$Ta[N(CH_3)_2]_5$ + H_2/He plasma	275°C	---	Cu/(2)TaN_x/SiO_2/Si<100>, resistivity is lower and adhesion and wettability is improved compared with similar films deposited by sputtering or thermal ALD				TEM, XPS, XRF, SEM	[115]

2.6.1.2 Refractory metal alloys

Intertransition metallic alloys offer an excellent combination of high conductivity, glass-forming ability and thermal stability. This group comprises refractory metals-late transition metals and refractory metals-Rh or Ir systems. The glass-forming composition of these alloys falls into a region near the eutectic composition and overlaps with the composition of intermetallic phases [55,65]. The diffusion barrier performance of several sputtered binary amorphous alloys has been investigated and the type, condition and source of deposition, the crystal structure and resistivity of the film, the stack configuration, the maximum time/temperature combination at which the barrier is stable, the phases formed and the characterization techniques are tabulated in Table 2-3. Studying the phase diagrams of these systems revealed that the compositions of the barriers based on Ta-Ni [116], $ZrIr_x$ [117], $TaCo_x$ [118], $TaFe_x$ [119], $MoSi_x$ [120] and $Ta_{0.75}Ni_{0.25}$ [120] fall into the regions of stability of intermetallic compounds. In contrast, the compositions of low-lying eutectic reactions have been utilized for $Ta_{0.0.25}Ni_{0.0.75}$ [120], $MoNi_x$ [121], $TaIr_x$ [120] and $NbNi_x$ [122] barrier systems. It should be noted that, traditionally, the composition of the refractory metal alloys being studied for potential diffusion barrier applications has been selected based on information extracted from phase diagrams. However, this scheme does not lead to a prediction of the range of amorphous phase formation. This indicates the importance of developing a materials selection scheme that can predict the glass-forming composition of refractory metal alloys. One such scheme is developed in the current work and explained in Section 2.7.

Failure of these metallic amorphous barriers occurs by either dissociation of the alloy into its constituents (alloy partitioning) followed by reaction with underlying Si (rows 1, 4 and 6 in Table 2-3) or by crystallization and diffusion of Cu through grain boundaries (rows 2, 5 and 7-8 in Table 2-3). Crystallization of these amorphous alloys follows a sequence of structural changes before reaching the final stage of crystallization, including the appearance of several metastable phases in the form of small crystallites which are well-separated by the amorphous matrix [54]. A similar sequence has been observed during annealing

of diffusion barriers where failure by grain boundary diffusion is delayed to the last stage of crystallization where at a critical volume fraction crystallites will merge and form grain boundaries perpendicular to the film [123,124]. A common observation among all these studies is that the presence of the Cu overlayer reduces the stability temperature of the amorphous refractory metal alloys. Li *et al* [125] speculated that the difference in the coefficient of thermal expansion (CTE) of Cu and Si increases the magnitude of tensile stress formed in the barrier layer as a result of annealing. Consequently, the activation energy for crystallization or alloy partitioning is decreased in the presence of Cu, as the presence of tensile stress can facilitate the diffusion of atoms [125].

As can be seen in Table 2-3 under the reaction morphology column, the failure of the majority of these alloys results in formation of various Cu-silicides and refractory metal-silicides. However, it is not clear whether the failure is triggered by diffusion of Cu through the barrier and formation of Cu-silicides, followed by formation of refractory metal silisides, or is triggered by reaction of the barrier with the Si substrate followed by indiffusion of Cu.

Table 2-3 Summary of the properties and deposition processes of the various studied refractory metal alloy diffusion barriers. For description of acronyms refer to the caption in Table 2-2.

No	Process	Source	Structure	Film resistivity ($\mu\Omega$cm)	Stack properties (nm)	Stability temperature/ annealing ambient	Reaction morphology	Characterization techniques	Ref
1	DC magnetron sputtering	----	Amorphous $Ta_{0.50}Ni_{0.50}$	240	Cu/(20, 50, 100)$TaNi_x$/ Si<100>	650°C/5 min (RTA in vacuum)	$TaSi_2$+$NiSi_2$+Ta_5Si_3+Cu_3Si	FPP, XRD, TEM	[126]
			Amorphous $Ta_{0.65}Ni_{0.35}$	170		20, 50 nm: 650°C/5 min 100 nm: 650°C/5 min (RTA in vacuum)	$TaSi_2$+$NiSi_2$+Ta_5Si_3+Cu_3Si		
2	Magnetron sputtering	----	Amorphous $Ir_{0.84}Zr$	----	Cu/(270) $IrZr_x$/ Si<100>	700°C/2 hr (air)	Ir_3Zr+Cu_4Si+ Cu_5Si	XRD, RBS, AES, FPP	[124]
			Polycrystalline $Ir_{2.85}Zr$			600°C/2 hr (air)	Partially crystallized (Ir_3Zr)+Cu_4Si+ Cu_5Si		
3	RF sputtering	Ni or Si target covered partially with Nb, Mo or W	Amorphous 55-57 at% Ni-Nb	200-230	Cu/(1µm) barrier/ Si<100>	500°C/1 hr (vacuum, Ti gettering)	----	XRD, FPP	[123]
			Amorphous $Ni_{0.55}Mo_{0.45}$	110-130	Si/barrier (1µm)	Crystallization at 525°C (vacuum, Ti gettering)			
			Amorphous $Mo_{0.60}Si_{0.40}$	160-200		Crystallization at 550°C (vacuum, Ti gettering)			
4	DC magnetron sputtering	----	Amorphous $Ta_{0.5}Fe_{o.5}$	247	Cu/(20) barrier/ Si<100>	600°C/5 min (RTA in vacuum)	Cu_3Si+Ta_5Si_3+ $TaSi_2$	FPP, XRD, SEM, TEM, SIMS	[127]
			Amorphous $Ta_{0.50}Co_{o.50}$	147		650°C/5 min (RTA in vacuum)			

No	Process	Source	Structure	Film resistivity ($\mu\Omega$cm)	Stack properties (nm)	Stability temperature/ annealing ambient	Reaction morphology	Characterization techniques	Ref
5	RF sputtering	Ni target covered partially with Nb	Amorphous $Nb_{0.40}Ni_{0.60}$	----	Cu/(500) $NbNi_x$/ Si<100>	600°C/1 hr (vacuum, Ti gettering)	----	AES	[88]
6	DC magnetron sputtering	----	Amorphous $Ta_{0.25}Ni_{0.75}$	----	Cu/(20) $TaNi_x$/ Si<100>	500°C/5 min (RTA in vacuum)	Cu_3Si+NiSi+ +$TaSi_2$+$NiSi_2$	FPP, XRD, SEM, TEM/EDX, AES	[128]
			Amorphous $Ta_{0.75}Ni_{0.25}$			550°C/5 min (RTA in vacuum)			
7	Dual electron gun evaporation	Ta and Ir targets + substrate temperature = liquid-N_2	Amorphous $Ir_{0.45}Ta_{0.55}$	----	Cu/(30) $IrTa_x$/ Si<100>	700°C/30 min (vacuum)	----	RBS, TEM	[87]
8	Co-sputtering	Pure Ta and Zr targets	Amorphous $Ta_{50}Zr_{50}$	160	Cu/(50) $TaZr_x$/SiO_2/ Si<100>	600°C/5 min (RTA in Ar)	Cu_3Si+ +$TaSi_2$+$ZrSi_2$	FPP, XRD, TEM	[125]

2.6.2 Functional barriers

As explained in Section 2.2, with the continued shrinking of the minimum feature size, conventional dual damascene processing technologies are facing significant challenges. These are mainly due to the complexity and challenges associated with obtaining a functional adhesion/diffusion barrier/seed layer at the continuously reducing barrier thickness and increasing aspect ratio of the vias [5]. One potential solution is to reduce the number of layers by developing diffusion barriers that possess other functionality (functional barriers). An example is seedless barriers, as explained in Section 2.5.2. One such barrier under consideration is Ru, which belongs to the list of elements identified by Lane *et al* [8] and is conducive to direct electrodeposition of Cu. Pure Ru films, however, are polycrystalline and suffer from premature failure due to grain boundary diffusion [129]. Additionally, it has been shown that Ru does not adhere well to the dielectric layer [130]. Consequently, several methods have been utilized to improve the barrier performance of Ru-based barriers. One approach is to alloy Ru with suitable alloying elements to facilitate the formation of an amorphous structure (refer to Section 2.5.1 for glass-forming conditions); hence, removing the high diffusivity paths. A 7.8 nm thick film of Ru-Cr alloy (Ru:Cr=10.06:1) has been shown to form an amorphous structure and to remain stable in contact with Si and Cu up to 650°C for 30 min. In comparison, a Si/(7.8 nm)Ru/Cu stack failed at 450°C [131]. Alternatively, alloying elements with an atomic size much smaller than Ru (*e.g.*, P) have also been utilized to form an amorphous alloy of Ru. A 12 nm thick film of Ru(P) alloy has been shown to remain stable after annealing at 500°C for 30 min or at 700°C for 5 min [132]. Another approach, developed by Kumar *et al* [133], involves deposition of monolayers of TaN and Ru by PEALD to form a mixture of an amorphous TaN matrix and embedded Ru grains. This latter study demonstrated that the elements identified by Lane *et al* [8] maintain their unique surface chemical characteristics upon alloying and can be designed to perform both as a robust barrier and as a Cu direct electrodeposition layer.

Another approach has involved the growth of Cu containing an alloying element (*e.g.*, Mn) and subsequent annealing of the structure. The latter causes the diffusion of the alloying element towards oxygen containing dielectrics to form a so-called "self-formed" barrier layer [134]. In these studies, the Cu-Mn alloy was deposited by sputtering and required the presence of oxygen and Si in the substrate to form $MnSi_xO$. The satisfactory performance of these barriers has triggered studies on depositing MnO_x barriers directly onto SiO_2 with a MOCVD process [135,136]. This latter approach, however, requires deposition of a seed layer and therefore belongs to the category of inert barriers (Section 2.6.1).

2.7 Material design process employed for selection of a diffusion barrier

As described in Section 2.5, the candidate diffusion barrier material must meet a list of properties including high conductivity, thermal stability, glass-forming ability and possibility of direct Cu electrodeposition. In this section, the set of selection criteria used to choose a suitable material system for diffusion barrier applications is explained. The material specifications for glass forming ability and direct Cu electrodeposition are explained in Sections 2.5.1.1 and 2.5.2, respectively. The list of metals that allow for direct Cu electrodeposition together with their enthalpies of oxidation is given in Table 2-1. These metals are called seedless elements and the list includes Pt, Pd, Ru, Rh, Ir and Ag [8]. Silver offers the lowest resistivity among these metals, but has very poor electromigration resistance and is a fast diffuser in SiO_2 and Si [7,137]. Consequently, Ag was eliminated from the list. Two separate investigations have demonstrated that upon alloying these seedless elements retain their unique properties for direct electrodeposition of Cu [8,133].

As described in Section 2.5.1, intertransition metal alloys offer high glass-forming ability and low electrical resistivity. As such, this study focused on intertransition metal amorphous diffusion barriers where one of the alloying elements is chosen from the seedless elements and the other is Ta. Tantalum was selected as it has a high T_m at 3017°C, forms a thermodynamically stable interface with Cu [138] and its compatibility with dual damascene fabrication methods is

widely recognized. Studying the phase diagrams of Cu-Pt and Cu-Pd systems revealed that both these elements form intermetallic compounds with Cu and are not suitable barrier materials [120]. Platinum and Pd were then eliminated from the list of alloying elements, leaving three potential systems: Ta-Ru, Ta-Rh and Ta-Ir. At this stage, the glass-forming ability of these three systems was studied using the model suggested by Donald and Davis [67], explained in Section 2.5.1.1. The values of ΔT^* were calculated using Equation 2-15, and were 0.28, 0.26, and 0.25 for Ta-Rh, Ta-Ir, and Ta-Ru, respectively [120]. According to this model, a larger ΔT^* value indicates superior glass-forming ability ($\Delta T^* > 0.2$). It is speculated that Ta-Rh alloys satisfy the requirements for an amorphous, conductive and seedless barrier. The next step was to select a stable amorphous Ta-Rh composition. To achieve this, a systematic thermodynamic study, based on the Miedema and Niessen model (explained in Section 2.5.1.2), was performed to select the most stable amorphous composition in Ta-Rh system (Chapter 4).

2.8 Characterization and evaluation of barriers

The ability of a diffusion barrier film to prevent diffusion of Cu under thermal and electrical driving forces can be evaluated by monitoring either the metallurgical or the electrical characteristics of the metallization stack. The metallurgical mode monitors one of the following properties: *i*) the concentration of Cu in the barrier layer or in the underlying substrate and *ii*) the change in the morphology of the barrier stack and formation of new phases and reaction products. The electrical mode monitors the change in the electrical characteristics of the device under the barrier as a function of Cu diffusion [6,15]. These characterization modes and the techniques associated with them are described in the following sections.

2.8.1 Metallurgical mode

The metallurgical mode of characterization was the primary method of failure analysis of barriers developed for Al-based metallization systems. These techniques can be categorized into two main groups: *i*) depth profiling techniques which monitor the concentration of Cu in the metallization stack as a function of

depth below the surface and *ii*) microstructural techniques which monitor the change in microstructure and detect formation of reaction products. Most investigations are performed on blanket films of the barrier film directly deposited onto Si, Si/SiO_2 or Si/low-κ dielectrics. The stacks are annealed to create a thermal driving force for diffusion (Equation 2-8). The annealing is performed in a vacuum environment or purged with N_2, forming gas ($5\%H_2/N_2$), Ar or He. In some cases a rapid thermal anneal (RTA) is used (refer to stability temperature/annealing ambient in Table 2-2 and Table 2-3). The characterization techniques used for several studies on TaN_x and metallic alloy barriers are tabulated in Table 2-2 and Table 2-3. The most common of the depth profiling techniques are Rutherford backscattering (RBS), Auger electron spectroscopy (AES) and secondary ion mass spectroscopy (SIMS). To detect microstructural changes, several techniques have been used; namely X-ray diffraction (XRD), scanning electron microscopy (SEM), transmission electron microscopy (TEM) and four point probe resistivity measurements (FPP) [6,49]. In this section, the techniques used in this thesis and their limitations are outlined and briefly discussed.

2.8.1.1 Auger electron spectroscopy (AES)

AES utilizes a source of high energy electrons (2-10 keV) to produce Auger electrons. The electron sources are similar to SEM sources and are discussed in Section 2.8.1.4. The emitted Auger electrons are analyzed by a cylindrical or hemispherical analyzer, which separates the electrons based on their kinetic energy resulting in a spectrum of intensity as a function of the kinetic energy of the electrons. The usual method of presenting AES data is the differentiated signal rather than the raw data. This presentation removes the background signal and accentuates the position of the peak as well as its fine structure. Two useful capabilities of AES analysis for diffusion barrier characterization are depth profiling and surface analysis. The latter is accomplished by rastering the electron beam over the surface and collecting the Auger signal to perform point, line or mapping analysis. Depth profiling is accomplished by controlled sputtering of the surface using the incorporated ion guns. The Auger signal is collected between

sputtering steps, constructing an elemental profile as a function of depth below the surface [139].

Auger excitation is a result of inelastic interaction of the beam electrons with the core-level electrons. Through excitation by an incident electron, a hole is created in an inner shell (*e.g.*, K shell) leaving the atom in an excited state. The energy of the atom is lowered when an electron from an outer shell (*e.g.*, L_3 shell) lowers its energy by filling the hole. This is followed by one of the following two processes:

i. X-ray photons are produced with an energy equal to the difference in energy between the levels involved in the transition (*e.g.*, $E_{K\alpha 1} = E_K - E_{L3}$). The emitted X-rays are characteristic of the atom undergoing the transition (characteristic X-rays) and are the signal used in energy dispersive X-ray (EDX) spectroscopy.

ii. Auger electrons are produced when the resulting released energy is not channeled into creation of a photon, but instead is absorbed to eject an electron from a third shell (*e.g.*, $M_{2,3}$ shell). The energy of the ejected electron is determined by the energy of the three shells involved in the transition (*e.g.*, $E_{KL3M2,3} = E_K - E_{L3} - E_{M2,3}$).

Auger electrons are low-energy electrons (50 eV – 3 keV) and, therefore, only those electrons derived from the first few atomic layers on the surface escape into the vacuum and can be detected. The lateral spatial resolution of the region of analysis depends on the size of the electron probe on the surface and, to a lesser extent, on the interaction volume of Auger electrons. The former is a function of the electron optics of the probe formation, specifically the electron source type and lens aberrations. With a field emission electron gun, a spatial resolution of 10 nm or lower can be achieved. The detection limit of AES ranges from about 0.1 at% to 1 at%, depending on the Auger electron yield of the element [139]. It has been established that Cu concentrations exceeding 10^{13} at/cm^3 can detrimentally affect the Si device performance [15]. Assuming a density and molar weight of 2.329 g/cm^3 and 28.08 g/mole for Si [140], a detection limit of 2×10^{-8} at% or

better is required to detect such low concentrations of Cu. In this respect, AES is used for analyzing the elemental composition of reaction products formed as a result of barrier failure rather than tracing the diffusion of Cu by depth profiling.

2.8.1.2 Secondary ion mass spectroscopy (SIMS)

SIMS utilizes a source of high energy ions to bombard the surface and sputter the surface layers. This process releases neutral atoms, and positive and negative ions into the vacuum. The released ions are accelerated and focused into the spectrometer, which identifies the mass or mass/charge ratio and the abundance (intensity) of ions. One type of spectrometer (available at the Alberta Centre for Surface Engineering and Science (ACSES)) is a time-of-flight (ToF) spectrometer which records the time for an ion of a specific kinetic energy to reach the detector (time-of-flight). The time-of-flight is related to mass/charge ratio and the detector counts the number of ions at a specific mass/charge ratio. Similar to AES, analysis can be made on the surface or as a function of the depth below the surface. The lateral resolution of the analysis depends mainly on the size of the ion probe on the surface, which depends on the ion source type and the optics of the instrument. An ion probe with a diameter of 0.1 μm can be formed on the surface and rastered to perform point analysis, line scanning or mapping on the surface. With appropriate standards, SIMS is capable of detecting atomic concentrations in the part per billion (ppb) range. Additionally a ToF-SIMS instrument is capable of detecting all elements. Depth profiling by SIMS has been used extensively in monitoring the Cu diffusion profile through the diffusion barrier layer. The sputtering ion sources frequently employed are Ar^+, O_2^-, Cs^+ and Ga^+. Chemically active sources (O_2^-, Cs^+ and Ga^+) are used to promote sputtering of a desirable type of ions, *i.e.*, O_2^- for sputtering electropositive species and Cs^+ and Ga^+ to promote sputtering of electronegative species [139].

2.8.1.3 X-ray diffraction (XRD)

XRD is a nondestructive technique utilized to characterize the crystal structure, lattice strain and crystalline grain size, to name a few. In this technique, a beam of monochromatic X-rays is focused onto a sample. The crystalline

structure of the sample, or the regular array of atoms in the lattice, interacts with the incoming X-rays. The atoms act as scattering centers and the X-rays are diffracted at those particular angles of incidence that satisfy Bragg's law or Laue equations. The diffraction angles depend on the Bravais point lattice and the unit cell dimensions. The intensity of the diffracted beams, on the other hand, depends on the type of atoms and the atomic coordinates in the lattice. This results in a diffraction pattern, which is characteristic of the crystal structure and composition of the material. The extension of XRD methods developed for bulk samples to thin films requires modification to the geometry of the experiment. Since X-rays penetrate deeply into the sample, their path through the thin film is too short to produce a signal with significant intensity. Consequently, diffraction of X-rays is usually dominated by the Si substrate rather than the metallization layers. One solution is to make the films appear thicker to the X-ray film by employing grazing incidence XRD. In this method, the angle of incidence of X-rays is kept at a constant, small value (2-7°). The focal point of the X-ray source, the sample and the detector slit are all located on the circumference of a circle (Seeman-Bohlin diffraction geometry). The sample and X-ray source are stationary while the detector is rotated to collect the diffracted beams at various angles [141].

2.8.1.4 Scanning electron microscopy (SEM)

In an SEM, an image is formed by scanning a focused electron beam of high energy (1 keV – 30 keV) on the surface of the sample and by collecting the signals produced as a result of electron-sample interactions and simultaneously constructing an image point-by-point. The electromagnetic lenses in an SEM column demagnify the image of the electron source and scanning coils scan the beam across the sample surface. A number of different electron sources have been developed and they operate based on either a thermionic emission or a field emission principle. The most common thermionic emission sources are a W hairpin or a LaB_6 filament. These thermionic sources rely on high temperatures to enable some of the electrons in the filament to overcome the work function barrier and escape into the vacuum. Field emission sources rely on a high electric field at the tip of a sharp filament that allows the electrons to tunnel directly through

barrier. An important measure of electron gun performance is its brightness, which is given by the current density per solid angle of electrons. Field emission guns (FEG) can generate an appreciably higher brightness compared to thermionic emission sources. The image resolution in SEM can be improved by reducing the electron beam size without losing current in the probe. The electron beam size is limited by several parameters including the spherical and chromatic aberrations of the lenses, the beam current, the working distance and the accelerating voltage. To obtain the highest resolution image, a FEG source together with an immersion lens can be used. In the latter, the sample is placed directly inside the objective lens gap to minimize spherical aberrations effects. These types of lenses, however, are limited to small sample sizes [142].

A high energy electron penetrating a solid sample undergoes several scattering processes and results in various signals that can be collected by appropriate detectors and used to construct an image. The most common imaging signals are secondary electrons, backscattered electrons and characteristic X-rays. Secondary electron imaging relies on low energy electrons that originate from the top 1-20 nm of the surface. Due to the geometry of the detector, this signal provides mainly topographic contrast with great depth of focus. Backscattered electrons are high energy beam electrons that are elastically scattered by angles greater than 180° and escape from the surface. The backscatter yield of the material depends on the average atomic number. Consequently, backscattered signal provides compositional information with some topographic contrast. Backscattered images possess relatively poor resolution due to the large volume from which the electrons are emitted (interaction volume). Additionally, the characteristic X-rays ejected as a result of electron-sample interaction (Section 2.8.1.1) can be collected to analyze the composition of the area interacting with the electron beam. The most common X-ray detectors used in TEMs and SEMs are energy dispersive spectrometers (EDX). The X-ray signal can be collected from a point, a line or an area. A signal from an area can be used to construct a chemical map of the specimen. The spatial resolution of EDX analysis in SEM is limited by the large interaction volume of X-rays in the bulk sample [142]. The

interaction volume depends mainly on the beam energy and spatial resolution in sub-micron range is achievable at low beam energies. The poor spatial resolution (at conventional beam energies) together with the relatively poor detection limit of EDX (~0.1 at%) has limited application of SEM in mapping the elemental distribution across the interface of a barrier [6]. Consequently, SEM/EDX is mainly utilized to detect defects on the surface of the barrier or on the Cu layer (see Table 2-2 and Table 2-3 for examples).

2.8.1.5 Transmission electron microscopy (TEM)

TEM utilizes a high energy source of electrons (100 keV- 300 keV) to obtain information from samples that are thin enough to transmit electrons. The types of electron sources used are similar to those used for SEM (Section 2.8.1.4). Starting from the top of the column, there are four main electromagnetic lenses; namely condenser, objective, intermediate and projector lenses. Depending on the type of microscope, these lenses consist of several smaller lenses. The sample is usually placed in the objective lens, which forms the first image of the sample and, therefore, is the most important lens of the system. Depending on the focal conditions, the two basic modes of TEM operation are imaging mode and diffraction mode. The elastic scattering of electrons by the regular array of atoms in the lattice (similar to XRD) forms a diffraction pattern on the back focal plane of the objective lens. The diffraction pattern can be collected by forming an image of this plane by adjusting the post-specimen lenses. Diffraction patterns provide information about the defects and crystal structure of the phases in the sample. Alternatively, in imaging mode, the image plane of the objective lens forms the object for post-specimen lenses [143].

The electron wave can change both its amplitude and phase as it interacts with the sample, giving rise to amplitude and phase contrast in imaging mode. Two main types of amplitude contrast are mass-thickness and diffraction contrast. The latter can be obtained by selecting either the direct beam (bright field) or a diffracted beam (dark field) in the diffraction pattern by inserting an aperture on the back focal plane of the objective lens. Mass-thickness contrast is present for

nearly all samples and arises from incoherent elastic scattering (Rutherford scattering). It is most important for non-crystalline samples such as polymers or biological samples. Phase contrast arises when more than one beam contributes to the image. This is the type of contrast exploited to image the atomic structure of thin samples. The highest spatial resolution can be obtained in phase contrast mode [143].

The resolution of TEM imaging is controlled by the diffraction limit on resolution, given by the Rayleigh criterion, and by lens aberrations and astigmatism. For a given divergence angle, the resolution is improved by increasing the accelerating voltage. However, radiation damage becomes more significant with increasing accelerating voltage. Spherical aberration corrector systems have been made available commercially and are able to reduce the spherical aberration effects on resolution. Chromatic aberrations depend on the energy spread of the electron gun and on the chromatic aberration coefficient of the objective lens system. The inelastic scattering in the sample also adds to chromatic aberration effects. By minimizing the effect of aberration and astigmatism and by using a FEG source, sub-nanometer spatial resolution is attainable [143].

A variation on the TEM that is particularly useful for compositional analysis is scanning TEM or STEM. While TEM uses a parallel beam of electrons on the surface of the sample, STEM focuses the electron beam on the surface. The beam is scanned over the area of interest, similar to SEM, and the image is built on the screen simultaneously. A number of detectors are available and used for imaging in STEM mode. The bright-field (BF) detector collects the direct beam and the scattered beam at relatively small collection angles (<10 mrad), giving rise to diffraction contrast similar to TEM bright field mode. Two other detectors are the annular dark field detector (ADF) which surrounds the BF detector and a high-angle annular dark field detector (HAADF) which surrounds the ADF detector. The ADF results in dark field STEM images while HAADF collects images in which Rutherford scattering effects are maximized (Z-contrast images) [143].

Similar to SEM, inelastic scattering interactions generate signals that contain information on the chemical composition of the sample. Collecting these signals transforms TEM/STEM into an analytical tool. Examples include characteristic X-rays (EDX) and electron energy loss spectroscopy (EELS). EDX analysis in TEM/STEM offers better spatial resolution compared with SEM. The spatial resolution is a function of beam size and beam spreading. With thin samples and higher electron energy, the total interaction volume is reduced giving a more localized X-ray signal source. The detection limit of EDX in TEM/STEM depends on the spatial resolution. As the interaction volume decreases, the signal levels are lowered and small peaks will be less detectable. This demonstrates the importance of utilizing a high brightness source, which offers a higher current at smaller beam size. EDX analysis is also limited by sample drift and contamination or damage during analysis. EELS involves the analysis of the energy distribution of electrons that are inelastically scattered through the specimen and provides information about the chemistry and the electronic structure of the sample. EELS analysis offers better spatial resolution and detection limit than EDX and can detect and quantify all elements, especially light elements. Similar to EDX, EELS analysis can be performed on a point, line or an area of the sample [143].

TEM and STEM imaging is routinely utilized to analyze the sharpness of the interfaces, changes in the barrier microstructure and formation of reaction products. The crystal structure of the reacted phases is usually identified by diffraction analysis. To measure Cu concentration at different depths of the barrier layer or the substrate, EDX and EELS compositional analysis are performed on the cross-section of annealed metallization stacks [6]. Successful TEM analysis is strongly dependent on the availability of a thin cross-section or plan-view sample. Conventional TEM analysis requires samples that are 100 nm or thinner while high resolution TEM and EELS analysis require much thinner samples (<50 nm). Two sample preparation methods that are utilized in this thesis are conventional dimpling/sputtering and focused ion beam (FIB) methods. Most of the plan-view samples were prepared by mechanical thinning from the backside of the wafer to preserve the metallization layer, followed by final thinning and polishing in an Ar

ion mill. The FIB instrument is often an SEM with a built-in ion gun. Secondary electron imaging in SEM allows for imaging of the surface and finding an area of interest. The ion gun (usually a Ga source) is used to mill two trenches on the surface, leaving a thin lamella in between. The lamella can be extracted using a probe and attached to a supporting grid where it can be further thinned and polished. Some of the issues associated with sample preparation using FIB are Ga contamination, damage to the surface and smearing of top layers over the bottom layers [6].

2.8.1.6 Four point probe resistivity measurement (FPP)

A simple and fast technique to evaluate a barrier's thermal stability is to measure the resistivity of the Cu/barrier/Si stack after annealing. This method is classified under metallurgical mode category since resistivity is basically a measure of the formation of high resistivity reaction products. FPP, therefore, does not measure the impact of Cu on the Si substrate or the dielectric layer integrity. The electrical resistance, R, of an object is defined as the ratio V/I, where V is the voltage that causes the current I to flow through the object. The resistivity, ρ, of an object is related to resistance through a correction factor, G_{corr}, as follows:

$$\rho = G_{corr}\frac{V}{I} \qquad \text{Equation 2-20}$$

To measure the resistivity using direct current, connections have to be made to the object to apply a voltage and measure the current. If two probes are used, the resistivity of the contacts contributes to the measured resistivity values. To separate the contact resistivity from substrate resistivity, a four probe configuration is used. In this setup the voltage is applied between the two central contacts (2 and 3), while the current is measured using the outer contacts (1 and 4), as shown in the schematic drawing in Figure 2–8. In semiconductor industry standard measurements, these four probes are arranged in a line with equal probe spacing, s_{res}. The correction factor, G_{corr}, is dependent on the geometry of the sample and on the arrangement and spacing of the probes. The correction factors

for various geometries of samples are compiled by several sources and an easily accessible source is the book by Schroeder [144]. For a thin rectangular slice of sample with a thickness $t_{res} < s_{res}/2$ the correction factor is given by:

$$G_{corr} = \frac{\pi}{ln2} . t_{res} . F(\frac{b_{res}}{s_{res}}, \frac{a_{res}}{b_{res}}) \qquad \text{Equation 2-21}$$

where $\frac{\pi}{ln2} . t_{res}$ is the geometric factor for an infinitely large slice of thickness t_{res} << s_{res}, $F(\frac{b_{res}}{s_{res}}, \frac{a_{res}}{b_{res}})$ is an additional correction factor to account for the finite, rectangular shape and b_{res} and a_{res} are the dimensions of the slice as shown in Figure 2–8. Values of F are tabulated for various values of a_{res}, b_{res} and s_{res} [144]. Failure of a barrier is accompanied by formation of silicides (Table 2-2 and Table 2-3) and an abrupt increase in the resistivity of the stack. Therefore, FPP resistivity measurements are used repeatedly in detecting the onset of reaction in Cu metallization stacks.

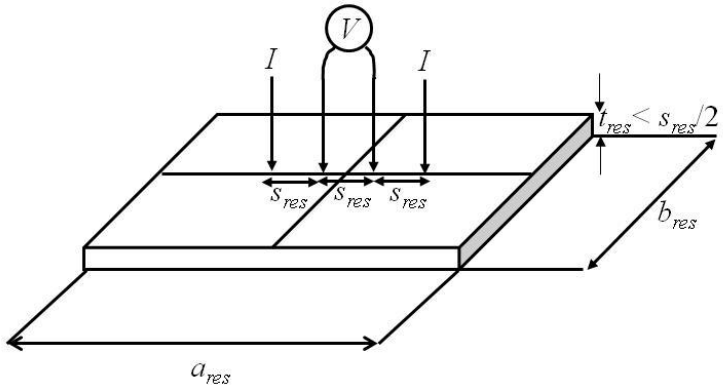

Figure 2–8 Schematic showing the configuration for four point probe measurement and the geometry of a thin rectangular slice.

2.8.2 Electrical mode

Copper can affect Si properties at concentrations exceeding 10^{13} at/cm^3 and it can affect the Si/SiO_2 interface at a surface concentration of 10^{10} ions/cm^3 [145]. Most of the techniques listed in Section 2.8.1 are not capable of detecting the diffusion of Cu at such low concentrations. The detection of the onset of Cu diffusion and device degradation is a challenging but very important task.

Electrical measurements usually detect the effect of low Cu contamination on the electrical properties of the devices. Examples of devices routinely used for diffusion barrier characterization are p-n junctions [28,90,146] and MOS capacitors [147-149]. The measurement of leakage current of a reverse-biased shallow Cu/barrier/p-n junction diodes is regularly utilized for evaluation of diffusion barrier performance. The diodes are usually thermally annealed in an inert gas or vacuum environment followed by leakage current measurement and metallurgical characterization. It is well established that penetration of Cu through the barrier is responsible for an increase in leakage current of the shallow junction. However, the mechanism responsible for the failure of diodes is not well understood. A number of studies observed degradation of diodes at temperatures 50-100°C lower than the failure temperature observed by metallurgical characterization. These studies suggested that degradation of diodes occurred by diffusion of Cu to the junction area [90,146]. Other researchers observed that degradation of diode leakage current was accompanied by the formation of Cu-silicide particles [86,150-152]. Baumann *et al* [28] demonstrated that diffusion of Cu into the Si bulk does not affect the leakage current of reversed-biased p-n junctions unless the entire diode structure is destroyed by the formation of Cu-silicide spikes. Therefore, monitoring a p-n junction leakage current only detects failure when the bulk concentration of Cu is high enough to cause formation of Cu-silicide particles. Additionally, according to Equation 2-8, the atomic flux of Cu through the barrier depends on the combination of both temperature of operation and electric field. It has to be noted that under thermal annealing the p-n junction diode is only subjected to thermal stress which does not represent the true operating conditions of the device. Alternatively, subjecting MOS capacitors to bias temperature stress (BTS) testing successfully includes both of these driving forces in the reliability test. This technique is further described in the following section.

2.8.2.1 Evaluation of electrical properties of MOS capacitors

The acronym MOS stands for metal-oxide-semiconductor, which consists of a semiconductor substrate, a dielectric layer and a metal electrode called a gate, as

shown in Figure 2–9. The MOS capacitor is not widely used in semiconductor devices. MOS transistors, on the other hand, are one of the most frequently used devices and these consist of a MOS capacitor with two p-n junctions flanking the capacitor. The energy band diagram of a p-type MOS capacitor with $V_g = 0$ is shown in Figure 2–10(a), where V_g is the voltage at the gate. The subscripts "*m*" and "s" indicate the properties of the metal and substrate, respectively. The work function, $q\varphi$, is the energy difference between the Fermi level (E_F) and the vacuum level (E_o). Also shown are the conduction (E_C) and the valence band edges (E_V). At thermal equilibrium, the Fermi level (E_F) has to remain constant and the vacuum level has to remain continuous across the device. To accommodate the work function difference between metal and semiconductor, the semiconductor bands bend downwards [38,153].

If a negative voltage, equal to the difference in the work functions, is applied to the gate ($V_g = \varphi_m - \varphi_s$), the energy band of the substrate becomes flat at the Si/SiO_2 interface. This condition is called the flatband condition and the gate voltage is called the flatband voltage, V_{FB} (Figure 2–10(b)). If the gate voltage is more negative than V_{FB}, the semiconductor band at the Si/SiO_2 interface bends upward, bringing E_V closer to E_F at the interface. A large number of holes accumulate near the surface and form an accumulation layer. This condition is known as surface accumulation. For an n-type substrate, the accumulation region holds an excess concentration of electrons. If a gate voltage more positive than V_{FB} is applied (for a p-type substrate), the band diagram bends downward, separating E_F from E_V and bringing it closer to E_C. In this condition the density of holes becomes small and a depletion region near the Si/SiO_2 interface is created. With an increasingly more positive gate voltage the bands bend further downward and at some threshold voltage (V_T), E_F will be close enough to E_C that the surface is at the threshold of inversion. At $V_g > V_T$ the surface will be inverted from p-type to n-type due to accumulation of electrons at the interface [38,153].

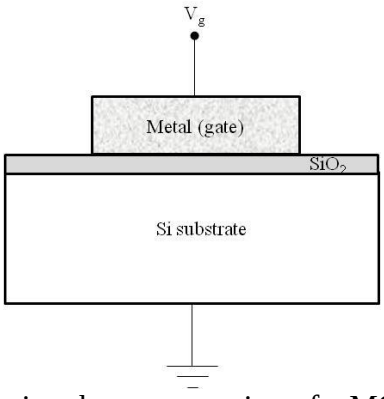

Figure 2–9 Schematic showing the cross-section of a MOS capacitor. Reproduced from [153].

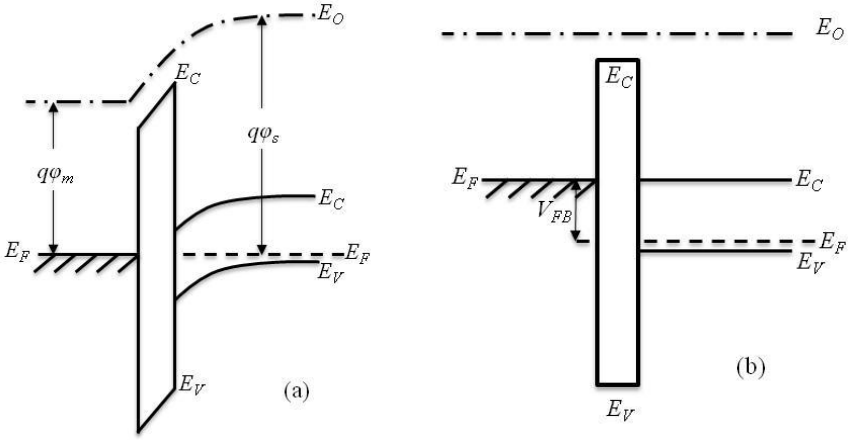

Figure 2–10 (a) Energy band diagram of an unbiased MOS capacitor with a p-type substrate, (b) energy band diagram of the MOS capacitor in (a) after a voltage equal to V_{FB} is applied to the gate (flatband condition). Reproduced from [38].

The capacitance of a MOS device is given by the ratio of total substrate charge (Q_{sub}) to the gate voltage according to:

$$C = -\frac{dQ_{sub}}{dV_g} \qquad \text{Equation 2-22}$$

The negative sign arises from the fact that the voltage is measured at the gate while the charge is measured at the substrate. The capacitance-voltage (*C*-*V*) characteristics of MOS devices are usually measured by applying a DC bias voltage to the gate, V_g, and a high frequency alternating current (AC) signal (>10^5 Hz) to the capacitor and measuring the capacitive current with an AC meter. A

typical *C-V* curve for a p-type MOS capacitor under high frequency measurement is shown in Figure 2–11. The three regions of accumulation, depletion and inversion are marked on the plot. In accumulation the MOS capacitor behaves like a simple capacitor with a capacitance equal to the oxide capacitance, C_{ox}. It is assumed that the AC frequency is high enough that generation-recombination rates in the depletion region are lower than voltage variation. In this case, the inversion charge will not respond to the AC signal and remains constant at its DC value. The capacitance becomes saturated at V_T as shown in Figure 2–11. The capacitance per unit area in the depletion region (C) is given by:

$$\frac{1}{C^2} = \frac{1}{C_{ox}^2} + \frac{2(V_g - V_{FB})}{qN_a\varepsilon_s} \qquad \text{Equation 2-23}$$

where N_a is the substrate doping concentration, q is the charge of an electron and ε_s is the semiconductor permittivity. The flatband voltage can be calculated using Equation 2-23 by plotting $1/C^2$ vs. V_g within the depletion region [38,153].

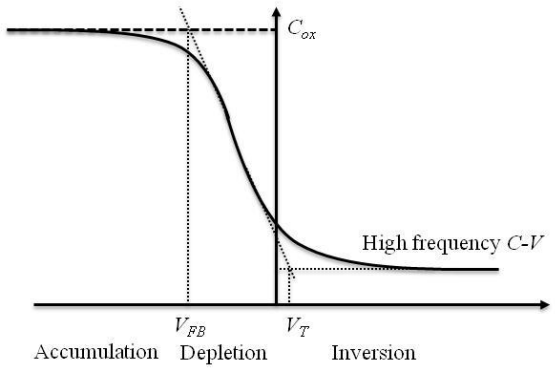

Figure 2–11 Typical high frequency *C-V* characteristic of a MOS capacitor with p-type substrate. Reproduced from [153].

The presence of charge in the oxide creates an intrinsic electric field in the oxide and therefore modifies the initial band diagram of MOS capacitor in Figure 2–10(a). There are several types of oxide charge. Interface trapped charges, fixed oxide charges, oxide trapped charges and mobile ionic charges are some examples. The flatband voltage shifts by a value depending on the amount of charge and the location of charge in the oxide. A sheet of charge will exert

maximum influence on the flatband voltage if it is located near the semiconductor interface. The shift in flatband voltage for the case of an arbitrary charge distribution with the volume density of $\rho(x_{ox})$ is given by:

$$V_{FB} = -\frac{1}{C_{ox}t_{ox}}\int_0^{t_{ox}} x_{ox}\rho(x_{ox})dx_{ox} \qquad \text{Equation 2-24}$$

where t_{ox} is the oxide thickness and x_{ox} is the distance from the metal/oxide interface [38]. As explained in Section 2.3, interstitial Cu is positively charged [6] and its transport in the oxide causes a negative shift in the flatband voltage, according to Equation 2-24.

Therefore, high frequency *C-V* measurements provide a powerful tool for detecting mobile ions in the dielectric layer by monitoring the flatband voltage shift. In this respect, several studies have used MOS devices to understand the Cu transport phenomena under thermal stress [154-156] or a combination of thermal and electrical stresses (BTS) [7,13,84,147,149,157]. In these studies, individual MOS devices were subjected to BTS under electric fields ranging from 0.3 MV/cm to 4 MV/cm while heated to temperatures ranging from 100°C to 300°C [84,147-149,155,157-161]. Most of these tests were performed under an inert ambient or vacuum in a light-tight box. The MOS devices were fabricated by one of the following three methods: *i*) thermal oxidation, deposition of the diffusion barrier and the Cu layer followed by patterning and etching of individual devices [84,147,155], *ii*) thermal oxidation, deposition and patterning of the photoresist, deposition of the diffusion barrier and the Cu layer, followed by lift-off of excess metal in an ultrasonic bath [148,149] and *iii*) thermal oxidation followed by deposition of the diffusion barrier and the Cu layer through a shadow mask [157,161]. The *C-V* characteristics of devices were measured before and after BTS. In addition to a positive flatband voltage shift associated with diffusion of Cu, several other changes in the *C-V* characteristics were observed. Some examples are given here:

i. An increase in the inversion capacitance after BTS, which is related to the deep level states created by Cu in Si. The generation-recombination centers created by presence of Cu reduce the minority carrier lifetime. Consequently, the inversion charge will be able to follow changes in the AC signal [148,155,157,159,162].

ii. Deep depletion where the capacitance in the depletion region continues to drop as voltage is increased above V_T (for a p-type substrate). This behavior is attributed to the increased conductivity of the oxide as a result of diffusion of Cu. A conductive oxide enables the leakage of minority carriers generated at the inversion layer and, therefore, a drop in inversion capacitance [162,163].

iii. A decrease in the absolute value of the slope of the depletion region (non-parallel shift of *C-V* curve). This behavior is related to the interface states generated by diffusion of Cu [158,162].

In summary, monitoring the electrical properties of MOS capacitors subjected to BTS has proven to be a sensitive and reliable technique for evaluation of new diffusion barrier materials. Simultaneous application of electrical and thermal stresses reproduces the operating condition of diffusion barriers in real devices. The electrical measurements after BTS provide a sensitive tool for detecting low concentrations of Cu in the oxide layer and Si substrate.

2.9 References

[1] P.V. Zant, Microchip Fabrication (McGraw-Hill, USA, 2004) pp. 401-15.
[2] H.S. Rathore, K. Chanda, Semiconductor Manufacturing Handbook (McGraw-Hill, USA, 2005) pp. 4.1,4.13.
[3] S. Franssila, Introduction to Microfabrication (John Wiley & Sons, UK, 2004) pp. 277-85.
[4] T. Gupta, Copper Interconnect Technology (Springer, USA, 2009).
[5] A.E. Kaloyeros, E.T. Eisenbraun, K. Dunn, O. van der Straten, Chem. Eng. Commun. **198**, 1453-81 (2011).
[6] A.A. Istratov, E.R. Weber, J. Electrochem. Soc. **149**, G21-30 (2002).
[7] J.D. McBrayer, R.M. Swanson, T.W. Sigmon, J. Electrochem. Soc. **133**, 1242-6 (1986).
[8] M.W. Lane, C.E. Murray, F.R. McFeely, P.M. Vereecken, R. Rosenberg, Appl. Phys. Lett. **83**, 2330-2 (2003).
[9] International Technology Roadmap for Semiconductors, 2007.
[10] R.W. Olesinski, G.J. Abbaschian, Bull. Alloy Phase Diag. **7**, 170-8 (1986).
[11] R.N. Hall, J.H. Racette, J. Appl. Phys. **35**, 379-97 (1964).
[12] X. Yan, Y.A. Chang, J. Alloys Compounds. **308**, 221-9 (2000).
[13] K.-. Kim, Y.-. Joo, K.-. Kim, J.-. Kwon, J. Appl. Phys. **100,** 063517.1-6 (2006).
[14] S.K. Estreicher, Phys. Rev. B **60**, 5375-82 (1999).
[15] A.A. Istratov, C. Flink, E.R. Weber, Phys. Status Solidi B **222**, 261-77 (2000).
[16] A.A. Istratov, C. Flink, H. Hieslmair, E.R. Weber, T. Heiser, Phys. Rev. Lett. **81**, 1243-6 (1998).
[17] A.A. Istratov, E.R. Weber, Appl. Phys. A **66**, 123-36 (1998).
[18] E. Nes, G. Lunde, J. Appl. Phys. **43**, 1835-7 (1972).
[19] G. Das, J. Appl. Phys. **44**, 4459-67 (1973).
[20] M. Ronay, R.G. Schad, Phys. Rev. Lett. **64**, 2042-5 (1990).
[21] M. Seibt, K. Graff, J. Appl. Phys. **63**, 4444-50 (1988).
[22] M. Setton, J. Van Der Spiegel, B. Rothman, Appl. Phys. Lett. **57**, 357-9 (1990).
[23] J.K. Solberg, Acta Cryst. **A34**, 684-98 (1978).
[24] N. Benouattas, A. Mosser, D. Raiser, J. Faerber, A. Bouabellou, Appl. Surf. Sci. **153**, 79-84 (2000).
[25] H. Gottschalk, Phys. Status Solidi A **137**, 447-61 (1993).
[26] A. A. Istratov, O.F. Vyvenko, C. Flink, T. Heiser, H. Hieslmair, E.R. Weber, MRS Proc. **510**, 313-318 (1998).
[27] M. Miyazaki, M. Sano, S. Sumita, N. Fujino, J. J. Appl. Phys. Part 2 **30**, L295-7 (1991).
[28] J. Baumann, C. Kaufmann, M. Rennau, T. Werner, T. Gessner, Microelectron. Eng. **33**, 283-91 (1977).
[29] C.S. Liu, L.J. Chen, Thin Solid Films. **262**, 187-98 (1995).
[30] C.S. Liu, L.J. Chen, J. Appl. Phys. **74**, 3611-3 (1993).
[31] C.S. Liu, L.J. Chen, J. Appl. Phys. **74**, 5507-9 (1993).

[32] J.M.E. Harper, A. Charai, L. Stolt, F.M. d'Heurle, P.M. Fryer, Appl. Phys. Lett. **56**, 2519-21 (1990).
[33] W.B. Henley, D.A. Ramappa, L. Jastrezbski, Appl. Phys. Lett. **74**, 278-80 (1999).
[34] A.A. Istratov, H. Hedemann, M. Seibt, O.F. Vyvenko, W. Schröter, T. Heiser, C. Flink, H. Hieslmair, E.R. Weber, J. Electrochem. Soc. **145**, 3889-98 (1998).
[35] R. Sachdeva, A.A. Istratov, E.R. Weber, Appl. Phys. Lett. **79**, 2937-9 (2001).
[36] H.H. Busta, H.A. Waggener, J. Electrochem. Soc. **124**, 1424-9 (1977).
[37] G. Raghavan, C. Chiang, P.B. Anders, S.-. Tzeng, R. Villasol, G. Bai, M. Bohr, D.B. Fraser, Thin Solid Films. **262**, 168-76 (1995).
[38] S.M. Sze, M.K. Lee, Semiconductor Devices: Physics and Technology (Wiley, USA, 2012).
[39] R.W. Balluffi, J.M. Bkakely, Thin Solid Films. **25**, 363-92 (1975).
[40] P. Shewmon, Diffusion in Solids (The Minerals, Metals & Materials Society, USA, 1989).
[41] P.S. Ho, Thin Solid Films. **96**, 301-16 (1982).
[42] D. Gupta, P.S. Ho, Thin Solid Films. **72**, 399-418 (1980).
[43] L.G. Harrison, Trans. Faraday Soc. **57**, 1191-9 (1961).
[44] A.E. Kaloyeros, E. Eisenbraun, Ann. Rev. Mater. Sci. **30**, 363-85 (2000).
[45] N.A. Gjostein, Diffusion (American Society for Metals, USA, 1973).
[46] L.I. Ning, D.N. Ruzic, R.A. Powell, J. Vac. Sci. Tech. B **22**, 2734-42 (2004).
[47] X. Chen, G.G. Peterson, C. Goldberg, G. Nuesca, H.L. Frisch, A.E. Kaloyeros, B. Arkles, J. Sullivan, J. Mater. Res. **14**, 2043-52 (1999).
[48] H.Y. Wong, N.F. Mohd Shukor, N. Amin, Microelectron. J. **38**, 777-82 (2007).
[49] S.-. Wang, MRS Bull. **19**, 30-40 (1994).
[50] A. Jain, O. Adetutu, B. Ekstrom, G. Hamilton, M. Herrick, R. Venkatraman, E. Weitzman, MRS Proc. **564**, 269-80 (1999).
[51] C.E. Ramberg, E. Blanquet, M. Pons, C. Bernard, R. Madar, Microelectron. Eng. **50**, 357-68 (2000).
[52] M.-. Nicolet, Thin Solid Films. **52**, 415-43 (1978).
[53] H.S. Chen, Rep. Prog. Phys. **43**, 353-432 (1980).
[54] T. Masumoto, R. Maddin, Mater. Sci. Eng. **19**, 1-24 (1975).
[55] H.S. Chen, Mater. Sci. Eng. **25**, 59-69 (1976).
[56] D. Turnbull, Contemp. Phys. **10**, 473-88 (1969).
[57] S. Mader, Recrystallization, Grain Growth and Textures (American Society for Metals, Ohio, 1966) pp. 523-37.
[58] H.A. Davies, Amorphous metallic alloys (Butterworths & Co, London, 1983) pp. 8-25.
[59] M.G. Scott, Amorphous metallic alloys (Butterworths & Co, London, 1983) pp. 144-68.
[60] P.I. Loeff, A.W. Weeber, A.R. Miedema, J. Less-Common Met. **140**, 299-305 (1988).
[61] R. Coehoorn, G.J. Van Der Kolk, J.J. Van Den Broek, T. Minemura, A.R. Miedema, J. Less-Common Met. **140**, 307-16 (1988).

[62] P. Haussler, Topics in Applied Physics (Springer-Verlag, Berlin, 1994) pp. 163-207.
[63] J.J. Gilman, Science. **208**, 856-61 (1980).
[64] T. Egami, Y. Waseda, J. Non Cryst. Solids. **64**, 113-34 (1984).
[65] R. Ray, B.C. Giessen, N.J. Grant, Scripta Metallur. **2**, 357-9 (1968).
[66] J. Hafner, Topics in Applied Physics (Springer-Verlag, Berlin, 1981) pp. 93-140.
[67] I.W. Donald, H.A. Davies, J. Non Cryst. Solids. **30**, 77-85 (1978).
[68] G.J. Van der Kolk, A.R. Miedema, A.K. Niessen, J. Less-Common Met. **145**, 1-17 (1988).
[69] M. Marcus, D. Turnbull, Mat. Sci. Eng. **23**, 211-4 (1976).
[70] A.K. Niessen, F.R. de Boer, R. Boom, P.F. de Châtel, W.C.M. Mattens, A.R. Miedema, Calphad. **7**, 51-70 (1983).
[71] A.K. Niessen, A.R. Miedema, Phys. Chem. Chem. Phys. **87**, 717-25 (1983).
[72] A.R. Miedema, F.R. de Boer, R. Boom, Calphad. **1**, 341-59 (1977).
[73] A.R. Miedema, P.F. de Châtel, F.R. de Boer, Physica B+C. **100**, 1-28 (1980).
[74] A.K. Niessen, A.R. Miedema, F.R. de Boer, R. Boom, Physica B+C. **151**, 401-32 (1988).
[75] S. Goldbach, B. Van Den Bossche, T. Daenen, J. Deconinck, F. Lapicque, J. Appl. Electrochem. **30**, 1-12 (2000).
[76] Y. Shacham-Diamand and Y. Sverdlov, Proceedings of Advanced Metallization Conference (Montreal, 2001), 67-72.
[77] Y Marumo, H Sato, M Jomen. Electroless Plating Method and Apparatus. US Patent 2005/0164499 A1.
[78] L.C. Lane, T.C. Nason, G.-. Yang, T.-. Lu, H. Bakhru, J. Appl. Phys. **69**, 6719-21 (1991).
[79] K. Holloway, P.M. Fryer, Appl. Phys. Lett. **57**, 1736-8 (1990).
[80] C.-. Chang, C.-. Hu, Appl. Phys. Lett. **57**, 617-9 (1990).
[81] J.S. Reid, E. Kolawa, R.P. Ruiz, M.-. Nicolet, Thin Solid Films. **236**, 319-24 (1993).
[82] E. Kolawa, P.J. Pokela, J.S. Reid, J.S. Chen, M.-. Nicolet, Appl. Surf. Sci. **53**, 373-6 (1991).
[83] C.-. Chang, J. Appl. Phys. **67**, 6184-8 (1990).
[84] H. Kizil, G. Kim, C. Steinbrüchel, B. Zhao, J. Electron. Mater. **30**, 345-8 (2001).
[85] K. Holloway, P.M. Fryer, C. Cabral Jr., J.M.E. Harper, P.J. Bailey, K.H. Kelleher, J. Appl. Phys. **71**, 5433-44 (1992).
[86] P.J. Pokela, C.-. Kwok, E. Kolawa, S. Raud, M.-. Nicolet, Appl. Surf. Sci. **53**, 364-72 (1991).
[87] R. de Reus, R.J.I.M. Koper, H. Zeijlemaker, F.W. Saris, Mater. Lett. **9**, 500-3 (1990).
[88] R.E. Thomas, K.J. Guo, D.B. Aaron, E.A. Dobisz, J.H. Perepezko, J.D. Wiley, Thin Solid Films. **150**, 245-52 (1987).
[89] S.-. Wang, I. Raaijmakers, B.J. Burrow, S. Suthar, S. Redkar, K.-. Kim, J. Appl. Phys. **68**, 5176-87 (1990).

[90] M.H. Tsai, S.C. Sun, C.E. Tsai, S.H. Chuang, H.T. Chiu, J, Appl. Phys. **79**, 6932-8 (1996).
[91] J. Zhou, H. Chen, Y. Li, Trans. Nonferr. Met. Soc. **17**, 733-8 (2007).
[92] H. Okamoto, J. Phase Equilib. Diffus. **29**, 291 (2008).
[93] T. Riekkinen, J. Molarius, T. Laurila, A. Nurmela, I. Suni, J.K. Kivilahti, Microelectron. Eng. **64**, 289-97 (2002).
[94] J.H. Wang, L.J. Chen, Z.C. Lu, C.S. Hsiung, W.Y. Hsieh, T.R. Yew, J.Vac. Sci. Tech. B **20**, 1522-6 (2002).
[95] G.S. Chen, P.Y. Lee, S.T. Chen, Thin Solid Films. **353**, 264-73 (1999).
[96] X. Sun, E. Kolawa, J. Chen, J.S. Reid, M. Nicolet, Thin Solid Films. **236**, 347-51 (1993).
[97] S. Tsukimoto, M. Moriyama, M. Murakami, Thin Solid Films. **460**, 222-6 (2004).
[98] H. Kim, Surf. Coat. Tech. **200**, 3104-11 (2006).
[99] T. Oku, E. Kawakami, M. Uekubo, K. Takahiro, S. Yamaguchi, M. Murakami, Appl. Surf. Sci. **99**, 265-72 (1996).
[100] J. Nazon, M.-. Berger, J. Sarradin, J.-. Tedenac, N. Fréty, Plasma Processes Polym. **6**, S844-8 (2009).
[101] J. Nazon, B. Fraisse, J. Sarradin, S.G. Fries, J.C. Tedenac, N. Fréty, Appl. Surf. Sci. **254**, 5670-4 (2008).
[102] M. Hecker, D. Fischer, V. Hoffmann, H.-. Engelmann, A. Voss, N. Mattern, C. Wenzel, C. Vogt, E. Zschech, Thin Solid Films. **414**, 184-91 (2002).
[103] T. Laurila, K. Zeng, J.K. Kivilahti, J. Molarius, T. Riekkinen, I. Suni, Microelectron. Eng. **60**, 71-80 (2002).
[104] H. Wang, A. Tiwari, A. Kvit, X. Zhang, J. Narayan, Appl. Phys. Lett. **80**, 2323-5 (2002).
[105] H. Wang, A. Tiwari, X. Zhang, A. Kvit, J. Narayan, Appl. Phys. Lett. **81**, 1453 (2002).
[106] M. Kumar, Rajkumar, D. Kumar, A.K. Paul, Microelectron. Eng. **82**, 53-9 (2005).
[107] E. Wieser, M. Peikert, C. Wenzel, J. Schreiber, J.W. Bartha, B. Bendjus, V.V. Melov, H. Reuther, A. Mücklich, B. Adolphi, D. Fischer, Thin Solid Films. **410**, 121-8 (2002).
[108] W.-. Wu, K.-. Ou, C.-. Chou, C.-. Wu, J. Electrochem. Soc. **150**, G83-9 (2003).
[109] H.-. Chung, C.-. Liu, Surf. Coat. Tech. **200**, 3122-6 (2006).
[110] R. Fix, R.G. Gordon, D.M. Hoffman, Chem. Mater. **5**, 614-9 (1993).
[111] H.-. Chiu, W.-. Chang, J. Mater. Sci. Lett. **11**, 96-8 (1992).
[112] Y.Y. Wu, A. Kohn, M. Eizenberg, J. Appl. Phys. **95**, 6167-74 (2004).
[113] O. Van Der Straten, Y. Zhu, K. Dunn, E.T. Eisenbraun, A.E. Kaloyeros, J. Mater. Res. **19**, 447-53 (2004).
[114] H. Kim, A.J. Kellock, S.M. Rossnagel, J. Appl. Phys. **92**, 7080-5 (2002).
[115] A. Furuya, H. Tsuda, S. Ogawa, J. Vac. Sci. Tech. B **23**, 979-83 (2005).
[116] H. Okamoto, J. Phase Equilib. **21**, 497 (2000).
[117] H. Okamoto, J. Phase Equilib. Diffus. **28**, 496 (2007).
[118] Z.-. Liu, Y.A. Chang, Calphad. **23**, 339-56 (1999).

[119] L.J. Swartzendruber, E. Paul, Bull. Alloy Phase Diagr. **7**, 254-9 (1986).
[120] ASM Handbook, Vol. 3 Alloy Phase Diagram (ASM International, USA, 1992).
[121] R.E.W. Casselton, W. Hume-Rothery, J. Less-Common Met. **7**, 212-21 (1964).
[122] H. Okamoto, J. Phase Equilib. **18**, 444-445 (1992).
[123] J.D. Wiley, J.H. Perepezko, J.E. Nordman, G. Kang-jin, IEEE Trans. Ind. Electron. **IE-29**, 154-157 (1982).
[124] H. Yang, C.M. Gilmore, D.E. Ramaker, J. Vac. Sci. Tech. A. **11**, 1454-7 (1993).
[125] C. Li, J.H. Hsieh, Z.Z. Tang, Surf. Coat. Tech. **202**, 5676-9 (2008).
[126] J.S. Fang, T.P. Hsu, G.S. Chen, J. Electron. Mater. **33**, 1176-81 (2004).
[127] J.S. Fang, T.P. Hsu, G.S. Chen, J. Electron. Mater. **35**, 15-20 (2006).
[128] J.S. Fang, T.P. Hsu, H.C. Chen, J. Electron. Mater. **36**, 614-22 (2007).
[129] R. Chan, T.N. Arunagiri, Y. Zhang, O. Chyan, R.M. Wallace, M.J. Kim, T.Q. Hurd, Electrochem. Solid-State Lett. **7**, G154-7 (2004).
[130] X.-. Qu, J.-. Tan, M. Zhou, T. Chen, Q. Xie, G.-. Ru, B.-. Li, Appl. Phys. Lett. **88**, 151912.1-3 (2006).
[131] K.-. Hsu, D.-. Perng, J.-. Yeh, Y.-. Wang, Appl. Surf. Sci. **258**, 7225-30 (2012).
[132] D.-. Perng, K.-. Hsu, S.-. Tsai, J.-. Yeh, Microelectron. Eng. **87**, 365-9 (2010).
[133] S. Kumar, D. Greenslit, E. Eisenbraun, ECS Trans. **6**, 77-88 (2007).
[134] J. Koike, M. Wada, Appl. Phys. Lett. **87**, 041911.1-3(2005).
[135] K. Matsumoto, K. Neishi, H. Itoh, H. Sato, S. Hosaka, J. Koike, Proc. IITC (Japan, 2009), 197-199.
[136] N. Jourdan, L. Carbonell, N. Heylen, J. Swerts, S. Armini, A. Maestre Caro, S. Demuynck, K. Croes, G. Beyer, Z. Tökei, S. Van Elshocht, E. Vancoille, ECS Trans. **34**, 515-521 (2011).
[137] J.D. McBrayer, R.M. Swanson, T.W. Sigmon, J. Bravman, Appl. Phys. Lett. **43**, 653-4 (1983).
[138] P.R. Subramanian, D.E. Laughlin, Bull. Alloy Phase Diagr. **10**, 652-5 (1989).
[139] M. Ohring, The materials science of thin films (Academic Press, UK, 1992).
[140] ASM Handbook, Vol 2. Properties and Selection: Nonferrous Alloys and Special-Purpose Materials (ASM International, USA, 1992).
[141] B.D. Cullity, S.R. Stock, Elements of X-ray Diffraction, 3rd edn. (Prentice Hall, USA, 2001).
[142] J.I. Goldstein, P.E. Newbury, D.C. Joy, A.D. Romig, C.E. Lyman, C. Fiori, E. Lifshin, Scanning Electron Microscopy and X-ray Microanalysis, 2nd edn. (Plenum Press, USA, 1992).
[143] D.B. Williams, C.B. Carter, Transimission electron microscopy: A textbook for materials science, 2nd edn. (Springer, New York, USA, 2009).
[144] D.K. Schroder, Semiconductor material and device characterization, 3rd edn. (John Wiley & Sons, USA, 2006).
[145] A.G. Milnes, Deep Impurities in Seminconductors (Wiley, USA, 1973).

[146] W.L. Yang, W.-. Wu, D.-. Liu, C.-. Wu, K.L. Ou, Solid-State Electron. **45**, 149-58 (2001).
[147] H. Kizil, C. Steinbrüchel, Thin Solid Films. **449**, 158-65 (2004).
[148] M.S. Angyal, Y. Shacham-Diamand, J.S. Reid, M.-. Nicolet, Appl. Phys. Lett. **67**, 2152 (1995).
[149] H. Wojcik, U. Merkel, A. Jahn, K. Richter, M. Junige, C. Klein, J. Gluch, M. Albert, F. Munnik, C. Wenzel, J.W. Bartha, Microelectron. Eng. **88**, 641-5 (2011).
[150] M.T. Wang, Y.C. Lin, M.C. Chen, J. Electrochem. Soc. **145**, 2538-45 (1998).
[151] J. Chiou, M. Chen, J. Electrochem. Soc. **141**, 2804-10 (1994).
[152] T.-. Chang, W.-. Wang, L.-. Wang, J.-. Hwang, F.-. Huang, J. Appl. Phys. **75**, 7847-51 (1994).
[153] C.C. Hu, Modern Semiconductor Devices for Integrated Circuits (Prentice Hall, 2010).
[154] C.J. Liu, J.S. Chen, Appl. Phys. Lett. **80**, 2678-80 (2002).
[155] A. Kohn, M. Eizenberg, Y. Shacham-Diamand, J. Appl. Phys. **94**, 3015-24 (2003).
[156] S.-. Rha, S.-. Lee, W.-. Lee, Y.-. Hwang, C.-. Park, D.-. Kim, Y.-. Lee, C.-. Whang, J. Vac. Sci. Tech. **16**, 2019-25 (1998).
[157] Y. Shacham-Diamand, A. Dedhia, D. Hoffstetter, W.G. Oldham, J. Electrochem. Soc. **140**, 2427-32 (1993).
[158] B.K. Lim, H.S. Park, L.K. Chin, S.W. Woo, A.K.H. See, C.S. Seet, T.-. Lee, N.L. Yakovlev, J. Vac. Sci. Tech. **22**, 1844-50 (2004).
[159] F. Braud, J. Torres, J. Palleau, J.L. Mermet, M.J. Mouche, Appl. Surf. Sci. **91**, 251-6 (1995).
[160] M.Y. Kwak, D.H. Shin, T.W. Kang, K.N. Kim, Thin Solid Films. **339**, 290-3 (1999).
[161] M. He, Y. Ou, P.-. Wang, T.-. Lu, Appl. Phys. Lett. **96,** 222901.1-3 (2010).
[162] I. Fisher, M. Eizenberg, Thin Solid Films. **516**, 4111-21 (2008).
[163] A. Kohn, E. Lipp, M. Eizenberg, Y. Shacham-Diamand, Appl. Phys. Lett. **85**, 627-9 (2004).

3 Thermal and electrical stability of TaN_x diffusion barriers[1]

3.1 Introduction

The increasing effort to achieve smaller and faster devices has resulted in shrinking of feature sizes, higher resistance metal lines, enhanced number of metallization layers and closely spaced lines [1]. Employing Cu as the multilevel interconnect material can ameliorate the subsequent problem of increased RC time delay. Copper offers lower bulk resistivity and higher activation energy for electromigration and stress voiding when compared with its Al counterpart [2]. Copper, however, is a fast diffuser in Si as evidenced by its small value of activation energy for diffusion (0.18 eV or 17.4 kJ/mole) [3]. The fast diffusivity of Cu is attributed to its unusual electronic configuration compared with other 3d metals and the small ionic radius of Cu^+ as explained in Section 2.3 [4]. Additionally, in contact with Si, Cu readily forms silicides at temperatures as low as 200°C resulting in device failure [5]. Copper also drifts into SiO_2 under electrical and thermal stresses and affects dielectric breakdown of the oxide [6]. A diffusion barrier layer is, therefore, needed between the Si substrate/dielectric material and Cu to prevent diffusion/drift.

Diffusivity of Cu through the barrier layer is controlled by the relative contributions from bulk and high diffusivity paths, including grain boundaries and dislocations. According to the model suggested by Balluffi and Blakely for fcc metals [7], the diffusion mechanism at an operation temperature $T < 0.5T_m$ (where T_m is the melting temperature of the substrate) is dominated by high diffusivity paths, especially grain boundaries (Section 2.4.2). Bulk diffusion rates, on the other hand, become significant at $T > 0.5T_m$ and scale inversely with T_m [8]. Therefore, a combination of a high T_m material, to minimize bulk diffusion, and an amorphous or a single crystal structure, to minimize high diffusivity paths, can potentially offer satisfactory barrier properties. However, deposition of single

[1] *A version of this chapter has been published. N. Dalili, Q. Liu, D.G. Ivey, J. Mat. Sci.* ***48****, 489-501 (2013).*

crystal barriers has process-related issues in terms of the excessive thermal budget (>500°C) required to form a single crystal structure [9,10].

In current Cu interconnect technology a great deal of research has focused on TaN_x compounds, with $x \leq 1$, due to their high melting temperature [11], high thermal stability (large absolute value of enthalpy of formation [12]) and low electrical resistivity [13]. In addition, Ta is immiscible with Cu, forms a thermodynamically stable interface with Cu [14] and enhances electromigration stability of the metallization stack by inducing a (111) texture in Cu [15]. The cost effectiveness and excellent reliability of sputtering methods has driven their application for depositing diffusion barriers. Several modifications, such as collimated and ionized techniques, have been made to the sputtering process to meet the stringent requirement of shrinking feature sizes [16]. The stoichiometry of the TaN_x system is controlled by the deposition process and post-deposition treatments. The phases deposited by increasing N_2 partial pressure during reactive sputtering are bcc or tetragonal pure Ta, bcc-Ta(N) solid solution, hcp or amorphous-Ta_2N, fcc-TaN and high resistivity Ta_5N_6 [13,17-19]. In addition to these phases, some studies have found that a mixture of fcc-TaN and an amorphous phase will form at larger than equilibrium N:Ta ratios (~1.63) [20-22] or by applying a negative bias to the substrate [18]. The resistivity of the TaN_x phases increases with increasing N:Ta ratios and reaches 4 mΩcm with the formation of the above mentioned amorphous TaN phase [21]. Alternatively, an amorphous TaN_x phase can form by reactive sputtering at a composition near Ta_2N [13,19,23,24] or by N_2 plasma treatment resulting in significantly lower values of resistivity (≤380 $\mu\Omega$cm) [25-27]. A comprehensive review of the various conditions employed to deposit amorphous TaN_x films can be found in Section 2.6.1.1.

As described in Section 2.8, failure of a diffusion barrier can be classified into two modes: *i*) metallurgical mode and *ii*) electrical mode which can happen prior to metallurgical failure. The onset of metallurgical failure is usually characterized using changes in resistivity, elemental depth profiling techniques

and electron microscopy. Holloway *et al* [28] studied the metallurgical stability of 50 nm thick films of nanocrystalline Ta_2N and detected no diffusion of Cu into Si up to 750°C. Ta_2N reacts with the Si substrate at 700°C to form Ta_5Si_3. This is followed by failure by diffusion of Cu through local defects in the Ta_2N layer and formation of Cu_3Si precipitates at the Ta_2N/Si interface accompanied by partial transformation of Ta_5Si_3 to $TaSi_2$. Similar studies by Wu *et al* [25] on 10 nm thick N_2 plasma treated TaN_x found the formation of $TaSi_2$, Ta_5Si_3 and Cu_3Si after barrier failure. The formation of $TaSi_2$, however, preceded Ta_5Si_3 formation. Other studies on reactively deposited amorphous Ta_2N did not find any evidence of Ta_5Si_3 formation [19,23]. The following has been assumed as evidence for Cu diffusion through local defects in TaN_x layer: 1) Cu-silicide formation at the Cu/Si interface [25,26,29-31] and 2) diffusion of Cu detected by elemental depth profiling [27,28,32].

The atomic flux (J) of a multicomponent system is given by Equation 2–8 which is given here:

$$J = -D\nabla c - \frac{Dc}{kT}\left[\nabla\left(\mu(c)\right) - qE\right] + \cdots \qquad \text{Equation 3-1}$$

where D is the diffusion coefficient, c is the concentration of diffusing species, k is the Boltzmann's constant, T is the temperature, $\mu(c)$ is the internal chemical free energy, q is the charge and E is the electric field [8,33]. It is evident from this expression that the atomic flux of Cu through the barrier layer depends on the combination of both temperature of operation and electrical field and it is important to include both in any reliability test. The various methods of electrical characterization of diffusion barriers are described in detail in Section 2.8.2. The electrical failure of TaN_x barriers can be detected by measuring the leakage current of a p-n junction after being annealed at high temperatures [25,34,35] or by monitoring the characteristics of a MOS capacitor after being exposed to thermal and electrical stresses [36]. The correlation between degradation of MOS devices with amorphous TaN_x diffusion barriers and interfacial reaction/diffusion has not yet been examined. Additionally, a comprehensive review of the available

literature (Section 2.6.1.1) indicated the wide range of failure temperatures and mechanisms reported for TaN_x barriers. Therefore, prior to testing any new barrier material system, the reliability of TaN_x barriers had to be investigated to create a baseline for future investigations. The main focus of this chapter is to understand the crystallization mechanism of amorphous TaN_x deposited with a composition near Ta_2N, to examine the Cu diffusion mechanism and reactions and to correlate these with electrical failure. This was accomplished by annealing reactively sputtered amorphous TaN_x barriers deposited on Si and SiO_2 and by BTS testing of MOS devices. The metallurgical failure mode of the samples was investigated via detailed electron microscopy observations, elemental depth profiling, XRD analysis and resistivity measurements. The electrical failure mode of the MOS capacitors was investigated by monitoring the leakage current and flatband voltage followed by electron microscopy and elemental depth profiling analysis on failed samples.

3.2 Materials and methods

The Cu and TaN_x metallization stacks were deposited onto <100> oriented, n-type Si wafers from planar targets using a quasi-DC PE 4410 delta magnetron sputtering system. The base pressure for each run was about $2.0x10^{-7}$ torr and the total gas pressure was kept constant at 15 mtorr for deposition of TaN_x and at 10 mtorr for deposition of Cu. Prior to deposition, the Si substrate was *in-situ* cleaned by RF etching at -300 V under a 10 mtorr Ar pressure. Three different metallization structures of $Si/SiO_2/TaN_x/Cu$, $Si/TaN_x/Cu$ and Si/TaN_x were prepared. The oxide layer on Si/SiO_2 substrates was grown by dry oxidation at 1000°C to a total thickness of 382 nm. The TaN_x layer was deposited by reactive sputtering and the N_2 and Ar pressures in the chamber were controlled by mass flow controllers (98 and 5 sccm for Ar and N_2, respectively). The intended thicknesses of TaN_x films on the Si substrate were 10 nm and 50 nm. The average thickness of deposited TaN_x films was 225 nm on Si/SiO_2 substrates and 14 and 62 nm on Si substrates as measured from cross-sectional TEM images. The deviations in the deposited thickness values from the intended values are due to the error in deposition rate calibration performed by the crystal deposition rate

monitor. Copper films, 227 to 255 nm in thickness, were deposited on the barrier layers without breaking the vacuum. All the films were deposited in the Micralyne MEMS Foundry. The wafers were diced into coupons 8 mm × 9 mm in size and annealed in a tube furnace under flowing 5% H_2/95% N_2 gas for 30 minutes at various temperatures ranging from 300 to 900°C. The tube was purged with gas for about 15 min prior to annealing. The samples were cooled outside the furnace but under flowing gas to prevent oxidation of metallization layers. A calibration curve was generated for the temperature inside the quartz tube under flowing gas using a thermocouple prior to all annealing treatments. A batch of three samples was placed inside the tube and annealed at the same time. A temperature difference of about 30°C was measured across a batch.

Preliminary assessment of reactions in the metallization stacks was performed by grazing incidence XRD and FPP resistivity measurement. XRD analyses were performed on a Bruker Discover 8 diffractometer using monochromatic CuKα radiation (wavelength = 0.15406 nm). The data was collected over a 2θ range of 20-110°, while the incoming radiation angle was kept constant at 2°. The resistivity data were corrected for the small dimensions of the rectangular samples and for the film thickness as explained in Section 2.8.1.6.

The structure and morphology of the metallization stacks were characterized by TEM observation in a JEOL-2010 instrument operated at 200 kV, equipped with an EDX spectrometer, and by electron diffraction analysis. Cross-section TEM samples were prepared either using a Hitachi NB 5000 dual beam FIB/SEM or by a standard dimpling/sputtering procedure. To avoid any ion beam modification to the surface of the top layer (Cu) of the stacks, a 50 nm layer of C (Gatan Precision Etching Coating System – Model 682) was deposited onto the bulk samples prior to FIB processing. A method similar to that given by Giannuzzi and Stevie [37] was used to prepare a thin section. A protective tungsten layer was deposited by ion beam induced deposition. Bulk milling of the sample was accomplished using a 40 keV Ga^+ beam, with currents ranging from 65 nA to 100 pA. Subsequent polishing was done using a 10 keV Ga^+ beam, with

currents of 80 pA and lower to a final thickness 50-100 nm. All sample preparation by FIB were performed at the National Research Council - National Institute for Nanotechnology (NRC-NINT). The approximate thickness of the final lamellae prepared by FIB, mounted on Mo grids, was 100 nm. Plan-view TEM samples of the thin layers were prepared by dimpling/sputtering from the Si side of the sample, preserving the layer of interest. To prepare plan-view samples from the TaN_x layer, the Cu overlayer was removed by immersing in a solution of $2H_2SO_4$:$5CH_3COOH$:$5HNO_3$ for about 30 s. A 200 kV FEI Tecnai F20 FEG TEM/STEM instrument, with an EDX spectrometer, was employed to investigate the elemental distribution in reacted layers. The nominal probe diameter for the analytical electron microscopy experiments was 1 nm. The samples were characterized both as-deposited and after annealing.

Interdiffusion between the layers was characterized with depth profiling using SIMS. The Cu layer was removed by chemical etching after annealing and prior to all SIMS depth profiling analysis, to avoid knock-on of Cu into Si caused by ion bombardment during depth profiling [32]. Depth profiles were obtained using a TOF-SIMS IV instrument (ION-TOF GmbH). The analytical Bi^+ ion source was operated under 25 kV bias and the sputtering Cs^+ ion source was operated under 1 kV bias, producing an ion current of approximately 70 nA. The sputtered crater was about 200×200 μm^2 in size and elemental information was obtained from an 34×34 μm^2 area located at the center of the craters. The secondary ions that were collected for analysis were ^{63}Cu, ^{30}Si, ^{195}TaN and ^{16}O. The detection limit of the instrument for Cu in Si is expected to be in the vicinity of 10^{17} atoms/cm^3.

The MOS capacitor structures were fabricated using <100> oriented, n-type wafers. The wafers were initially cleaned using an RCA-clean procedure and the gate oxide was grown in dry oxygen at 1000°C to a thickness of 26.4 $\pm$ 1.4 nm and annealed at the oxidation temperature in N_2 ambient for 40 min. The thickness of the oxide was measured at 5 different points on the wafer using a Nanospec AFT. The oxidation process was performed at the Carleton University

MicroFabrication Facility (CUMFF). The gate contact consisted of 10.5 $\pm$ 0.3 nm thick TaN_x diffusion barrier and 292.5 $\pm$ 0.5 nm thick Cu dots, which were deposited by sputtering through a shadow mask with 0.5 mm radius holes, in the Micralyne MEMS Foundry. The wafers were diced into individual MOS capacitor devices using a Disco DAD 321 Dicing saw. BTS was performed under either 2 MV/cm or 4 MV/cm positive bias applied to the gate metal at 140°C for various times in a light-tight box, but not under controlled environment. A HP4156 semiconductor analyzer was used for BTS which was only capable of applying voltage to one capacitor at a time. The heating rate of the stage was about 2.3°C/min. *C-V* characteristics of each device were examined before and after BTS at room temperature using an HP4156 semiconductor analyzer, with a DC signal sweeping from -6 V to 3 V and a superimposed AC signal of 10 mV at 2 MHz frequency. Current-voltage (*I-V*) measurements were also taken before and after BTS with the electric field swept from -2 MV/cm to 2 MV/cm. A MOS device is considered as leaky if the leakage current exceeds a value of 10^{-6} A/cm^2 at the applied electric field of 1.2 MV/cm. The FEI Tecnai F20 FEG TEM/STEM, described above, was employed to investigate the cross section morphology of leaky capacitors prepared by FIB methods. SIMS elemental depth profiling was performed on a 34×34 μm^2 area to examine diffusion of Cu into the device. The Cu layer was removed prior to SIMS depth profiling.

3.3 Results and discussion

3.3.1 Metallurgical failure characterization

3.3.1.1 Resistivity measurement

Figure 3–1 shows the variation in resistivity for as-deposited and annealed Si/TaN_x (14 nm)/Cu, Si/TaN_x (62 nm)/Cu and Si/SiO_2/TaN_x (336 nm)/Cu samples. The data mainly represents the properties of the outermost Cu layer since Cu has a significantly lower resistivity value than TaN_x compounds or any other reaction products. The resistivity of the Cu layer decreases slightly with annealing at low temperatures as a result of a decrease in the defect density and grain growth [25]. The resistivity of samples with oxide between the barrier layer and Si

substrate increased by only 7.4 and 14.8% when annealed at 800°C and 900°C, respectively. In contrast, annealing of Si/TaN_x (62nm)/Cu samples at 800°C resulted in a dramatic increase in resistivity by 150 times compared with the as-deposited sample. The samples with thinner TaN_x layers, Si/TaN_x (14nm)/Cu, remained stable up to 700°C and suffered the most significant increase (1200 times) after being annealed at 800°C. It has been shown that the abrupt increase in resistivity can be attributed to the formation of high resistivity reaction products such as Ta- and/or Cu-silicides [25,28,31]. This confirms that a combination of a thicker barrier, resulting in a longer diffusion distance, with the existence of a SiO_2 layer results in superior thermal stability for the Si/SiO_2/TaN_x (336nm)/Cu structure. The addition of the oxide layer reduces the thermodynamic driving force for diffusion in the Cu/SiO_2 system vs. the Cu/Si system (the driving force is given by the second group of terms in Equation 2–8) [38,39] and results in better stability for the structure.

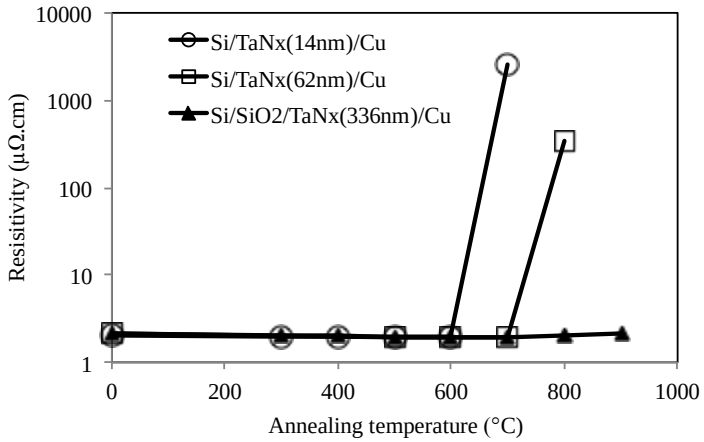

Figure 3–1 Variation in resistivity for Cu/TaN_x/Si and Cu/TaN_x/SiO_2/Si samples as a function of annealing temperature. Note that 0°C indicates the as-deposited samples and the lines are for emphasizing the trend and have no physical meaning.

3.3.1.2 Si/SiO_2/TaN_x/Cu metallization stack

The XRD pattern of the as deposited Si/SiO_2/TaN_x/Cu sample (Figure 3–2) shows a broad peak at low diffraction angles (full width at half maximum or FWHM=6°) indicating the existence of an amorphous TaN_x phase. This amorphous structure persists up to 500°C and crystallizes to a hexagonal Ta_2N

phase at this temperature and higher. Figure 3–3(a) shows a plan-view BF TEM micrograph of the as deposited TaN_x film together with the corresponding selected area diffraction (SAD) pattern taken using a 0.8 μm diameter aperture. The observed diffuse diffraction pattern and the lack of diffraction contrast in BF mode, while tilting the sample (not shown here), provided additional evidence for an amorphous structure. Elemental analysis using EDX analysis (not shown here) showed no evidence of O impurity in the as-deposited amorphous films. The micrograph in Figure 3–3(a) was taken at slightly under focus conditions and reveals the network-like structure of amorphous TaN_x. The contrast of the image was inverted under over-focus conditions indicating areas of lower density among the domains of the amorphous material [40]. The cross-sectional TEM image of the layer, shown in Figure 3–3(b), reveals that these low density networks run across the thickness forming a columnar structure. Tsukimoto *et al* [20] observed a similar structure in reactively sputtered amorphous TaN_x films. According to the zone model suggested by Thornton [41], a sufficiently low substrate temperature during deposition ($T/T_m < 0.3$) can constrain the mobility of the adatoms on the surface and result in formation of open boundaries caused by a shadowing effect. A smooth substrate can enhance the adatom mobility, resulting in denser boundaries (zone T structure). It is believed that the structure observed in Figure 3–3 conforms to a zone T structure.

The XRD patterns for samples annealed at 500°C-800°C (Figure 3–2) consist of Cu and Ta_2N reflections. Upon annealing at 900°C, very weak reflections appear at approximately 22° and 28° (marked with arrows on the pattern), which can be indexed to the second and third most intense lines of a $Ta_{2.11}O_5$ phase (PDF# 65-5464). The formation of Ta oxides on the surface is a preliminary indication of outdiffusion of Ta to the Cu surface at this temperature. To directly observe the phase formation at this temperature, cross-sectional and plan-view TEM samples were examined and the results are shown in Figure 3–4(a) and (b), respectively. As seen in Figure 3–4(a), both the Cu and Ta_2N layers consist of large elongated, columnar grains. Grooving of grain boundaries and the formation of small precipitates on the Cu surface at the grain boundaries (40-150 nm in

diameter) can be clearly seen in this micrograph. The precipitates (marked by an arrow) project as triangles in the cross-section and consist mainly of Ta and O, as confirmed by EDX analysis (not shown here). The W layer in this image is deposited as part of sample preparation procedure by FIB. The plan-view TEM sample prepared of the Cu surface further confirms the formation of precipitates at the grain boundaries of Cu (marked by arrows on Figure 3–4(b)). To identify the structure of the particles, detailed diffraction analysis (SAD and convergent beam electron diffraction (CBED)) was performed on the particles. An example of a large area SAD pattern, shown in Figure 3–4(b), reveals a series of diffraction rings originating from hexagonal $Ta_{2.11}O_5$ particles. Superimposed on this pattern are diffraction rings originating from polycrystalline Cu grains underneath the $Ta_{2.11}O_5$ particles. The reaction associated with the slight resistivity rise at 800°C and 900°C (Figure 3–1) is, therefore, correlated with the outdiffusion of Ta to form Ta_2O_5 at the Cu surface.

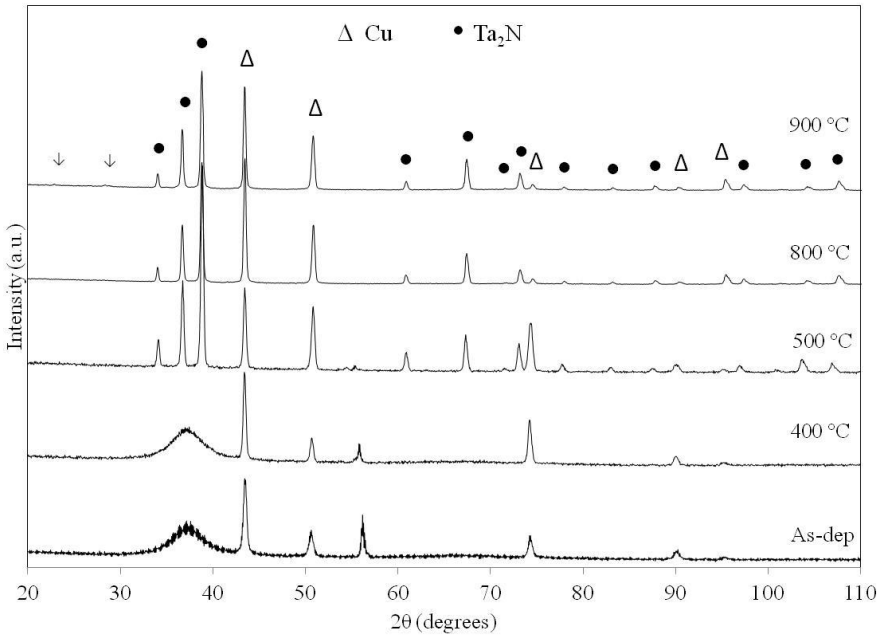

Figure 3–2 XRD patterns obtained from $Si/SiO_2/TaN_x/Cu$ samples upon annealing at various temperatures.

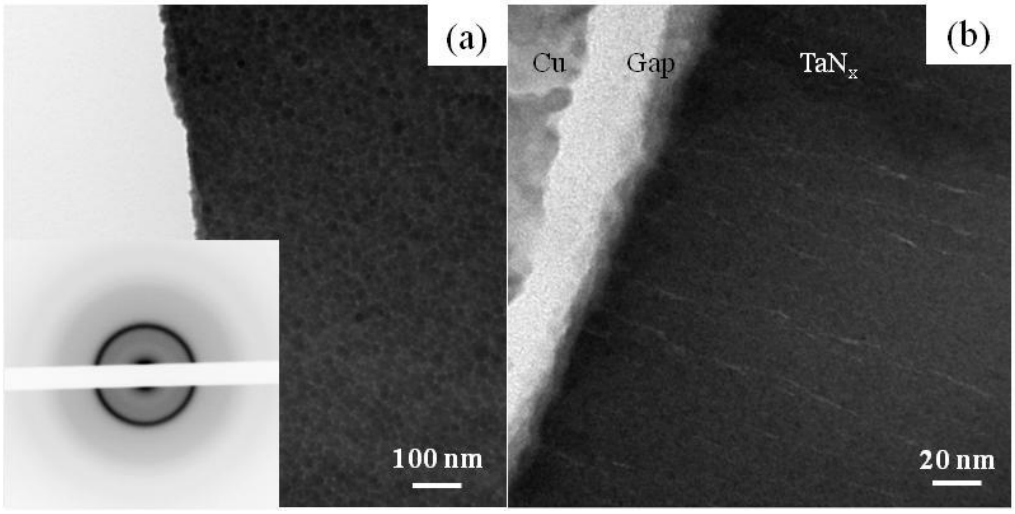

Figure 3–3 TEM BF micrographs of as-deposited $Si/SiO_2/TaN_x/Cu$ sample prepared by conventional dimpling and sputtering methods. (a) Plan-view sample prepared from TaN_x layer after removing the Cu film. (b) Cross-sectional view of TaN_x layer showing the low density networks running through the thickness. Note that the Cu layer is detached from the surface as a result of sample preparation.

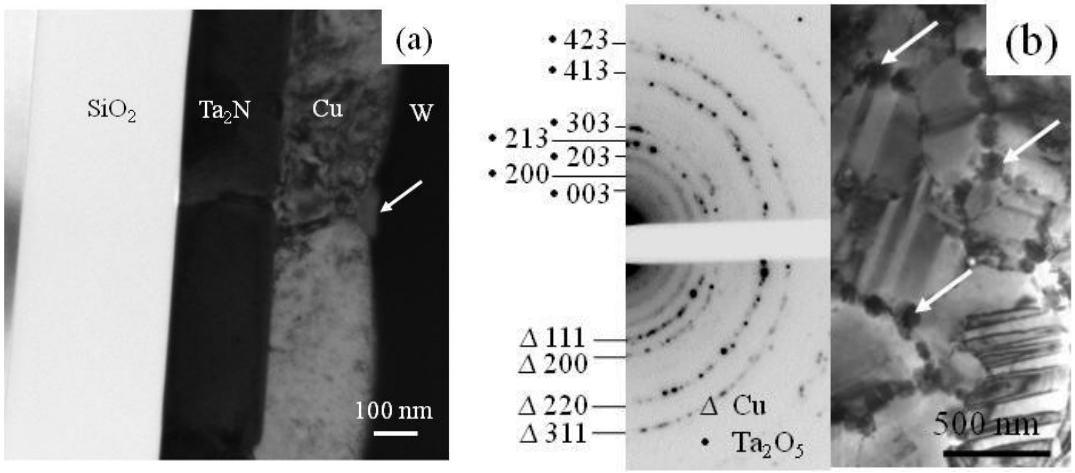

Figure 3–4 TEM BF micrographs of $Si/SiO_2/TaN_x/Cu$ sample after annealing at 900°C for 30 min. (a) Cross-sectional view of the sample prepared by FIB technique. (b) Plan-view sample prepared from top Cu layer together with the corresponding SAD pattern. The precipitates are marked by arrows in both micrographs.

Outdiffusion of Ta to the Cu surface has previously been observed for pure Ta barriers [24,28]. Stable Ta_2N barriers in contact with Si, however, fail by reaction at the Ta_2N/Si interface without any outdiffusion of Ta to the Cu surface [28]. The thermodynamic equilibrium is most likely altered by addition of O to the $SiO_2/Ta_2N/Cu$ multilayer. Based on simplified calculations of ternary and

quaternary phase diagrams, Chen *et al* [42] predicted that Ta-silicides would form when Ta/SiO_2 and Ta_2N/SiO_2 interfaces are annealed at 900°C. Tantalum silicides, however, were not observed in this study. Instead, it appears that Ta moves to the Cu surface to form Ta-oxides. This can be explained by the large negative value of standard Gibbs free energy of formation for Ta_2O_5 ($\Delta G°$ = -2330 kJ/mol) compared with other possible phases at this temperature, *i.e.*, $\Delta G°$ (Ta_2N) = -428, $\Delta G°$ ($TaSi_2$) = -239 kJ/mol and $\Delta G°$ (Ta_5Si_3) = -808 kJ/mol. Therefore, the significant affinity of Ta for O_2 (large negative value of $\Delta G°$ (Ta_2O_5)), provides a large driving force for outdiffusion of Ta and its subsequent oxidation at the Cu surface.

3.3.1.3 Si/TaN_x/Cu metallization stack

Figure 3–5 shows XRD patterns for Si/TaN_x (14nm) /Cu and Si/TaN_x (62nm) /Cu samples after annealing in forming gas at various temperatures for 30 min. A strong Cu (111) peak is observed for the as-deposited samples indicating a <111> preferred crystallographic orientation. It has been reported that the electromigration resistance of Cu lines improves significantly with a strong <111> film texture [43]. The broad peak at low diffraction angles indicates formation of an amorphous TaN_x phase on the Si substrate, similar to the film deposited on SiO_2 substrates. The 62 nm thick amorphous film crystallizes to hexagonal Ta_2N upon annealing at 600°C. The polycrystalline Ta_2N film prevents intermixing and reaction up to 800°C. For the sample with 14 nm TaN_x annealed at 600°C, the broad amorphous peak becomes asymmetrical in shape indicating partial crystallization of the film. This is followed by complete crystallization at 700°C in tandem with complete failure of the barrier layer. Failure of the polycrystalline barriers occurred by interlayer reaction and formation of Cu_3Si and $TaSi_2$ products. The equilibrium phase precipitated from a Si matrix supersaturated with Cu is reported to be η-Cu_3Si which has three polymorphs. The structure of the room temperature phase has been identified by electron diffraction to have a two-dimensional long-period superlattice with a hexagonal sublattice [44]. The reflections from Cu_3Si precipitates in Figure 3–5 can be indexed to a hexagonal sublattice (PDF#59-262). The information from the superlattice reflections is

most likely washed out by background scattering. The thermal stability of the barrier layer scales with the thickness of the film. According to the thin film solution to the Fick's second law and assuming an initial infinite solute (Cu) concentration at the interface, the diffusion distance (X), *i.e.*, the distance from the interface that the concentration of Cu drops by 1/e times, is given by:

$$t = X^2/4D \qquad \text{Equation 3-2}$$

In this equation, t is the annealing time and D is the diffusion coefficient of Cu in TaN_x at the failure temperature (T_f), *i.e.*, 800°C for Si/TaN_x (62 nm) /Cu and 700°C for Si/TaN_x (14 nm) /Cu. According to this equation a smaller annealing time or temperature (lower D) would be required for the Cu species to travel the shorter diffusion distance (X) provided by thinner barriers [8].

To understand the crystallization behavior of the amorphous phase, a plan-view TEM sample was prepared from the 14 nm thick TaN_x layer after annealing at 600°C. Figure 3–6 shows a BF TEM micrograph of the layer and the corresponding SAD pattern obtained from the area marked on the micrograph, which reveals a single-crystal array of spots that can be indexed to the [0001] zone axis of Ta_2N. The crystallites of Ta_2N are embedded in an amorphous matrix and show no preferred crystallographic orientation. This type of crystallization can start heterogeneously from either of the interfaces or from pre-existing nuclei formed from regions of short-range order within the as-deposited amorphous structure [45]. The possible catalytic effect of Si or Cu interface on crystallization, however, requires further investigation.

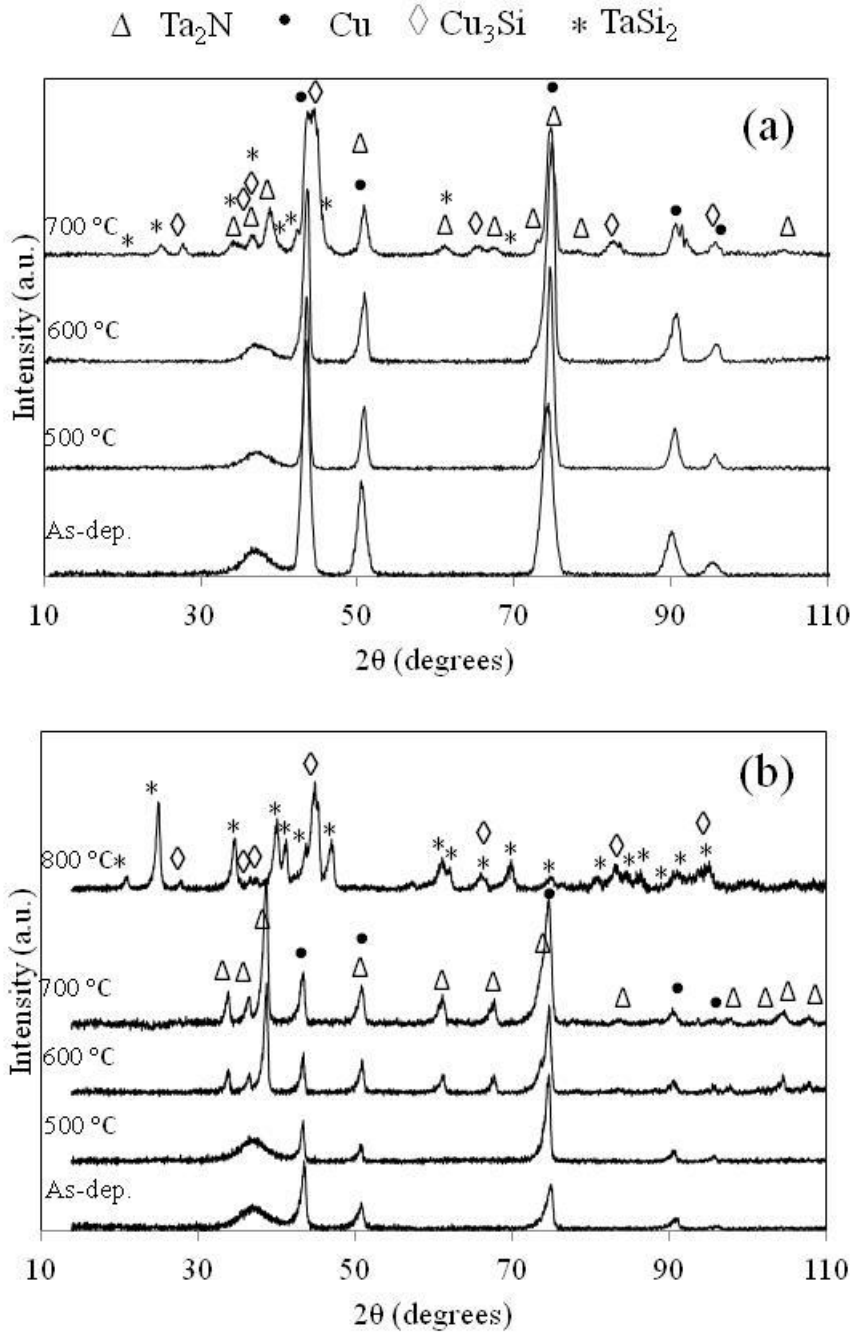

Figure 3–5 XRD patterns obtained from (a) Si/TaN_x (14 nm)/Cu and (b) Si/TaN_x (62 nm)/Cu samples upon annealing at various temperatures.

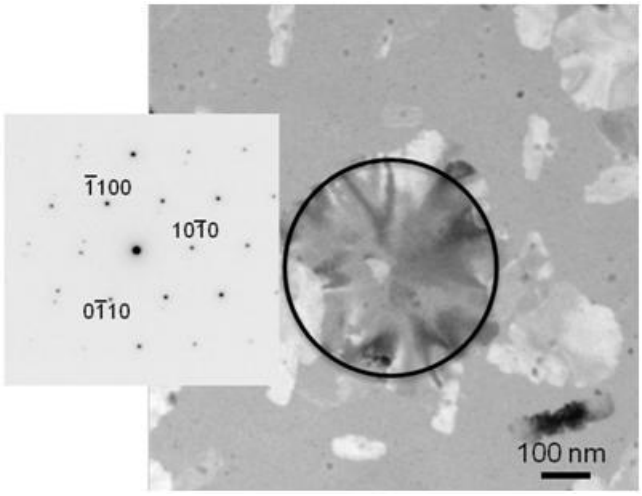

Figure 3–6 Plan-view TEM BF micrograph of TaN_x layer annealed at 600°C and the corresponding SAD pattern obtained from the region marked showing an hcp-Ta_2N grain close to a [0001] zone axis. The Ta_2N crystals are embedded in an amorphous matrix marking the onset of crystallization.

The samples annealed at the failure temperature (T_f) showed a hazy, silvery appearance and were covered with an array of small, star-shaped precipitates. SEM examination of the surface showed several large precipitates, protruding from surface, which were 1-2 μm wide for the 14 nm thick samples and 3-5 μm wide for 62 nm thick samples. In order to examine the morphology of the barrier failure, cross-sectional TEM samples were prepared from the precipitates and the surrounding area. The samples were coated with a thin C layer prior to W deposition as part of the FIB sample preparation process to create a discernible interface between the topmost reacted layers and the W layer. Figure 3–7(a) shows a BF micrograph of a Si/TaN_x (62 nm)/Cu sample after annealing at 800°C. The composition and structure of the numerous phases in this micrograph were identified by EDX and diffraction analysis. Many of the precipitates had a near trapezoidal shape and there were regions of Cu-silicides (area 1), which were separated by an amorphous Si oxide layer (area 2). Growth of Si oxide has been previously reported to occur during exposure to air as a result of the catalytic effect of silicide precipitates on oxidation [46,47]. The catalytic effect has been explained based on dissociation of Cu-Si bonds by oxygen species leading to formation of SiO_2 and Cu. Copper then readily moves to the Si interface and forms a new Cu silicide phase (Section 2.3). The irregular network-like

morphology of the Cu silicides in area 1 can be explained by this reconstitution process [48]. Figure 3–7(b) shows an enlarged view of the upper dark surface layers and the corresponding EDX line scan profiles taken from the black line drawn on the micrograph. The profiles indicate a variation in intensity for the TaL_{β}, SiK_{α} and CuL_{α} signals at each point of the scan. It should be noted that the SiK_{α} signal overlaps with the TaM_{α} signal and, therefore, the intensity of SiK_{α} profile has to be analyzed in combination with the variation in the TaL_{β} signal. The line scan profiles reveal the complex morphology of the surface layers, including two layers of Ta-silicide particles (area 3) embedded in a matrix rich in Cu and Si (area 4).

To identify the topmost reacted layers, a plan-view TEM sample was prepared including the Cu silicide and Ta silicide particles. Figure 3–8 shows a TEM BF micrograph of Cu silicide precipitates together with the corresponding SAD pattern. Some of the diffraction spots in the pattern are attributable to double diffraction as explained here. Two on-axis grains positioned on top of each other perpendicular to the beam are responsible for the Moiré fringes in the BF micrograph, which was collected by positioning the aperture over the main beam and four of double diffraction spots around it, as shown in Figure 3–8(b). The strong reflections in the pattern can be indexed to the $[3\bar{3}1]$ zone axis for hexagonal Cu_3Si (PDF#59-262) or the [111] zone axis of orthorhombic η''-Cu_3Si (grain 1) [44]. Detailed examination of the diffraction pattern revealed a second pattern that can be indexed to the $[\bar{1}01]$ zone axis of η''-Cu_3Si (grain 2). The details in the pattern are made clear in the accompanying drawing in which the closed circles correspond to grain 1, open circles to grain 2 and "x" to double diffraction of beams from grain 1 by grain 2. The plan-view sample also includes several grains of Ta-silicide surface layers (not shown), which were identified as hexagonal $TaSi_2$ (PDF#3-65-3548).

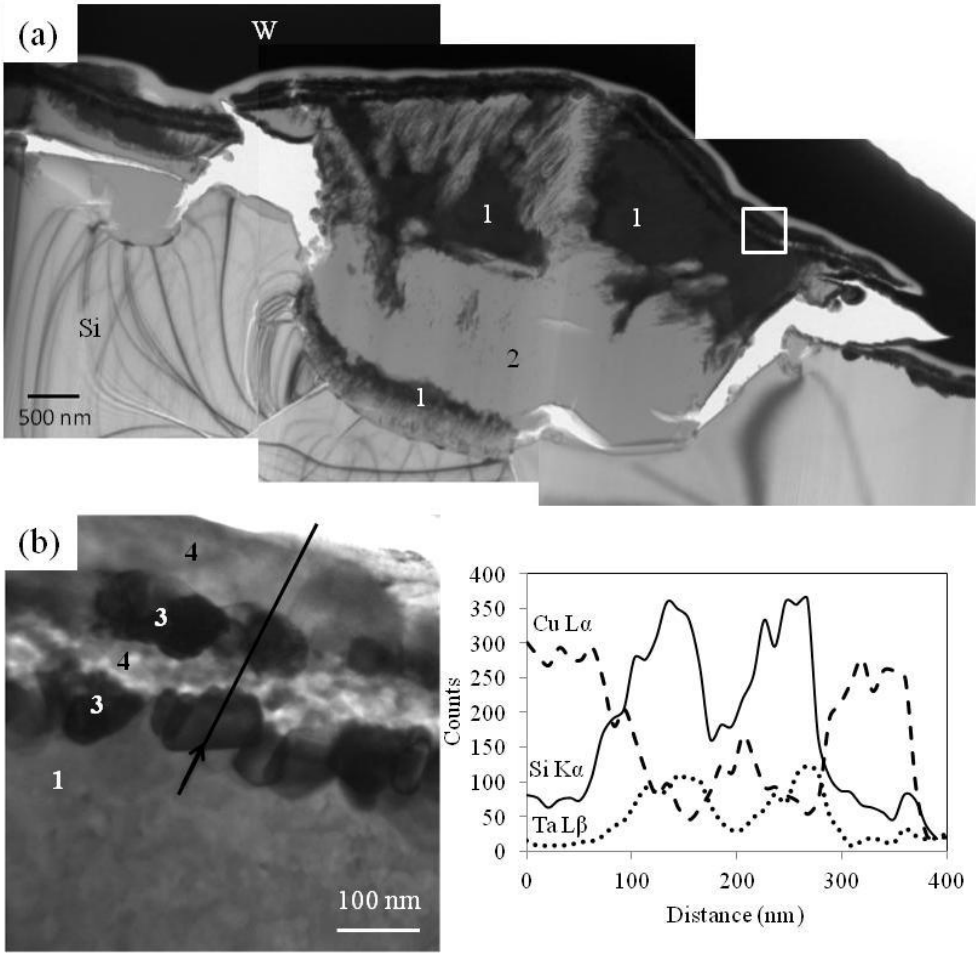

Figure 3–7 (a) Cross-sectional TEM BF micrograph of Si/TaN_x (62 nm)/Cu annealed at 800°C for 30 min. (b) Higher magnification BF micrograph of area marked with the rectangle in (a) together with EDX line scan profiles obtained from the line marked in micrograph (b). The direction of the scan is shown by an arrow on the line. The reacted regions are identified as 1,4: Cu_3Si; 2: SiO_2; 3: $TaSi_2$.

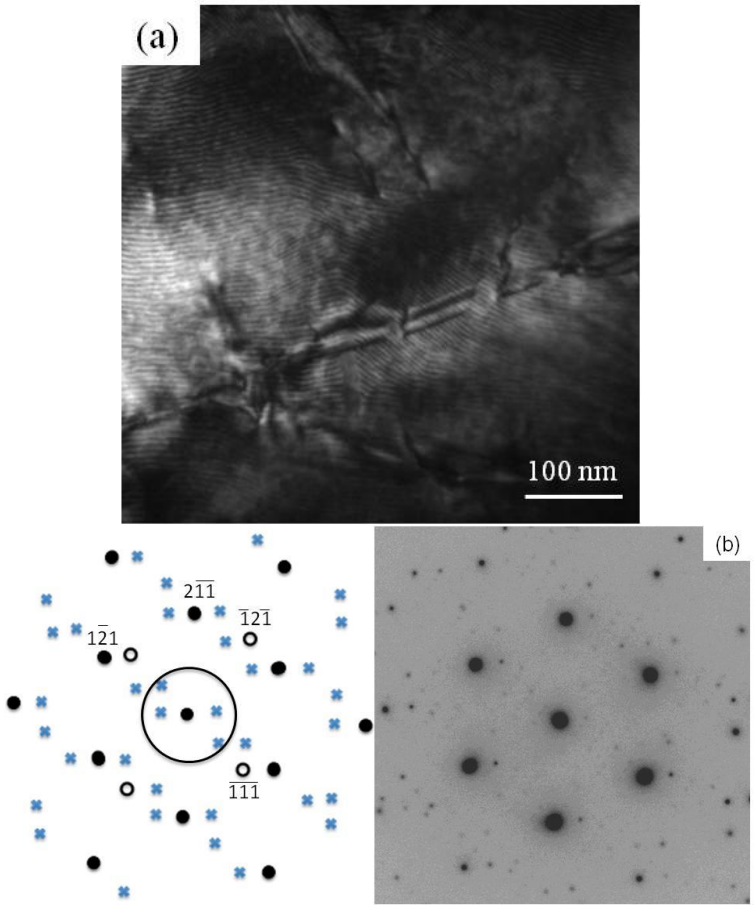

Figure 3–8 (a) Plan-view TEM BF micrograph of top reacted layers of Si/TaN_x (14nm)/Cu sample annealed at 700°C for 30 min. (b) SAD pattern taken from the Cu-silicide particle in (a). The details of the pattern are plotted in the drawing where the closed circles represent reflections from the [111] zone axis of η´´-Cu_3Si, open circles show the[$\bar{1}$01] zone axis for η´´-Cu_3Si and the "x" symbols mark the spots formed by double diffraction.

In order to observe the early stages of Cu diffusion and barrier failure, SIMS depth profiling was performed on as-deposited and annealed Si/TaN_x (62 nm)/Cu samples. The SIMS depth profiles are shown in Figure 3–9. The peaks in the O and Cu profiles on the surface are a result of chemical etching, surface contamination and oxidation after etching. The increase in intensity of profiles near the surface may also be an artifact due to non-uniform sputtering during the initial stages of depth profiling [49]. The O profile at the TaN_x/Si interface indicates the presence of a thin (~1-2 nm) Si oxide layer, despite the in-situ cleaning performed prior to reactive sputtering of TaN_x. There is no evidence of Cu penetration into the TaN_x layer or Si outdiffusion to the surface when annealed

at 700°C and lower temperatures. No conclusion, however, can be drawn about the outdiffusion of Ta to the Cu surface since the Cu layer was removed prior to depth profiling.

In order to determine the effect of Cu diffusion on silicidation of Ta, a 62 nm thick amorphous TaN_x layer was deposited onto a Si substrate. The samples were annealed in forming gas at temperatures up to 800°C followed by XRD analysis and cross-sectional TEM observation (not shown). Similar to samples with a Cu overlayer, TaN_x/Si samples crystallized at 600°C. The presence of Cu, therefore, does not promote early crystallization of amorphous TaN_x. The TaN_x film showed no reaction with the Si substrate upon annealing at 800°C. On comparison of these results with those obtained from the annealed Si/TaN_x (62 nm)/Cu samples, it is evident that the presence and diffusion of Cu promotes non-equilibrium formation of $TaSi_2$. The unit cell of Cu_3Si has a much larger volume (0.046 nm^3/Si atom) than that of Si (0.020 nm^3/Si atom). Following reaction of Cu with Si at the Si/Cu interface and formation of one Cu_3Si unit cell, a volume change of 0.026 nm^3/Si atom has to be accommodated by the Si lattice. This means that 1.3 Si interstitials will be emitted as one Cu_3Si unit cell forms. These Si interstitials are suggested to be highly reactive and capable of breaking the Ta-N bonds to form $TaSi_2$ at temperatures lower than predicted for equilibrium [4].

The series of reactions observed for Cu and Si in contact with TaN_x is shown schematically in Figure 3–10. Copper is the dominant diffusing species in the system. The isolated morphology of crystallites within the amorphous matrix (Figure 3–6) and the absence of high diffusivity paths contribute to the excellent barrier performance of TaN_x up to the crystallization temperature. The reaction at T_f appears to be initiated by localized formation of large particles of orthorhombic η''-Cu_3Si at the Si/TaN_x interface. The formation of these large particles triggers the dissociation of the barrier into dispersed $TaSi_2$ precipitates. The resulting discontinuous morphology of the Ta-rich layer facilitates motion of all moving species. Formation of Cu_3Si particles on the surface on top of the $TaSi_2$ particles occurs by the subsequent diffusion of Si to the surface to react with Cu (Figure 3–

7(b)). Despite the observed rough reaction morphology at T_f, *i.e.*, 800°C for the 62 nm barrier and 700°C for the 14 nm barrier, diffusion is suppressed at lower temperatures and the barrier remains stable up to high temperatures. Holloway *et al* [28] also evaluated the stability of 50 nm Ta_2N films in contact with Si and Cu and observed very high stability up to 800°C. They, however, described a different series of reactions, *i.e.*, both Ta_5Si_3 and $TaSi_2$ were reported to form on the surface [28]. The electron diffraction analysis done in this work of the plan-view sample taken from the topmost reacted layer merely showed the formation of $TaSi_2$.

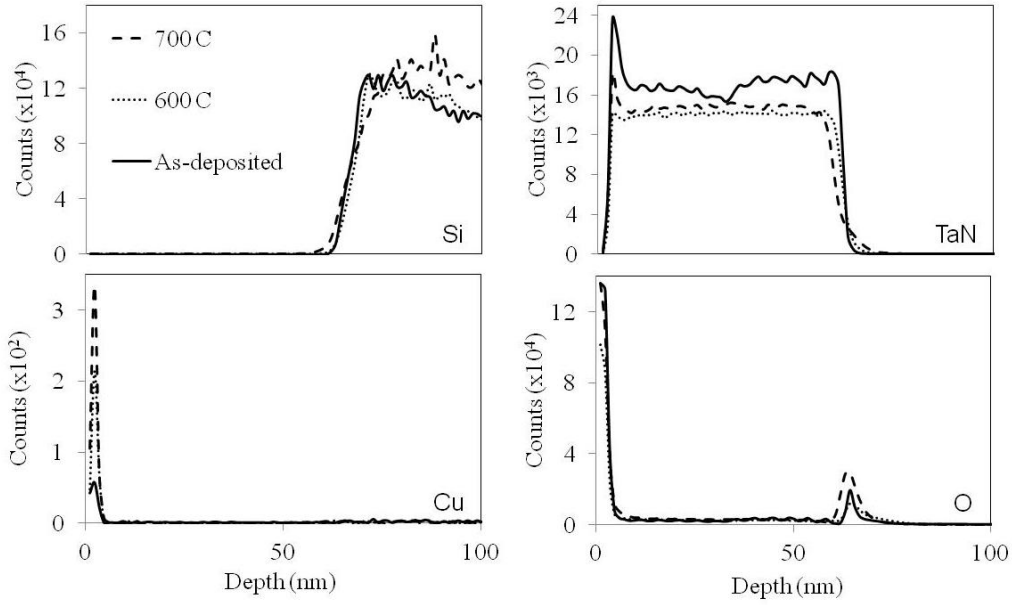

Figure 3–9 SIMS depth profiles of as deposited and annealed Si/TaN_x (62 nm)/Cu samples. Note that the Cu layer has been removed after annealing and prior to depth profiling.

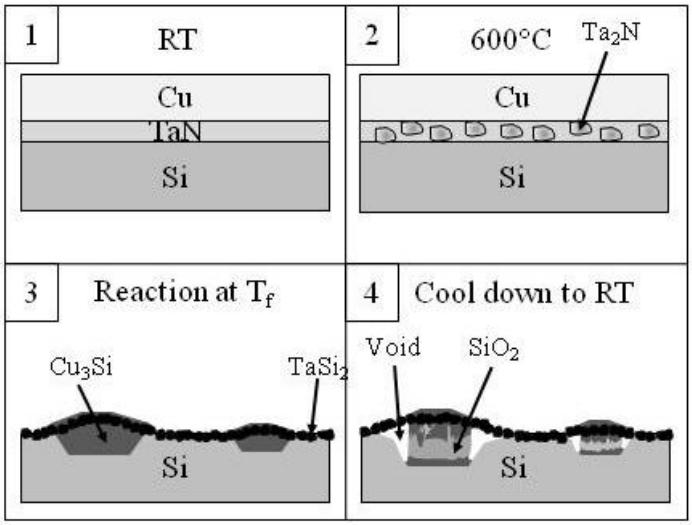

Figure 3–10 Schematic showing the series of reactions happening as Si/TaN_x/Cu stacks are annealed. 1) As-deposited sample at room temperature (RT) with sharp interfaces; 2) partial crystallization to Ta_2N; 3) reaction at T_f accompanied by localized formation of Cu_3Si particles and a continuous layer of $TaSi_2$ on surface; 4) growth of SiO_2 and formation of voids as a result of cooling and exposure to air.

3.3.2 Electrical failure characterization

The MOS capacitors (n-Si/26 nm SiO_2/10 nm TaN_x/292 nm Cu) were subjected to BTS at 2 MV/cm and 4 MV/cm positive gate bias (V_g) and 140°C for up to 60 min. The effect of BTS on *C-V* behavior of MOS capacitors was studied by monitoring the flatband voltage value (V_{FB}) before and after BTS. The shift in flatband voltage ($\Delta V_{FB} = V_{FB\text{-}After} - V_{FB\text{-}Before}$) is related to the concentration of mobile ions in the dielectric material according to Equation 2–24. A negative ΔV_{FB} value can be attributed to an increase in concentration of positively charged species, such as Cu^+ or alkali ions, in the oxide. The flatband voltage was determined by finding the slope and intercept of a linear regression of $1/C^2$ vs. V_g (gate voltage) data based on Equation 2–23. A summary of the values calculated for V_{FB} before and after BTS and the corresponding ΔV_{FB} are presented in Table 3-1. The variations in the initial V_{FB} values are within experimental error. For all the BTS conditions a time dependent positive shift in V_{FB} value was observed with a larger ΔV_{FB} value at longer BTS times. A positive shift in the *C-V* curve is generally attributed to improvement in the quality of oxide via annealing of sputtering damage [50,51]. It has been shown that an initial annealing treatment

will ensure that all capacitors exhibit similar *C-V* characteristics [36,52]. This initial annealing was not performed in this study. The positive ΔV_{FB} value is, therefore, likely related to the annealing of sputter damage during BTS which exceeds the negative ΔV_{FB} that might occur as a result of diffusion of positive ions. Fisher and Eizenberg [51] and Ki-Su Kim *et al* [53] showed that diffusion of Cu to the Si/SiO_2 interface and the subsequent deep trap level states formed in the bandgap of Si can affect the inversion capacitance by reducing the minority carrier lifetime. The inversion capacitance of the devices tested in this study, however, did not show significant increase after BTS.

Table 3-1 Flatband voltage (V_{FB}) of $Si/SiO_2/TaN_x/Cu$ capacitors before and after BTS at 140°C and under various gate bias and time conditions.

Gate bias	**2 MV/cm**			**4 MV/cm**	
BTS time	**15 min**	**30 min**	**60 min**	**15 min**	**30 min**
V_{FB} **before BTS**	-0.55 ± 0.11	-0.70 ± 0.18	-0.72 ± 0.12	-0.49 ± 0.16	-0.56 ± 0.12
V_{FB} **after BTS**	0.01 ± 0.03	0.05 ± 0.07	0.12 ± 0.11	-0.06 ± 0.10	0.06 ± 0.08
ΔV_{FB}	0.56	0.75	0.83	0.43	0.62

For all the samples discussed above, *I-V* measurements were also taken at room temperature before and after BTS. According to the literature, a MOS capacitor is defined as leaky if the leakage current density at an applied electric field of 1.2 MV/cm exceeds a value of 10^{-6} A/cm^2 [36]. Figure 3–11 shows the percentage of non-leaky devices (cumulative non-failure) as a function of BTS time at various positive bias values applied to the gate metal. An initial failure of 5% prior to BTS was evident for these samples. The cumulative non-failure data at non-zero BTS condition does not include the initially failed samples. It is clear that the 10 nm TaN_x barriers do not fail when a positive bias of 2 MV/cm is applied to the gate metal. In comparison, 20% and 40% of the devices failed when biased at 4 MV/cm and 140°C for 15 and 30 min, respectively. According to Equation 2–8, the contribution of the applied bias to the flux of charged species through the dielectric is given by the term *-qEDC/kT*. The larger survival rate at 2

MV/cm can be, therefore, due to the lower driving force for diffusion at lower applied bias (*E*).

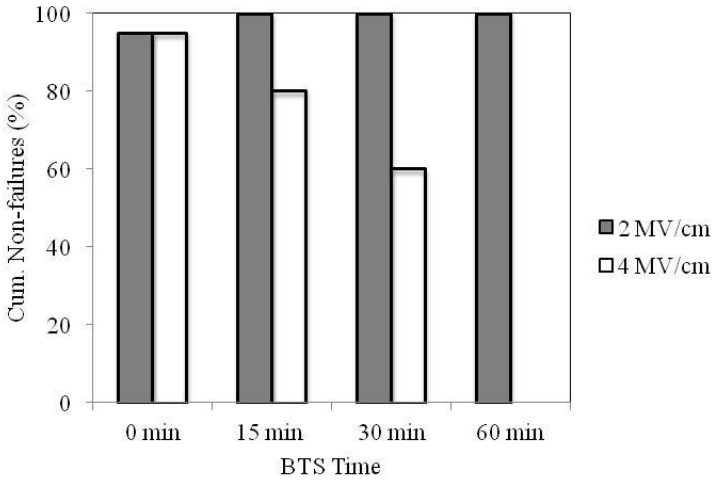

Figure 3–11 Cumulative non-failures (fraction of non-leaky capacitors) as a function of BTS time for two different BTS conditions: 140°C, 2 MV/cm and 140°C, 4 MV/cm.

It is noteworthy that all the capacitors showing large leakage current in *I-V* measurements did not show a negative ΔV_{FB} in *C-V* measurements. To understand the origin of these discrepancies, cross-section TEM samples were prepared by FIB method from capacitors with low ($2x10^{-8}$ A/cm^2), intermediate ($6x10^{-5}$ A/cm^2) and large ($3x10^{-3}$ A/cm^2) leakage current densities. The samples were prepared from the area of applied bias in the BTS test. Figure 3–12(a) and (b) show TEM BF micrographs of MOS capacitors stressed at 140°C and 2 MV/cm for 15 min (leakage current density of $2x10^{-8}$ A/cm^2) and at 140°C and 4 MV/cm for 15 min (leakage current density of $3x10^{-3}$ A/cm^2), respectively. It is evident that, despite the high leakage current density observed for the sample tested at 4 MV/cm, the TaN_x layer remains intact during the BTS test. EDX point analysis of the SiO_2 layer (not included here) showed no indication of Cu diffusion into the SiO_2 layer for either of the samples. SIMS analysis offers better sensitivity and therefore was employed to obtain the diffusion profile of Cu in the oxide. Depth profiling was performed on a capacitor stressed at 140°C and 4 MV/cm for 15 min (leakage current density of $3x10^{-3}$ A/cm^2) and for an as-deposited capacitor. The Cu layer was removed by chemical etching after annealing to avoid knock-on

of Cu into Si caused by ion bombardment during depth profiling [32]. As can be seen in Figure 3–13, the SIMS profiles show a stable TaN_x diffusion barrier and no discernable diffusion of Cu into SiO_2. The increase in intensity for the Cu profiles near the surface is likely due to Cu residue from the chemical etching process or an artifact due to non-uniform sputtering during the initial stages of depth profiling [49].

Kizil and Steinbruchel [36] also studied TaN diffusion barriers subjected to BTS and observed similar discrepancies between the *I-V* and *C-V* measurements. A direct correlation between large leakage current and diffusion of Cu, measured by SIMS analysis, was reported [36]. The *I-V* failures, observed in this study, are likely due to instability in the oxide. The lack of annealing treatment prior to BTS and oxidation of the Cu gate during BTS can result in the discrepancies observed in *C-V* measurements. This points to the requirement for improvement of the experimental design, where MOS capacitors with proper pre-annealing treatments are subjected to BTS under reducing or inert ambient for longer durations. This work is presented in Chapter 6.

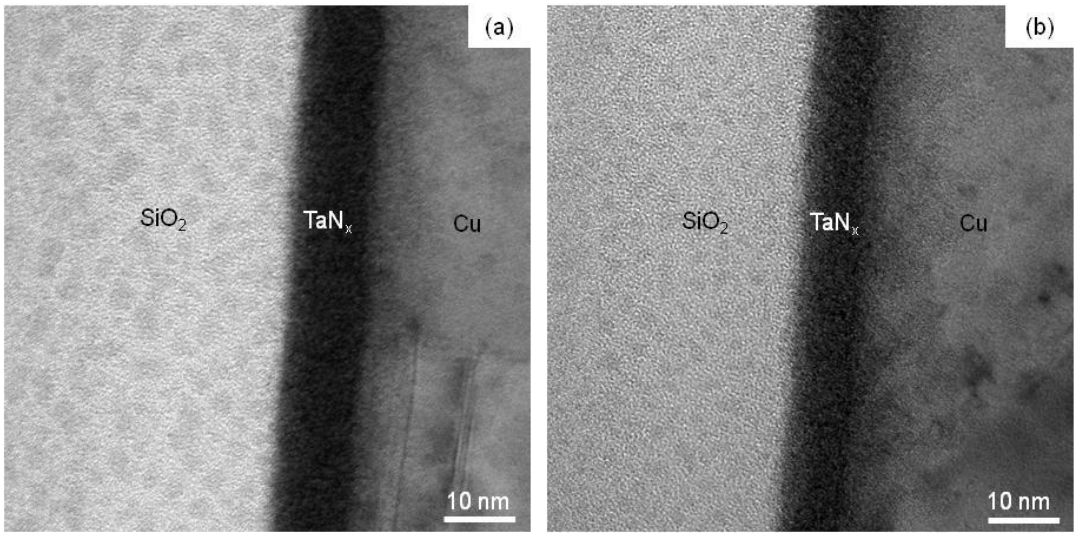

Figure 3–12 Cross-sectional TEM BF micrograph of MOS capacitors stressed at (a) 140°C and 2 MV/cm for 15 min (leakage current density of $2x10^{-8}$ A/cm^2) and (b) 140°C and 4 MV/cm for 15 min (leakage current density of $3x10^{-3}$ A/cm^2).

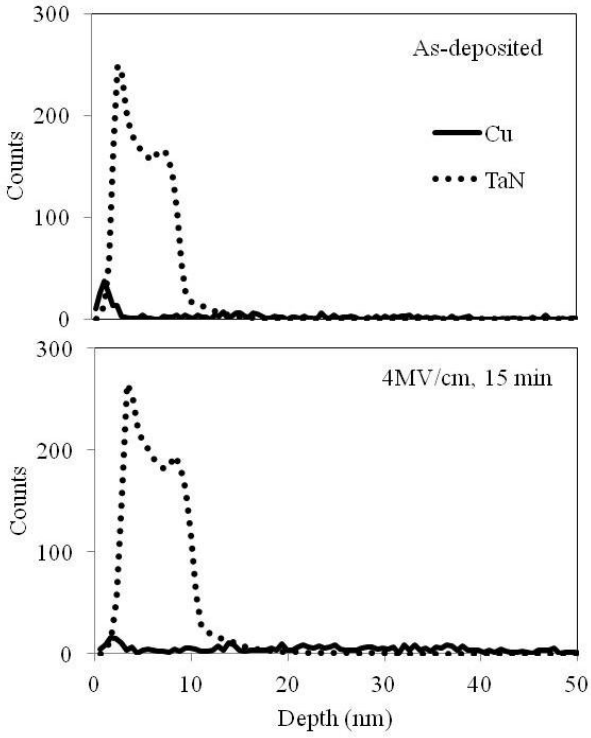

Figure 3–13 SIMS depth profiles of Cu and Ta in a capacitor stressed at 140°C and 4 MV/cm for 15 min (leakage current density of $3x10^{-3}$ A/cm^2) compared with an as-deposited capacitor. Note that the Cu layer has been removed after annealing and prior to depth profiling.

3.4 Conclusions

Microstructural characterization was performed on various thicknesses of amorphous TaN_x thin films to understand the crystallization mechanism and performance as a diffusion barrier for Cu metallization. TEM observations showed that the amorphous TaN_x film, deposited by reactive sputtering near the Ta_2N composition range, crystallized to Ta_2N at around 600°C. In order to further evaluate the performance of TaN_x in contact with Cu, these films were deposited on Si and Si/SiO_2 substrates followed by deposition of Cu. Si/SiO_2/(336nm)TaN_x/Cu metallization stacks showed superior stability when compared to Si/TaN_x/Cu stacks. This was due to the role of SiO_2 as an additional barrier and the thicker barrier layer for $Si/SiO_2/TaN_x$/Cu stacks. These stacks remained stable to 800°C and disintegrated at 900°C by outdiffusion of Ta to the Cu surface to form Ta_2O_5 on the surface. The latter phase was shown to be the thermodynamically stable phase in the system. Si/TaN_x/Cu metallization stacks

failed by diffusion of Cu to the Si/TaN_x interface followed by formation of orthorhombic η´´-Cu_3Si particles at 800°C for 62 nm and 700°C for 14 nm barrier thicknesses. The formation of these particles dissociated the barrier and facilitated the motion of all species, *i.e.*, outward diffusion of Si to form Cu_3Si on the surface and $TaSi_2$ particles.

The electrical failure mode for MOS capacitors (n-Si/26 nm SiO_2/10 nm TaN_x/292 nm Cu) was investigated by monitoring the leakage current and flatband voltage values before and after BTS and studying the failed samples by electron microscopy and SIMS analysis. The samples showed a positive flatband voltage shift and no increase in the inversion capacitance after BTS at 140°C and 2 or 4 MV/cm for up to 60 min. This was attributed to the lack of annealing prior to BTS and the oxidizing ambient of BTS. The leakage current determined from *I-V* measurements showed that up to 40% of the devices failed when biased at 4 MV/cm for 30 min. TEM observation and SIMS depth profiling of the leaky capacitors, however, showed no evidence of Cu diffusion to SiO_2.

3.5 References

[1] P.V. Zant, Microchip Fabrication (McGraw-Hill, USA, 2004) pp. 401-15.
[2] H.Y. Wong, N.F. Mohd Shukor, N. Amin, Microelec. J. **38**, 777-82 (2007).
[3] A.A. Istratov, C. Flink, H. Hieslmair, E.R. Weber, T. Heiser, Phys. Rev. Lett. **81**, 1243-6 (1998).
[4] A.A. Istratov, E.R. Weber, J. Electrochem. Soc. **149**, G21-30 (2002).
[5] M.T. Wang, Y.C. Lin, M.C. Chen, J. Electrochem. Soc. **145**, 2538-45 (1998).
[6] E.P. Burte, W. Aderhold, Solid-State Electron. **41**, 1021-5 (1997).
[7] R.W. Balluffi, J.M. Bkakely, Thin Solid Films. **25**, 363-92 (1975).
[8] P. Shewmon, Diffusion in Solids (The Minerals, Metals & Materials Society, USA, 1989).
[9] H. Wang, A. Tiwari, A. Kvit, X. Zhang, J. Narayan, Appl. Phys. Lett. **80**, 2323-5 (2002).
[10] H. Wang, A. Tiwari, X. Zhang, A. Kvit, J. Narayan, Appl. Phys. Lett. **81**, 1453 (2002).
[11] H. Okamoto, J. Phase Equilib. Diffus. **29**, 291 (2008).
[12] P. Violet, E. Blanquet, O. Le Bacq, Microelectro. Eng. **83**, 2077-81 (2006).
[13] X. Sun, E. Kolawa, J. Chen, J.S. Reid, M. Nicolet, Thin Solid Films. **236**, 347-51 (1993).
[14] P.R. Subramanian, D.E. Laughlin, Bull. Alloy Phase Diagr. **10**, 652-5 (1989).
[15] J. Zhou, H. Chen, Y. Li, Trans. Nonferr. Met. Soc. **17**, 733-8 (2007).
[16] A.E. Kaloyeros, E.T. Eisenbraun, K. Dunn, O. van der Straten, Chem. Eng. Commun. **198**, 1453-81 (2011).
[17] T. Riekkinen, J. Molarius, T. Laurila, A. Nurmela, I. Suni, J.K. Kivilahti, Microelectron. Eng. **64**, 289-97 (2002).
[18] J.H. Wang, L.J. Chen, Z.C. Lu, C.S. Hsiung, W.Y. Hsieh, T.R. Yew, J. Vac. Sci. Tech. B **20**, 1522-6 (2002).
[19] G.S. Chen, P.Y. Lee, S.T. Chen, Thin Solid Films. **353**, 264-73 (1999).
[20] S. Tsukimoto, M. Moriyama, M. Murakami, Thin Solid Films. **460**, 222-6 (2004).
[21] M. Stavrev, D. Fischer, C. Wenzel, K. Drescher, N. Mattern, Thin Solid Films. **307**, 79-88 (1997).
[22] H.B. Nie, S.Y. Xu, S.J. Wang, L.P. You, Z. Yang, C.K. Ong, J. Li, T.Y.F. Liew, Appl. Phys. A **73**, 229-36 (2001).
[23] H.-. Chung, C.-. Liu, Surf. Coat. Tech. **200**, 3122-6 (2006).
[24] M. Hecker, D. Fischer, V. Hoffmann, H.-. Engelmann, A. Voss, N. Mattern, C. Wenzel, C. Vogt, E. Zschech, Thin Solid Films. **414**, 184-91 (2002).
[25] W.-. Wu, K.-. Ou, C.-. Chou, C.-. Wu, J. Electrochem. Soc. **150**, G83-9 (2003).
[26] M. Kumar, Rajkumar, D. Kumar, A.K. Paul, Microelectron. Eng. **82**, 53-9 (2005).
[27] E. Wieser, M. Peikert, C. Wenzel, J. Schreiber, J.W. Bartha, B. Bendjus, V.V. Melov, H. Reuther, A. Mücklich, B. Adolphi, D. Fischer, Thin Solid Films. **410**, 121-8 (2002).

[28] K. Holloway, P.M. Fryer, C. Cabral Jr., J.M.E. Harper, P.J. Bailey, K.H. Kelleher, J. App. Phys. **71**, 5433-44 (1992).
[29] J. Nazon, M.-. Berger, J. Sarradin, J.-. Tedenac, N. Fréty, Plasma Processes Polym. **6**, S844-8 (2009).
[30] J. Nazon, B. Fraisse, J. Sarradin, S.G. Fries, J.C. Tedenac, N. Fréty, Appl. Surf. Sci. **254**, 5670-4 (2008).
[31] T. Oku, E. Kawakami, M. Uekubo, K. Takahiro, S. Yamaguchi, M. Murakami, Appl. Surf. Sci. **99**, 265-72 (1996).
[32] P. Bai, G.-. Yang, L. You, T.-. Lu, D.B. Knorr, J. Mater. Res. **5**, 989-97 (1990).
[33] P.S. Ho, Thin Solid Films. **96**, 301-16 (1982).
[34] S.-. Nakao, M. Numata, T. Ohmi, J. J. Appl. Phys. Part 1 **38**, 2401-5 (1999).
[35] W.L. Yang, W.-. Wu, D.-. Liu, C.-. Wu, K.L. Ou, Solid-State Electron. **45**, 149-58 (2001).
[36] H. Kizil, C. Steinbrüchel, Thin Solid Films. **449**, 158-65 (2004).
[37] L.A. Giannuzzi, F.A. Stevie, Micron. **30**, 197-204 (1999).
[38] R.W. Olesinski, G.J. Abbaschian, Bull. Alloy Phase Diag. **7**, 170-8 (1986).
[39] H. Wendt, H. Cerva, V. Lehmann, W. Pamler, J. Appl. Phys. **65**, 2402-5 (1989).
[40] D.B. Williams, C.B. Carter, Transimission electron microscopy: A textbook for materials science, 2nd edn. (Springer, New York, USA, 2009).
[41] J.A. Thornton, Ann. Rev. Mater. Sci. **7**, 239-60 (1977).
[42] Z. Chen, V. Misra, R.P. Haggerty, S. Stemmer, Phys. Status Solidi (B) Basic Research. **241**, 2253-67 (2004).
[43] M. Kageyama, K. Abe, Y. Harada, H. Onoda, MRS Proc. **514**, 91-102 (1998).
[44] J.K. Solberg, Acta Cryst. **A34**, 684-98 (1978).
[45] S. Mader, Recrystallization, Grain Growth and Textures (American Society for Metals, Ohio, 1966) pp. 523-37.
[46] J.M.E. Harper, A. Charai, L. Stolt, F.M. d'Heurle, P.M. Fryer, Appl. Phys. Lett. **56**, 2519-21 (1990).
[47] C.S. Liu, L.J. Chen, Thin Solid Films. **262**, 187-98 (1995).
[48] J. Hafner, Topics in Applied Physics (Springer-Verlag, Berlin, 1981) pp. 93-140.
[49] D. Briggs, J. C. Riviere, Practical Surface Analysis (John Wiley & Sons, UK, 1983) pp. 85-141.
[50] T. Suwwan De Felipe, S.P. Murarka, S. Bedell, W.A. Lanford, Thin Solid Films. **335**, 49-53 (1998).
[51] I. Fisher, M. Eizenberg, Thin Solid Films. **516**, 4111-21 (2008).
[52] A.L.S. Loke, C. Ryu, C.P. Yue, J.S.H. Cho, S.S. Wong, IEEE Electron Device Lett. **17**, 549-51 (1996).
[53] K.-. Kim, Y.-. Joo, K.-. Kim, J.-. Kwon, J. Appl. Phys. **100,** 063517.1-3 (2006).

4 Stability and failure mechanism of the Ta-Rh amorphous structures[1]

4.1 Introduction

In current Cu interconnect technology, sputter-deposited amorphous TaN_x barriers with $x \leq 1$ are the material of choice [1]. The incorporation of TaN_x barriers requires deposition of a seed layer to facilitate electrodeposition of Cu [1]. The combined thickness of the barrier and seed layers occupies a large volume of the interconnect, which would otherwise be available for Cu electrodeposition [1]. As described in Section 2.5.2, one potential solution is direct electrodeposition of Cu on barrier layers conducive to nucleation of Cu. The list of metals that allow for direct electrodeposition of Cu is compiled by Lane *et al* [2] and includes Pt, Pd, Ru, Rh, Ir and Ag (seedless elements). The candidate diffusion barrier material must satisfy a stringent list of properties including high conductivity, thermal stability, glass forming ability and catalytic properties. The selection criteria used to design a diffusion barrier system based on seedless elements is described in Section 2.7 in detail. In summary, alloys of Ta-seedless metals are considered due to their low resistivity, high glass forming ability and possibility of direct electrodeposition of Cu. Tantalum has a high T_m and, therefore, low bulk diffusivity, does not form any compounds with Cu and its compatibility with the dual damascene process is well known [3,4]. Palladium and Pt were eliminated from the list due to their reactivity with Cu [3]. Silver was not considered as it is a fast diffuser in Si and SiO_2 [5,6]. The criterion by Donald and Davis [7], explained in Section 2.5.1.1, was employed to select the alloy with superior glass-forming ability and thermal stability. A study of established thermodynamic data showed that Ta-Rh is likely to perform well as a diffusion barrier [3].

[1] *A version of this chapter has been published. N. Dalili, Q. Liu, D.G. Ivey, Acta Mater.* ***61****, 5365-74 (2013).*

The main focus of this chapter is to select a stable amorphous $TaRh_x$ composition and to evaluate the selected alloy as a diffusion barrier in contact with Si and Cu. A systematic study has been performed to find the most stable amorphous composition in the Ta-Rh system. This was accomplished by estimating the Gibbs free energies of formation for solid solution, amorphous and intermetallic phases. The theoretically predicted amorphization range was then verified by the deposition of various compositions of $TaRh_x$ alloys. The structure of the deposited films was characterized using XRD and TEM. The selected amorphous Si/$TaRh_x$ (13 nm)/Cu stacks were then annealed in 5% H_2/95% N_2 for 30 min at various temperatures and studied by resistivity measurements, XRD and TEM analysis to assess the failure mechanism of these novel barriers.

4.2 Materials and methods

In order to verify the thermodynamic model, various compositions of $TaRh_x$ films were co-sputtered on <100> oriented, n-type Si wafers. Prior to deposition, the Si substrates received a standard organic cleaning process consisting of a 15 min dip in a mixture of 3:1 concentrated H_2SO_4 to 30% H_2O_2 solution followed by 10% HF cleaning to remove the native oxide. The $TaRh_x$ films were deposited by co-sputtering from two pure targets. Deposition rates vary linearly with the DC power and were measured beforehand with a crystal deposition rate monitor using an AJA ORION8 DC magnetron sputtering system in Ar ambient. The optimum deposition condition was determined by establishing the dependence of composition ratio of the film with the DC power. The base pressure in the chamber was 4×10^{-8} torr or less prior to deposition. The gas pressure was kept constant at 4 mtorr and the target-to-substrate distance was 13 cm. The final thickness of the $TaRh_x$ films was 50 nm. The thicknesses of all deposited layers in this study were measured by cross-sectional TEM observations. The resistivity of the films was assessed by FPP resistivity measurements and the data were corrected for the film thickness according to Section 2.8.1.6. The structure and composition of the as-deposited films were studied by grazing incidence XRD and TEM observations. The details of XRD analysis can be found in Section 3.2. Lower resolution TEM analysis, including imaging, electron diffraction and EDX,

was done with a JEOL-2010 instrument operated at 200 kV and equipped with an EDX spectrometer. High resolution TEM (HRTEM) was performed in a Hitachi HF 3300 instrument operated at 300 kV. Plan-view TEM samples were prepared by direct sputtering of 10 nm thick films onto a 10 nm silicon nitride membrane. The thermodynamic modeling and the detailed characterization results facilitated selection of an alloy suitable for diffusion barrier applications.

The Cu film and selected $TaRh_x$ compositions were deposited on <100> oriented, n-type Si wafers. The wafers were cleaned following the procedure described above. The thicknesses of the deposited Cu and $TaRh_x$ layers were 220-230 nm and 13 nm, respectively. To evaluate the performance of the selected $TaRh_x$ alloy as a diffusion barrier, the wafers were diced into coupons 8 mm × 9 mm in size and annealed in a tube furnace at various temperatures (300-700°C) for 30 min under flowing 5% H_2/95% N_2. The annealing condition and the calibrations are explained in Section 3.2. Preliminary assessment of reactions in the metallization stacks was performed by grazing incidence XRD and FPP resistivity measurements. The structure and morphology of the metallization stacks were characterized by TEM observation of plan-view and cross-section samples. Cross-section TEM samples were prepared using a FIB instrument (refer to Section 3.2 for details). Plan-view TEM samples were thinned by standard dimpling and sputtering from the Si side using the procedure explained in Section 3.2. A 200 kV JEOL-2200 FESTEM, equipped with an EDX detector, was employed to investigate the composition of the reacted layers. Phase analysis of the reaction region was accomplished through electron diffraction analysis.

4.3 Thermodynamic calculations

The amorphous composition range for transition metal alloys can be estimated using the model suggested by Miedema and Niessen (MN model) [8]. According to this model, the amorphization region can be predicted by comparing the Gibbs free energies of formation for the competing phases, *i.e.*, the amorphous phase, solid solutions and structurally simple compounds. The Gibbs free energies of formation for solid solution (ΔG_{ss}^{f}) and amorphous (ΔG_{a}^{f}) phases are given by:

$$\Delta G_{ss}^{f} = \Delta H_{ss}^{f} - T\Delta S^{M}$$ Equation 4-1

$$\Delta G_{a}^{f} = \Delta H_{l}^{M} - T\Delta S^{M} + [x_A \Delta \bar{G}_{a-s}^{A} + x_B \Delta \bar{G}_{a-s}^{B}]$$ Equation 4-2

where T is the deposition temperature (298 K), ΔS^{M} is the entropy of mixing, ΔH_{ss}^{f} and ΔH_{l}^{M} are the enthalpy of formation for the solid solution and the enthalpy of mixing for the liquid alloy, respectively, x_A and x_B are the molar fractions of the constituent metals and $\Delta \bar{G}_{a-s}^{i}$ is the difference between the Gibbs free energies of undercooled liquid (amorphous) and the crystalline states for the corresponding pure metal i. Assuming that the heat capacity difference between the undercooled liquid and the crystalline solid is zero [9], the value of $\Delta \bar{G}_{a-s}^{i}$ can be estimated by:

$$\Delta \bar{G}_{a-s}^{i} = \frac{\Delta H_{a-s}^{i}}{T_{m}^{i}} (T_{m}^{i} - T)$$ Equation 4-3

where ΔH_{a-s}^{i} is the corrected enthalpy of fusion and T_{m}^{i} is the melting temperature of the pure metals. In amorphous alloys there is a certain degree of structural relaxation towards the solid state when compared with liquid alloys. The enthalpy of fusion values, therefore, need to be corrected for amorphous alloys [10]. The corrected enthalpy value was estimated by an empirical constant (α= 3.5 $Jmol^{-1}K^{-1}$) as suggested by van der Kolk *et al* [10]:

$$\Delta H_{a-s}^{i} = \alpha (T_{m}^{i} - T)$$ Equation 4-4

The entropies of mixing for the solid solution and amorphous phases (ΔS^{M}) were approximated based on the integral molar entropy of mixing for an ideal solution:

$$\Delta S^{M} = -R[x_A \ln x_A + x_B \ln x_B]$$ Equation 4-5

where R is the gas constant. The MN semi-empirical model was employed to estimate the enthalpy of mixing for the liquid alloy (ΔH_{l}^{M}) and the enthalpy of formation for the solid solutions (ΔH_{ss}^{f}) [8]. The enthalpy of formation for a statistical solid solution is given by the sum of three contributions:

$$\Delta H_{ss}^{f} = \Delta H_c + \Delta H_e + \Delta H_{str}$$ Equation 4-6

where ΔH_c is the chemical term that accounts for the re-distribution of charge at the interface of atoms A and B when they are brought together in an alloy, ΔH_e is the elastic energy term due to the atomic size mismatch and ΔH_{str} is the structural term related to the preference of transition metals to crystallize in one of the three simple structures, *i.e.*, fcc, bcc or hcp [11]. The chemical term can be estimated by the weighted average of the solution enthalpies for dilute solutions of A in B and B in A.

$$\Delta H_c = x_A x_B (x_B \Delta H_c^{A\ in\ B} + x_A \Delta H_c^{B\ in\ A})$$ Equation 4-7

Values for the dilute solutions of A in B are given by:

$$\Delta H_c^{A\ in\ B} = x_A (V_A^{alloy})^{2/3} f_B^A \Delta H_{ampl}$$ Equation 4-8

where V_A^{alloy} is the molar volume corrected by taking into account changes in atomic volume upon alloying, due to charge transfer effects, f_B^A is the degree by which atoms of one type (A) are surrounded by neighbors of another type (B) and ΔH_{ampl} is an amplitude term associated with the magnitude of chemical interaction defined by:

$$\Delta H_{ampl} = \frac{-P(\Delta \emptyset^*)^2 + Q(\Delta n_{ws}^{1/3})^2}{(n_{ws}^A)^{-1/3} + (n_{ws}^B)^{-1/3}}$$ Equation 4-9

Δn_{ws} is the difference in the electron densities of the Wigner-Seitz cell as derived for the pure elements in metallic form, $\Delta \emptyset^*$ is the difference in the electronegativities of the pure metallic elements and *P* and *Q* are constants determined empirically (*P* = 14.1 and *Q* = 132.54). The numerical values for these constants were taken from reference [11] and are tabulated in Table 4-1. For random solutions $f_B^A = x_B^S$, where x_B^S and x_A^S are surface concentration functions and x_A^S is given by:

$$x_A^S = \frac{x_A (V_A^{alloy})^{2/3}}{x_A (V_A^{alloy})^{2/3} + x_B (V_B^{alloy})^{2/3}}$$ Equation 4-10

where x_B^s is given by a similar relationship. In order to correct for the changes in atomic volume that arise as a result of charge transfer, the following approximate correction is suggested based on the MN model [12]:

$$(V_A^{alloy})^{2/3} = (V_A^{pure})^{2/3} \times (1 + a f_B^A(\emptyset_A^* - \emptyset_B^*)) \quad \text{Equation 4-11}$$

where a is a proportionality constant determined from experimental volume contractions in compounds (a = 0.04 for Ta-Rh alloys). It should be noted that since the alloy volume is a function of f_B^A, which depends on the alloy volume, an iteration procedure was necessary to calculate the alloy volume values. Six iterations were needed to reach convergence.

Table 4-1 Parameters needed for the chemical term contribution to the formation enthalpy of solid solutions. The units for $n_{ws}{}^{1/3}$ are in density units (d.u.: 4×10^{22} electron/cm^3) [11].

Transition metal	$\emptyset^*$ **(Volt)**	$n_{ws}{}^{1/3}$**(d.u.)**	$(V^{pure})^{2/3}$**(cm^2)**
Ta	4.05	1.63	4.9
Rh	5.40	1.76	4.1

Similarly, the elastic energy term (ΔH_e) is given by the weighted average of the solution enthalpies for dilute solutions of A in B and B in A:

$$\Delta H_e = x_A x_B (x_B \Delta H_e^{A\ in\ B} + x_A \Delta H_e^{B\ in\ A}) \quad \text{Equation 4-12}$$

The values for the dilute solutions are estimated based on classical elasticity theory and the sphere in hole model [13] and are given by:

$$\Delta H_e^{A\ in\ B} = \frac{2K_A G_B (V_B^{alloy} - V_A^{alloy})^2}{3K_A V_B^{alloy} + 4G_B V_A^{alloy}} \quad \text{Equation 4-13}$$

where K and G are the bulk modulus and shear modulus values for the bulk pure metals. These values were taken from reference [13]. The structural term (ΔH_{str}) is calculated assuming that the structural-dependent energies for solid solutions vary with the average number of valence electrons per atom, similar to the pure

transition metals. The structural enthalpies of the three main structures (fcc, bcc and hcp) for 4d and 5d transition metals, in relation to the number of valence electrons per atom, are tabulated by Niessen and Miedema [13].

The elastic size mismatch and structural terms are absent for ordered compounds and liquid solutions. The mixing enthalpy of the liquid alloy is, therefore, approximated by:

$$\Delta H_l^M = \Delta H_c \qquad \text{Equation 4-14}$$

In calculation of the chemical term (ΔH_c) for ordered compounds, the area of contact will be larger than that of a random solution and, therefore, the surface area function, f_B^A, can be estimated from the following empirical expression:

$$f_B^A = x_B^s(1 + 8(x_B^s x_A^s)) \qquad \text{Equation 4-15}$$

In this study only the influence of the simple intermetallic compounds was considered, based on the assumption that compounds with a complex structure will not form due to the large diffusion distances required for their formation under rapid deposition conditions [14]. Only the compound $TaRh_3$ has a relatively simple structure, *i.e.*, cubic structure [15], and was, therefore, considered here.

4.4 Results and discussion

4.4.1 Gibbs free energy calculation and $TaRh_x$ alloy properties

The Gibbs free energy curves for the amorphous state and the relevant fcc and bcc solid solution phases (Rh and Ta solid solutions, respectively) are shown in Figure 4–1, as calculated according to the MN model. The only compound in the system that appears to have a relatively simple crystallographic structure ($AuCu_3$ structure) is $TaRh_3$. The free energy of this compound at the stoichiometric composition of 25 at% Ta was estimated with f_B^A calculated from Equation 4-15 and is marked on Figure 4–1. The limited mobility of adatoms during the sputtering process creates a kinetic constraint against phase separation and the common tangent rule generally does not hold [16]. The stable phases need to be predicted from the lowest value of the Gibbs free energy. The amorphization

composition range is, therefore, the composition range where the Gibbs free energy of the amorphous phase becomes more negative than that of the competing crystalline solid solutions, *i.e.*, 37–66 at% Ta. Various compositions of the Ta-Rh films, *i.e.*, 0, 10, 20, 27, 35, 45, 52, 60, 63, 70, 80 and 100 at% Ta, were deposited on Si substrates for XRD analysis and resistivity measurements and onto 10 nm-SiN membranes for TEM observation. The film compositions were verified by EDX analysis. All films deposited within the composition range of 27-70 at% Ta showed a broad peak at low diffraction angles (XRD) and a diffuse electron diffraction pattern in the TEM analysis. These compositions are marked on Figure 4–1 as "Experiment-amorphous". Figure 4–2(a) and (b) show plan-view HRTEM micrographs of the 27 at% and the 52 at% Ta films, respectively. The film with 27 at% Ta is partially amorphous with crystalline regions which extend beyond 4 nm in size. This two phase amorphous + crystalline type microstructure was also observed for the 70 at% Ta films. The micrograph in Figure 4–2(b) is representative of all the amorphous structures observed in this study (35, 45, 52, 60 and 63 at% Ta). The dominant feature of these structures is areas of short-range order with dimensions smaller than 1 nm. The experimentally determined amorphization range depends on several factors such as deposition composition and substrate temperature and is, therefore, specific to the condition used in this study. Nevertheless, the width of the concentration range predicted based on the MN model (37–66 at% Ta) agrees well with the experimentally determined amorphization range (35-63 at% Ta). Wang *et al* [17] studied the amorphization range of multilayer films of $TaRh_x$ prepared by ion beam mixing at four different compositions and predicted an amorphization range of 43-65 at% Ta. This study has shown a wider predicted amorphization range (37-66 at%). The model constants used by Wang *et al* were not made available, making any comparison difficult. In addition, the stability of the $TaRh_3$ phase was not considered in their model and only four compositions were considered experimentally.

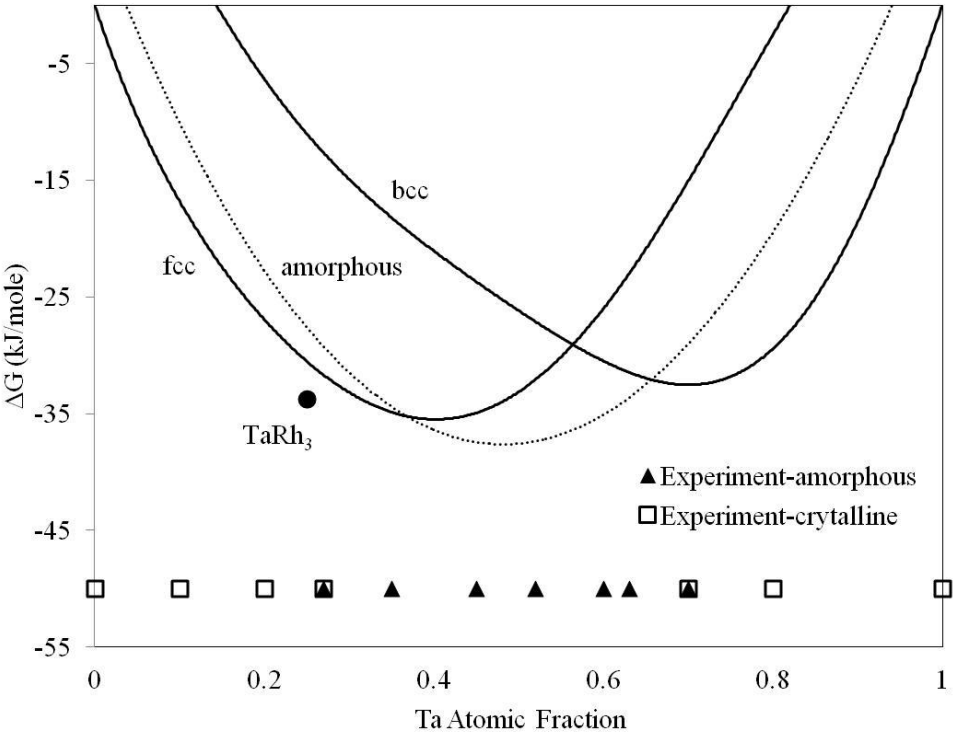

Figure 4–1 Calculated Gibbs free energies of the amorphous, intermetallic and the relevant bcc and fcc solid solutions phases for the Ta-Rh system at 298 K calculated using the Miedema and Niessen model. The region of stability for the amorphous phase and crystalline phases as determined by experimental observations are also marked. Films with 27 and 70 at% Ta have a two phase crystalline + amorphous structure.

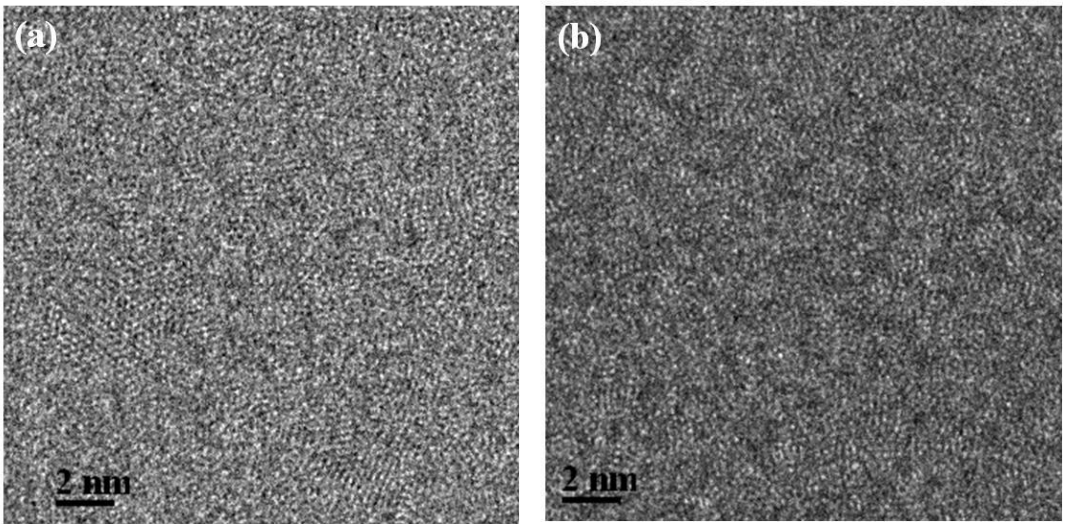

Figure 4–2 High resolution TEM micrographs of as-deposited $TaRh_x$ films with (a) 27 at% Ta and (b) 52 at% Ta.

Figure 4–3(a) shows selected area diffraction (SAD) patterns for pure Rh and films with 10 at% and 20 at% Ta collected from the corresponding TEM plan-view samples. Pure Rh and the $Ta_{10}Rh_{90}$ solid solution form with the stable crystallographic structure of pure Rh (fcc) in agreement with the thermodynamic model in Figure 4–1. Substitution of 10 at% of Rh atoms by larger Ta atoms (Table 4-1) creates a considerable increase in interatomic spacing and the average lattice parameter increases by 3.7% relative to pure Rh (a = 0.379 nm). Giessen *et al* [15] observed a 0.63% increase in the average lattice parameter of arc melted Ta_8Rh_{92} relative to pure Rh. The large lattice distortion observed in this study can be attributed to the intrinsic stress developed during thin film growth [18]. The addition of 20 at% Ta to Rh stabilizes the cubic-$TaRh_3$ phase (PDF# 65-7150) [19]. According to the equilibrium Ta-Rh phase diagram, $TaRh_3$ is a non-stoichiometric compound which is stable over the composition range of 22-31 at% Ta at 1000°C [15]. In this study, however, $TaRh_3$ forms at 20 at% Ta. The film with 27 at% Ta, on the other hand, shows a two phase structure, *i.e.*, crystalline and amorphous phases. According to the thermodynamic calculations, the Gibbs free energy of stoichiometric $TaRh_3$ is lower than that of the competing crystalline and amorphous phases (Figure 4–1) and $TaRh_3$ should be stable at 25 at% Ta. The values calculated for the intermetallic compounds based on the MN model only apply to those compositions that exist in the equilibrium phase diagram [12]. The thermodynamic calculations done here were based on T = 298 K. Information for the stable composition range for $TaRh_3$ at room temperature, however, is lacking. Consequently, the MN model cannot predict the stability of non-stoichiometric compositions of $TaRh_3$.

Figure 4–3(b) shows SAD patterns for pure Ta and $Ta_{80}Rh_{20}$ films collected from the corresponding TEM plan-view samples. The reflections from both compositions can be indexed to tetragonal-Ta (PDF#25-1280) [20] structures. Several studies have shown that pure and solid solution Ta films sputtered in Ar plasma grow predominantly with the tetragonal β structure [21]. The $Ta_{80}Rh_{20}$ films deposited in this study show a strong <411> texture.

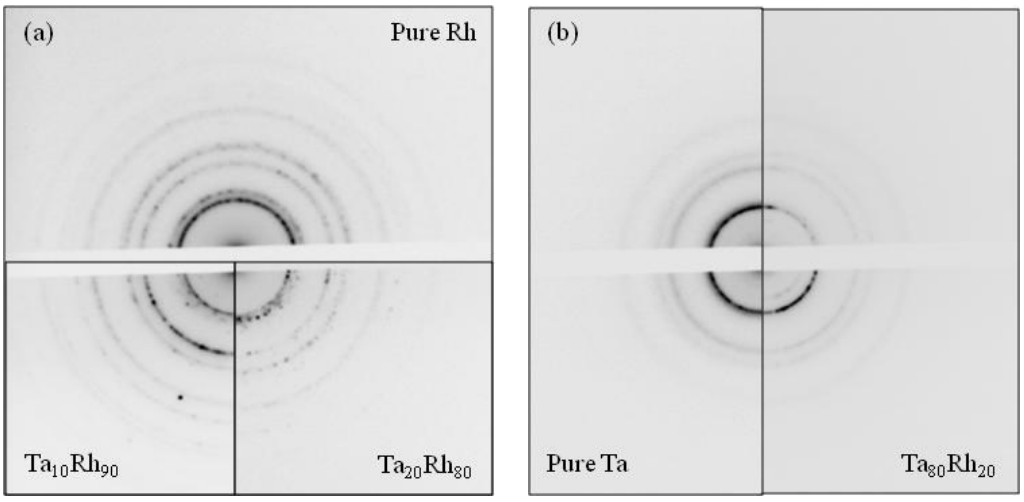

Figure 4–3 SAD patterns collected from plan-view TEM samples of (a) pure Rh, $Ta_{10}Rh_{90}$ and $Ta_{20}Rh_{80}$ and (b) pure Ta and $Ta_{80}Rh_{20}$.

How well suited the amorphous $TaRh_x$ alloys are for diffusion barrier applications depends on their resistivity values. The variation in resistivity for various compositions of as-deposited Si/$TaRh_x$ (50 nm) are shown in Figure 4–4, with the maximum resistivity observed for 35 at% Ta. The addition of an alloying element to a pure metal distorts the lattice and increases the electron scattering cross-section, thereby increasing the resistivity. The random atomic arrangement of atoms in amorphous structures, on the other hand, scatters the electrons and results in a higher resistivity compared with the competing crystalline phase [22]. The impurity contribution to the resistivity of a random solid solution can be predicted by Nordheim's rule [23]. According to the combined Matthiessen and Nordheim rules, the resistivity of a solid solution of A in B is given by:

$$\rho = \rho_{matrix} + C_{Nordheim} x_A x_B \qquad \text{Equation 4-16}$$

where ρ_{matrix} is the resistivity of the matrix due to scattering from thermal vibration and all defects except for impurities and $C_{Nordheim}$ is the Nordheim constant [23]. The best fit for the resistivity data for a solid solution of Ta in Rh (excluding the intermetallic phase at 20 at% Ta) gives $C_{Nordheim}$ = 836 $\mu\Omega$cm. This fit is shown in Figure 4–4 and is in good agreement with the experimental data. The resistivity of $TaRh_3$ at 20 at% Ta is significantly lower than the value predicted by Nordheim's rule, which is based on a random solid solution

assumption. Scattering effects are reduced as a result of the ordered crystalline structure of this phase, resulting in its low resistivity value. On the other hand, the resistivity values of the solid solution of Rh in Ta deviate significantly from Nordheim's rule and the Nordheim's constant for the Ta solid solution cannot be extracted from this study. Nevertheless, resistivity values of the amorphous $TaRh_x$ films (106-202 $\mu\Omega$cm) are lower than the reported resistivity values for amorphous TaN_x films (267 $\mu\Omega$cm) in Section 3.3.1.1 and are expected to lower the overall resistance of the metallization stack.

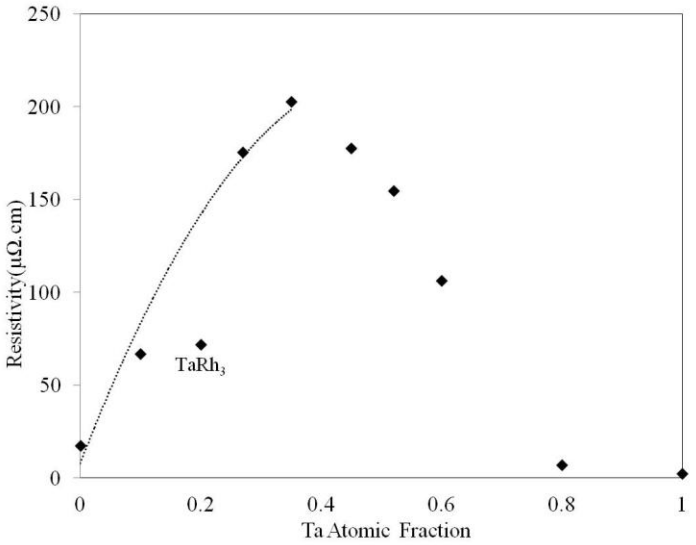

Figure 4–4 Variation in resistivity for as-deposited Si/$TaRh_x$ (50 nm) samples as a function of composition. The dotted line shows the best fit for solid solution resistivity for Ta dissolved in Rh according to the Matthiessen and Nordheim rules.

In summary the detailed characterization of the deposited films confirms the predictions made based on the MN scheme. These calculations provide a useful guide for selecting a glass forming composition suitable for diffusion barrier applications for Cu metallizations.

4.4.2 Diffusion barrier performance of amorphous $TaRh_x$

According to the thermodynamic modeling and the detailed characterization of as-deposited $TaRh_x$ films, alloys with 35-63 at% Ta constitute the amorphization range in the Ta-Rh system. To understand the stability of

amorphous $TaRh_x$, 13 nm thick films with 45 and 52 at% Ta were evaluated as diffusion barriers in contact with Cu and Si. Both compositions showed similar failure temperatures and reaction morphology and all the results presented henceforth are representative of $Ta_{45}Rh_{55}$ and $Ta_{52}Rh_{48}$ diffusion barrier films. Figure 4–5 shows the XRD patterns for Si/$Ta_{45}Rh_{55}$ (13 nm)/Cu samples after annealing in 5% H_2/95% N_2 gas at various temperatures for 30 min. A strong (220) Cu peak at approximately 74° 2θ is observed for the as-deposited sample indicating a <110> preferred crystallographic orientation. This peak becomes stronger upon annealing at 500°C as a result of grain growth. Upon annealing at 550°C, very weak reflections appear at approximately 43° and 44° 2θ (marked with arrows on the pattern) which can be indexed to the (200) peak for hexagonal $TaSi_2$ (PDF#3-65-3548) [24] and to the most intense peak for hexagonal Cu_3Si (PDF#59-262) [25], respectively. This is an indication of the onset of interlayer reaction and the formation of Cu_3Si and $TaSi_2$ products. As discussed in Chapter 2, the room temperature equilibrium phase precipitating from Cu contaminated Si has a two-dimensional long-period orthorhombic type superlattice with a hexagonal type sublattice [26]. Interlayer reaction and failure were also studied by FPP resistivity measurements on the as-deposited and annealed samples. The resistivity of the Cu film was decreased by about 15% as a result of annealing at 500°C. This drop in resistivity can be attributed to a decrease in defect density and grain growth (in agreement with the XRD results). Annealing at 550°C was accompanied by a dramatic increase in resistivity, by 36 times, which can be attributed to interlayer reaction and formation of higher resistivity silicide particles.

The samples annealed at 550°C showed a somewhat hazy surface appearance when viewed visually. SEM observation of the surface (Figure 4–6(a)) revealed the presence of several precipitates (0.5-5 μm wide) protruding from the surface. To understand the morphology of the barrier failure, cross-sectional TEM samples were prepared from these particles and the surrounding area. Figure 4–6(b) shows a BF micrograph of the Si/$Ta_{45}Rh_{55}$ (13nm)/Cu sample after annealing at 550°C. The composition and structure of the resulting reaction morphology were

identified by EDX and diffraction analysis. The surface particles observed in SEM analysis had a near trapezoidal shape and were about 1 μm deep. These were Cu-silicide particles as confirmed by EDX analysis (not shown here). Diffraction patterns collected from these particles (not shown here) could be indexed to either orthorhombic η´´-Cu_3Si [26] or hexagonal Cu_3Si (PDF#59-262) [25]. The Cu_3Si particles were separated from the Si substrate by the growth of amorphous Si oxide. The formation of a Si oxide layer in association with Cu_3Si particles has been reported repeatedly and was attributed to the catalytic effect of silicide precipitates on oxidation [27]. The morphology of the Cu_3Si and Si oxide particles observed here was similar to those formed as a result of the failure of amorphous TaN_x barriers (Section 3.3.1.3).

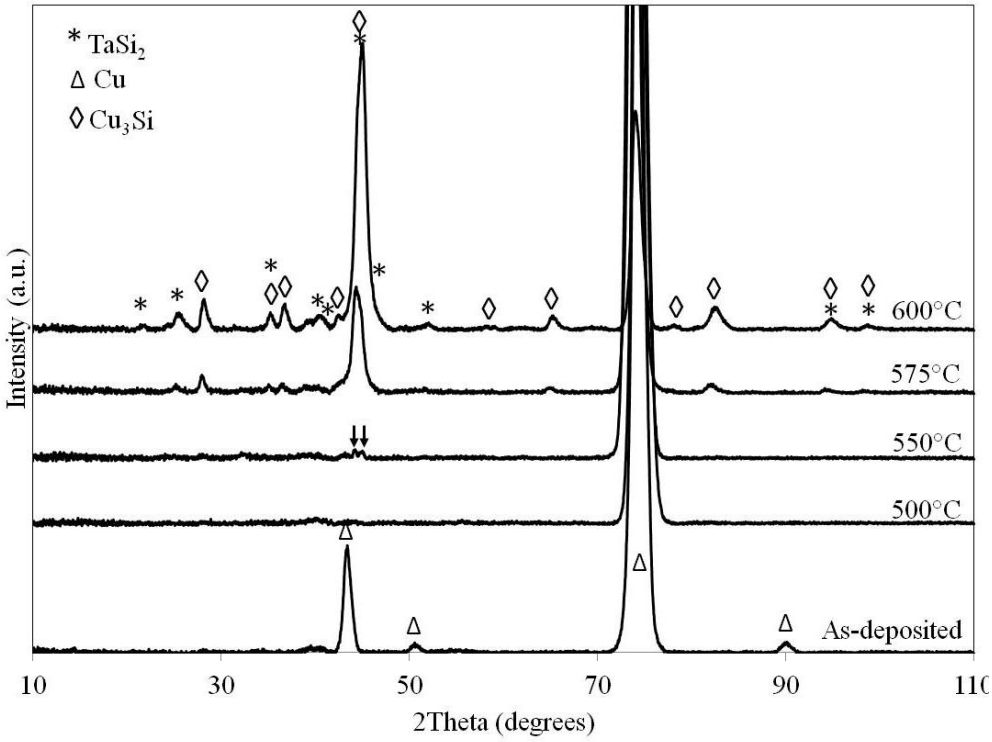

Figure 4–5 XRD patterns obtained from $Si/Ta_{45}Rh_{55}$ (13 nm)/Cu samples after annealing at various temperatures in 5% H_2/95% N_2 gas for 30 min.

Detailed examination of the remnants of the barrier layer on top of the Cu_3Si particles revealed a discontinuous morphology as marked by arrows in Figure 4–6(b). A plan-view TEM sample was prepared from the topmost reacted layers and

diffraction analysis was performed to identify the reaction morphology. The formation of Cu_3Si is observed to be associated with dissociation of the barrier into a discontinuous film of hexagonal $TaSi_2$ and dispersed particles of orthorhombic RhSi (PDF#1-74-6099) [28]. The $TaRh_x$/Si interface at locations away from the Cu_3Si particles had a different morphology. Figure 4–6 shows a HRTEM micrograph of the Si/$Ta_{45}Rh_{55}$ interface, which shows evidence of reaction and formation of several particles at the interface. The particles are faceted and grow into the Si side of the interface. The barrier layer was intact despite reaction and the formation of particles. EDX analysis showed the presence of Rh and Si within these particles. To identify the phase, a plan-view sample was prepared by standard dimpling and ion milling from the Si side after removing the Cu layer by chemical etching. This method provided a TEM sample that included the Rh-silicide particles and the $Ta_{45}Rh_{55}$ diffusion barrier layer. Figure 4–7 shows a BF micrograph of the plan-view sample together with a SAD pattern. The diffraction spots can be indexed to a polycrystalline orthorhombic RhSi phase (PDF#1-74-6099) [28]. Superimposed on this pattern is a diffuse diffraction halo at around 0.225 nm originating from the amorphous $Ta_{45}Rh_{55}$ layer underneath the particles.

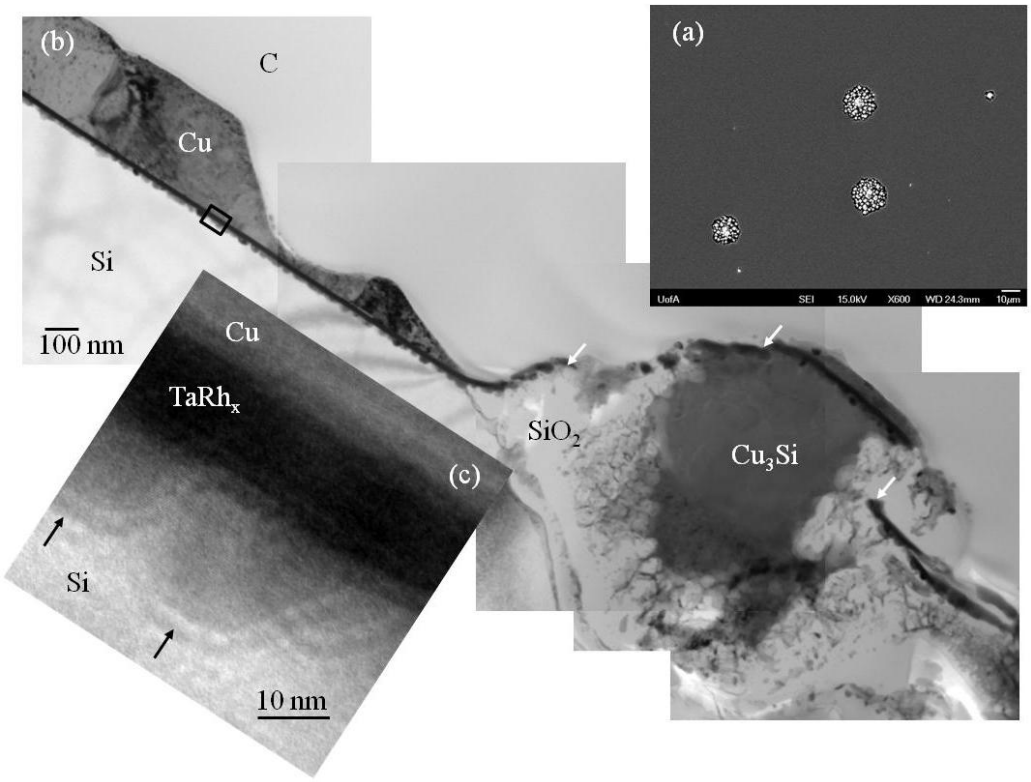

Figure 4–6 (a) Secondary electron (SE) micrograph of the top surface of Si/$Ta_{45}Rh_{55}$ (13nm)/Cu annealed at 550°C for 30 min showing the precipitates formed on the surface. (b) Cross-sectional TEM BF micrograph from a region with the particles shown in (a). (c) Higher magnification BF micrograph of the area marked with a rectangle in (b) showing the RhSi particles formed at the Si/$Ta_{45}Rh_{55}$ interface which are marked by arrows.

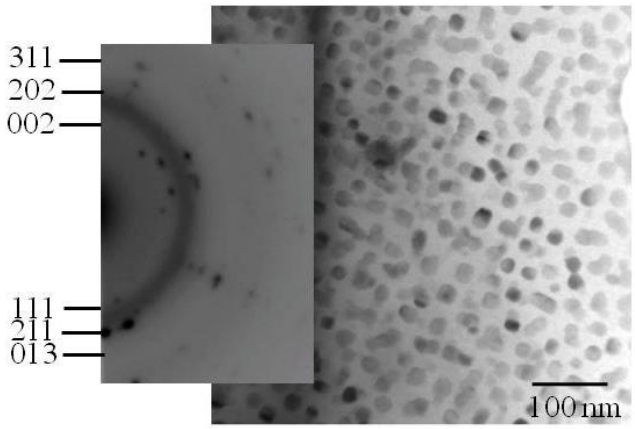

Figure 4–7 Plan-view TEM BF micrograph of a sample prepared from the reacted area at Si/$Ta_{45}Rh_{55}$ interface of Si/$Ta_{45}Rh_{55}$ (13 nm)/Cu sample annealed at 550°C. A large area SAD pattern showing the presence of RhSi particles at the interface is also included.

In order to determine the effect of Cu diffusion on silicidation of $TaRh_x$ diffusion barriers, a 50 nm thick amorphous $Ta_{45}Rh_{55}$ layer was deposited onto a Si substrate. The samples were annealed and characterized by XRD analysis and TEM observation. In the absence of Cu, the $Ta_{45}Rh_{55}$ film remained stable up to 700°C. Figure 4–8 shows a BF TEM image and a large area SAD pattern of a plan-view sample prepared from the sample annealed at 700°C. The $Ta_{45}Rh_{55}$ film dissociated and reacted with the Si substrate to form orthorhombic RhSi and hexagonal $TaSi_2$ at this temperature. This form of alloy partitioning and reaction with the Si substrate had been previously observed for films of refractory metals and near-noble metals in contact with Si. It is suggested that the reaction starts with diffusion of the near-noble metal into Si and the formation of silicides at low temperatures. This is followed by outward diffusion of Si through the silicide particles to react with the refractory metal at higher temperature [29]. The morphology of the reacted films observed for the $Ta_{45}Rh_{55}$ layer reveals a similar series of reactions. The observations in this work revealed that silicidation of Rh and Ta occurred simultaneously at 700°C and preceded crystallization of the amorphous layer. Nevertheless, it is evident from the comparison of these results with those obtained from the annealed Si/$Ta_{45}Rh_{55}$ (13 nm)/Cu samples that the presence of Cu promoted dissociation of the $TaRh_x$ layer at 550°C.

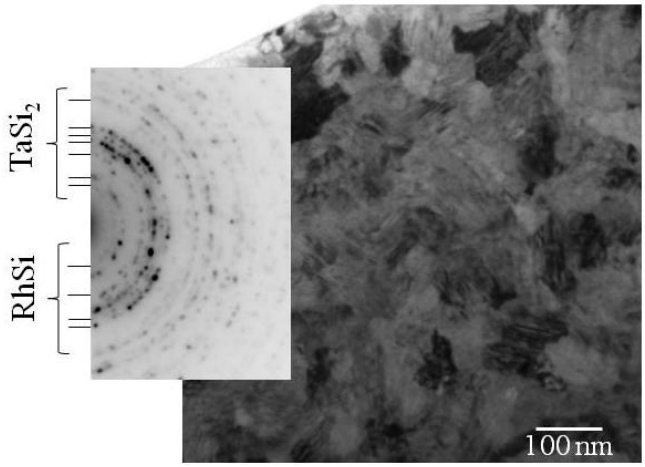

Figure 4–8 Plan-view TEM BF micrograph of a sample prepared from $Si/Ta_{45}Rh_{55}$ (50 nm) sample annealed at 700°C. A large area SAD pattern showing alloy partitioning and formation of $TaSi_2$ and RhSi particles is also included.

In summary, the series of reactions observed for Cu and Si in contact with amorphous $Ta_{45}Rh_{55}$ and $Ta_{48}Rh_{52}$ indicate that the reaction at the failure temperature occurred by alloy partitioning in the $TaRh_x$ layer and reaction with the Si substrate to form RhSi particles. However, it is not clear whether the reaction of Rh with the Si substrate preceded the formation of Cu_3Si or vice versa. To better understand the sequence of reactions, *in-situ* TEM studies were performed on $Si/TaRh_x/Cu$ metallization stacks and the results are presented in Chapter 5. Formation of large orthorhombic η''-Cu_3Si particles at the $Si/TaRh_x$ interface was accompanied by the formation of a discontinuous $TaSi_2$ layer and large dispersed RhSi particles. The formation of $TaSi_2$ was not observed at locations with no Cu_3Si particles. It is evident that the formation of Cu_3Si particles triggers further silicidation of the $TaRh_x$ layer. Similar behavior was observed for TaN_x barriers where formation of Cu_3Si particles catalyzes silicidation of Ta (Section 3.3.1.3). The formation of a Cu_3Si unit cell is accompanied by a volume change of 0.026 nm^3/Si atom which has to be accommodated by the Si lattice. It has been suggested that the Si lattice will emit 1.3 Si interstitials per Cu_3Si unit cell [30]. These Si interstitials are highly reactive and can react with Ta to lower the formation temperature of $TaSi_2$. Despite the

observed rough reaction morphology at 550°C, Cu diffusion was suppressed at lower temperatures and the barrier remained stable.

The need for high conductivity and amorphous structures has prompted several studies of amorphous metallic diffusion barriers. Fang *et al* [31-33] studied the crystallization and failure of 20 nm thick Ta-X (X=Fe, Co, Ni) diffusion barriers. Amorphous Ta-Fe and Ta-Co films failed at 650°C and 700°C after being annealed for 5 min [32]. Ta-Ni (20 nm) diffusion barriers had a failure temperature between 550°C and 700°C depending on the composition [31,33]. Similar work involving a thick (500 nm) layer of $Ni_{0.6}Nb_{0.4}$ exhibited failure of Si/barrier/Cu stacks after annealing at temperatures higher than 600°C for 1 hr in vacuum [29]. De Rues *et al* [34] investigated the stability of sputtered amorphous $Ir_{0.45}Ta_{0.55}$ diffusion barriers. A 30 nm thick barrier failed after annealing in vacuum for 30 min at 750°C [34]. All these barriers were thicker than the $TaRh_x$ barriers (10 nm) in this work.

According to the thin film solution to Fick's second law, given in Equation 3–3, a smaller annealing time or temperature (lower *D*) would be required for the Cu species to travel the shorter distance (*X*) provided by the thinner barrier of this study [35]. This explains the lower failure temperature observed for the thinner $TaRh_x$ barriers in this study compared with the barriers discussed in the previous paragraph and makes direct comparison difficult. One attribute of amorphous $TaRh_x$ films is that they offer the possibility of direct electrodeposition of Cu. The strategy of employing a diffusion barrier layer that enables direct electrodeposition of Cu without the need for a seed layer has received a lot of interest, as explained is Section 2.6.2. One such element under consideration is Ru. Ruthenium has been shown to be a poor barrier and a 20 nm thick Ru barrier failed by grain boundary diffusion after annealing at 500°C for 10 min. Several methods have been used to enhance the diffusion barrier performance of Ru. One approach is the combination of Ru with amorphous TaN to improve the diffusion barrier properties of Ru [36]. The various annealing conditions and metallization

stacks used in these investigations makes any comparison to the results of this work challenging.

TaN_x-based barriers have been the most commonly adopted material for diffusion barriers for Cu metallization. Comparison of the results from this chapter with those for Si/TaN_x (14nm)/Cu metallization stacks, presented in Chapter 3, indicates that the failure temperature for $TaRh_x$ films (550°C) is lower than that for TaN_x (700°C). However, amorphous $TaRh_x$ films offer several advantages such as lower resistivity and the possibility of direct electrodeposition of Cu. The results of this study show that $TaRh_x$ barriers capable of direct Cu plating could be a potential candidate for advanced metallization.

This chapter examines the effectiveness of $TaRh_x$ films as a diffusion barrier to Cu using a thin film approach (metallurgical mode). It should be noted that the atomic flux of Cu through the barrier layer depends on a combination of both temperature of operation and electrical fields (Equation 2–8). The stability of MOS capacitors with $TaRh_x$ as the diffusion barrier between Cu and the dielectric layer based on BTS tests is examined and presented in Chapter 6.

4.5 Conclusions

The detailed study of the Ta-Rh binary system showed that thermodynamic calculations, based on the Miedema-Niessen model, provide a suitable guide for selecting a stable amorphous structure for diffusion barriers for Cu metallizations. Detailed structural analysis of co-sputtered $TaRh_x$ films revealed that deposits with 35-63 at% Ta were amorphous while deposits with 27 and 70 at% Ta had a two-phase amorphous plus crystalline structure. Based on the thermodynamic calculations and structural characterization results, $Ta_{45}Rh_{55}$ and $Ta_{52}Rh_{48}$ were selected as candidate diffusion barriers for Cu metallization and their performance was assessed by metallurgical characterization of annealed Si/$TaRh_x$ (13 nm)/Cu metallization stacks. The metallization stacks remained stable up to 550°C. The barrier disintegrated by reaction with the Si substrate to form RhSi and large particles of Cu_3Si. The formation of Cu_3Si particles triggered silicidation of the remaining barrier to form $TaSi_2$. The generation of Si interstitial defects in

association with Cu_3Si formation facilitated silicidation of Ta. The formation of RhSi and $TaSi_2$ was not observed for samples without a Cu overlayer at temperatures lower than 700°C. The presence of Cu, therefore, lowered the temperature at which the barrier disintegrated and reacted with the Si substrate.

4.6 References

[1] A.E. Kaloyeros, E.T. Eisenbraun, K. Dunn, O. van der Straten, Chem. Eng. Commun. **198**, 1453-81 (2011).
[2] M.W. Lane, C.E. Murray, F.R. McFeely, P.M. Vereecken, R. Rosenberg, Appl. Phys. Lett. **83**, 2330-2 (2003).
[3] ASM Handbook, Vol. 3 Alloy Phase Diagram (ASM International, USA, 1992).
[4] ASM Handbook, Vol 2. Properties and Selection: Nonferrous Alloys and Special-Purpose Materials (ASM International, USA, 1992).
[5] J.D. McBrayer, R.M. Swanson, T.W. Sigmon, J. Electrochem. Soc. **133**, 1242-6 (1986).
[6] J.D. McBrayer, R.M. Swanson, T.W. Sigmon, J. Bravman, Appl. Phys. Lett. **43**, 653-4 (1983).
[7] I.W. Donald, H.A. Davies, J. Non-Cryst. Solids. **30**, 77-85 (1978).
[8] A.R. Miedema, A.K. Niessen, Calphad. **7**, 27-36 (1983).
[9] H. Kui, D. Turnbull, J. Non-Cryst. Solids. **94**, 62-9 (1987).
[10] G.J. Van der Kolk, A.R. Miedema, A.K. Niessen, J. Less-Common Met. **145**, 1-17 (1988).
[11] A.R. Miedema, F.R. de Boer, R. Boom, Calphad. **1**, 341-59 (1977).
[12] A.K. Niessen, F.R. de Boer, R. Boom, P.F. de Châtel, W.C.M. Mattens, A.R. Miedema, Calphad. **7**, 51-70 (1983).
[13] A.K. Niessen, A.R. Miedema, Phys. Chem. Chem. Phys. **87**, 717-25 (1983).
[14] B.X. Liu, Phys. Status Solidi A **94**, 11 (1986).
[15] B.C. Giessen, H. Ibach, N.J. Grant, Trans. Metall. Soc. AIME. **230**, 113-22 (1964).
[16] J.A. Thornton, Annu. Rev. Mater. Sci. **7**, 239-60 (1977).
[17] W.C. Wang, J.H. Li, Y. Dai, B.X. Liu, Scr. Mater. **59**, 3-6 (2008).
[18] R.C. Cammarata, Prog Surf Sci. **46**, 1-38 (1994).
[19] A.E. Dwight, P.A. Beck, Trans. Metall. Soc. AIME. **215**, 976-9 (1959).
[20] B.T. Moseley, C.J. Seabrook, Acta Crystallogr. **B29**, 1170-1 (1973).
[21] M. Stavrev, D. Fischer, C. Wenzel, K. Drescher, N. Mattern, Thin Solid Films. **307**, 79-88 (1997).
[22] GJ Shiflet, Y Leng, JW Hawk. Metallic Glasses. Ullmann's Encyclopedia of Industrial Chemistry (Wiley, USA, 2000).
[23] S.O. Kasap, Principles of Electronic Materials and Devices (McGraw-Hill, USA, 2006) pp. 113-91.
[24] H. Nowotny, H. Schachner, R. Kieffer, F. Benesovsky, Monatsh. Chem. Verw. Tl. **84**, 1-12 (1953).
[25] N. Mattern, R. Seyrich, L. Wilde, C. Baehtz, M. Knapp, J. Acker, J. Alloy. Compd. **429**, 211-5 (2007).
[26] J.K. Solberg, Acta Cryst. **A34**, 684-98 (1978).
[27] J.M.E. Harper, A. Charai, L. Stolt, F.M. d'Heurle, P.M. Fryer, Appl. Phys. Lett. **56**, 2519-21 (1990).
[28] S. Petersson, R. Anderson, J. Baglin, J. Dempsey, W. Hammer, F. D'Heurle, S. Laplaca, J. Appl. Phys. **51**, 373-82 (1980).

[29] R.E. Thomas, K.J. Guo, D.B. Aaron, E.A. Dobisz, J.H. Perepezko, J.D. Wiley, Thin Solid Films. **150**, 245-52 (1987).
[30] A.A. Istratov, E.R. Weber, J. Electrochem. Soc. **149**, G21-30 (2002).
[31] J.S. Fang, T.P. Hsu, H.C. Chen, J Electron. Mater. **36**, 614-22 (2007).
[32] J.S. Fang, T.P. Hsu, G.S. Chen, J Electron. Mater. **35**, 15-20 (2006).
[33] J.S. Fang, T.P. Hsu, G.S. Chen, J Electron. Mater. **33**, 1176-81 (2004).
[34] R. de Reus, R.J.I.M. Koper, H. Zeijlemaker, F.W. Saris, Mater Lett. **9**, 500-3 (1990).
[35] P. Shewmon, Diffusion in Solids (The Minerals, Metals & Materials Society, USA, 1989).
[36] S. Kumar, D. Greenslit, E. Eisenbraun, ECS Trans. **6**, 77-88 (2007).

5 *In-situ* TEM study of stability of $TaRh_x$ diffusion barriers[1]

5.1 Introduction

It is common practice to initially assess the reliability of new barrier materials using conventional annealing in an inert atmosphere (metallurgical failure mode) followed by characterization using resistivity measurements, elemental depth profiling techniques and electron microscopy [1]. The reliability of amorphous $TaRh_x$ films as a diffusion barrier for Cu metallization was investigated *ex-situ* by electron microscopy of annealed samples. The results are discussed in Chapter 4. Failure occurred by reaction of Rh and Si to form RhSi and diffusion of Cu to the $Si/TaRh_x$ interface to form Cu_3Si particles. The sequence of the phenomena, however, was only speculated based on the reaction morphology of the annealed samples after cooling and was not observed directly during reaction (Chapter 4). Diffusion of Cu through the barrier layer usually occurs rapidly at the failure temperature and results in the formation of several compounds. The exact failure mechanism of diffusion barriers is usually speculated by examination of the post-failure, complex reaction morphology. In this respect, *in-situ* TEM is an excellent technique for direct observation of atomic diffusion mechanisms involved in the failure of diffusion barriers.

Special care must be given in the successful execution of *in-situ* TEM heating experiments. Grid compatibility with the sample must be considered as the typical FIB lift out grid material is made from Cu; therefore during lamella preparation through FIB there is potential for grid material to be sputtered and re-deposited onto the polished surface. In addition, Cu atoms when exposed to the low pressure of an electron microscope exhibit high mobility at temperatures exceeding 600°C or under intense electron beam radiation and tend to nucleate and grow on the surface without any catalyst [2-4]. Unexpected melting of thin Cu lamellae at temperatures below the bulk melting temperature is another

[1] *A version of this chapter has been published. N. Dalili, P. Li, M. Kupsta, Q. Liu, D.G. Ivey, Micron, DOI: 10.1016/j.micron.2013.11.002.*

encountered issue [2]. The formation and the growth of voids at the Cu/diffusion barrier interface have been observed with *in-situ* heating temperatures as low as 200°C which consume the Cu film, leaving small particles of Cu behind [5,6]. This behavior is attributed to stress-assisted diffusion of Cu along grain boundaries as a result of constraint from the substrate [5]. The thermal stresses occurred due to the difference in the thermal expansion coefficients of the elements in the stack.

The objective of this chapter is to understand and analyze the atomic diffusion mechanisms responsible for metallurgical failure of $Si/TaRh_x/Cu$ metallization stacks using *in-situ* heating in the TEM. A new sample preparation technique was developed to address the challenges associated with *in-situ* heating of Cu in a TEM.

5.2 Materials and methods

Amorphous $Ta_{0.55}Rh_{0.45}$ films were co-sputtered from two pure targets (Ta and Rh) onto n-type, <100> oriented Si wafers using an AJA ORION8 DC magnetron sputtering system. The substrate cleaning procedure and the deposition conditions are explained in Section 4.2. The average thicknesses of deposited $TaRh_x$ layers were 13 nm and 43 nm, as measured from cross-sectional TEM observation. Copper films, 203-207 nm in thickness, were deposited on the barrier afterward without breaking the vacuum. *Ex-situ* metallurgical characterization of barriers was performed by annealing in a tube furnace under flowing 5% H_2/95% N_2 gas for 30 min at various temperatures ranging from 400 to 600°C. The reaction morphology was assessed by grazing incidence XRD, four point probe resistivity measurements and TEM observations and the results are discussed in Chapter 4. *In-situ* TEM investigations were performed using cross-sectional TEM specimens prepared from as-deposited samples. A Hitachi NB5000 dual beam FIB/SEM was used and the details of sample preparation is given in Section 3.2. Prior to performing in-situ heating in the TEM, a layer of C was deposited onto the polished surfaces in order to suppress surface diffusion, void formation and evaporation of Cu. The C layer was deposited by one of the two methods:

sputtering (hereafter referred to as C1) using a Gatan 682 precision etching and coating system with an 8 keV Ar ion beam and a base pressure of 6.67×10^{-3} Pa (5×10^{-5} torr) at a deposition rate of 0.01 nm/s or through electron beam evaporation (hereafter referred to as C2) on a Kurt J. Lesker PVD75 electron beam evaporator with a base pressure of 6.67×10^{-4} Pa (5×10^{-6} torr) and a deposition rate of 0.02 nm/s. Both surfaces of the TEM lamella were coated with C. The approximate thicknesses of the deposited C layers were 5 nm and 10 nm, which were measured by a crystal deposition rate monitor. As a control, some samples did not receive a protective C layer coating on the polished surface.

In-situ heating experiments were performed with two microscopes: 1) a Hitachi H-9500 environmental TEM (ETEM) operated at 300 kV with a Hitachi double-tilt heating holder and 2) a JEOL 2200 FS TEM/STEM operated at 200 kV with a Gatan 628 single tilt heating holder. Characterization of the reaction morphology was performed by EDX spectroscopy and electron diffraction analysis in the JEOL microscope. The nominal probe size for analytical microscopy was 1.5 nm. Initial *in-situ* heating of the samples was conducted from room temperature to 500°C at a rate of 50°C/min. Subsequently, samples were heated at a rate of 5°C/min and were kept isothermally for 10-20 min at temperature intervals of 50°C. Once the reaction started, the temperature was maintained constant for prolonged times (35 - 102 min). The relevant time durations are stated throughout this chapter where applicable. Image series were recorded automatically using Gatan DigitalMicrograph^{TM} script at an average collection rate of 1 frame per 2 s. All images during heating were recorded in BF mode and were processed using DigitalMicrograph^{TM}. The surface topography of some of the *in-situ* annealed samples was inspected after annealing using an in-lens, cold FEG electron source, ultrahigh resolution SEM (Hitachi S5500) operated at 5 kV accelerating voltage. The composition of the surface of some of the samples was studied after *in-situ* annealing using a JEOL Auger scanning microprobe (JAMP 9500F) to identify surface diffusing species.

5.3 Results and discussions

5.3.1 Evolution of TEM sample design

The first set of heating experiments was conducted on cross-sectional TEM lamellae of Si/(13 nm)$TaRh_x$/Cu stacks. The general features of the as-deposited samples are shown in Figure 5–1(a) and were similar for all samples without annealing. The Cu layer showed a predominantly columnar structure with a number of twinning defects. The amorphous nature of the $TaRh_x$ film is discussed in Chapter 4. Upon isothermal annealing at 450°C, grain growth occurred in the Cu layer resulting in the formation of a single Cu grain across the lamella. This was followed by nucleation and propagation of voids in the Cu layer after 34 min at 550°C, as shown by the sequence of BF images in Figure 5–1(b). The void advanced approximately 240 nm in a period of 10 s indicating the fast flux of atoms. Further heating of the samples resulted in delamination of the $TaRh_x$/Cu stack from the Si substrate. Dehm *et al* [7] analyzed the stress-temperature behavior of a 500 nm thick Cu film sputtered onto 500 µm Si wafers coated with a 50 nm amorphous SiO_x layer and a 50 nm SiN_x layer and concluded that the as-deposited Cu film was in a biaxial tensile stress state. Thermal annealing at temperatures above 240°C relaxed the tensile stress and created compressive stress in the film [7]. In conjunction, An and Ferreira [5] observed void formation in 180 nm Cu interconnects upon *in-situ* heating at temperatures as low as 250°C and attributed this to the residual tensile thermal stresses that occurred during fabrication. Therefore, it can be inferred that increasing the temperature relaxes the tensile stresses and simultaneously enhances void formation (assisted by surface diffusion). At a critical temperature of 250°C, characteristic of the 180 nm Cu interconnects tested by An and Ferreira [5], the tensile stresses are sufficiently high and surface diffusion is rapid enough that voids can be formed [5]. To suppress surface diffusion and therefore prevent formation of voids, both surfaces of the lamella were coated with 5 nm of C (C1 or C2). Carbon was chosen as it forms no stable compounds with Cu and the solubility of C in Cu is extremely low. Therefore, C is expected to remain stable at elevated temperatures in contact with Cu [8]. In addition, C is a light element and therefore has a relatively small

Rutherford scattering cross-section. In other words, a 5-10 nm thick C film is expected to have negligible effect on the mass/thickness contrast of the lamellae. Additionally, the sputtered and/or evaporated C films for this study are amorphous and, therefore, do not contribute to the diffraction contrast of the encapsulated lamella. However, surface diffusion and void formation was not prevented, so that 5 nm of C film was insufficient.

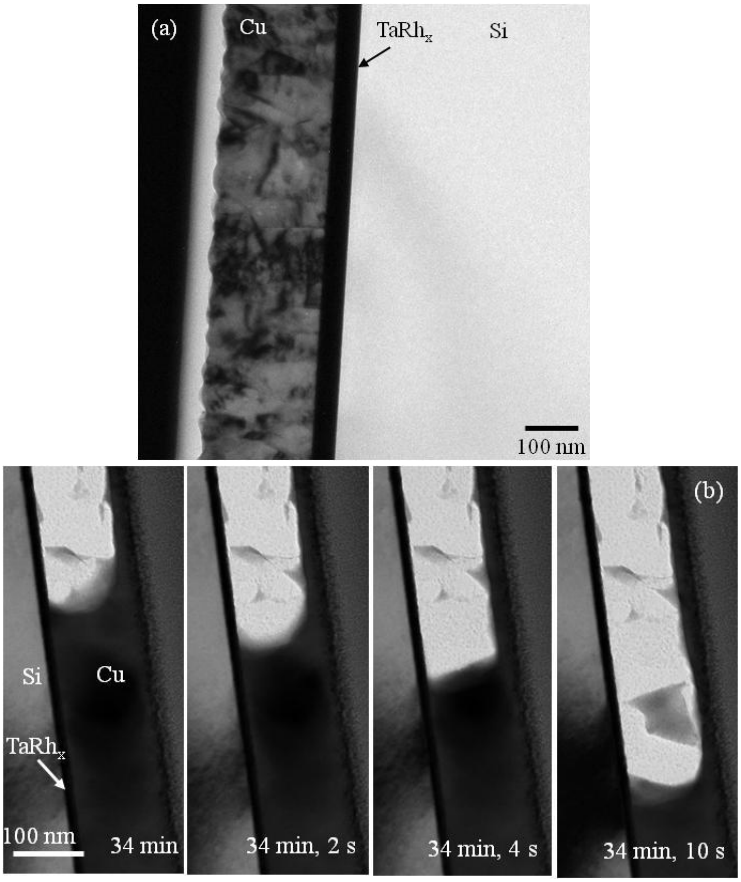

Figure 5–1 (a) TEM BF micrograph of as-deposited Si/(43 nm)$TaRh_x$/Cu prepared by FIB. (b) Sequence of BF TEM micrographs of Si/(13 nm)$TaRh_x$/Cu sample showing void growth during *in-situ* heating at 550°C.

For Si/(43 nm)$TaRh_x$/Cu stacks, grain growth of Cu was delayed to higher temperatures, *i.e.*, 700°C, and void formation was not observed. A thicker $TaRh_x$ film, therefore, alters the magnitude and distribution of residual thermal stresses in the Cu film, thereby relaxing the stresses that caused void formation in Si/(10 nm)$TaRh_x$/Cu stacks. The series of images in Figure 5–2 shows a selected area of

the Si substrate after isothermal heating at 750°C for 1002 s recorded at time intervals of 4 s. The composition of the diffusing species was determined by EDX analysis. The sequence of BF images shows fast movement of the Cu species over the Si. It is evident that Cu does not readily form silicides with Si as it moves freely like a two-dimensional liquid on the Si surface, forming mobile islands that disappear to reform on other parts of the surface (marked by the arrows on Figure 5–2). The extent of diffusion of Cu over Si after *in-situ* heating at 750°C for 35 min and cooling down to room temperature is shown in the BF image in Figure 5–3(a). Some of the Cu clusters on Si surface are marked by arrows in Figure 5–3. To distinguish between surface and bulk diffusion phenomena, the surface topography of *in-situ* annealed sample was imaged using an in-lens, cold FEG SEM and the surface composition was determined using AES. AES was chosen since Auger electrons originate from the top 5 – 10 nm of the surface, which makes this method particularly suited for analysis of nanoscale surface particles [9]. A secondary electron (SE) image of the sample surface, taken at 5 kV accelerating voltage, is shown in Figure 5–3(b). The sample is tilted 40° relative to the electron beam. It is evident that the $TaRh_x$ barrier and the Si substrate are covered with particles that are protruding from the surface. AES analysis revealed that the particles are rich in Cu and are within the top 5 – 10 nm of the surface. Copper, therefore, diffuses on the surface rather than through the bulk of the $TaRh_x$ layer.

It has been previously observed that Cu diffuses rapidly on amorphous C and graphite substrates when exposed to a combination of low pressure and either high temperature (higher than 600°C) or under intense electron beam radiation [2-4]. This behavior can be attributed to the small activation energy for diffusion of Cu on the surface of C and/or the relatively high vapor pressure of Cu [10,11]. Zhang and Su [12] studied the stability of Cu grids coated with amorphous C or Si oxide films. The formation of Cu nanoparticles was observed after heating the Cu grids with amorphous C as the support film. In contrast to C films, surface diffusion of Cu was not observed during *in-situ* heating of a Cu grid with amorphous Si oxide as the support film. This behavior was attributed to the

interaction of Cu with Si oxide [12]. The solubility of Cu in Si is extremely low (maximum solubility of 0.002 at% Cu between 1200 and 1300°C) but Cu readily interacts with Si at temperatures as low as 200°C. The equilibrium phase precipitated from a Si matrix supersaturated with Cu is reported to be Cu_3Si (T_m = 853°C), which is stable at the maximum temperature of the *in-situ* heating experiment in this study (750°C) [13]. Copper is, therefore, expected to form Cu_3Si upon interaction with Si at this temperature. Surface diffusion of Cu on clean bulk Si has been studied extensively. Ikeda *et al* ([14,15]) studied the surface diffusion mechanism for Cu/Si surfaces and observed that Cu does not diffuse directly along the surface of Si. Instead Cu dissolves and diffuses through the bulk of Si. This is followed by segregation of Cu atoms onto the surface of Si [14,15]. It should be noted that ion beam bombardment during FIB sample preparation modifies the surface of Si and is known to disturb the original crystal structure and composition of the Si surface [16]. Therefore, the interaction between Cu and this modified Si layer is expected to be different from Cu/Si interaction with a clean Si surface. Thus the surface diffusion mechanism reported in [15,17] is not the dominant mechanism for the FIB-prepared lamella without the C coating. Copper diffuses rapidly on the FIB damaged Si surface and the formation of Cu-silicides was not observed on the surface. Therefore, in the uncoated case, it appears that diffusion of Cu is dominated by surface diffusion rather than diffusion through the bulk of the $TaRh_x$ and Si layers, which does not represent the diffusion mechanism seen in bulk metallization stacks. This result justified the need for a modified sample preparation technique that provided sample encapsulation while permitting the reaction to be observed in the TEM during *in-situ* heating.

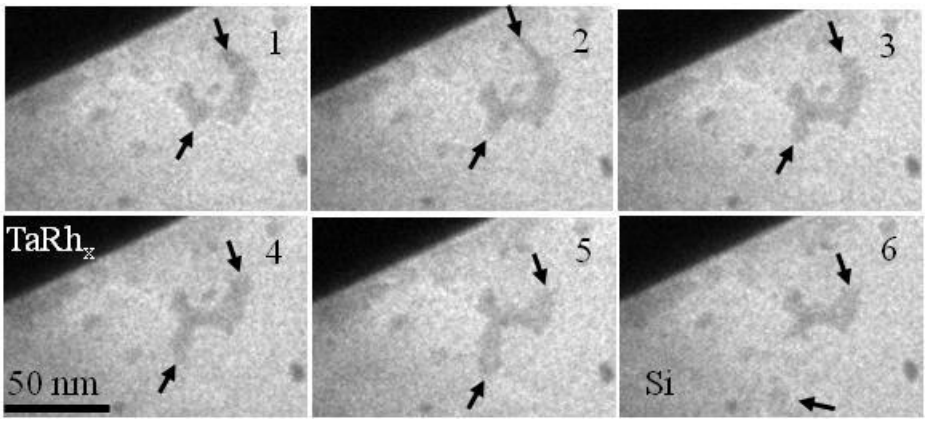

Figure 5–2 Series of BF TEM micrographs of Si/(43 nm)TaRh$_x$/Cu sample showing rapid surface diffusion of Cu on the surface of Si during *in-situ* heating at 750°C. Image 1 was recorded after isothermal heating for 16 min and 42 s. Images 2-6 were recorded at time intervals of 4 sec. Some of the Cu clusters on the Si surface are marked by the black arrows.

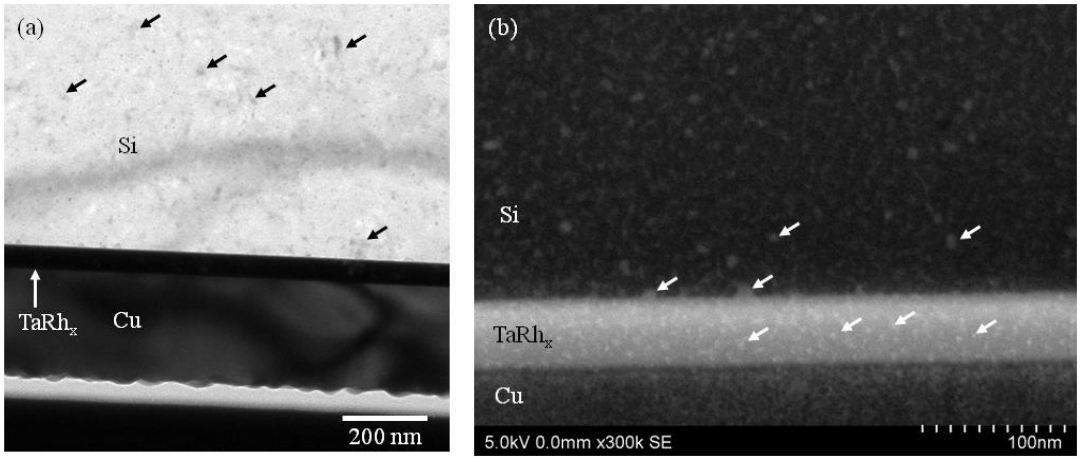

Figure 5–3 (a) Room temperature BF TEM micrograph of Si/(43 nm)TaRh$_x$/Cu sample after *in-situ* annealing at 750°C for 35 min showing the extent of diffusion of Cu on Si surface and the single crystalline nature of the Cu film. Some of the Cu clusters on the Si surface are marked by the black arrows. (b) Room temperature SE micrograph of Si/(43 nm)TaRh$_x$/Cu sample after *in-situ* annealing at 750°C for 35 min revealing surface diffusion of Cu on TaRh$_x$ and Si layers, as evidenced by the particles protruding from the surface. The particles are marked by the white arrows on the micrograph. The image was taken at 40° tilt relative to the electron beam.

To circumvent the issue of surface diffusion, Si/(43 nm)$TaRh_x$/Cu lamellae were coated with 5-10 nm of C (sputtered (C1) or electron beam evaporated (C2)). Both thicknesses of the C1 film (5 and 10 nm) and the thin C2 film (5 nm) were ineffective in preventing surface diffusion of Cu and showed features similar to samples with no C layer. The lamellae with a thick C2 layer (10 nm) on both surfaces, however, successfully prevented surface diffusion of Cu. The underlying mechanisms responsible for the effectiveness of the C2 film and the ineffectiveness of the C1 film are not clear and require further investigation. Regardless, a 10 nm thick C2 coated lamella was stable during *in-situ* heating experiments and provided evidence for the diffusion mechanism of Cu though the barrier layer, which is discussed in the following section.

5.3.2 Diffusion mechanism and compound growth

The Si/(43 nm)$TaRh_x$/Cu lamellae coated with 10 nm of C2 film on both sides remained stable upon *in-situ* isothermal heating at 750°C for about 50 min. No void formation, grain growth or surface diffusion of Cu was observed in these samples. Deposition of 10 nm of C2 film, therefore, successfully addressed the issues related to *in-situ* heating of Cu in a TEM column. The first indication of diffusion/reaction was observed after heating to 750°C for 52 min as shown in the series of BF images (from the same region) in Figure 5–4. Images 1-3 were recorded at a time interval of 200 s, while image 4 shows the same particle after prolonged isothermal heating (102 min). Figure 5–5(a) shows the same particle (the first particle to form and therefore the largest) and corresponding EDX line scan profiles superimposed on the image. The profiles indicate the variation in intensity for the $TaL_{\beta 3}$, SiK_{α}, $RhL_{\alpha 1}$ and $CuL_{\alpha 1\text{-}2}$ signals at each point of the scan. It should be noted that the SiK_{α} signal overlaps with the TaM_{α} signal and, therefore, the intensity of the SiK_{α} profile has to be analyzed in combination with the variation in the TaL_{β} signal. The line scan profile reveals that the particle actually consists of two grains, *i.e.*, a Cu-silicide (left side) and a Rh-silicide (right side). The crystal structure of the Rh-silicide was confirmed using nanodiffraction. A BF micrograph of the Rh-silicide grain tilted to a strongly diffracting condition, together with a diffraction pattern obtained using a 1.5 nm

nominal size probe, is shown in Figure 5–5(b). The pattern can be indexed as close to the [5̲33] zone axis of orthorhombic RhSi [18]. It can be seen that the Cu-silicide grain has been damaged during the EDX line scanning process and, as such, a nanodiffraction pattern was not collected from this grain.

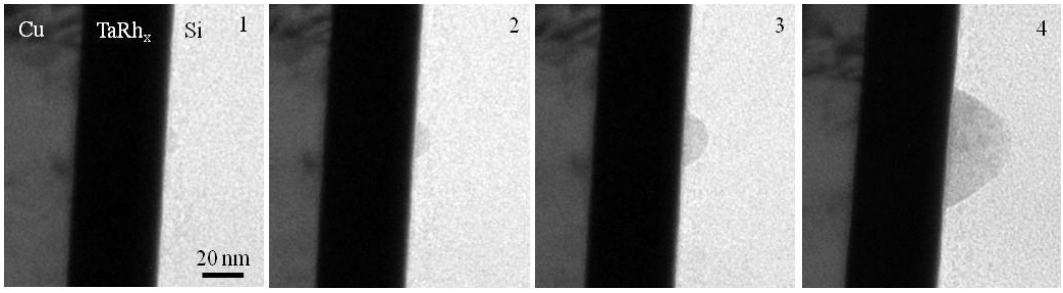

Figure 5–4 Series of BF TEM micrographs of Si/(43 nm)TaRh$_x$/Cu lamella coated with 10 nm of C2 film on both surfaces and then heated *in-situ* at 750°C for (1) 52 min, (2) 55 min and 20 s, (3) 58 min and 40 s and (4) 102 min. The series shows the nucleation and growth of a protrusion at the TaRh$_x$/Si interface.

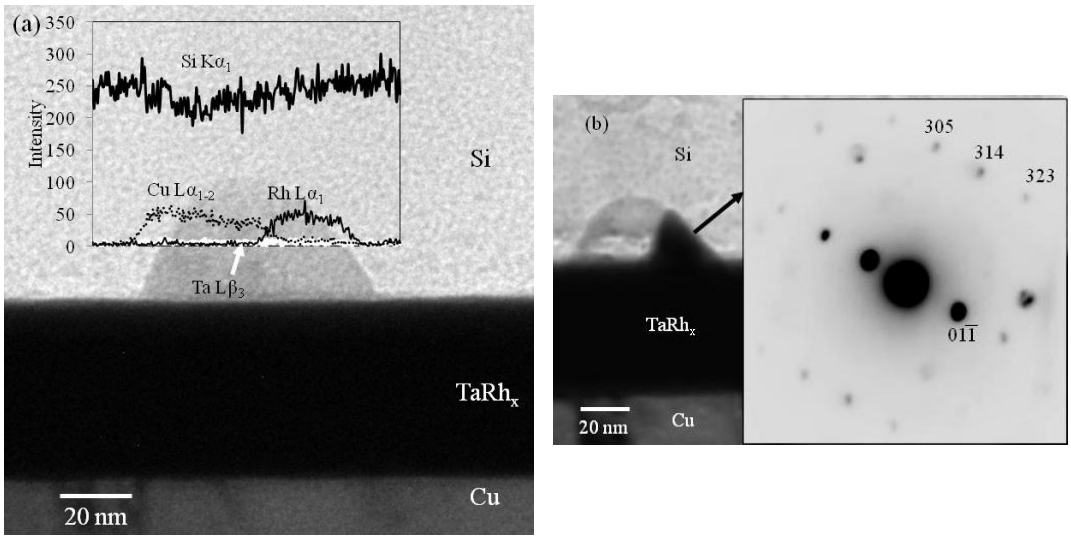

Figure 5–5 (a) BF TEM micrograph of the first particle to nucleate and grow on Si/(43 nm)TaRh$_x$/Cu lamella coated with 10 nm of C2 on both surfaces after *in-situ* heating at 750°C for 102 min. EDX line scan profiles for TaL$_{\beta 3}$, SiK$_\alpha$, RhL$_{\alpha 1}$ and CuL$_{\alpha 1\text{-}2}$ signals are superimposed on the micrograph. (b) Nanodiffraction pattern taken from the Rh-rich grain component of the particle shown in (a); the grain is indexed to orthorhombic RhSi near the [5̲33] zone axis.

EDX line scanning was also performed on other particles at their initial stages of nucleation and growth. One such particle and the corresponding line scan profile are shown in Figure 5–6(b). As can be seen, the particle consists mainly of Rh and Si (*i.e.*, Rh silicide). These observations reveal the diffusion/failure mechanism responsible for the failure of the $TaRh_x$ barriers. Failure begins by reaction of Rh with the Si substrate to form RhSi, which results in the formation of areas of low density in the $TaRh_x$ layer. Copper can diffuse through these low density areas reaching the Si substrate to form Cu-silicides.

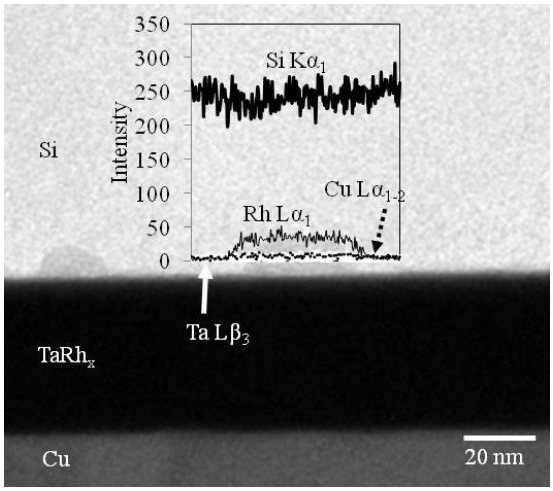

Figure 5–6 BF TEM micrograph of a smaller particle at an earlier stage of growth on Si/(43 nm)$TaRh_x$/Cu lamella coated with 10 nm of C2 on both surfaces, after *in-situ* heating at 750°C for 102 min. Also shown are EDX line scan profiles for $TaL_{\beta 3}$, SiK_{α}, $RhL_{\alpha 1}$ and $CuL_{\alpha 1\text{-}2}$ signals superimposed on the micrograph.

Ex-situ metallurgical characterization of barriers was performed by annealing a bulk Si/(13 nm)$TaRh_x$/Cu sample in a tube furnace under flowing 5% H_2/95% N_2 gas for 30 min at various temperatures as previously reported in Chapter 4. Figure 5–7(a) shows a BF micrograph of the Si/(13 nm)$TaRh_x$/Cu sample after annealing at 550°C. As explained in Section 4.4.2, the composition and crystalline structure of the reacted morphology were identified by EDX and electron diffraction analysis. The large, near trapezoidal shape particles were indexed to either orthorhombic η´´-Cu_3Si [19] or hexagonal Cu_3Si [20]. These particles were separated from the Si substrate by an amorphous Si oxide layer. The $TaRh_x$/Si

interface at locations away from the Cu_3Si particles showed evidence of reaction and formation of several particles (marked by an arrow in Figure 5–7(a)). The morphology of these particles was similar to those found in the *in-situ* sample (arrows in Figure 5–7(b)). A selected area diffraction (SAD) pattern obtained from one of these particles is also shown in Figure 5–7(a). The pattern reveals a single-crystal array of spots that can be indexed as close to the [2$\underline{5}$1] zone axis of orthorhombic RhSi [18].

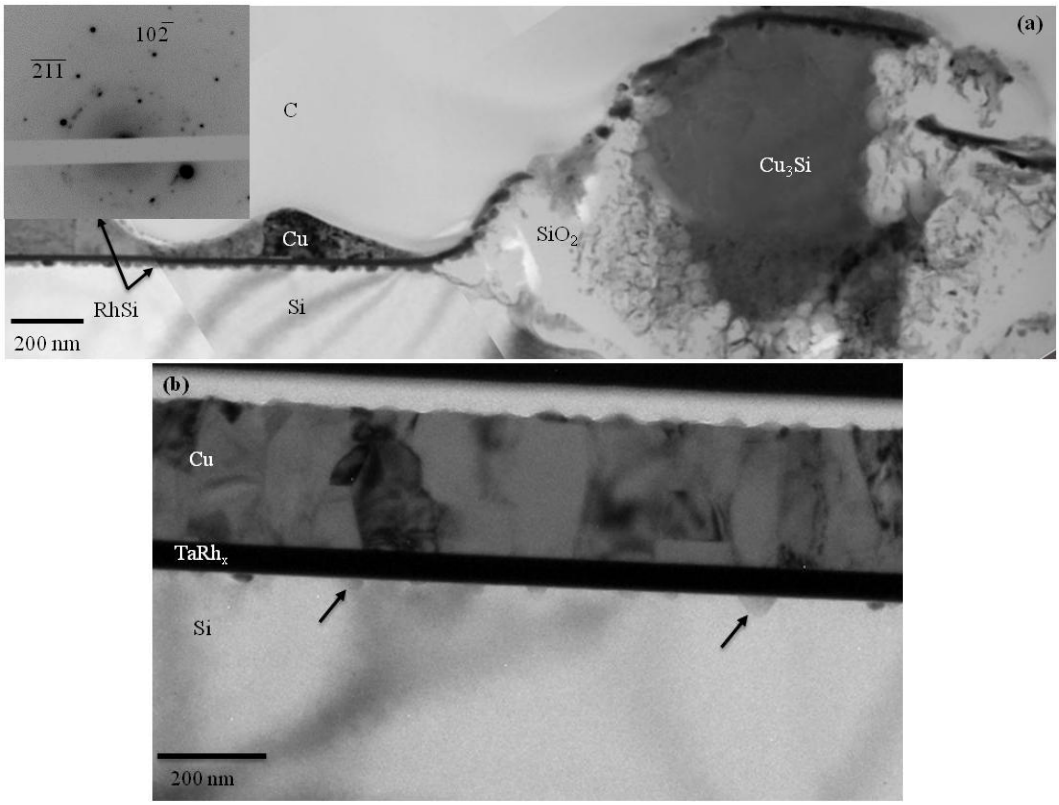

Figure 5–7 (a) Cross-sectional BF TEM micrograph of Si/(13 nm)$TaRh_x$/Cu sample showing the complex reaction morphology after *ex-situ* annealing at 550°C for 30 min. The SAD pattern is collected from an orthorhombic RhSi particle near the [2$\underline{5}$1] zone axis. (b) Room temperature BF TEM micrograph of Si/(43 nm)$TaRh_x$/Cu lamella coated with 10 nm of C2 on both surfaces after *in-situ* annealing at 750°C for 102 min showing the distribution of Rh silicide particles at the Si/$TaRh_x$ interface.

Based on the above results, it can be concluded that an equivalent mechanism is taking place when comparing *ex-situ* and *in-situ* heated samples (Figure 5–7(a) and (b)). The morphology of the *in-situ* sample reveals the earlier stages of

diffusion and reaction. It is evident that reaction starts with nucleation of RhSi at the $TaRh_x$/Si interface. Diffusion of Cu occurs through low density areas formed in $TaRh_x$ adjacent to the nucleation sites of RhSi particles. This results in nucleation of Cu_3Si particles. Further growth of Cu_3Si particles requires a source of mobile Cu species. The 200 nm thick Cu layer on the *ex-situ* heated bulk sample provides a source of Cu that can be assumed infinite in two-dimensions. The Cu layer at areas surrounding the Cu_3Si particles is, therefore, depleted as can be seen in Figure 5–7(a) in the process of Cu_3Si growth. In comparison, the TEM lamella used for *in-situ* heating only provides a limited source of Cu due to its thin nature, resulting in restricted growth of the Cu_3Si particles. Additionally, the *in-situ* experiments were performed with a thicker barrier layer (*i.e.*, 43 nm for *in-situ* and 13 nm for *ex-situ*). A higher annealing time or temperatures is required for the diffusion species to travel the longer diffusion distance associated with the thicker barrier. This explains the difference in the failure temperature of the two experiments, *i.e.*, 750°C for *in-situ* and 550°C for *ex-situ* samples. Despite these dissimilarities, the TEM sample preparation method presented here successfully addresses the issues related to *in-situ* heating of a TEM cross-section containing thin films of Cu. The *in-situ* heating experiment on this sample provides important information on diffusion/reaction mechanisms responsible for failure of $TaRh_x$ diffusion barriers. This method of sample preparation and *in-situ* heating experiments can be applied to studying other potential barriers.

5.4 Conclusions

In-situ TEM heating was used for direct observation of atomic diffusion mechanisms involved in the failure of diffusion barriers. This work demonstrates and addresses the common issues related to *in-situ* TEM heating of Cu metallization stacks. Void formation in the Cu layer and delamination of the Si substrate from $TaRh_x$ films were the dominant features of *in-situ* heated Si/(13 nm)$TaRh_x$/Cu stacks. These processes occurred prior to any diffusion and/or reaction between layers. Encapsulating the TEM lamella with a 5 nm C film had a negligible effect on the nature of residual stresses in the films and was proven ineffective. In contrast, the Si/(43 nm)$TaRh_x$/Cu stacks showed no indication of

delamination. For the non-encapsulated case, Cu diffused over the $TaRh_x$ layer and on the Si surface instead of diffusing though the bulk of the barrier layer. To obstruct the rapid surface diffusion of Cu, C films were deposited on the TEM lamellae after FIB sample preparation and prior to *in-situ* heating. Carbon with an approximate thickness of 10 nm, deposited by electron beam evaporation, successfully prevented diffusion of Cu along the surface. Failure of the barrier was triggered by nucleation of RhSi particles at the $TaRh_x$/Si interface. Diffusion of Cu through the $TaRh_x$ layer was facilitated by the low density areas that formed in the $TaRh_x$ layer adjacent to the RhSi nucleation sites. Copper reacted with Si to nucleate and grow Cu silicide particles. The morphology of the *in-situ* annealed samples was similar to that encountered in *ex-situ* bulk annealed Si/(13 nm)$TaRh_x$/Cu stacks. The density and size of the particles were smaller in the *in-situ* heated samples due to the limited source of the diffusion species. Additionally, a thicker barrier layer was used for the *in-situ* heating experiments resulting in a higher failure temperature for the *in-situ* experiments. The designed *in-situ* heating experiments successfully reproduced the bulk reaction mechanisms and the sample preparation method and the *in-situ* heating experiments of this work provide a useful tool for studying the atomic diffusion mechanisms responsible for failure of diffusion barriers.

5.5 References

[1] S.-. Wang, MRS Bull. **19**, 30-40 (1994).
[2] D. Kiener, Z. Zhang, S. Šturm, S. Cazottes, P.J. Imrich, C. Kirchlechner, G. Dehm, Philos. Mag. **92**, 3269-89 (2012).
[3] Z. Liu, Y. Bando, Adv. Mater. **15**, 303-5 (2003).
[4] P.-. Wang, Y.-. Zhao, G.-. Wang, T.-. Lu, Nanotechnology. **15**, 218-22 (2004).
[5] J.H. An, P.J. Ferreira, Appl. Phys. Lett. **89**, 151919.1-3 (2006).
[6] M. Martinez, M. Legros, T. Signamarcheix, L. Bally, S. Verrun, L. Di Cioccio, C. Deguet, Thin Solid Films. **530**, 96-9 (2013).
[7] G. Dehm, D. Weiss, E. Arzt, Mater. Sci. Eng. A. **309-310**, 468-72 (2001).
[8] ASM Handbook, Vol. 3 Alloy Phase Diagram (ASM International, USA, 1992).
[9] C.C. Chang, Surf. Sci. **25**, 53-79 (1971).
[10] R.E. Honig, D.A. Kramer, Nanotechnology. **30**, 285-305 (1969).
[11] J.R. Arthur, A.Y. Cho, Surf. Sci. **36**, 641-60 (1973).
[12] Z. Zhang, D. Su, Ultramicroscopy. **109**, 766-74 (2009).
[13] R.W. Olesinski, G.J. Abbaschian, Bull. Alloy Phase Diagr. **7**, 170-8 (1986).
[14] T. Ikeda, Y. Kawashima, H. Itoh, T. Ichinokawa, Surf. Sci. **342**, 11-20 (1995).
[15] T. Ikeda, T. Watanabe, H. Itoh, T. Ichinokawa, Surf. Rev. Lett. **3**, 1377-85 (1996).
[16] T.L. Matteson, S.W. Schwarz, E.C. Houge, B.W. Kempshall, L.A. Giannuzzi, J. Electron. Mater. **31**, 33-9 (2002).
[17] A.E. Dolbak, R.A. Zhachuk, B.E. Olshanetsky, Cent. Eur. J. Phys. **1**, 463-73 (2003).
[18] S. Petersson, R. Anderson, J. Baglin, J. Dempsey, W. Hammer, F. D'Heurle, S. Laplaca, J. Appl. Phys. **51**, 373-82 (1980).
[19] J.K. Solberg, Acta Cryst. **A34**, 684-98 (1978).
[20] N. Mattern, R. Seyrich, L. Wilde, C. Baehtz, M. Knapp, J. Acker, J. Alloy. Compd. **429**, 211-5 (2007).

6 Evaluation of $TaRh_x$ diffusion barriers using bias temperature stress[1]

6.1 Introduction

The metallurgical failure mode of amorphous $TaRh_x$ diffusion barriers is discussed in Chapters 4 and 5 using *ex-situ* and *in-situ* heating experiments. It has been established that Cu can deteriorate device performance if its bulk concentration in Si exceeds 10^{13} cm^{-3} [1]. However, the sensitivity of the techniques used for metallurgical characterization is not sufficient to detect such concentrations. It was therefore essential to employ the more sensitive electrical characterization techniques to evaluate the performance of diffusion barriers. One such method is monitoring the *C-V* characteristics of MOS capacitors as explained in detail in Section 2.8.2.1. Several studies have used MOS devices to understand the Cu transport phenomena under thermal stress [2-4] or a combination of thermal and electrical stresses [5-10]. It is important to note that the atomic flux of Cu depends on a combination of temperature and electric field [11] and it is necessary to include both in any diffusion barrier reliability test (*i.e.*, BTS). High frequency *C-V* measurements of MOS capacitors provide an effective method of detecting mobile ions in the dielectric layer. Diffusion of Cu^+ ions in the oxide under electrical and/or thermal stresses causes a negative shift in the flatband voltage, according to Equation 2-24. This equation was given for a random distribution of the volume density of charge. Assuming that all the Cu^+ ions are accumulated at the oxide/Si interface, Equation 2-24 is simplified to the following:

$$V_{FB} = -\frac{Q_{ox}}{C_{ox}} \qquad \text{Equation 6-1}$$

where Q_{ox} is the accumulated positive charge at the interface [12]. A number of studies have used this simplified model to estimate the diffusivity of Cu in various

[1] *A version of this chapter has been published. N. Dalili, D.G. Ivey, Journal of Materials Science: Materials in Electronics, DOI: 10.1007/s10854-013-1662-8.*

dielectric and diffusion barrier materials [13-15]. However, Raghavan *et al* [16] reported that Cu movement through the oxide under BTS progresses via three stages with time. In the first stage Cu neutrals and ions diffuse into the dielectric under thermal and electrical driving forces. The presence of Cu^+ ions in the dielectric results in redistribution of electric field inside the dielectric. The second stage proceeds mainly by temperature driven diffusion of ions and neutrals, which results in degradation of the dielectric and an increase in the leakage current. The third stage involves neutralization of Cu^+ ions by the previously increased electron current which allows for further injection of Cu^+ ions into the dielectric. According to this model, no significant accumulation of Cu species at the Si/SiO_2 interface occurs in the first two stages [16]. Therefore, care must be taken when using Equation 6-1 to ensure that Cu diffusion is at its final stage and has reached the Si/SiO_2 interface.

In addition to the shift in the flatband voltage, failure of the barrier and penetration of Cu^+ can also result in distortion of the *C-V* characteristics. A number of possible distortions and the related explanations are listed here: *i*) Smearing of the *C-V* curve as a result of interface states created by Cu at the Si/SiO_2 interface [12]; *ii*) an increase in the inversion capacitance, to a value similar to low frequency measurements, as a result of the deep level states generated by Cu in Si and the associated reduction in the minority carrier lifetime [5,13]; *iii*) no inversion layer or deep depletion behavior as a result of the increased conductivity of the oxide. This allows for the leakage of minority carriers though the oxide and, consequently, an inversion layer cannot be maintained [17].

The main focus of this chapter is to evaluate the electrical failure mode of $TaRh_x$ diffusion barriers by BTS stressing of MOS test structures. The stability of these barriers is compared with the stability of MOS test structures with amorphous TaN_x barriers and with no barrier. The *C-V* characteristics of the MOS devices are studied in detail and compared with depth profiling information and cross-sectional TEM observations.

6.2 Materials and methods

Barrier test structures were prepared using n-type, 4'' (100 mm) diameter, <100> Si wafers coated with a 25 nm thick thermally grown SiO_2 film. The Si wafers were cleaned in a standard RCA clean prior to oxidation to remove the organic residue and the native oxide. After cleaning a high quality oxide was grown at a temperature of 1000°C in dry O_2 followed by a 40 min anneal in N_2 at the oxidation temperature. Contact to the backside was made by locally removing the oxide with buffered HF followed by deposition of a 500 nm thick Al layer by evaporation. The oxide thickness uniformity was better than 5% across a wafer as measured at 5 different points on the wafer using a Nanospec AFT. The oxidation and backside metallization processes were performed at the Carleton University MicroFabrication Facility (CUMFF).

The effectiveness of $TaRh_x$ diffusion barriers was studied by comparing the stability of 3 different metallization stacks: *i*) $TaRh_x$/Cu, *ii*) TaN_x/Cu and *iii*) no barrier/Cu. The Al/Si/SiO_2/$TaRh_x$/Cu MOS test structures were fabricated by deposition of $TaRh_x$/Cu stacks onto the oxidized wafers. The $TaRh_x$ films with 52 at% of Ta were deposited by co-sputtering from two pure targets. The details of sputtering of $TaRh_x$ films are given in Section 4.2. $TaRh_x$ films deposited under these conditions are amorphous, as explained in Chapter 4. The average thickness of the $TaRh_x$ films was 10 nm. The thicknesses of all the as-deposited metal films in this study were measured by cross-sectional TEM. Copper films, 220-230 nm in thickness, were deposited on the barrier layer without breaking the vacuum.

Prior to deposition of metal layers photolithography was performed to define the area of capacitors. The capacitor area was 0.5 mm in radius with 3 mm spacing between adjacent capacitors. A smaller capacitor area will reduce current leakage through the oxide, while a larger capacitor area will minimize perimeter effects on the capacitance [13]. As a compromise between these two effects, a capacitor radius of 0.5 mm was chosen. A photomask was designed using the CAD software L-Edit. The photomasks were patterned at the University of Alberta NanoFab on 5 in. square soda lime glass substrates. The pattern was

generated on the photomask using a high resolution laser mask writer. The features on the photomask were defined by a Cr coating about 70 nm in thickness. The photomask were generated with a 1:1 scale for soft contact photolithography. Prior to photoresist deposition, a layer of hexamethyl disilazane (HDMS) was deposited on the substrate using a YES HDMS oven. HDMS promotes the adhesion of photoresist to the SiO_2 substrate. A layer of positive photoresist (HPR504) was then spin-coated on the oxidized wafers. The type of photoresist and its viscosity affect the resolution of the pattern features. However, since the geometry of MOS capacitors did not involve deep etching or fine features, the standard spin coating procedure outlined by the manufacturer was used. After spin coating, the photoresist was soft baked at 115°C for 90 s. The wafers were left for 10 min in the room ambient for rehydration of the photoresist. An ABM mask aligner and UV system was used to transfer the pattern to the substrates. The photoresist was exposed for 3 s. The exposed areas of the photoresist were then removed by immersing the wafer in an agitated developer solution for 25 to 30 s. The exposure and development durations are critical parameters. A long exposure or development time will degrade the features, while short exposure or development time will leave residues in the features. The exposure and duration times were determined by inspecting the surface with an optical microscope and by an Alpha step IQ profilometer after development. All the photolithography steps were performed in the class 1K cleanroom at the University of Alberta Nanofab and the wafers were transferred to the sputtering equipment for deposition of metallization layers within 24 hr. Following metal deposition, circular capacitors were delineated by placing the wafers in a sonicated acetone bath and removing the unexposed photoresist. The wafers were then cleaned in ethanol and deionized water baths, consecutively.

To distinguish between instabilities due to mere oxide effects and those due to the presence of Cu, reference capacitors with Al metal gates were fabricated following a fabrication procedure similar to that used for $Al/Si/SiO_2/TaRh_x/Cu$ test structures. Aluminum was used as a reference since Al is considered as a stable MOS metallization material on thermal SiO_2 [18]. Additionally,

Al/Si/SiO_2/Cu MOS structures (no barrier) were fabricated by a lift-off technique following the deposition of Cu. No diffusion barrier was deposited between SiO_2 and Cu layer for this latter structure. The Al/Si/SiO_2/TaN_x/Cu test structures consisted of a 10 nm thick TaN_x diffusion barrier and 290 nm thick Cu dots, which were deposited by sputtering though a shadow mask with 0.5 mm radius holes. Details of the deposition conditions for TaN_x/Cu MOS capacitors are given in Chapter 3. The Al/Si/SiO_2/TaN_x/Cu test structures were deposited in the Micralyne MEMS Foundry.

Prior to BTS, as deposited capacitors were annealed in a tube furnace at 300°C for 30 min in 5% H_2/95% N_2 ambient. Kizil *et al* [7] showed that appropriate thermal annealing prior to BTS is crucial for reproducible *C-V* measurements. It is known that low-temperature annealing in H_2 ambient removes most of process-related oxide-trapped charges and the interface charges. The *C-V* measurements presented in Chapter 3 were performed without proper pre-annealing treatment and the BTS testing was performed in room ambient. These testing conditions resulted in inconclusive results and demonstrated the necessity of improving the experimental design. To achieve this, an electrically grounded, light-tight probe station setup was designed within our laboratory. This setup is capable of stressing 50 devices simultaneously under a controlled environment. The top view image and a schematic of various parts of the setup are shown in Figure 6–1(a) and (b), respectively. The heating stage was stationed inside a stainless steel vacuum chamber (part 1). The stage consisted of a 1 cm thick Cu plate (part 2) which was machined and attached to the resistive heating element (part 3). The temperature controller was positioned outside the chamber and the leads of the thermocouple were transferred through the vacuum chamber wall using a Type K thermocouple feed through (part 4). The wafers were diced into square pieces with 50 capacitors. The wafer was positioned directly on the Cu plate with the capacitors facing up. Connections to the individual capacitors were made by spring-loaded connector pins (part 5). The pins were attached to a Cu plate (part 6) with spacings similar to that of the capacitors. The connectors pins were aligned with the capacitors using four alignment holes that were machined

though the plate (part 7). The wafer was sandwiched between the heating stage and the connector plate using 4 screws (part 8). This configuration puts the gate in contact with the connector plate and the substrate in contact with the heating stage. A multi-pin threaded feedthrough was used to connect the connector plate and the heating stage to the DC power supply system outside the chamber. The chamber was sealed prior to introducing 5% H_2/95% N_2 gas. The inlet and outlet tubes are marked on Figure 6–1. The chamber was purged with forming gas for 30 min prior to heating the stage. This setup allowed for testing of 50 devices simultaneously under a controlled environment.

BTS was performed under 2 MV/cm positive bias applied to the gate metal (connector plate at 5V and the heating stage grounded) at temperatures of 150°C and 200°C for various times. The capacitors remained under bias while cooling to prevent back-diffusion of Cu^+ ions. To perform statistical analysis of the *C-V* behavior, a total of 44 to 46 MOS devices were tested at each BTS condition. In order to distinguish between device degradation due to thermal stress and due to the additional electric field, some of the devices were merely subjected to thermal stress (TS). The room temperature *C-V* characteristics of each device were examined before and after BTS using an HP4156 semiconductor analyzer. *C-V* measurements were conducted with a DC signal sweeping from -9 V to 3 V and a superimposed AC signal of 10 mV and 1 MHz frequency. The main observations in the *C-V* measurements were the flatband voltage, the smearing of the depletion region and the inversion capacitance.

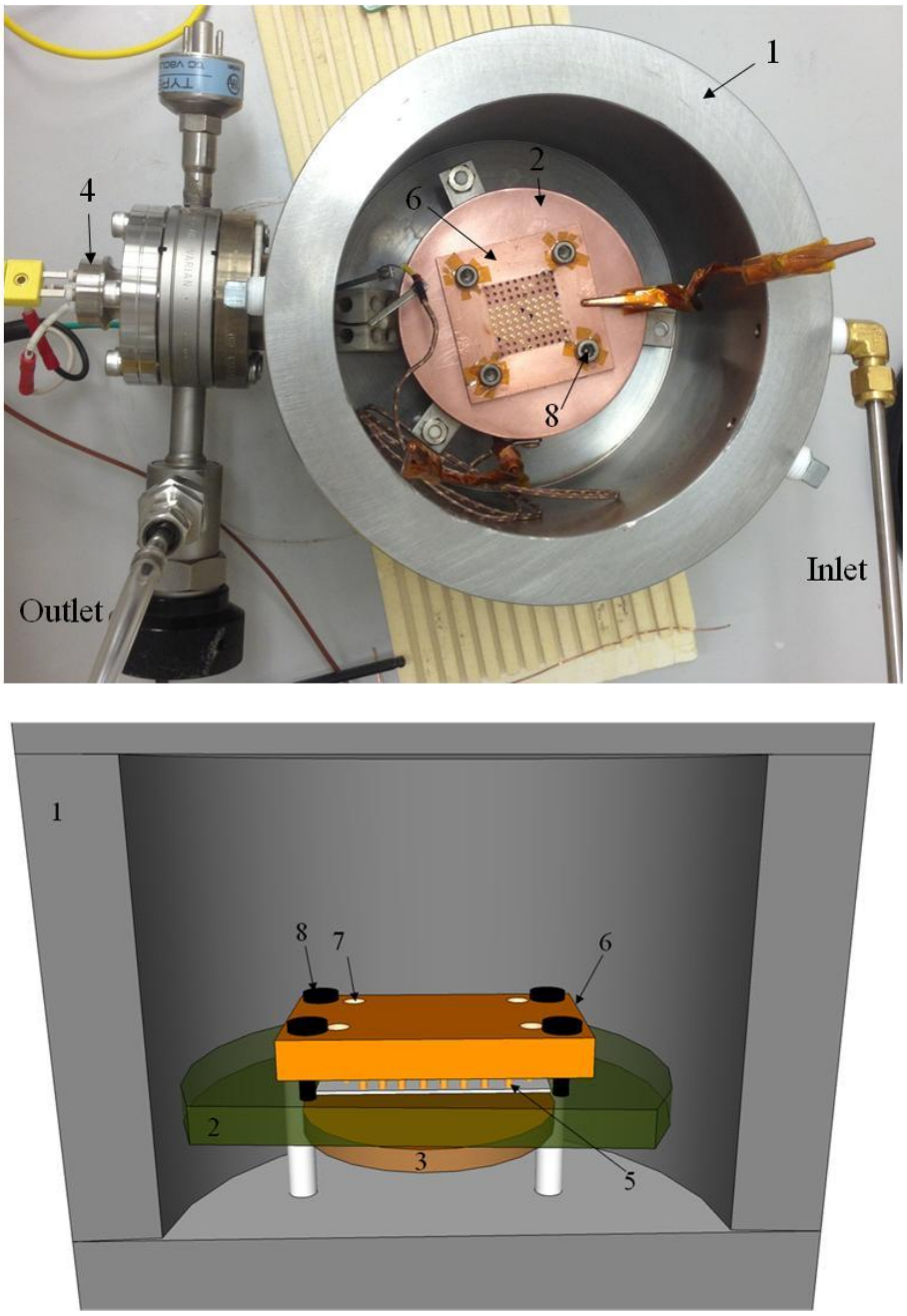

Figure 6–1. (a) Top view of the probe station used for BTS testing and (b) a schematic showing the various parts of the setup. 1) Stainless steel vacuum chamber, 2) heating stage, 3) heating element, 4) thermocouple feed through, 5) connector pins, 6) connector plate, 7) alignment holes and 8) screws to ensure proper contact.

The structure and morphology of the MOS test structures were characterized by cross-sectional TEM observations and SIMS depth profiling. The cross-sectional TEM samples were prepared by FIB following the procedure outlined in

Section 3.2. TEM analysis was done with a Philips CM20 TEM/STEM instrument operated at 200kV and equipped with an EDX spectrometer. SIMS depth profiling was performed on both the top and backside of the wafer. Prior to topside SIMS depth profiling, the Cu layer was removed by chemical etching to prevent knock-on of Cu into Si caused by ion bombardment. Prior to backside SIMS depth profiling, the wafers were diced into individual MOS capacitors. Access to the oxide and barrier layer was obtained by removal of the Si substrate from the backside. The sample was prethinned by mechanical polishing from the backside to an approximate thickness of 100 µm. A Fischione model 160 specimen grinder was used to ensure that the interfaces and the polished backside remained parallel. The sample was then glued to a glass slide, using epoxy M-bond 610 adhesive, with the Cu side down. During curing, the sample was held in place on the glass slide, using small weights. After the epoxy was cured, a second layer of epoxy was added to cover the edges of the sample to prevent sidewall etching. The remaining Si layer was then removed by an anisotropic deep reactive ion etching process using a continuous SF_6 and O_2 plasma at cryogenic temperatures (-110°C). This process was used since it provides a high etch selectivity of Si relative to SiO_2. The thicknesses of the initial and the remaining Si layer were monitored using an Alpha step IQ profilometer. The etching process was stopped when the Si layer was completely removed and the SiO_2 layer was exposed. Depth profiling was performed with a SIMS-TOF IV instrument (ION-TOF GmbH). The analytical Bi^+ ion source was operated at 25 kV and the sputtering Cs^+ ion source was operated at 0.25 kV bias. Secondary ions were collected from a 40 × 40 μm^2 area and the sputtered crater was about 300 × 300 μm^2 in size. Electron beam charge neutralization was used to prevent charging of the insulating SiO_2 layer.

6.3 Results and discussions

6.3.1 Capacitance measurements

Typical normalized *C-V* curves for the MOS capacitors with $TaRh_x$/Cu gate metallization before and after BTS at 2 MV/cm and 200°C for various times are

presented in Figure 6–2(a). The curve for $TaRh_x$/Cu gate capacitors after TS at 200°C for 180 min is also presented. Normalized capacitance was used to emphasize the flatband voltage shift and the change in the slope of depletion region. The curves presented here are representative of the 44 to 46 MOS devices that were tested under each condition, excluding the distorted curves. Distortion of the *C-V* characteristic makes it difficult to calculate the flatband voltage shift [19]. No significant flatband voltage shift was observed for thermal annealing. Copper, therefore, did not diffuse under thermal stress alone and the structure remained stable. Following BTS, the flatband voltage shifted to more negative values and an increasingly more negative flatband voltage value was obtained for longer BTS times. As mentioned before, transport of positive charge in the oxide results in a negative shift in the flatband voltage [12]. This shift can be attributed to Cu^+ or mobile alkali ions such as Na^+. To separate the effect of mobile alkali ions and Cu^+, reference capacitors with $TaRh_x$/Al gate metallization were subjected to BTS at 2MV/cm at 200°C for 90 min and the normalized *C-V* curves are shown in Figure 6–2(b). For Al gate capacitors a flatband voltage shift of 0.10±0.05 V was determined, whereas for Cu gate capacitors subjected to the same biasing condition a flatband voltage shift of 1.04±0.06 V was determined. Aluminum does not diffuse in thermally grown SiO_2 and the observed shift for $TaRh_x$/Al gate capacitors can be attributed to the presence of mobile alkali ions. Therefore, 0.94 V (1.04 V - 0.10 V) of the flatband voltage shift observed for $TaRh_x$/Cu gate capacitors (Figure 6–2(a)) can be attributed to the diffusion of Cu into the dielectric. This reference value for mobile alkali ions was used for all capacitors to separate the effect of Cu^+ ions from mobile alkali ions. All the flatband voltage shift values reported henceforth are obtained by subtracting the flatband voltage shift for Al reference capacitors from the measured value. No smearing of the *C-V* characteristics was observed for $TaRh_x$/Cu gate capacitors, which indicates that diffusion of Cu does not create interface-trapped charges at the Si/SiO_2 interface [12].

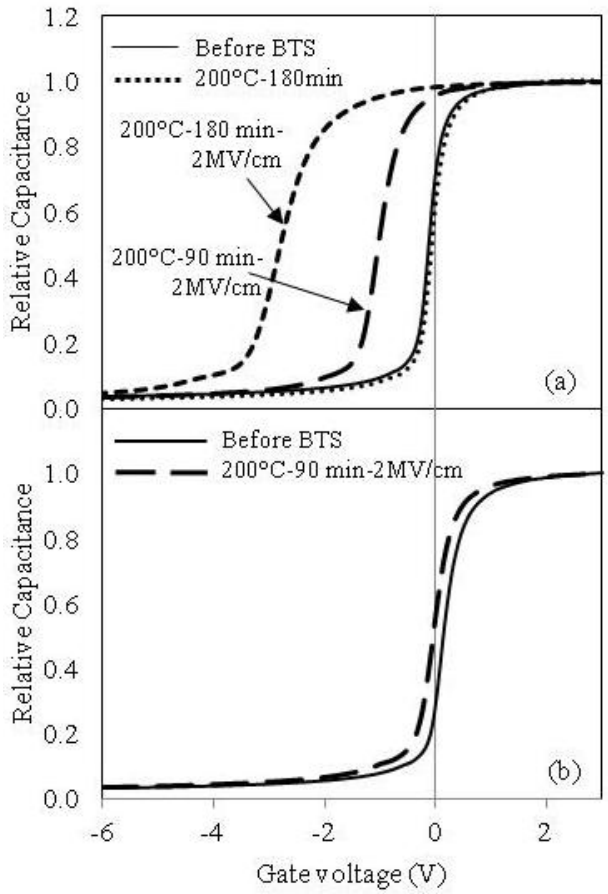

Figure 6–2 Typical *C-V* characteristics of (a) capacitors with $TaRh_x$/Cu gate metallization before and after being subjected to TS at 200°C for 180 min and after BTS at 2 MV/cm at 200°C for various times and (b) capacitors with $TaRh_x$/Al gate metallizations after being subjected to BTS at 2 MV/cm at 200°C for 90 min.

Figure 6–3 shows typical normalized *C-V* curves for capacitors with TaN_x/Cu, $TaRh_x$/Cu and no barrier/Cu gate metallization after BTS at 2 MV/cm at 200°C for 90 min. Capacitors with no barrier showed the largest flatband voltage shift of 2.90±0.60 V. The *C-V* characteristics for the capacitors with TaN_x as the diffusion barrier showed a slight negative flatband voltage shift (0.10±0.03 V), whereas the capacitors with $TaRh_x$ as the diffusion barrier showed a larger negative shift of 0.94±0.06 V. The flatband voltage shift values are listed in Table 6-1. Assuming that the flatband voltage shift is mainly due to Cu^+ ions as opposed to mobile alkali ions and that all the charge is accumulated near the Si/SiO_2 interface, Equation 6-1 can be used to estimate the concentration of Cu^+ ions in

the oxide. It should be noted that according to Equation 2–24 and Equation 6-1, an interface charge assumption underestimates the Cu^+ concentration while the assumption of the absence of any mobile alkali ions overestimates the Cu^+ concentration. Despite these errors, Equation 6-1 can give a semi-quantitative estimate of the concentration of diffused Cu^+ ions. The calculated values are listed in Table 6-1. The dielectric constant of thermal SiO_2 is taken as 3.84 [19]. It is clear that $TaRh_x$ diffusion barriers are effective diffusion barriers that improve the stability of MOS capacitors as evidenced by the calculated Cu^+ concentration for $TaRh_x$ barriers (8.0×10^{11} at/cm^2) which is about 32% of the value for capacitors with no barrier (2.5×10^{12} at/cm^2). However, based on the flatband voltage values, TaN_x outperforms $TaRh_x$ in preventing Cu drift.

As mentioned before, in calculation of the average flatband voltage shift values the data from distorted curves were excluded. Examples of the distorted *C-V* curves of capacitors with TaN_x/Cu, $TaRh_x$/Cu and no barrier/Cu gate metallizations after BTS at 2 MV/cm at 200°C for 90 min are presented in Figure 6–4. These distortions are also an indication of Cu penetration and can be related to the increase in the density of surface states in Si [5] or leakage of minority carriers due to degradation of the dielectric [17], among others. As can be seen in Figure 6–4, the *C-V* characteristics of capacitors with TaN_x as the diffusion barrier were completely overwhelmed and equilibrium *C-V* behavior was unattainable. In comparison, the *C-V* characteristics of samples with $TaRh_x$/Cu gate metallization showed a slight decrease in the value of accumulation capacitance, as the gate voltage was increased to positive values. The *C-V* characteristics of capacitors with no barrier/Cu metallization revealed a significant drop in accumulation capacitance value (Figure 6–4). No such catastrophic change was observed for $TaRh_x$/Cu gate metallization capacitors. Kohn *et al* [17] observed that subjecting MOS devices to prolonged BTS stressing eventually results in a drop in inversion capacitance due to increased oxide leakage and a resulting leakage of minority carriers. A similar analysis approach is used here to explain the observed drop in accumulation capacitance for $TaRh_x$/Cu and no barrier/Cu gate metallization. The diffusion of Cu^+ ions through the oxide generates defects and degrades the oxide

quality. Consequently, the oxide conductivity is increased which enables leakage of electrons accumulated at the Si/SiO_2 interface for n-type Si in accumulation mode. As a result, an accumulation capacitance cannot be maintained and a drop in capacitance is measured.

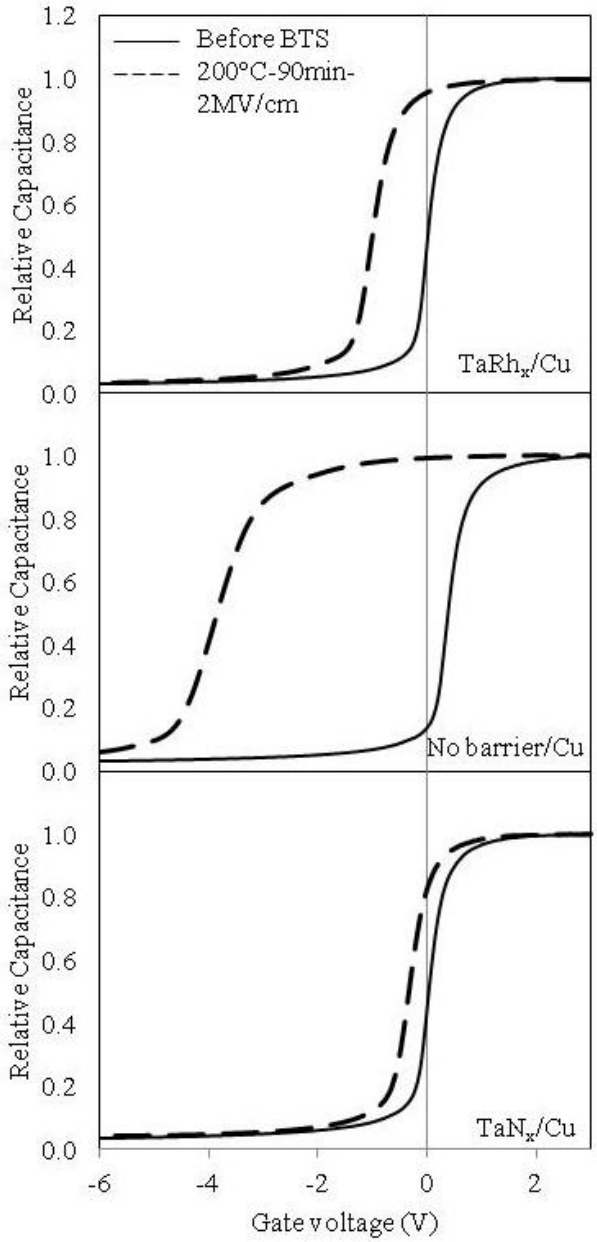

Figure 6–3 Typical *C-V* characteristics of capacitors with $TaRh_x$, no barrier and TaN_x before and after being subjected to BTS at 2MV/cm at 200°C for 90 min.

Table 6-1 Flatband voltage shift (ΔV_{FB}) and Cu^+ concentration values for MOS capacitors with no barrier/Cu, $TaRh_x$/Cu and TaN_x/Cu gate metallizations after being subjected to BTS at 2MV/cm at 200°C for 90 min. Note that the flatband voltage shift values are calculated by subtracting the reference flatband voltage shifts from the measured values.

Gate metallization	No barrier/Cu	$TaRh_x$/Cu	TaN_x/Cu
ΔV_{FB} (V)	-2.90±0.60	-0.94±0.06	-0.10±0.03 V
Cu^+ concentration (at/cm^2)	2.5×10^{12}	8.0×10^{11}	8.5×10^{10}

The cumulative percentage of deformed *C-V* curves for $TaRh_x$/Cu, TaN_x/Cu and no barrier/Cu gate metallization after BTS at 2 MV/cm and 200°C for 90 min are compared in Figure 6–5. About 90% of the curves for capacitors with no barrier were distorted and were not included in the flatband voltage measurements. It is clear that both TaN_x and $TaRh_x$ improve the stability of MOS capacitors and, based on the percentage of deformed C-V curves, they perform quite similarly. As a comparison, the flatband voltage values and the calculated Cu^+ concentrations (Table 6-1) reveal that TaN_x is a more effective diffusion barrier than $TaRh_x$ in preventing drift of Cu into thermal SiO_2.

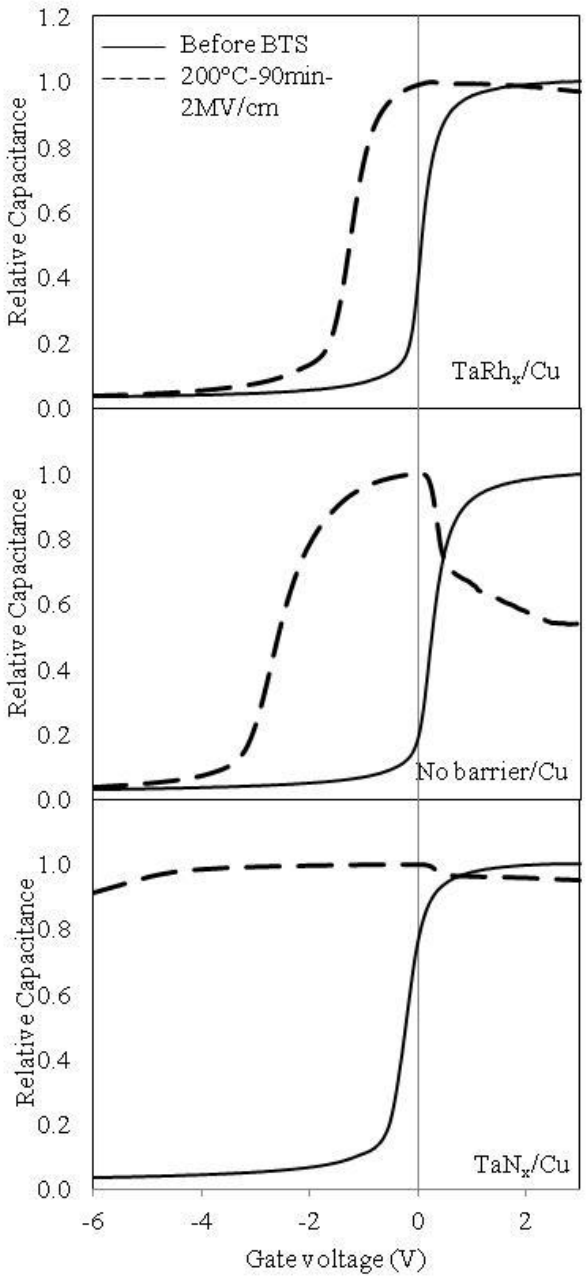

Figure 6–4 Examples of deformed *C-V* characteristics of capacitors with $TaRh_x$, no barrier and TaN_x before and after being subjected to BTS at 2MV/cm at 200°C for 90 min.

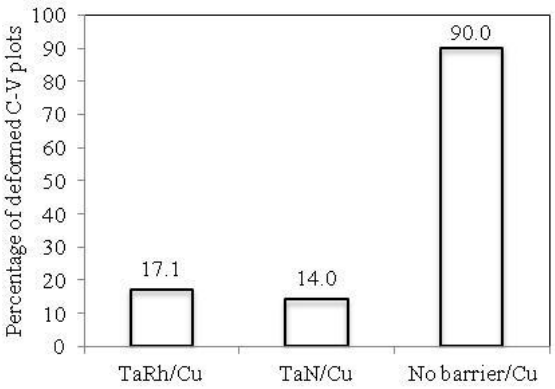

Figure 6–5 Percentage of deformed *C-V* curves of capacitors with $TaRh_x$, TaN_x and no barrier after being subjected to BTS at 2MV/cm at 200°C for 90 min.

6.3.2 SIMS depth profiling

SIMS analysis was performed on both the topside and the backside of the capacitors. Prior to analysis on the topside, the Cu layer was removed to prevent knock-on of Cu into the underlying layers [20]. The topside SIMS depth profiles of capacitors with $TaRh_x$/Cu gate metallization are shown in Figure 6–6. The increase in intensity for both the Cu and Rh profiles near the surface is likely an artifact due to non-uniform sputtering during the initial stages of depth profiling [21]. The spike in the Cu signal can also be attributed to Cu residue from the chemical etching process. After a brief transient region on the surface of the sample, the as-deposited capacitor and the capacitor stressed at 2 MV/cm and 200°C for 180 min showed similar Cu and Rh depth profiles through SiO_2 and Si. There is also some smearing of the profiles as a result of ion bombardment during depth profiling.

The concern is whether the elements of interest (Cu and Rh), which are present as continuous films of $TaRh_x$ and Cu above the SiO_2 layer, are diffusing into the SiO_2 layer or have been implanted during sputtering. To circumvent this issue, backside depth profiling was performed on a capacitor thermally stressed at 200°C for 180 min, a capacitor stressed at 2 MV/cm and 200°C for 180 min and an as-deposited capacitor. The depth profiles for Na, Cu and Rh are presented in Figure 6–7. The final stage of sample preparation for SIMS analysis involved an

anisotropic deep reactive ion etching process with a nominal etch rate selectivity of 1:1000 for SiO_2:Si. During this step, part of the oxide layer was removed and the final thickness of the oxide layer varied for different samples. Consequently, the depth profiles in Figure 6–7 start from various depths inside the SiO_2 layer. Despite these differences, the backside SIMS depth profiling successfully minimizes the smearing of elemental profiles. The peaks observed in all the signals at the $SiO_2/TaRh_x$ can be attributed to the well-known matrix effect [21]. All capacitors showed similar Na profiles, indicating that the Na concentration was below the detection limit of the instrument. The shape of the Cu profile was similar for all capacitors through the SiO_2 layer. The $TaRh_x$/Cu interface broadens as a result of TS and BTS treatment indicating slight intermixing of the barrier and the Cu layer. The observed flatband voltage shift for the BTS stressed capacitors is 2.6 V which corresponds to a Cu^+ concentration of 2.2×10^{12} at/cm^2 at the Si/SiO_2 interface. The range of Cu^+ concentration detected by *C-V* measurements is below the detection limit of SIMS.

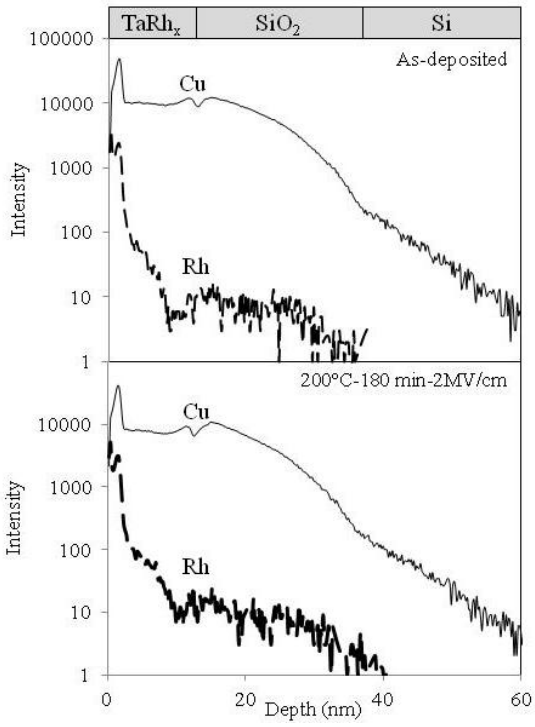

Figure 6–6 Topside SIMS depth profiles of Cu and Rh for an as-deposited capacitor and a capacitor with $TaRh_x$/Cu gate metallization stressed at 2 MV/cm at 200°C for 180 min.

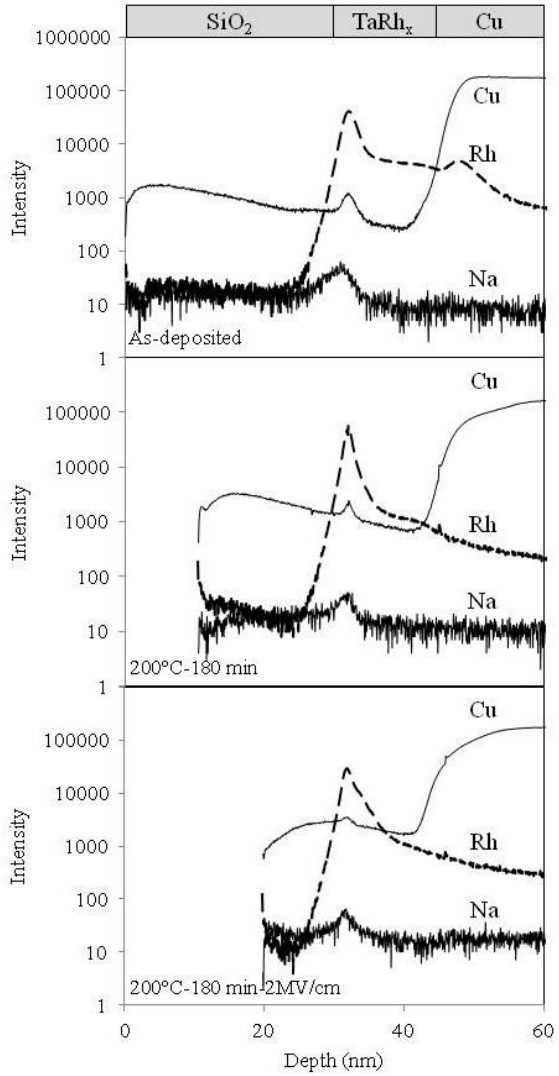

Figure 6–7 Backside SIMS depth profiles of Na, Rh and Cu for an as-deposited capacitor, a capacitor thermally stressed at 200°C for 180 min and a capacitor stressed at 2MV/cm at 200°C for 180 min.

6.3.3 TEM observations

To investigate the morphology of the stressed samples, cross-section TEM samples were prepared by FIB methods from a capacitor stressed at 2 MV/cm and 200°C for 90 min (ΔV_{FB} = 1.0 V) and an as-deposited capacitor. The sample from the stressed capacitor was prepared from the area of applied bias. To avoid redeposition of Cu during FIB thinning, the Cu layer was removed by chemical etching, prior to FIB sample preparation. TEM bright field (BF) micrographs of the as-deposited and BTS stressed sample are shown in Figure 6–8(a) and (b),

respectively. The C layer on top of the structures was deposited as part of the FIB sample preparation procedure. EDX point analysis of the SiO_2 layer (not included here) showed no indication of Cu diffusion into the SiO_2 layer. This is expected since EDX analysis is incapable of detecting such low concentrations, *i.e.*, $[Cu^+] \approx 8.5 \times 10^{11}$ at/cm^2. The thickness of the $TaRh_x$ layer increases from about 10 nm to 16 nm and the thickness of the oxide layer decreases by about 9%. This indicates some intermixing of the barrier layer with the adjacent layers, *i.e.*, Cu and SiO_2 layers. However, no indication of diffusion of Cu through the barrier layer was found by EDX point analysis. To the authors' knowledge, there is no available evidence in the literature for a change in the morphology of BTS stressed MOS devices that shows a Cu^+ concentration level similar to that observed in this study. Wendt *et al* [22] studied the impact of Cu on the quality of the gate oxide by contaminating the wafers with Cu from the backside followed by extreme rapid thermal annealing conditions at 900-1200°C. TEM observations revealed that failure of the gate oxide was related to the formation of Cu-silicides at the Si/SiO_2 interface. It should be noted that no electrical measurements were performed to assess the gate oxide quality. Additionally, the extreme temperatures of Wendt's study resulted in very high Cu contamination levels (10^{17}-10^{18} at/cm^3), which creates a large amount of supersaturation during cooling. Therefore, it can be concluded that for the concentration of Cu in the current study, the supersaturation, which is the driving force for precipitation, is basically diminished. McBrayer *et al* [23] subjected MOS devices with Ag gate metallization to a severe BTS condition (5 MV/cm at 300°C for 90 min) and measured the diffused Ag concentration by Rutherford backscattering. They observed Ag particles at the SiO_2/Si interface using cross-sectional TEM for samples with Ag concentration higher than 10^{15} at/cm^2. However, their *C-V* measurements resulted in completely shorted capacitors and no data was collected. In comparison, the *C-V* measurements of the $TaRh_x$/Cu gate metallization devices in this work indicate a much lower concentration of Cu and therefore Cu diffusion was not detected when examined by EDX analysis. These results point to the importance of performing electrical measurements when

evaluating new materials for potential barriers. It is common practice to initially assess the reliability of new barrier materials using conventional annealing methods. Preliminary assessment of $TaRh_x$ barriers was performed using conventional annealing and the results are described in Chapters 4 and 5. The electrical measurements results presented from the current study are complimentary to the results from conventional annealing tests. It appears that the performance of the amorphous $TaRh_x$ barrier towards Cu diffusion is inferior to that of amorphous TaN_x. It should be noted that other potential seedless barrier materials under study, such as Ru, are also shown to be less stable than stoichiometric TaN under similar biasing conditions [8]. However, these materials offer several advantages such as lower resistivity (Chapter 4) and the possibility of direct deposition of Cu without any seed layer and continue to be considered as potential barriers.

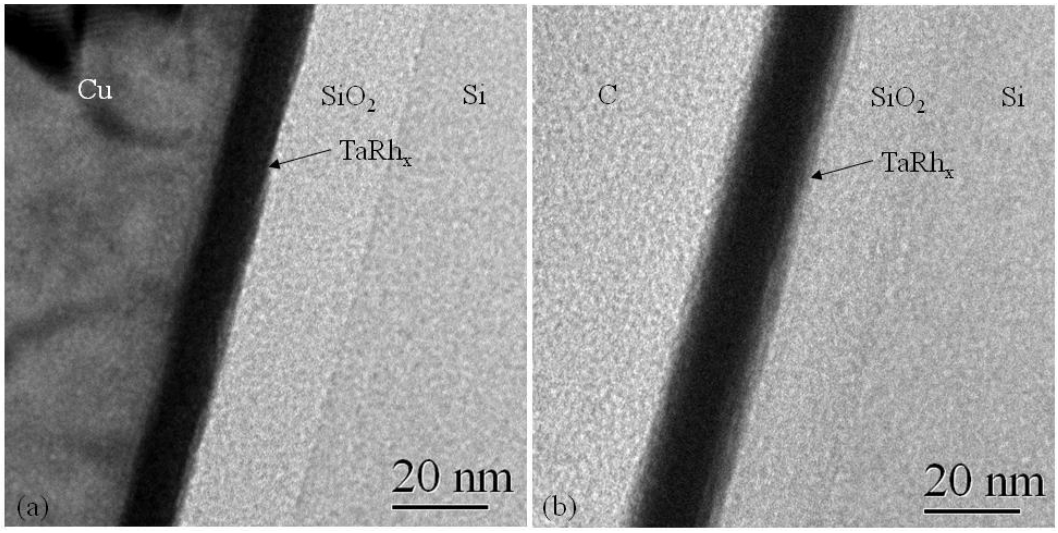

Figure 6–8 Cross-sectional TEM BF micrograph of (a) an as-deposited MOS capacitors and (b) a capacitor stressed at 200°C for 90 min. In (b) the Cu layer has been removed prior to FIB sectioning.

6.4 Conclusions

Capacitors with $TaRh_x$/Cu, $TaRh_x$/Al, TaN_x/Cu and no barrier/Cu gate metallization were subjected to BTS treatment to assess the reliability of amorphous $TaRh_x$ barriers. Two criteria were used to investigate reliability: the percentage of deformed *C-V* curves and the flatband voltage shift. The percentage

of deformed *C-V* curves demonstrated quite similar performance for $TaRh_x$ and TaN_x barriers. The *C-V* measurements on capacitors with $TaRh_x$/Cu gate metallization showed the presence of bulk mobile charges in the oxide with little or no interface charge. The presence of mobile alkali ions was confirmed by testing capacitors with $TaRh_x$/Al gate metallization. The $TaRh_x$ diffusion barrier layer reduced the Cu^+ concentration in the oxide to about 32% of that for capacitors with no barrier layer. However, TaN_x barriers showed superior performance, compared with $TaRh_x$ barriers, as evidenced by the lower concentration of Cu^+ ions in the oxide. TEM observation and SIMS depth profiling of $TaRh_x$/Cu capacitors with relatively large mobile ion concentrations showed no indication of structural or compositional changes. These metallurgical characterization methods, therefore, were not capable of detecting the small Cu^+ ion concentrations that were indirectly measured through *C-V* measurements.

6.5 References

[1] A.A. Istratov, C. Flink, E.R. Weber, Phys. Status Solidi B **222**, 261-77 (2000).
[2] C.J. Liu, J.S. Chen, Appl. Phys. Lett. **80**, 2678-80 (2002).
[3] A. Kohn, M. Eizenberg, Y. Shacham-Diamand, J. Appl. Phys. **94**, 3015-24 (2003).
[4] S.-. Rha, S.-. Lee, W.-. Lee, Y.-. Hwang, C.-. Park, D.-. Kim, Y.-. Lee, C.-. Whang, J. Vac. Sci. Tech. B **16**, 2019-25 (1998).
[5] Y. Shacham-Diamand, A. Dedhia, D. Hoffstetter, W.G. Oldham, J. Electrochem. Soc. **140**, 2427-32 (1993).
[6] H. Kizil, C. Steinbrüchel, Thin Solid Films. **449**, 158-65 (2004).
[7] H. Kizil, G. Kim, C. Steinbrüchel, B. Zhao, J Electron Mater. **30**, 345-8 (2001).
[8] H. Wojcik, U. Merkel, A. Jahn, K. Richter, M. Junige, C. Klein, J. Gluch, M. Albert, F. Munnik, C. Wenzel, J.W. Bartha, Microelectron. Eng. **88**, 641-5 (2011).
[9] J.D. McBrayer, R.M. Swanson, T.W. Sigmon, J. Electrochem. Soc. **133**, 1242-6 (1986).
[10] K.-. Kim, Y.-. Joo, K.-. Kim, J.-. Kwon, J. Appl. Phys. **100**, 063517.1-1 (2006).
[11] P. Shewmon, Diffusion in Solids (The Minerals, Metals & Materials Society, USA, 1989).
[12] S.M. Sze, M.K. Lee, Semiconductor Devices: Physics and Technology (Wiley, USA, 2012).
[13] I. Fisher, M. Eizenberg, Thin Solid Films. **516**, 4111-21 (2008).
[14] F. Braud, J. Torres, J. Palleau, J.L. Mermet, M.J. Mouche, Appl. Surf. Sci. **91**, 251-6 (1995).
[15] A.L.S. Loke, C. Ryu, C.P. Yue, J.S.H. Cho, S.S. Wong, IEEE Electron. Device Lett. **17**, 549-51 (1996).
[16] G. Raghavan, C. Chiang, P.B. Anders, S.-. Tzeng, R. Villasol, G. Bai, M. Bohr, D.B. Fraser, Thin Solid Films. **262**, 168-76 (1995).
[17] A. Kohn, E. Lipp, M. Eizenberg, Y. Shacham-Diamand, Appl. Phys. Lett. **85**, 627-9 (2004).
[18] A. Nandan, S.P. Murarka, A. Pant, C. Shepard, W.A. Lanford, MRS Proc. **260**, 929-934 (1992).
[19] Annual Book of ASTM Standards, Standard Test Methods for Characterization of Metal-Oxide-Silicon (MOS) Structures by Capacitance-Voltage measurements (ASTM, 1992).
[20] P. Bai, G.-. Yang, L. You, T.-. Lu, D.B. Knorr, J. Mater. Res. **5**, 989-97 (1990).
[21] D. Briggs, J. C. Riviere, Practical Surface Analysis (John Wiley & Sons, UK, 1983) pp. 85-141.
[22] H. Wendt, H. Cerva, V. Lehmann, W. Pamler, J. Appl. Phys. **65**, 2402-5 (1989).
[23] J.D. McBrayer, R.M. Swanson, T.W. Sigmon, J. Bravman, Appl. Phys. Lett. **43**, 653-4 (1983).

7 General discussion and conclusions

7.1 Overview and summary

This thesis presents efforts towards the development of an amorphous alloy suitable for diffusion barriers for Cu metallization. During this development a systematic study was performed to select an appropriate system. The main achievements of this work include:

i. Development of a guide, based on evaluation of thermodynamic data and performance of thermodynamic modeling, for selecting a stable amorphous alloy to be applied as a diffusion barrier for Cu metallization. This work was reviewed and disseminated in the journal Acta Materialia [1].

ii. The first comprehensive thermodynamic evaluation of the glass-forming composition range in Ta-Rh system. The thermodynamic model was verified by experimental observations. This work was reviewed and disseminated in the journal Acta Materialia [1].

iii. Evaluation of amorphous $TaRh_x$ diffusion barriers, for the first time, by detailed structural and morphology characterization after thermal annealing and by monitoring the *C-V* characteristics of MOS capacitors after BTS. Comparison of the electrical and metallurgical characterization methods provided evidence for the importance of employing electrical characterization methods. Part of this work was reviewed and disseminated in the journal Acta Materialia [1]. The rest of this work is reviewed and disseminated in the Journal of Materials Science: Materials in Electronics [2].

iv. The first development of a novel sample preparation method for *in-situ* TEM heating experiments for direct observation of atomic diffusion mechanisms involved in the failure of diffusion barriers. This work was reviewed and disseminated in the journal Micron [3].

v. Development of a probe station setup capable of stressing 50 MOS capacitors simultaneously under controlled environment.

vi. Development of a sample preparation technique for SIMS depth profiling on the backside of the wafer to be applied for diffusion studies on potential diffusion barrier materials.

The guide for selecting a suitable material system for diffusion barrier applications was developed based on the thermodynamic models by Donald and Davis [4] and Miedema and Niessen (MN) [5]. The alloying elements suitable for direct electrodeposition of Cu were studied. The former model was used to select an alloying system (*i.e.*, $TaRh_x$), while the MN model was used to select the composition with the most stable amorphous structure. This was accomplished by calculating the Gibbs free energies of formation for supersaturated solid solutions, amorphous phases and structurally simple intermetallic phases. The amorphization range predicted by the MN model (37–66 at% Ta) agreed well with the amorphization range observed by high resolution TEM observations on co-sputtered films of $TaRh_x$ (35-63 at% Ta). Detailed structural analysis revealed that deposits with 27 and 70 at% Ta had a two-phase amorphous plus crystalline structure. The developed model and structural characterization provided a suitable guide for selecting a stable amorphous structure. $Ta_{45}Rh_{55}$ and $Ta_{52}Rh_{48}$ were selected as candidate diffusion barrier and their performance was evaluated initially by metallurgical characterization.

Metallurgical characterization was performed by annealing Si/$TaRh_x$ (13 nm)/Cu metallization stack in 5% H_2/95% N_2 for 30 min at various temperatures. The failure mechanism was studied by FPP resistivity measurements, XRD and TEM analysis. The metallization stacks remained stable up to 550°C. Detailed diffraction analysis by XRD and TEM revealed the complex reaction morphology of the sample. The barrier disintegrated by reaction with the Si substrate to form particles of orthorhombic RhSi and orthorhombic Cu_3Si. The Cu_3Si particles were separated from the Si substrate by the growth of amorphous Si oxide. Formation of Si oxide in association with the formation of Cu_3Si particles was explained

based on the catalytic effect of silicide precipitates on oxidation. In comparison, the Si/(50 nm) $TaRh_x$ stack remained stable up to 700°C and formed RhSi and $TaSi_2$ at higher temperatures. The presence of Cu, therefore, promoted dissociation of the $TaRh_x$ layer at temperatures lower than the equilibrium temperature. At this point, it was not clear if the reaction of Rh with the Si substrate preceded the formation of Cu_3Si or vice versa.

In current ULSI devices, TaN_x barriers are the materials of choice and require deposition of a seed layer to facilitate electrodeposition [6]. A comprehensive review of the available literature (Section 2.6.1.1) revealed the wide range of failure temperature and reaction morphologies reported for TaN_x barriers. Therefore, to create a baseline for comparison, amorphous TaN_x films were deposited by reactive sputtering and evaluated as diffusion barriers. TEM observations revealed that the amorphous TaN_x film crystallized to Ta_2N at around 600°C. Si/ (14 nm) TaN_x/Cu metallization stacks failed by diffusion of Cu to the Si/TaN_x interface followed by the formation of orthorhombic Cu_3Si particles at 700°C. Similar to $TaRh_x$ barriers, the presence of Cu was shown to promote non-equilibrium formation of $TaSi_2$. This phenomenon was explained based on the lattice expansion associated with the formation of Cu_3Si. To accommodate the volume difference associated with silicide formation, Si atoms are forced out of the Si lattice forming Si self-interstitials. These Si interstitials are suggested to be highly reactive and capable of lowering the temperature of formation of $TaSi_2$. In order to further evaluate the performance of TaN_x in contact with Cu, these films were deposited on Si/SiO_2 substrates. Si/SiO_2/(336nm)TaN_x/Cu metallization stacks showed superior stability when compared with Si/TaN_x/Cu stacks and remained stable up to 800°C. TaN_x films in contact with Si/SiO_2 and Cu dissociated at 900°C by outdiffusion of Ta to the Cu surface to form Ta_2O_5 on the surface. Thermodynamic calculations revealed that Ta_2O_5 is the more stable phase in the system, which provides a large driving force for outdiffusion of Ta and its subsequent oxidation at the Cu surface. This work was reviewed and disseminated in the Journal of Material Science [7].

Comparison of the results from Si/TaN_x (14 nm)/Cu with those for Si/$TaRh_x$ (13 nm)/Cu indicates that the thermal stability of TaN_x barriers is superior to $TaRh_x$ barriers. However, one important attribute of $TaRh_x$ films is that they offer the possibility of direct electrodeposition of Cu while TaN_x barriers require the deposition of a seed layer. Additionally, the resistivity values of the amorphous $TaRh_x$ films (154-177 $\mu\Omega$cm) are lower than the resistivity values for amorphous TaN_x films (267 $\mu\Omega$cm). Due to these advantages, the seedless barrier systems continue to be considered as potential diffusion barriers.

The sequence of phenomena, discussed for metallurgical failure of $TaRh_x$ barriers, was speculated based on examination of the post-failure, complex reaction morphology after cooling. To directly observe diffusion and reaction, *in-situ* TEM was performed on Si/$TaRh_x$/Cu stacks. However, several issues were encountered while performing *in-situ* TEM heating experiments on cross-sectional TEM samples prepared by FIB technique. Grain growth of Cu to form a single crystal structure, nucleation and propagation of voids in the Cu layer, delamination of the $TaRh_x$/Cu stack from the Si substrate and, most importantly, surface diffusion of Cu over the entire stack rather than bulk diffusion through the barrier were some of the issues encountered. The first three issues were remedied by using a thicker $TaRh_x$ film, *i.e.*, 50 nm instead of 13 nm thick. It is possible that a thicker $TaRh_x$ film alters the magnitude and distribution of residual thermal stresses in the Cu film, thereby relaxing the stresses that caused void formation in Si/(13 nm)$TaRh_x$/Cu stacks. To obstruct the rapid surface diffusion of Cu, a C film was deposited on the TEM lamellae, after FIB sample preparation and prior to *in-situ* heating in TEM, by electron beam evaporation. A 10 nm thick C film was shown to be effective in preventing diffusion of Cu along the surface. Failure of the barrier was observed directly in TEM while heating the C-protected sample. Failure occurred by nucleation of RhSi particles at the $TaRh_x$/Si interface. Consequently, areas of low density were formed in the barrier adjacent to the RhSi nucleation sites. Diffusion of Cu occurred through these low density areas followed by reaction with the Si substrate to nucleate and grow Cu_3Si particles. Comparison of the *in-situ* and *ex-situ* heated samples showed that the designed

experiments successfully reproduced the bulk reaction mechanisms. The developed sample preparation method and the *in-situ* experiments provide a great tool for direct observation of metallurgical failure of potential diffusion barriers.

The atomic flux of Cu through the diffusion barrier is dependent on the presence and magnitude of both electrical and thermal driving forces. Additionally, the sensitivity of the metallurgical characterization techniques is not sufficient to detect the low concentration of Cu that can deteriorate device performance. The electrical failure mode of $TaRh_x$ and TaN_x barriers was evaluated by BTS stressing of MOS devices. The MOS devices were initially assessed without proper pre-annealing and in ambient atmosphere. The samples showed a positive flatband voltage shift after BTS at 140°C and 2 or 4 MV/cm for up to 60 min. This was attributed to the instabilities in the oxide and the oxidizing ambient for the BTS tests. This pointed to the requirement for improvement of experimental design. A probe station setup, capable of stressing 50 devices under controlled environment, was designed and built in our lab. The effectiveness of barriers was studied by comparing the stability of 4 different metallization stacks: *i*) $TaRh_x$/Cu, *ii*) TaN_x/Cu, *iii*) no barrier/Cu and *iv*) $TaRh_x$/Al. The *C-V* characteristics of 44–46 MOS capacitors was monitored under each BTS condition and compared with depth profiling information obtained by SIMS and cross-sectional TEM observations. Additionally, to distinguish between device degradation due to thermal stress and due to the additional electric field, some of the devices were merely subjected to thermal stress. The shift in flatband voltage and the percentage of deformed *C-V* curves were monitored. No significant flatband voltage shift was observed for thermal annealing. Copper, therefore, did not diffuse under thermal stress alone and the structure remained stable. The shift in flatband voltage of MOS devices with $TaRh_x$/Al metallization showed the presence of mobile alkali charges in the oxide and no interface charges. The concentration of Cu^+ ions in the oxide was reduced in the presence of a 13 nm thick $TaRh_x$ barrier to about 32% of that for capacitors with no barrier. In comparison, the capacitors with a TaN_x barrier showed a lower concentration of Cu^+ ions in the oxide and, therefore, superior barrier performance. TEM

observation revealed some intermixing of the barrier layer with the adjacent layers as evidenced by the thicker $TaRh_x$ and a thinner oxide layer after BTS at 200°C for 90 min under 2 MV/cm. However, EDX point analysis of the SiO_2 layer showed no indication of Cu diffusion into the SiO_2 layer. SIMS depth profiling on the topside of the capacitors showed smearing of the profiles as a result of ion bombardment during depth profiling. To circumvent this issue, back side depth profiling was performed on an as-deposited capacitor, a thermally stressed capacitor and a capacitor subjected to BTS. A sample preparation technique was developed to remove the Si layer from the backside of the capacitors by deep reactive ion etching. The shape of the Cu profile was similar for all capacitors through the SiO_2 layer revealing that the range of Cu^+ concentration detected by *C-V* measurements is below the detection limit of SIMS. This indicates that these metallurgical characterization methods are not capable of detecting the low concentration of Cu measured by *C-V* measurements.

7.2 Future work

The developed diffusion barrier system and the multiple characterization techniques employed point to multiple new research pathways.

i. Materials selection based on thermodynamic modeling. The thermodynamic model presented here provides a great tool for selecting a composition appropriate for diffusion barrier applications. A large number of materials systems have been studied since the integration of Cu interconnects. However, the composition of selected materials has been an arbitrary choice. These material systems can be revisited to appropriately select the most stable composition based on thermodynamic considerations.

ii. Direct electrodeposition of Cu on $TaRh_x$ barriers. Blanket and patterned substrates can be coated with various amorphous compositions of $TaRh_x$ barrier (35-63 at% Ta) followed by direct electrodeposition of Cu using industry standard acid-based baths. Further optimization of the plating bath may be required.

iii. Atomic layer deposition (ALD) of nano-laminate barriers. The low cost and excellent reliability of the sputtering process has made sputtering the process of choice for diffusion barrier layers. However, the overhang profile and the poor step coverage of sputtered films in small features have driven a great interest in processes that offer better control over barrier thickness, such as ALD. In this respect, ALD can be employed to deposited mixed phase or nano-laminate barriers. Alternating sequences of ALD Ta and ALD Rh can be employed to grow nano-laminates of the two elements with improved thickness control over conventional sputtering techniques. It may be beneficial to replace the Ta ALD step by TaN_x ALD. The latter has proven to be a more effective barrier than Ta and its ALD deposition is better developed than Ta.

iv. Effectiveness of sputtered C film. A 10 nm thick electron beam evaporated C film was proven effective in preventing surface diffusion of Cu during *in-situ* TEM studies. Sputtered C films, however, were ineffective. The underlying mechanisms responsible for the effectiveness of the electron beam evaporated film and ineffectiveness of the sputtered film are not clear and need to be further investigated.

v. Inclusion of N in the $TaRh_x$ film. It is expected that the $TaRh_x$/Si interface will become more stable in the presence of N, due to the higher activation energy required for formation of silicides in the presence of N. Additionally, it is expected that the smaller N atoms will fill the interstitial-like sites in the amorphous structure of the $TaRh_x$ film, thereby improving the resistance to Cu diffusion. Moreover, addition of a 3^{rd} element to a binary system can lead to the formation of a stable amorphous phase with a higher crystallization temperature than the binary alloys [8]. In this respect, various compositions of Ta-Rh-N diffusion barriers can be deposited by reactive sputtering or ALD and studied as potential diffusion barriers.

7.3 References

[1] N. Dalili, Q. Liu, D.G. Ivey, Acta Mater., **61**, 5365-74 (2013).
[2] N. Dalili, D.G. Ivey, J. Mat. Sci.: Mat. Electron, DOI: 10.1007/s10854-013-1662-8.
[3] N. Dalili, P. Li, M. Kupsta, Q. Liu, D.G. Ivey, Micron, DOI:10.1016/j.micron.2013.11.002.
[4] I.W. Donald, H.A. Davies, J. Non-Cryst. Solids. **30**, 77-85 (1978).
[5] G.J. Van der Kolk, A.R. Miedema, A.K. Niessen, J. Less-Common Met. **145**, 1-17 (1988).
[6] A.E. Kaloyeros, E.T. Eisenbraun, K. Dunn, O. van der Straten, Chem. Eng. Commun. **198**, 1453-81 (2011).
[7] N. Dalili, Q. Liu, D.G. Ivey, J. Mater. Sci. **48**, 489-501 (2013).
[8] A.E. Kaloyeros, E. Eisenbraun, Annu. Rev. Mater. Sci. **30**, 363-85 (2000).

Appendix A-1

A-1 Matlab code for thermodynamic calculations

```
%%%%%%%%%%%%%%%%%%%%%%%%%%%%%%%%%%%%%%%%%%%%%%%%%%%%%%%%%%%%%%%%%%%%%%%%%%%%
%%%%        Thermodynamic analysis on Ta-Rh system                      %%%%
%%%%        for amorphous composition determination                     %%%%
%%%%                Developed by: Neda Dalili                           %%%%
%%%%           Inputs: Temperature (T) in [Kelvins]                     %%%%
%%%%      Outputs: Gibbs free energy of formation of solid              %%%%
%%%%   solution, amorphous and intermetallic phases in                  %%%%
%%%%    [KJ/mole], solve for the tangent between amorphous              %%%%
%%%%   and solid solution phases and plot the calculated                %%%%
%%%%          values as a function of composition                       %%%%
%%%%%%%%%%%%%%%%%%%%%%%%%%%%%%%%%%%%%%%%%%%%%%%%%%%%%%%%%%%%%%%%%%%%%%%%%%%%

%%%%%%%% System Constants  %%%%%
alpha=3.5E-3;                 %[J/molK]       Empirical constant of
amorphous structural relaxation
Tm_Ta=2995.9+273;             %[K]            Melting temperature
Tm_Rh=1965.9+273;             %[K]            Melting temperature
R=8.3144E-3;                  %[kJ/molK]      Gas constant
Zrh=9;                        %[unitless]     Number of valence
electrons for Rh
Zta=5;                        %[unitless]     Number of valence
electrons for Ta
phi_Rh = 5.40;                %[V]            Atomic work function
of Rh
phi_Ta = 4.05;                %[V]            Atomic work function
of Ta
nWS_Rh = 1.76;                %[density unit] Electron density at
the boundary of Wigner-Seitz cell^1/3
nWS_Ta = 1.63;                %[density unit] Electron density at
the boundary of Wigner-Seitz cell^1/3
p = 14.1;                     %[unitless]     Empirical constant
q = 132.5;                    %[unitless]     Empirical constant
deltaH_TainRh = 28;           %[KJ/mole]      Elastic energy for
dilute solution of Rh in Ta
deltaH_RhinTa = 26;           %[KJ/mole]      Elastic energy for
dilute solution of Rh in Ta
c_Rh_dilute = [0.001,0.999]; %
%%%%%%%%%%%%%%%%%%%%%%%%%%%%%%%

%%%%%%%%%%%%%%%%%%%%%%%%%%%%%%%%%%%%%%%%%%%%%%%%%%%%%%%%%%%%%%%%%%%%%%%%%%%%
%%%%%%%%%%%%%%%%%%%% DeltaHstructure %%%%%%%%%%%%%%%%%
%%%%%%%%%%%%%%%%%%%%%% [KJ/mole] %%%%%%%%%%%%%%%%%%%
digits(4);                                          %Number of
significant digits = 4
Z=[5 5.5 6 7 8 8.5 9];                              %Range of valence
electrons
```

```
E_hcp=[10 15 13 -5 -10.5 -11 -8];                   %HCP structural
enthalpy for each valence electron
E_fcc=[9 14 11 -3 -9.5 -11 -9];                     %FCC structural
enthalpy for each valence electron
E_bcc=[-9.5 -14.5 -12 4 10 11 8.5];                 %BCC structural
enthalpy for each valence electron
E=[E_bcc;E_fcc;E_hcp];                              %
for i=1:7;                                          %
    Xrh(i)=(Z(i)-Zta)/(Zrh-Zta);                    %
    Xta(i)=1-Xrh(i);                                %
    E_Zave(i)=min(min(E(1,i),E(2,i)),E(3,i));       %Find the min
value of Ehcp, Efcc and Ebcc for each Z average
end                                                 %
for i=1:7;                                          %
    E_ref(i)=Xrh(i)*E_Zave(7)+Xta(i)*E_Zave(1);     %Define Eref as
the linear interpolation between E(Zrh) and E(Zta)
    deltaHstruc(i)=E_Zave(i)-E_ref(i);              %Find structural
enthalpy at each concentration
end                                                 %
%%%%%%%%%%%%%%%%%%%%%%%%%%%%%%%%%%%%%%%%%%%%%%%%%%%%%

%%%%%%%%%%%%%%%%%%%%%%%%%%%%%%%%%%%%%%%%%%%%%%%%%%%%%%%%%%%%%%%%%%%%%%
%%%%%%%%%%%%%%%%%%%%%%%%%%%%% DeltaHelastic %%%%%%%%%%%%%%%%%%%%%%%%
%%%%%%%%%%%%%%%%%%%%%%%%%%%%%%% [KJ/mole] %%%%%%%%%%%%%%%%%%%%%%%%%%
deltaHelast=Xta.^2.*Xrh*deltaH_RhinTa+Xrh.^2.*Xta*deltaH_TainRh;
%to calculate the elastic contribution using regular solution
model
%%%%%%%%%%%%%%%%%%%%%%%%%%%%%%%%%%%%%%%%%%%%%%%%%%%%%%%%%%%%%%%%%%%%%%

%%%%%%%%%%%%%%%%%%%%%%%%%%%%%%%%%%%%%%%%%%%%%%%%%%%%%%%%%%%%%%%%%%%%%%
%%%%%%%%%%%%%%%%%%%%%%%%%%%% DeltaHchemical %%%%%%%%%%%%%%%%%%%%%%%%
%%%%%%%%%%%%%%%%%%%%%%%%%%%%%%% [KJ/mole] %%%%%%%%%%%%%%%%%%%%%%%%%%
for i=1:2;
%
   x =alloyvolume (1-c_Rh_dilute(i), c_Rh_dilute(i));
%Call the function "alloyvolume" to find the values of volumes in
the alloy
   v_alloy_Ta (i) = x(1);
%
   v_alloy_Rh (i) = x(2);
%
   deltaH_ampl =((q*(nWS_Rh-nWS_Ta)^2)-(p*(phi_Rh-phi_Ta)^2))...
%
       /((1/nWS_Ta)+(1/nWS_Rh));
%Find the term concerning the chemical interaction between atoms
end
%
deltaH_RhinTa = 2*v_alloy_Rh(1)*deltaH_ampl;
%[KJ/mole] Find chemical enthalpy for dilute solution of Rh in Ta
deltaH_TainRh = 2*v_alloy_Ta(2)*deltaH_ampl;
%[KJ/mole] Find chemical enthalpy for dilute solution of Ta in Rh
deltaHchem=Xta.^2.*Xrh*deltaH_RhinTa+Xrh.^2.*Xta*deltaH_TainRh;
%[KJ/mole] Find the total chemical contribution using regular
solution model
%%%%%%%%%%%%%%%%%%%%%%%%%%%%%%%%%%%%%%%%%%%%%%%%%%%%%%%%%%%%%%%%%%%%%%

%%%%%%%%%%%%%%%%%%%%%%%%%%%%%%%%%%%%%%%%%%%%%%%%%%%%%%%%%%%
```

```
%%%%%%%%%%% DeltaGtotal for solid solution %%%%%%%%%%%%%%
%%%%%%%%%%%%%%%%%%%%%% [KJ/mole] %%%%%%%%%%%%%%%%%%%%%%%
deltaS=-R*(Xrh.*log(Xrh)+Xta.*log(Xta));                  %Entropy
value assuming an ideal solution model
deltaS(1)=0;deltaS(7)=0;                                  %Entropy
of mixing is zero for pure metals
deltaHss=deltaHstruc+deltaHchem+deltaHelast;              %Find the
total enthalpy of solid solution
deltaGss=deltaHstruc+deltaHchem+deltaHelast-T.*deltaS;    %Find the
total Gibbs free energy of solid solution
%%%%%%%%%%%%%%%%%%%%%%%%%%%%%%%%%%%%%%%%%%%%%%%%%%%%%%%%%

%%%%%%%%%%%%%%%%%%%%%%%%%%%%%%%%%%%%%%%%%%%%%%%%%%%%%%%%%
%%%%%%%%%%%%% DeltaGtotal for amorphous %%%%%%%%%%%%%%%%%
%%%%%%%%%%%%%%%%%%%%%% [KJ/mole] %%%%%%%%%%%%%%%%%%%%%%%
deltaGl=deltaHchem-T*deltaS;                              %Find
Gibbs free energy of mixing of liquids
deltaGa_sTa=alpha*(Tm_Ta-T);                              %The
difference between Gibbs free energies of undercooled liquid and
crystalline states
deltaGa_sRh=alpha*(Tm_Rh-T);                              %The
difference between Gibbs free energies of undercooled liquid and
crystalline states
deltaGa_s=Xta*deltaGa_sTa+Xrh*deltaGa_sRh;                %
deltaGamorph=deltaGl+deltaGa_s;                           %Find the
total Gibbs free energy of amorphous
DeltaG=[Xta',deltaGss',deltaGamorph'];                    %
cdes={'XTa','DeltaGss','DeltaGamorph'};                   %
rdes={'X1','X2','X3','X4','X5','X6','X7'};               %
r=[{'---'},cdes;rdes.',num2cell(DeltaG)];                 %
disp(r);                                                  %Display
the final values of Gibbs free energies as a function of
composition
%%%%%%%%%%%%%%%%%%%%%%%%%%%%%%%%%%%%%%%%%%%%%%%%%%%%%%%%%

%%%%%%%%%%%%%%%%%%%%%%%%%%%%%%%%%%%%%%%%%%%%%%%%%%%%%%%%%
%%%%%%%%%%%%% Finding the common tangents %%%%%%%%%%%%%%%%
%%%%%%%% between amorphous and solid solutions %%%%%%%%%%%%
Pamorph=[36.64 -109.9 134.9 -96.66 228.8 -190.2 6.793];     %Least
square fit of deltaGamorph plot
Pss=[-1169 3825 -4361 1988 -116.6 -166.6 0];              %Least
square fit of deltaGss plot
[x, fval]=fsolve(@(x) Tangent(x),[0.3;0.4]);              %Call
function '"Tangent" to solve the system of equations obtained by

%creating the best fit of solid solution and amorphous plots
deltaG_tangent1=[polyval(Pss,x(1));polyval(Pamorph,x(2))];  %
X_tangent1=[x(1);x(2)];                                     %
[x, fval]=fsolve(@(x) Tangent(x),[0.7;0.7]);                %
deltaG_tangent2=[polyval(Pss,x(1));polyval(Pamorph,x(2))];  %
X_tangent2=[x(1);x(2)];                                     %
DeltaG_tangent1 = [X_tangent1,deltaG_tangent1];             %
cdes={'XTa','DeltaGtangent1'};                              %
rdes={'X1','X2'};                                           %
r=[{'---'},cdes;rdes.',num2cell(DeltaG_tangent1)];          %
disp(r);
%Display the final values of the 1st common tangent
```

```
DeltaG_tangent2 = [X_tangent2,deltaG_tangent2];                    %
cdes={'XTa','DeltaGtangent2'};                                     %
rdes={'X1','X2'};                                                  %
r=[{'---'},cdes;rdes.',num2cell(DeltaG_tangent2)];                 %
disp(r);
%Display the final values of the 2nd common tangent
%%%%%%%%%%%%%%%%%%%%%%%%%%%%%%%%%%%%%%%%%%%%%%%%%%%%%%%%%%%%%%%%%%%

%%%%%%%%%%%%%%%%%%%%%%%%%%%%%%%%%%%%%%%%%%%%%%%%%%%%%%%%%%%%%%%%%%%
%%%%%%%%% DeltaGtotal for intermetallic phases %%%%%%%%%%%%%%%
%%%%%%%%%%%%%%%%%%%%%%% [KJ/mole] %%%%%%%%%%%%%%%%%%%%%%%%%%%%%%
c_Rh = [0.70, 0.725, 0.75];
%Concentrations of relatively stable intermetallic phases taken
from phase diagram
c_Ta = 1-c_Rh;                                                     %
for i=1:3;                                                         %
   x =alloyvolume (1-c_Rh(i), c_Rh(i));                            %Call
the function "alloyvolume" to find the values of volumes in the
alloy
   v_alloy_Ta (i) = x(1);                                          %
   v_alloy_Rh (i) = x(2);                                          %
   c_s (1,i) = (1-c_Rh(i))*v_alloy_Ta(i)/((1-c_Rh (i))...          %
       *v_alloy_Ta(i)+c_Rh (i)*v_alloy_Rh(i));                     %
Define first row of C_s matrix as the Ta surface concentration
values (csTa)
   c_s (2,i) = c_Rh(i)*v_alloy_Rh(i)/((1-c_Rh (i))...              %
       *v_alloy_Ta(i)+c_Rh (i)*v_alloy_Rh(i));                     %
Define the 2nd row of C_s matrix as the Rh surface concentration
values (csRh)
   f(i) = c_s(1,i)*c_s(2,i)*(1+8*(c_s(1,i)*c_s(2,i))^2);           %Find
the surface concentration
   deltaH(i) = 2*f(i)*(((1-c_Rh(i))*v_alloy_Ta(i))+...             %
       (c_Rh(i)*v_alloy_Rh(i)))*((q*(nWS_Rh-nWS_Ta)^2)...          %
       -(p*(phi_Rh-phi_Ta)^2))/((1/nWS_Ta)+(1/nWS_Rh));            %find
enthalpy of intermetallic phases
end;                                                               %
deltaGintermetallic = deltaH;                                      %Find
Gibbs free energy of intermetallic phases assuming deltaS is zero
for ordered compounds
DeltaG_intermetallic = [c_Ta',deltaGintermetallic'];               %
cdes={'XTa','DeltaGintermetallic'};                                %
rdes={'X1','X2','X3'};                                             %
r=[{'---'},cdes;rdes.',num2cell(DeltaG_intermetallic)];            %
disp(r);
%Display the final values Gibbs free enrgies of intermetallic
phase
%%%%%%%%%%%%%%%%%%%%%%%%%%%%%%%%%%%%%%%%%%%%%%%%%%%%%%%%%%%%%%%%%%%

%%%%%%%%%%%%%%%%%%%%%%%%%%%%%%%%%%%%%%%%%%%%%%%%%%%%%%%%%%%%%%%%%%%
%%%%%%%%% Plot the systems Gibbs free energies %%%%%%%%%%%%%%%%%
figure(1);                                                           %
grid off;                                                            %
hold on;                                                             %
plot(Xta,deltaGamorph,'-.kx','LineWidth',2.5,'MarkerSize',10);%
plot(Xta,deltaGss,'--ks','LineWidth',2.5,'MarkerSize',10);           %
plot(c_Ta,deltaGintermetallic,'ko','lineWidth',2.5,...               %
    'MarkerSize',10);                                                %
```

```
xlabel('Atomic Fraction of Ta [at.%]','FontSize',12);          %
ylabel('Gibbs Free Enrgy [KJ/mole]','FontSize',12);            %
legend('Amorphous','Solid Solution','Intermetallic');          %
%%%%%%%%%%%%%%%%%%%%%%%%%%%%%%%%%%%%%%%%%%%%%%%%%%%%%%%%%%%%%%%%

%%%%%%%%%%%%%%%%%%%%%% End of File %%%%%%%%%%%%%%%%%%%%%%%%%%%%%%
```

```
%%%%%%%%%%%%%%%%%%%%%%%%%%%%%%%%%%%%%%%%%%%%%%%%%%%%%%%%%%%%%%%%%%%%%%%
%%%              function alloyvolume                                %%%
%%%  This function takes the concentration of                        %%%
%%%  Ta and Rh and returns the vollume of them                       %%%
%%%  in alloy form using an iteration procedure                      %%%
%%%%%%%%%%%%%%%%%%%%%%%%%%%%%%%%%%%%%%%%%%%%%%%%%%%%%%%%%%%%%%%%%%%%%%%
function G = alloyvolume (c_Ta, c_Rh);                                 %
x0=[4.9;4.1];                                                          %Initial guess
G = fsolve(@volume, x0);                                               %Solve the
equations of volumes in alloy form
function F = volume (x);                                               %Function F
defines the equations for V_Ta ^2/3 and V_Rh^2/3 in alloy form
                                                                       %v_Ta and v_Rh
are V_Ta ^2/3 and V_Rh^2/3 in atomic form
a = 0.04;                                                              %
phi_Ta = 4.05;                                                         %
phi_Rh = 5.40;                                                         %
v_Rh = 4.1;                                                            %
v_Ta = 4.9;                                                            %
F = [v_Rh - x(2) + a*v_Rh*(phi_Rh - phi_Ta)*...                        %
    (c_Ta*x(1)/(c_Ta*x(1) + c_Rh*x(2)))*...                            %
    (1 + (8*c_Ta*c_Rh*x(1)*x(2)/(c_Ta*x(1)...                          %
    + c_Rh*x(2))));v_Ta - x(1) + a*v_Ta*....                           %
    (phi_Ta - phi_Rh)*(c_Rh*x(2)/(c_Ta*x(1)...                         %
    + c_Rh*x(2)))*(1 + (8*c_Ta*c_Rh*x(1)...                            %
    *x(2)/(c_Ta*x(1) + c_Rh*x(2))))];                                  %Page 135 of
labbook (Sept 10, 2012)
end                                                                    %
end                                                                    %
%%%%%%%%%%%%%%%%%% End of File %%%%%%%%%%%%%%%%%%%%%%%%
```

```
%%%%%%%%%%%%%%%%%%%%%%%%%%%%%%%%%%%%%%%%%%%%%%%%%%%%%%%%%%%%%%%%%%%%%%%%
%%%                Function Tangent                                   %%%
%%%     This function defines the series of                           %%%
%%%  equations required for finding the tanget                        %%%
%%%    between Gibbs free enrgies of amorphous                        %%%
%%%          and solid solution phases                                %%%
%%%%%%%%%%%%%%%%%%%%%%%%%%%%%%%%%%%%%%%%%%%%%%%%%%%%%%%%%%%%%%%%%%%%%%%%
function F= Tangent(x);                                               %x is a vector
of x(1) and x(2) which are Xta(s) and Xta(a) respectively
n=0;                                                                  %
Pamorph=[36.64 -109.9 134.9 -96.66...                                 %
    228.8 -190.2 6.793];                                              %Least square
fit of deltaGamorph plot
Pss=[-1169 3825 -4361 1988 -116.6 -166.6 0];                          %Least square
fit of deltaGss plot
X1=[x(1)^6 x(1)^5 x(1)^4 x(1)^3 x(1)^2 x(1) 1];                       %
X2=[x(2)^6 x(2)^5 x(2)^4 x(2)^3 x(2)^2 x(2) 1];                       %
derX1=[x(1)^5 x(1)^4 x(1)^3 x(1)^2 x(1) 1 0];                         %
derX2=[x(2)^5 x(2)^4 x(2)^3 x(2)^2 x(2) 1 0];                         %
der_amorph=[polyder(Pamorph), n];                                     %Make arrays of
the same size
der_ss=[polyder(Pss), n];                                             %
f1=Pss.*X1 + (1-x(1)).*der_ss.*derX1 -...                             %
    Pamorph.*X2 - (1-x(2)).*der_amorph.*derX2;                        % Define
equations of tangent (Equation 1 in notes)
f2=Pss.*X1 - x(1)*der_ss.*derX1 - Pamorph.*X2...                      %
    + x(2)*der_amorph.*derX2;                                         % Define
equations of tangent (Equation 2 in notes)
F1=sum(f1);                                                           %
F2=sum(f2);                                                           %
F=[F1;F2];                                                            %
end                                                                   %
%%%%%%%%%%%%%%%%%%%% End of File %%%%%%%%%%%%%%%%%%%%
```

Appendix A-2

A-2 A cryo-XPS study of electroplating solutions for Au-Sn solder packaging [1]

A-2.1 Introduction

The environmental concerns associated with the use and disposal of Pb-based solders have led to increased use of Au-Sn eutectic alloys in many micro/optoelectronic and microelectromechanical system packaging applications. These solders exhibit excellent mechanical and thermal properties. [1] The eutectic solders have been successfully electrodeposited from both single Au-Sn [2] and separate Au and Sn baths. [3] The disadvantage of co-deposition is limited bath stability resulting in the formation of nanosized Au particles, which promote the formation of nodules and defects in the deposit [4]. Due to the instability of aurous ions (Au^+) in aqueous solutions, Au plating baths are usually designed based on Au^+ complexes. Conventional Au plating solutions mostly use cyanide-based complexes of Au^+ in the form of $Au(CN)_2^-$ which has a stability constant of log β= 38 where β is defined as:

$$\beta = \frac{[Au(CN)_2^-]}{[Au^+][CN^-]^2} \qquad \text{Equation A-2 – 1}$$

where the square brackets show the concentration of the species [5]. The free cyanide ions in the plating solution, however, react with the carbonyl groups of the solution inhibitor of the positive photoresist resulting in bath contamination and also plating underneath the photoresist [1]. Photoresist incompatibility and toxicity of cyanide-based Au plating baths have created interest in sulfite-based plating baths which are non-toxic, have better throwing power than cyanide baths and form smooth, ductile and bright deposits [6]. In pure sulfite baths, in the

[1] *A version of this chapter has been published. N. Dalili, A. He, Q. Liu, D.G. Ivey, J. Electron. Mat.* ***39****, 1554-1561 (2010).*

presence of excess sulfite, Au exists in the form $[Au(SO_3)_2]^{3-}$. The stability constant values obtained from various literature sources are inconsistent and values of log β from 10 to 27 have been reported [1,5]. Nevertheless, the instability of $[Au(SO_3)_2]^{3-}$ complexes under neutral or acidic conditions, which are necessary for optimum resist compatibility, is consistently reported [1,5]. The dissociation of the Au^+ sulfite complex produces bisulfite ions (HSO_3^-) which reduce to dithionite ions ($S_2O_4^{2-}$). The latter is a strong reducing agent and promotes decomposition of $[Au(SO_3)_2]^{3-}$ according to:

$$2Au(SO_3)_2^{3-} + 2OH^- + S_2O_4^{2-} \rightarrow 2HSO_3^- + 4SO_3^{2-} + 2Au \qquad \text{Equation A-2 – 2}$$

The addition of stabilizing additives has been shown to improve bath stability. Zuntini *et al* [7] have isolated a Au^+-sulfite-amine compound by adding ethylene diamine to Au^{3+} chloride and sodium sulfite aqueous solutions and heating the mixture. The electroplating baths prepared by this method can operate in the pH range from 4.5 to 8. The long term stability of this bath, however, has not been studied [7]. In other work, 2,2́-dipyridine is reported to suppress the decomposition reaction of Au^+ sulfite baths via the formation of a stable Au^+ complex. This bath operates at a pH equal to or higher than 8 and, therefore, is not compatible with conventional photoresists [8]. Smith *et al* [9] have isolated a Na-Au sulfite complex which was used to prepare a cyanide-free Au plating bath using hexamethyleneamine as a stabilizing agent. This bath did not precipitate on standing. However, the operating pH condition was not reported [9]. Several other stabilizing additives such as a nitrogen-free diphosphonic compound, operating at pH values between 7 and 8, [10] and an organic polyamine or mixture of polyamines of molecular weight from 60 to 50,000, operating at pH values below 6.5, [11] are also reported in the patent literature.

In high volume microelectronics packaging, long-term bath stability, photoresist compatibility and non-toxicity are the decisive factors. In this respect, He *et al* [12] have developed an environmentally-friendly, slightly acidic (pH= 5.5) plating bath consisting of tri-ammonium citrate ($HOC(CO_2NH_4)(CH_2CO_2NH_4)_2$), sodium sulfite ($Na_2SO_3$) and potassium

tetrachloroaurate ($KAuCl_4$), which is not prone to decomposition for at least 12 months [12]. An Au-rich, eutectic Au-Sn solder was successfully deposited from this bath by sequential electrodeposition of Au and Sn layers followed by reflowing [3]. During development of these plating solutions, He *et al* [13] noticed that the plating solution stability is strongly dependent on the presence and the concentration of the chemical additives as well as on the order of mixing. For example, if sodium sulfite was added to a citrate solution before addition of the Au salt, the solution was unstable and precipitated on mixing. However, if the order of mixing was changed and the sulfite was added to the citrate solution already containing the Au salt, the solution was stable at room temperature for at least 12 months. On the other hand, citrate and Au salt solutions precipitated on mixing and the stability of sulfite and Au salt solutions was also dependent on the mixing order [13]. The type of Au complexes formed and the role of sodium sulfite and triammonium citrate in stabilizing these complexes is not well understood.

The objective of the present study is to elucidate the solution chemistry of He *et al*'s Au plating bath and to identify the complexes that give rise to a stable solution. Several techniques are utilized to characterize the solutions and precipitates, including turbidity measurements, electron microscopy and X-ray photoelectron spectroscopy (XPS). The XPS method is particularly novel, as the solutions are analyzed through cryo-freezing.

A-2.2 Materials and methods

The Au plating solution recipe developed by He *et al* [12] was adopted to study the chemistry and stability of Au complexes. Potassium tetrachloroaurate ($KAuCl_4$) was the initial source of Au^{3+}, sodium sulfite (Na_2SO_3) was used as a complexing agent for Au and tri-ammonium citrate ($HOC(CO_2NH_4)(CH_2CO_2NH_4)_2$) was initially added as a buffering agent to maintain a slightly acidic pH and was observed later to play an important role in stabilizing the solutions. All solutions were prepared using deionized water and stored in sealed vials at room temperature and in visible light. The composition

and order of mixing of the solutions studied are given in Table A-2-1. Solutions prepared from pure chemicals $KAuCl_4$, AuCl and tri-ammonium citrate were also studied to create a set of internal standards or reference peaks for Au^{3+}, Au^{+}, Cl^{-} and O. A standard peak for Au^{+} was, however, not obtained since AuCl is unstable in water and/or in the presence of X-ray radiation and decomposed to Au^{3+} and Au^{o}.

Table A-2–1 Composition of solutions studied.

Order of mixing	**Standard 1 (R1)**	**Standard 2 (R2)**	**Solution 1 (S1)**	**Solution 2 (S2)**
Tri-ammonium citrate (g/L)	100	----	100	100
$KAuCl_4$ (g/L)	----	20	5	5
Na_2SO_3 (g/L)	----	----	----	13.5

The stability of aged solutions was monitored utilizing a VWR Model 66120–200 Turbidity Meter which consists of a light source and a detector at a right angle to the incident beam to read the intensity of scattered light in nephelometric turbidity units (NTU). Suspended solid particles make the liquid appear turbid, scatter the incident light and give rise to higher turbidity values. Settled particles, however, do not contribute to light scattering. The solutions, therefore, were not agitated during aging in order to monitor the relative concentration of only suspended particles.

A Kratos AXIS-165 X-ray photoelectron spectroscopy (XPS) system, with a monochromatic Al Kα X-ray source (1486.6 eV) operated at 210 W and a liquid-N_2 cooled cryogenic stage, was utilized to study the chemical state of the species in the aqueous solutions. XPS makes use of X-rays to study the core level electron binding energy of an element in routine surface analysis. The binding energy of the electrons (E_B) in a specific atomic orbital can be calculated from their kinetic energy value (E_K) which is measured by the spectrometer. The binding energy (E_B) is calculated according to:

$$E_B = h\nu - E_K - \varphi \qquad \text{Equation A-2 – 3}$$

where $h\nu$ is the incident photon energy and φ is the spectrometer work function [14]. Liquid samples, however, are not compatible with the vacuum inside the XPS chamber and, therefore, the use of a cryogenic stage was necessary to obtain frozen liquid samples and to maintain the condition in the UHV environment. In the fast entry lock (FEL) of the instrument, a Cu stub (10 mm in diameter) was pre-cooled with liquid nitrogen. A drop of the solution was placed on the smooth surface of the stub causing it to freeze. The stub and FEL were kept in flowing dry nitrogen to drive away any atmospheric moisture. Pumping inside the FEL started after the solution drop froze. During this process, the temperature of the stub in the FEL continuously decreased. When the vacuum of the FEL was lower than $2x10^{-6}$ torr, the temperature of the stub in the FEL was about -150^{o}C and the temperature of the sample stage in the sample analytical chamber reached -150^{o}C. The frozen sample was then ready for analysis.

A survey scan in the binding energy range of 0-1100 eV was recorded with analyzer pass energy of 160 eV and a step size of 0.3 eV to identify the elements. This was followed by acquisition of high-resolution spectra (20 eV pass energy and a step size of 0.1 eV) around the elemental peaks of interest, *i.e.*, C, Au, O and Cl. The number of scans for high resolution spectra was determined according to the spectrum intensities of the elements to be analyzed. Charge neutralization was applied to stabilize spectra during spectra collection, because the solutions became insulating at very low temperatures. The XPS spectra were fitted and deconvoluted using Casa XPS software; the background model was obtained using a Shirley algorithm and the individual peaks were fitted with Gaussian-Lorentzian line-shapes. Sample charging was compensated for by taking the C 1s peak (284.65 eV) as an internal standard.

The morphology and composition of the suspended particles were investigated using a JEOL 2010 TEM, operated at 200 kV, and equipped with an EDX spectrometer. To prepare the samples for TEM analysis a droplet of solution (fresh or aged) was placed on a carbon coated copper grid and allowed to dry in

air. The solutions were agitated prior to TEM sampling to ensure extraction of both settled precipitates and suspended particles.

A-2.3 Results and discussions

Two different solutions (Table A-2–1) were investigated, of which S2 is the stable solution originally developed by He *et al* [12]. S1 is a mixture of tri-ammonium citrate and $KAuCl_4$ which was pale yellow in colour and transparent upon mixing. The turbidity of S1 (Figure A-2–1) increased in the initial hours after mixing and the solution colour became more intense and less transparent, indicating the formation of small solid particles. The turbidity peaked out at about 5 hr. The sudden drop in turbidity was accompanied with the formation of visible precipitates settled at the bottom of the solution. The addition of Na_2SO_3 to fresh S1 resulted in the formation of a stable, clear solution (S2) whose turbidity remained constant and low for 12 months. The stability of this solution has been attributed to the formation of a stable Au^+ complex of the form $[Au(SO_3)_2]^{3-}$ [13]. The stability of a solution consisting of $KAuCl_4$ and Na_2SO_3 is, on the other hand, very sensitive to the order of mixing and the solutions precipitate within two days to two months [12]. It is apparent that citrate plays an important role in stabilizing S2. The role of citrate, however, has not been considered in suggesting the formation of a $[Au(SO_3)_2]^{3-}$ type complex. Based on the above observations, attempts were made to identify the type of complexes and the nature of the precipitates using cryo-XPS and TEM analysis, respectively.

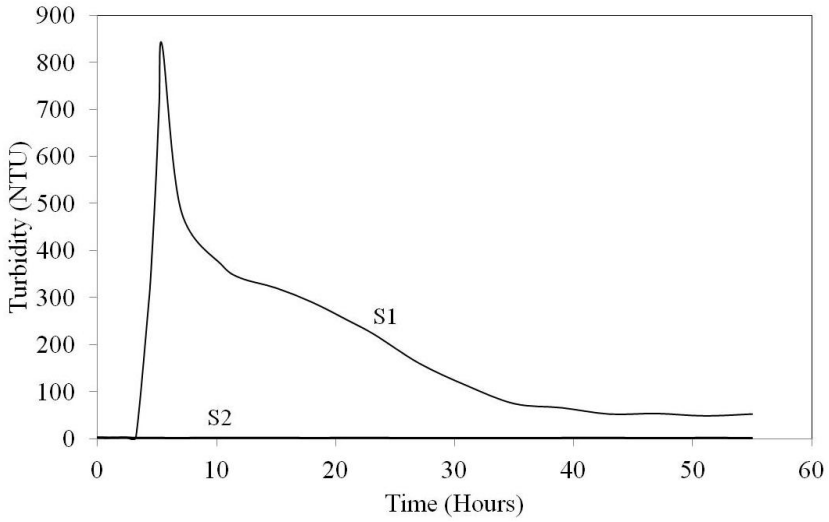

Figure A-2–1 Turbidity of solutions S1 and S2 as a function of aging time.

A-2.3.1 Solution 1 (S1)

To establish an internal standard for Au 4f chemical shifts (CS), a Au foil sample (R0), $KAuCl_4$ (R1) in solution and AuCl in solution were studied using the same instrument parameters. The binding energies for Au^{3+} (R1) and Au^{o} (R0) are tabulated in Table A-2–2. The standard value reported for Au^{+} was taken from the literature as the AuCl salt was not stable in solution and decomposed to Au^{3+} and Au^{o}. The binding energy shift for the Au 4f peak obtained from the Au^{+} species depends extensively on the environment for the Au atom and varies between 0.5 eV for tetraethyammonium Au^{+} halides [15] to 2.3 eV for AuCl [16].

Thermodynamic calculations have shown that for aqueous solutions soft ligands (less electronegative donors) such as CN^{-} form stable complexes with Au^{+} species while hard ligands such as Cl^{-} form stable species with Au^{3+} ($AuCl_4^{-}$) rather than Au^{+} ($AuCl_2^{-}$), and the latter goes through a disproportionation reaction according to:

$$3AuCl_2^{-} \rightarrow 2Au + AuCl_4^{-} + 2Cl^{-} \qquad \text{Equation A-2 – 4}$$

The stability of Au chloride complexes also depends on the presence of reducing agents and pH [17]. It is well established that at low pH (<5.8) the $AuCl_4^{-}$ complex is more stable in aqueous solutions. [18] A large chemical shift

(3.1 eV) was observed for an aqueous solution of $KAuCl_4$ (R1 in Table A-2–2), at a pH of 3.8, which was consistent with the formation of an $AuCl_4^-$ complex.

Table A-2–2 Binding energies (eV) for the Au 4f peaks of various standards and freshly prepared and aged S1 (peak indexing was performed with reference to the standards).

	Au $4f_{5/2}$	**Au $4f_{7/2}$**	**CS Au $4f_{7/2}$**	**Components**	**pH**
Au^o (R0)	87.95	84.25	----	----	----
Au^{+3} (R2)	90.95	87.35	3.1	----	3.8
Au^+ ([15, 16])	----	----	0.5-2.3	----	----
S1 fresh	88.37	84.77	0.52	Au^+	6.4
	89.90	86.15	1.90	Au^{3+}	
S1 3-h aged	88.15	84.65	0.40	Au^+ & Au^o	6.4
	89.90	86.15	1.90	Au^{3+}	
S1 20-h aged	87.95	84.35	0.10	Au^+ & Au^o	6.4
	90.15	86.35	2.1	Au^{3+}	

Figure A-2–2(a) shows the Au 4f XPS spectra for fresh S1 as well as solutions aged for 3 and 20 hr. Two sets of doublet peaks were identified by deconvolution to Gaussian-Lorentzian line shapes. The corresponding binding energies are given in Table A-2–2. By comparison with the standards provided (Table A-2–1), the doublet peaks at higher binding energies are assigned to Au^{3+} species for all solutions. The peak at 84.77 eV (CS= 0.52 eV) for the fresh solution was assigned to Au^+, while the peaks at 84.65 eV (CS= 0.40 eV) and 84.35 eV (CS= 0.10 eV) for 3-hr and 20-hr aged solutions are attributed to a mixture of Au^+ and Au^o species. It should be noted that the binding energies for Au^+ (bonded to chloride) and Au^o are very close. Figure A-2–2(a) also shows that the intensity of the Au^{3+} peaks increases relative to Au^+/Au^o peaks as S1 ages.

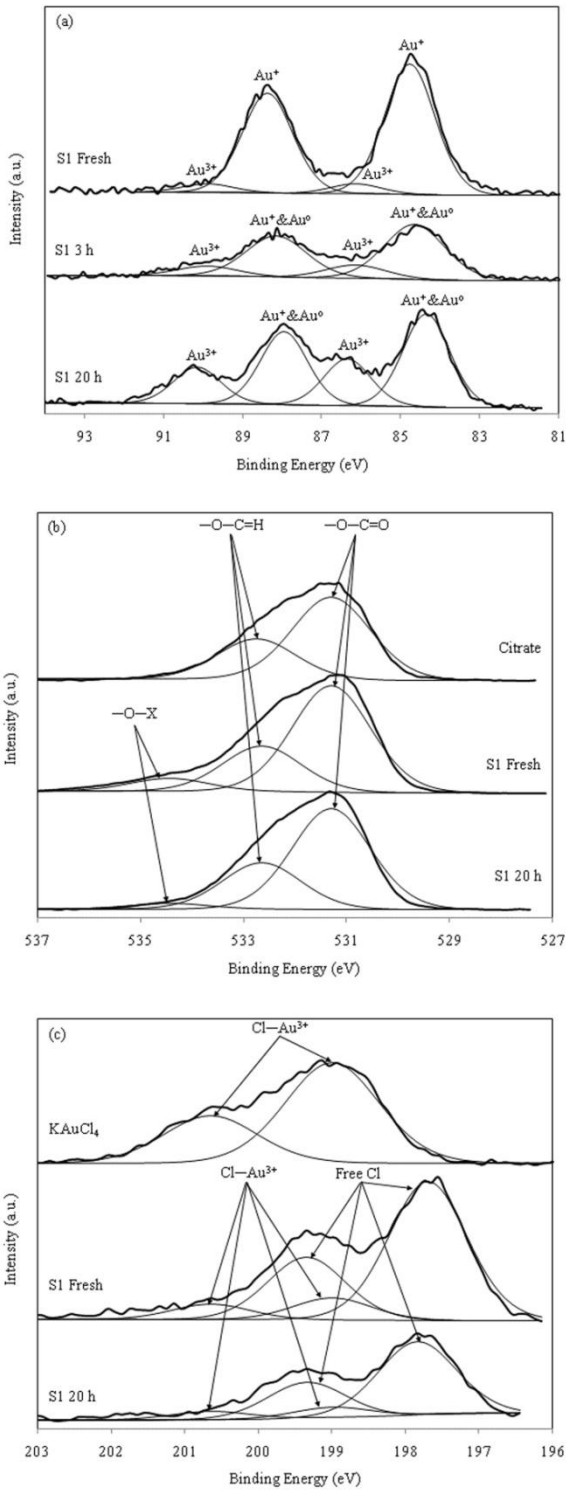

Figure A-2–2 XPS spectra for (a) Au 4f, (b) O 1s and (c) Cl 2p regions of fresh and aged S1 along with the internal standards.

The O 1s XPS spectra for fresh and 20 hr-aged S1 and tri-ammonium citrate (R1) are shown in Figure A-2–2(b) and the binding energy values are given in Table A-2–3. Two peaks were deconvoluted for tri-ammonium citrate corresponding to different O atom surroundings. The peak at 531.3 eV is assigned to O in ─O─C=O groups and the peak at 532.75 is assigned to ─C─O─H groups [19]. For S1, the peak corresponding to the ─O─C=O oxygen group occurred at binding energies similar to those for citrate (531.3 eV) while the peak for the ─C─O─H group is shifted slightly to lower binding energies (CS= 0.1 eV). This small shift can be attributed to the formation of a small amount of ─C=O type oxygen bonding. More importantly, upon addition of $KAuCl_4$ to the citrate solution, a weak O 1s peak was formed at 534.45 eV which was not observed for citrate solutions. This can be attributed to the formation of a bond with Au^{3+} or Au^{+} atoms which decreases the electron density of oxygen in the carboxyl group, thereby decreasing the screening of the core electrons and increasing their binding energy. It should be noted that the initial concentration of citrate (100 g/L) is much higher than the concentration of $KAuCl_4$ (5 g/L). This explains the low intensity of the peak at 534.45 eV which originates from bonding with Au.

Table A-2–3 Binding energies (eV) for the O 1s peaks of the citrate standard and freshly prepared and aged S1 (peak indexing was performed using reference [19]).

Oxygen bonding types	**O 1s**		
	─O─C=O	**─C─O─H**	**O─X**
Citrate (R1)	531.3	532.75	----
S1 Fresh	531.3	532.65	534.45
S1 20-h aged	531.3	532.65	534.45

Figure A-2–2 shows the XPS Cl 2p core level photoelectron spectra for $KAuCl_4$ (R2) and fresh and 20-hr aged S1. Two sets of doublet peaks were identified by peak fitting; the binding energies of these peaks are listed in Table A-2–4. The data suggest that most of the Cl atoms in both fresh and aged S1 are in free Cl^{-} form, while a very small amount of Cl atoms is bonded to Au^{3+} cations as confirmed by the low intensity doublet peaks at 200.65 eV and 199 eV.

Table A-2–4 Binding energies (eV) for the Cl 2p peaks of $KAuCl_4$ standard (R2) and freshly prepared and aged S1.

Cl peak types	Cl $2p_{1/2}$	Cl $2p_{3/2}$	Components
$KAuCl_4$ (R2)	200.65	199	----
AuCl [20]	----	198.6	----
S1 fresh	199.35	197.7	Free Cl^-
	200.65	199	$Cl{-}Au^{3+}$
S1 20-h aged	199.35	197.7	Free Cl^-
	200.65	199	$Cl{-}Au^{3+}$

A common method to prepare colloidal Au particles is the one developed by Turkevich *et al* [21] based on citrate reduction of $HAuCl_4$ at the solution boiling temperature. It has been suggested that the formation of Au particles is preceded by oxidation of citrate ions to acetonedicarboxylate which then forms clusters of multidentate complexes with unreduced Au^{3+} [21,22]. The envisaged reaction mechanism, however, does not account for the formation of Au^+ complexes which were observed in the present study. In a similar study, Rodriguez-Gonzalez *et al* [23] suggested that the formation of Au nanoparticles is controlled by the formation of $AuCl_2^-$ which then disproportionates into Au^{3+} and Au^o [23]. The role of citrate ions as a reducing agent, however, was not explored in this latter study.

Considering the cryo-XPS results presented in Figure A-2–2 and Table A-2–2, Table A-2–3 and Table A-2–4, the following series of reactions can be postulated to occur upon mixing the citrate solution with $KAuCl_4$:

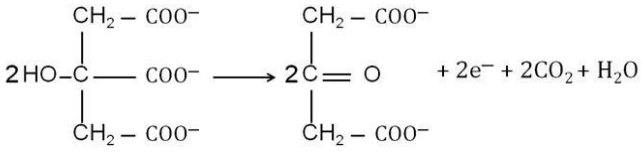

Equation A-2 – 5

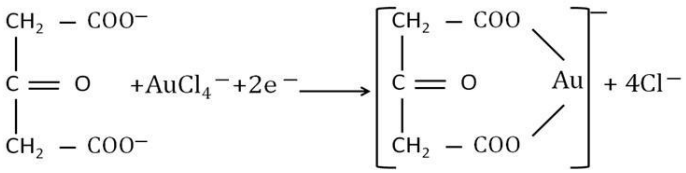

Equation A-2 – 6

Reduction of $AuCl_4^-$ and the formation of an unstable Au^+ complex, oxygen bonded to acetonedicarboxylate, explains the high binding energy O 1s peak at 534.45 eV observed for S1 (Table A-2–3) and also the high intensity of Cl 2p doublet peaks corresponding to free Cl^- ions (Table A-2–4). In this respect, the observed 0.1 eV chemical shift for the C─O─H group compared to pure citrate (Table A-2–3) can be attributed to oxidation of citrate and formation of the ─C=O bond in acetonedicarboxylate. The increase in turbidity (Figure A-2–1), gradual precipitation of particles and consumption of Au^+ followed by the formation of Au^{3+} (Figure A-2–2(a)) over time can be attributed to the disproportionation reaction of the above-mentioned unstable Au^+-acetonedicarboxylate complex according to:

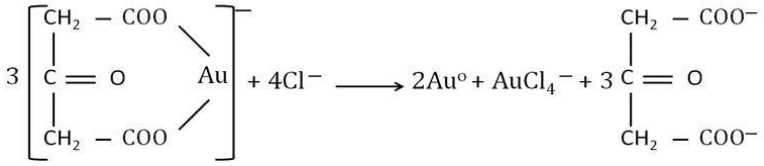

Equation A-2 – 7

The weak doublet Cl 2p peak corresponding to a Cl─Au^{3+} type bond (Figure A-2–2(c)) shows that Au^{3+} species formed by disproportionation are bonded to Cl instead of forming a Au─O type bond. It should be noted that 3 moles of Au^+ species form 2 moles of Au precipitates and 1 mole of Au^{3+} species. This explains the increase in the relative intensities of both Au^{3+} and Au^+/Au^o doublet peaks with solution aging.

TEM analysis was utilized to confirm the formation of Au particles as S1 ages. For this purpose, as described in the Experimental Procedure, a droplet of solution (fresh and aged) was placed on a carbon coated copper grid and allowed to dry in air. TEM bright field images of the samples extracted from fresh and 20 hr-aged solutions along with the SAD patterns are shown in Figure A-2–3. These

confirm the formation of Au particles. The number of particles in the freshly prepared solution was very small and their size was less than 40 nm. Closer examination of these particles shows that they are formed by agglomeration of nanosized primary particles. Chow and Zukoski [24] explained that the initial agglomeration of Au particles formed by citrate reduction is due to a combination of van der Waals, electrostatic and short-range repulsive interaction potentials. Figure A-2–3(b) shows a TEM image of the sample aged for 20 hr and indicates the formation of a network of Au particles. The mechanism of formation of this morphology is not clear and needs further investigation. However, it appears that the large aggregates are dispersed as the solution ages, likely as a result of an increase in surface repulsive potential.

A-2.3.1 Solution 2 (S2)

The Au 4f photoelectron spectra of freshly prepared and aged S2 (2040 hr) were obtained and are plotted in Figure A-2–4(a). The binding energy values are summarized in Table A-2–5. The addition of sodium sulfite to S1 stabilized the Au^{+} species with a 0.9-1 eV CS relative to the Au^{o} standard; the CS does not change appreciably with aging. This result shows that aging does not change the valence population of the 5d-orbitals for Au^{+}. The O 1s spectra (Figure A-2–4(b) and Table A-2–6) were similar to the spectra for S1 with two peaks attributed to ─O─C=O (531.3 eV) and ─C─O─H (532.65 eV) oxygen groups and an additional peak at 534.45 eV. This can be explained as follows: as the ─O─H bonds are replaced by $O─Au^{+}$ bonds the valence electron density of oxygen atoms decreases followed by an increase in binding energy. For Cl 2p spectra (Figure A-2–4(c)), only one set of doublet peaks was resolved and these originated from the presence of free Cl^{-}. Unlike S1, the Cl 2p spectra for S2 showed no evidence of Au-Cl type bonding. TEM observation of samples extracted from freshly prepared and aged S2 (2040 hr) confirmed that the long-term low turbidity and high stability of this solution is associated with the absence of any Au particles.

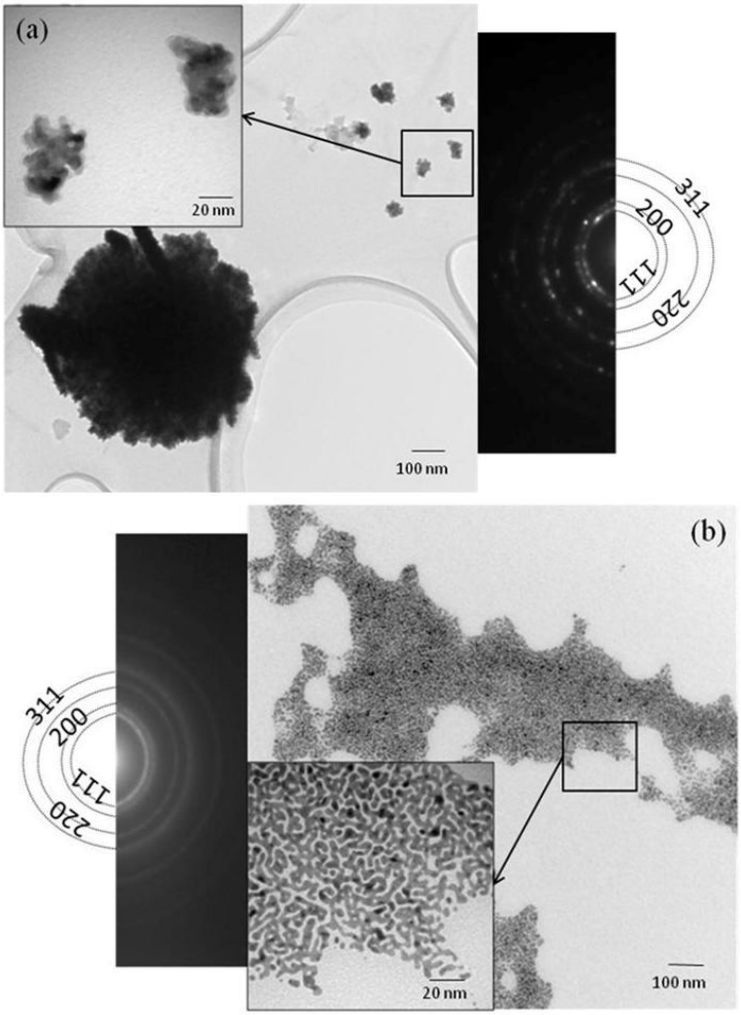

Figure A-2–3 TEM bright field images of samples extracted from (a) freshly prepared and (b) 20 hr-aged solutions together with corresponding indexed SAD patterns.

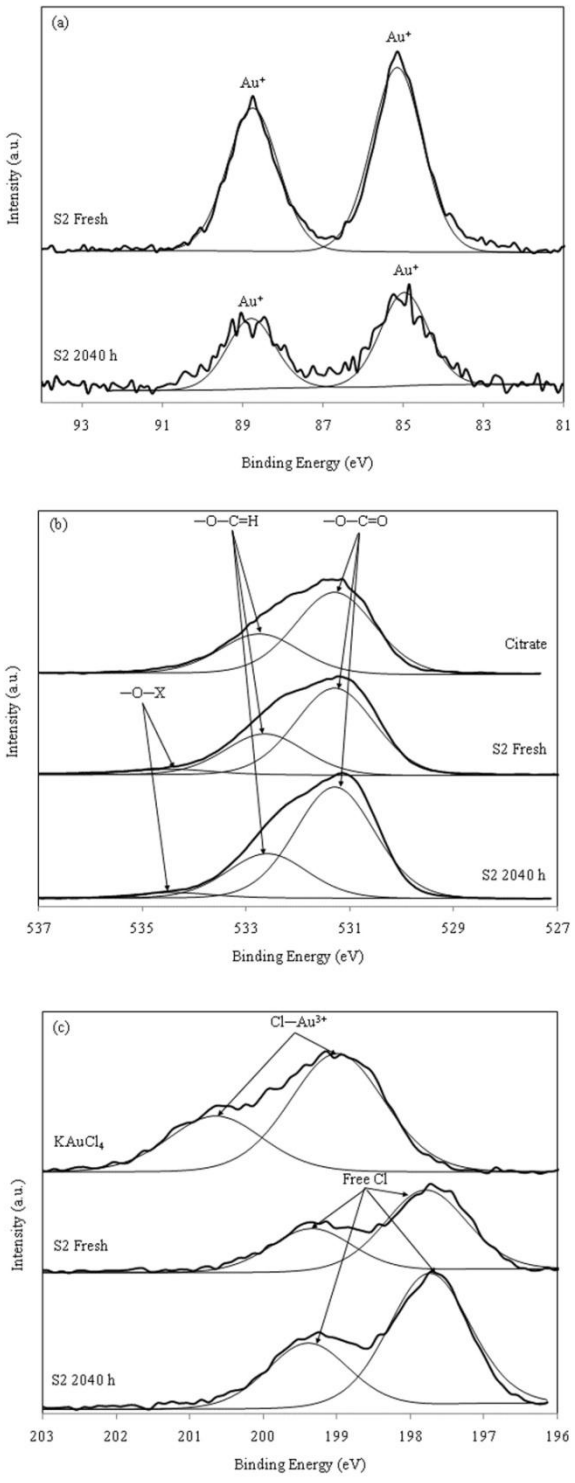

Figure A-2–4 XPS spectra for (a) Au 4f, (b) O 1s and (c) Cl 2p regions of fresh and aged S2 (2040 h) along with internal standards.

Table A-2–5 Binding energies (eV) for the Au 4f peaks of various standards, freshly prepared and aged S2 along with the pH values of the solutions (peak indexing was performed with reference to the standards).

Au peak types	Au $4f_{5/2}$	Au $4f_{7/2}$	CS Au $4f_{7/2}$	Components	pH
Au^{o} (R0)	87.95	84.25	----	----	----
Au^{+3} (R2)	90.95	87.35	3.1	----	3.8
Au^{+} ([15,16])	----	----	0.5-2.3	----	----
S2 fresh	88.75	85.15	0.9	Au^{+}	7.0
S2 2040-h aged	88.85	85.25	1.0	Au^{+}	6.9

Table A-2–6 Binding energies (eV) for the O 1s peaks of the citrate standard and freshly prepared and aged S2 (peak indexing was performed using reference [19]).

O bond types	O 1s		
	─O─C=O	**─C─O─H**	**O─X**
Citrate (R1)	531.3	532.75	----
S2 fresh	531.3	532.65	534.45
S2 2040-h aged	531.3	532.65	534.45

Reaction of sulfite with Au^{3+} ions gives $Au(SO_3)_4^{5-}$, which has a square-planar geometry with S-bonded sulfite and can be reduced by excess sulfite to $Au(SO_3)_2^{3-}$. The latter is expected to contain linear Au^{+} with S-bonded sulfite ligands [25]. The stabilities of the Au^{+} and Au^{3+} sulfite complexes are, therefore, dependent on the presence of reducing agents (such as sulfite) and also complexing agents. The Au^{+} sulfite plating solutions with no additional complexing agents are known to be unstable and disproportionate into metallic Au precipitates and Au^{3+} ions [8]. As described in the Section A-2.1, a mixture of $KAuCl_4$ and sodium sulfite precipitated within two days to two months depending on the order of mixing. Tri-ammonium citrate, therefore, plays a crucial role in stabilizing $Au(SO_3)_2^{3-}$ complexes in S2. Taking into account the order of mixing, *i.e.*, tri-ammonium citrate was mixed with $KAuCl_4$ to which Na_2SO_3 was added, it can be assumed that a Au^{+}-acetonedicarboxylate complex forms upon the first stage of mixing. The addition of Na_2SO_3 to this mixture then forms a stable Au^{+}

complex with likely one bond to acetonedicarboxylate through O and one bond to SO_3^{2-} through S according to:

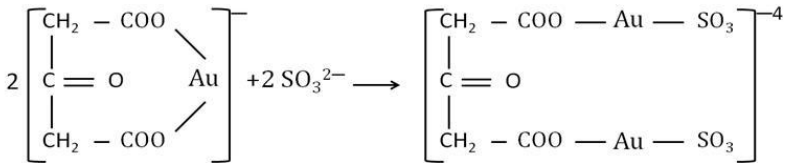

Equation A-2 – 8

The geometry and coordination of the suggested complex needs more investigation, however, this study provides evidence for the contribution of tri-ammonium citrate to the stability of Au^+-sulfite complexes via formation of an Au^+─O type bond.

A-2.4 Conclusions

The nature of complexes and precipitates and the stability of a sulfite-based Au plating solution were studied using turbidity measurements, cryo-XPS analysis and TEM observations. Tri-ammonium citrate reduced Au^{3+} in $KAuCl_4$ and formed an unstable Au^+-acetonedicarboxylate complex which decomposed upon aging to Au precipitates and Au^{3+} in $AuCl_4^-$ form. The addition of sulfite to this mixture formed a stable Au^+ complex in which Au^+ is likely bonded to both acetonedicarboxylate and sulfite groups. This study, therefore, revealed that presence of citrate greatly affects the stability of solutions via the formation of a stable complex with Au^+-sulfite. The chemistry of the Au^+ complexes resolved in this study is useful for understanding the effect of chemical components on solution stability and the mechanism of plating from this solution.

A-2.5 References

[1] T.A. Green, Gold Bull. **40**, 105-14 (2007).
[2] W. Sun, D.G. Ivey, Mater. Sci. Eng. B. **65**, 111-22 (1999).
[3] W. Tang, A. He, Q. Liu, D.G. Ivey, J. Electron. Mater. **37**, 837-44 (2008).
[4] A. He, Q. Liu, D.G. Ivey, Plat. Surf. Finish. **92**, 30-7 (2005).
[5] P. Wilkinson, Gold Bulletin. **19**, 75-81 (1986).
[6] Y. Okinaka, M. Hoshino, Gold Bull. **31**, 3-13 (1998).
[7] F Zuntini, G Aliprandini, J Gioria, A Meyer, S Losi. Amine Gold Complex Useful for the Electrodeposition of Gold and its Alloys. US Patent 1974/3787463.
[8] H. Honma, Y. Kagaya, J. Electrochem. Soc. **140**, L135-7 (1993).
[9] PT Smith. Gold Plating Bath and Process. US Patent 1962/3057789.
[10] DG Foulke, JM Deuber. Sulfite Gold Plating Bath and Process. US Patent 1976/3990954.
[11] RJ Morrissey. Non-cyanide electroplating solution for gold or alloys thereof. US Patent 1994/5277790.
[12] A. He, Q. Liu, D.G. Ivey, J. Mater. Sci.: Mater. Electron. **20**, 543-50 (2009).
[13] A. He, Q. Liu, D.G. Ivey, J. Mater. Sci.: Mater. Electron. **17**, 63-70 (2006).
[14] J.F. Watts, An introduction to surface analysis by XPS and AES (J. Wiley, New York, 2003).
[15] A. McNeillie, D.H. Brown, W.E. Smith, M. Gibson, L. Watson, J. Chem. Soc. Dalton. **5**, 767-70 (1980).
[16] H. Kitagawa, N. Kojima, T. Nakajima, J. Chem. Soc. Dalton. **11**, 3121-5 (1991).
[17] N.P. Finkelstein, R.D. Hancock, Gold Bull. **7**, 72-7 (1974).
[18] P. Pan, S.A. Wood, Geochim. Cosmochim. Acta. **55**, 2365-71 (1991).
[19] D. Atzei, C. Sadun, L. Pandolfi, Spectrochim. Acta A **56**, 531-40 (2000).
[20] K. Kishi, S. Ikeda, J. Phys. Chem. **78**, 107-12 (1974).
[21] J. Turkevich, P.C. Stevenson, J. Hillier, Discuss. Faraday Soc. **11**, 55-75 (1951).
[22] J. Turkevich, P.C. Stevenson, J. Hillier, J. Phys. Chem. **57**, 670-3 (1953).
[23] B. Rodríguez-González, P. Mulvaney, L.M. Liz-Marzán, Z. Phys. CHem. **221**, 415-26 (2007).
[24] M.K. Chow, C.F. Zukoski, J. Colloid Interf. Sci. **165**, 97-109 (1994).
[25] R.J. Puddephatt, Comprehensive Coordination Chemistry; Late Transition Elements (Pergamon Press, USA, 1987) pp. 861-923.